ADELAIDE
UNIVERSITY
AUSTRALIA

PETROGRAPHIC IMAGE ANALYSIS AS A TOOL TO QUANTIFY POROSITY AND CEMENT DISTRIBUTION

By
John J. Nejedlik

Thesis submitted
In Fulfilment of the Requirement for
The degree of

MASTER OF SCIENCE

In

RESERVOIR GEOSCIENCE

At

The National Centre for Petroleum Geology and Geophysics (NCPGG)

Of

The University of Adelaide

July 2001

DECLARATION

This thesis contains no material which has been accepted for the award of any other degree or diploma in any university and, to the best of my knowledge and belief, the thesis contains no material previously published or written by any other person except where due reference is made in the text of the thesis. The author consents to the thesis being made available for photocopying and loan if accepted for the award of the degree.

John Nejedlik

1st July, 2001

For *Family* and *Friends*,

PETROGRAPHIC IMAGE ANALYSIS AS A TOOL TO QUANTIFY POROSITY AND CEMENT DISTRIBUTION

By *John J. Nejedlik* B.Sc. (Hons)

ABSTRACT

Porosity style and distribution for reservoir simulation are obtained by petrography through a combination of techniques including transmitted light microscopy, petrographic image analysis (PIA) and routine core analysis (RCA). The research focuses into the ability of PIA to map and quantify heterogeneity of porosity within a clean quartz arenite from the Hutton Sandstone that is commonly considered homogeneous, with the intention of developing a set of rules for the use of PIA to effectively measure porosity at optimum magnification with an optimum number of fields of view. Porosity descriptions involved analyses of the size, shape and distribution of pore spaces. The data sets produced provide partial coverage, along with full coverage of porosity across thin sections from the Hutton Sandstone. Statistical analysis was then applied to the data with the aim of understanding the spatial correlation by developing statistical models that mimic the pore distribution.

Semi-variograms obtained from statistical analysis imply that porosity shows very little correlation within the Hutton Sandstone at a microscale. This means that a set of rules to model porosity distribution involve determining the range of porosity values in the measured areas, then randomly distributing the range of values within the cross-bed set or flow unit to which those values apply. Spatial displays produced showed that PIA could be used to identify some of the factors that control porosity in sandstones, such as silt layering. Unfortunately, an extremely large number of readings are required for these to be recognised.

Through the use of a random number generator, it was determined that between 30 and 40 readings were required to calculate average porosity within one standard deviation of the true mean porosity. The use of pore casting and mercury injection capillary pressure (MICP), in association with SEM, provided a three-dimensional (3D) visual assessment of the connectivity between the pores and pore throats.

A series of image processing techniques available through PIA led to the recognition that large pores appeared grouped around apparent concretionary centers. Concretionary centers were a combination of quartz, quartz cement and kaolinite. The identification of these concretions suggest that the Hutton Sandstone should not be considered a series of sand-sized grains separating intergranular pores, but rather, should be considered a series of concretions separating interconnected porous zones.

ACKNOWLEDGMENTS

I would like to thank the APCRC for providing me with a scholarship and Santos Ltd. for providing the core from which the study was conducted.

Special thanks must go to my primary supervisor Dr. Nicholas Lemon for his help, guidance and patience throughout the duration of this study. I would also like to thank Val Pinczewski from the University of NSW for his help during my stay at the Centre for Petroleum Engineering (CPE), along with the remaining staff that assisted me with my work. Thanks also to Lincoln Patterson and Mark Knackstedt for their input.

I would like to thank the staff and students at the NCPGG, especially those who provided technical assistance, including Trevor Dhu, Max Watson, Rosalie Pollock, Scott Reynolds and Jerry Meyer.

Most thanks must be expressed towards my family for their support and in particular, their patience, especially at the times when it looked like I might never finish!

TABLE OF CONTENTS

LIST OF FIGURES, PLATES AND TABLES

TABLES

Chapter 1 INTRODUCTION

1.1 BACKGROUND

Reservoir simulation is a technique used in petroleum production where a reservoir volume is populated with parameters to predict and define the flow of hydrocarbons during production. Laboratory measurements of relative permeability and residual oil saturation are used as inputs to reservoir-scale simulators, however variations in laboratory measurements can be large. In petroleum reservoir engineering, errors in reservoir performance prediction are caused by inaccurate characterisation of the reservoir. Inaccurate prediction leads to significant amounts of hydrocarbon remaining unrecovered, thus preventing exploitation of the full reservoir potential. Another source of error is a lack of understanding of the pore-scale mechanisms responsible for mobilisation and recovery of oil.

The fundamental parameters required for a reservoir simulation study include a description of the reservoir rock and fluid flow properties. Fluid flow in a reservoir is controlled by bed continuity, the presence of obstructions to flow, permeability distribution and fluid properties such as viscosity (Weber, 1992). In a sandstone reservoir, heterogeneities that influence fluid flow include: large-scale faults, thin shale interbeds, sedimentary structures, sand to silt distribution, cement distribution, dissolution patterns and pore scale features.

Reservoir simulation requires a multi-disciplinary approach to define the parameters that populate a reservoir model. For ease of computation, the reservoir model is reduced to a set of cells that incorporate varied information that are combined into *flow units*.

The original definition of
A flow unit modified by Ebanks Jr. *et al.* (1992) "as a mappable portion of the total reservoir within which geological and petrophysical properties that affect the flow of fluids are consistent and predictably different from the properties of other reservoir rock volumes".

Flow units share common characteristics, however there is no universally applicable set of rules by which flow units are defined. To divide a reservoir into flow units requires an integration of stratigraphic, sedimentological, structural, petrographic, petrophysical and field performance data (Ebanks Jr. *et al.*, 1992).

The shape of the reservoir and the reservoir spill or leak point, as determined by the lowest closing contour, is defined by interpretation of seismic supported by the feedback of information from a well or wells intersecting the reservoir. The reservoir engineer provides porosity and permeability data from routine core analysis (RCA), the oil water contact (OWC), gas oil contact (GOC), and the degree of pore connectivity within the reservoir and the column height. The role of the geologist is to provide reservoir models that give a sufficient description of those parameters that control the fluid flow relevant to the planned simulation study (Harris, 1975). These include the distribution of the reservoir unit (whether it be channel sands, crevasse splays, sheets or blocky sands) as well as constraining the geographic dimensions of the flow units within the reservoir. The petrologist determines the distribution of pore size and the pore interconnectivity within the reservoir and identifies the link between porosity style and sedimentary units.

Data associated with pore connectivity is obtained from both pore casts and mercury injection capillary pressure (MICP). The latter provides direct information on the size of the pore throats within the unit. The porosity style and distribution is obtained from petrography by a combination of transmitted light microscopy, petrographic image analysis (PIA) and RCA.

A new tool used to assist in determining porosity distribution and connectivity is micro X-ray tomography (micro-CT analysis). X-ray tomography was developed in 1979 and is used extensively in medicine, but more recently, the technique has been modified and applied to other science disciplines such as geology. X-ray tomography is a three-dimensional (3D) non-destructive imaging technique that allows the internal microstructure of an object to be imaged.

The micro-CT scanner is an adaptation of X-ray tomography that allows for its use in geology. It is now possible to study the internal pore structure of a reservoir unit, from which fluid flow can be simulated and permeability calculated assisting to constrain the various heterogeneity types that might influence oil recovery. It is a quantitative imaging technique producing excellent 3D resolution of porosity, fracture or throat patterns, drilling fluid invasion on a local scale, and quantification of complex mineralogies in addition to depth of correlation of core with wireline-logs (Wellington & Vinegar, 1987).

A limitation of the use of micro-CT scanning in petroleum geology is the small sample size required for analysis. The sample is only $0.5cm^3$, which is not a true representation of the reservoir unit because reservoirs can exhibit great variation over small distances, and no unit (reservoir or non-reservoir) can be perfectly homogeneous.

1.2 PROJECT AIMS AND OBJECTIVES

The project objective was to provide a full description of thin section porosity across a selected interval of core. The classification of porosity by PIA provides a useful two-dimensional simplification of a three dimensional parameter (Ehrlich *et al.,* 1984; Ruzyla, 1986), and thus, PIA was used to test its ability as a mapping tool to quantify heterogeneity within a core that might normally be considered homogeneous. Description of porosity involved analysis of the size, shape and distribution of the porosity, with the aim of then upscaling these descriptions so they could be used as a predictive tool for reservoir simulation across a larger reservoir interval. If the porosity heterogeneity in sandstone can be understood and even modelled then it might be possible to use the information obtained in conjunction with the micro-CT scanning results to develop a virtual core-testing laboratory.

The core for this study was obtained from the Hutton Sandstone in Gidgealpa-17 in the Eromanga Basin. The Hutton Sandstone acts as both a major aquifer and an oil reservoir in the Eromanga Basin and is predominantly a thickly bedded quartz arenite with occasional rock fragment-rich, pebble-dominated conglomerate.

Core analysis (porosity and permeability) was conducted across three feet of this sandstone, which was obtained from within a total of 7 feet of core. The three aspects to the study were:

- An investigation of the uses and usefulness of PIA.

PIA is a relatively new tool used primarily for porosity determination in thin section. Prior to the introduction of PIA, calculation of porosity and mineralogy was done by point counting, a technique that analyses a large number of points which are then reduced to a single value for each thin section. PIA measures porosity across areas rather than accumulating points, thereby providing information on porosity distribution on a micro-scale. This is important because within this porosity distribution lies information on the sorting, layering, cross bedding, nature of cementation, cement distribution, pore connectivity and permeability of the rock. PIA allows study of the controlling factors influencing porosity whilst measuring and analysing the pores, and if these controls are better understood, it will enhance the ability to better predict reservoir quality. Ultimately, the aim was to provide a set of rules for the use of PIA to effectively measure porosity using the optimum magnification and the optimum number of fields of view.

- Using PIA, an investigation was made to determine whether a sub-set of porosity measurements could be collected which might then be upscaled to fully describe porosity distribution. If this were so, there might then be an optimum pattern of the data collected to allow consistent porosity upscaling.

The aim was to determine whether the data could be applied to upscale porosity distribution by using statistics such as kriging to recreate thin section porosity, essentially producing a 2-D map of porosity. This would allow factors such as the most appropriate scale (magnification) to measure porosity distribution to be determined, along with the magnification that best defines a semi-variogram (part of kriging) that can then be used to assist in interpolation.

- The use of PIA to describe cement distribution in a clean quartz arenite.

The origin and controls on the distribution of quartz cement are still subject to disagreement and debate (Worden & Morad, 2000). Within the Hutton Sandstone samples, quartz cement and the primary quartz grains that constitute the framework of the rock are essentially the inverse of porosity, i.e. what is not quartz or quartz cement is porosity. By using PIA, it was anticipated it would be possible to determine the way in which cement invades reservoir sands.

Chapter 2 STUDY METHODS AND MATERIAL

2.1 MATERIAL

One metre of core had been collected from the Hutton Sandstone between depths of 1852.5 to 1854.8 metres in Gidgealpa-17 for a porosity-permeability study by micro-CT analysis. Since only a very small sample was used for the micro-CT study, the remainder was available for this study on reservoir heterogeneity.

2.2 METHODS

2.3 SAMPLING

The core had already been chosen, from which one piece was sent ($0.5cm^3$) for micro-CT scanning. The full oil field core obtained for sampling had a 1-inch continuous vertical plug or sub-core cut through it (Figure 2.1), which was sampled prior to the commencement of the project. From this sub-core, 14 thin sections were cut. The thin sections were cut end on end to give as near as complete continuous coverage of the core as possible. The remaining core already had routine core plug analysis (RCA) porosity and permeability data available. The sub-core was all sandstone. Unfortunately, it is not continuous across the entire interval because of thin silt interbeds, while the core from which the piece was sent for micro-CT scanning was not available for thin section analysis after preparation for scanning.

2.4 THIN SECTION PREPARATION AND ANALYSIS

Thin sections were prepared by Pontifex and Associates in Adelaide and were examined using an Olympus BHT petrographic microscope, to which a Video Pro 32 ™ image analyser was attached. The samples were cut perpendicular to the bedding plane and each slide was impregnated with blue-stained araldite prior to thin section preparation to facilitate description of porosity. Quantitative estimates of sandstone mineralogy (quartz, clays, feldspar, and cement) and porosity (including microporosity) were determined by area counts using petrographic image analysis (PIA). Photomicrographs were taken of all representative features of the thin sections using an Olympus camera on an Olympus BHSP Microscope. Traditional point counting was also conducted for two of the samples to check the accuracy of the PIA technique. The point count included quartz, feldspar, matrix, porosity, quartz cement and kaolin.

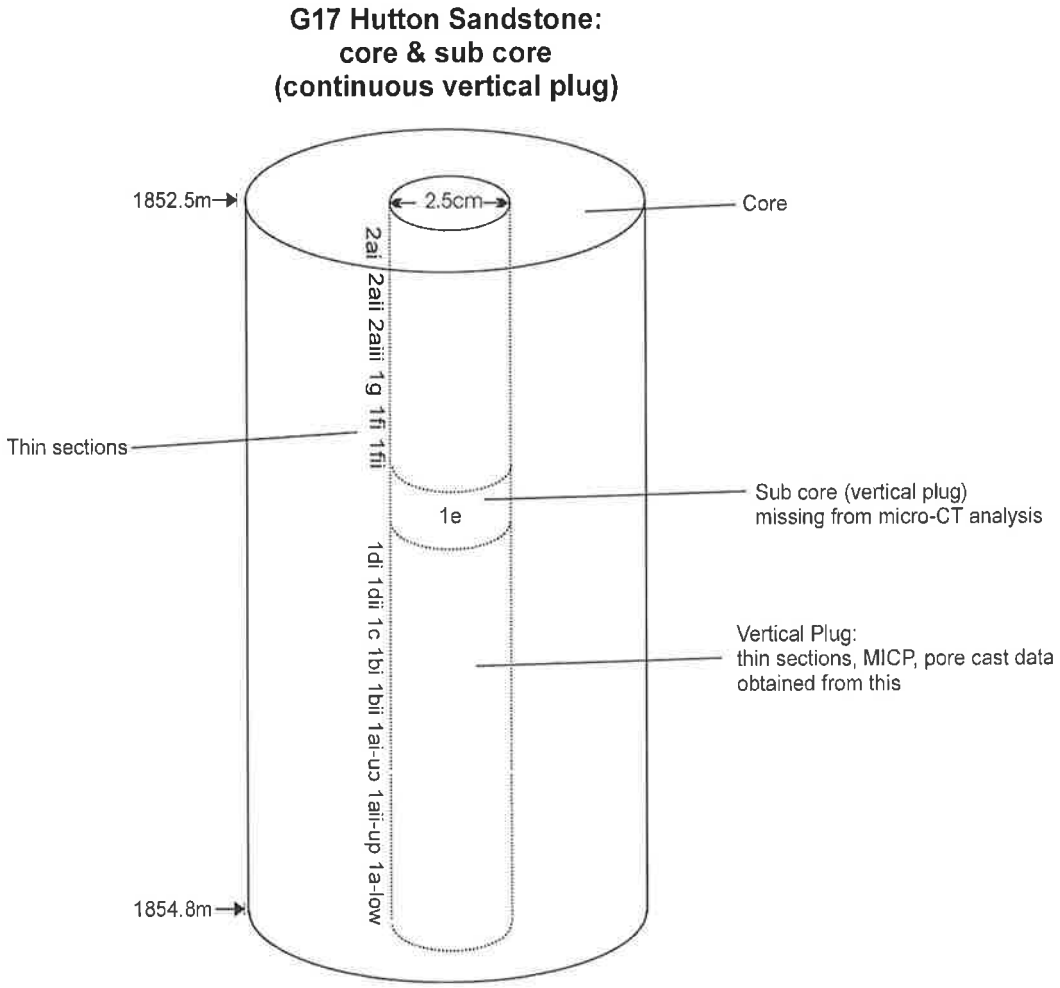

Figure 2.1: Schematic diagram of Hutton Sandstone core showing the depth, along with the position of thin sections obtained from the continuous vertical plug. The missing core is situated near the centre of the core. The numbering system was chosen to represent cross bed units (1 and 2), the pieces of core within those beds, (a-g) and the thin sections cut from each piece (i-ii, upper and lower).

2.5 PETROGRAPHIC IMAGE ANALYSIS (PIA)

2.5.1 Description of Technique:

Computer assisted analysis of microscopic images provides a means of making rapid, quantitative measurements of features observed in thin section. The software allows extraction and measurement of image features and provides a quantitative description of an image as numerical data. In this study, the PIA technique on thin sections was used in conjunction with point counting to evaluate relationships between porosity and pore geometry for the Hutton Sandstone samples. PIA was conducted on all 14 unpolished thin sections.

PIA can provide quantitative data on the size, shape and number of pores exposed in the thin section, which can then be correlated with petrophysical properties (Ehrlich & Davis, 1989). The principle of PIA has been described by Ehrlich *et al.*, (1984) and Ehrlich and Davis (1989). Figure 2.2 shows the equipment set-up used for PIA. The colour video camera is attached to an Olympus ™ BH-2 transmitted light microscope. The colour video camera acquires thin section images through the microscope, which were analysed by Video Pro 32 ™ software connected to the camera/microscope. This allows real-time computer screen display of video images of thin sections. The software allows extraction and measurement of image features and provides a quantitative description of an image as numerical data.

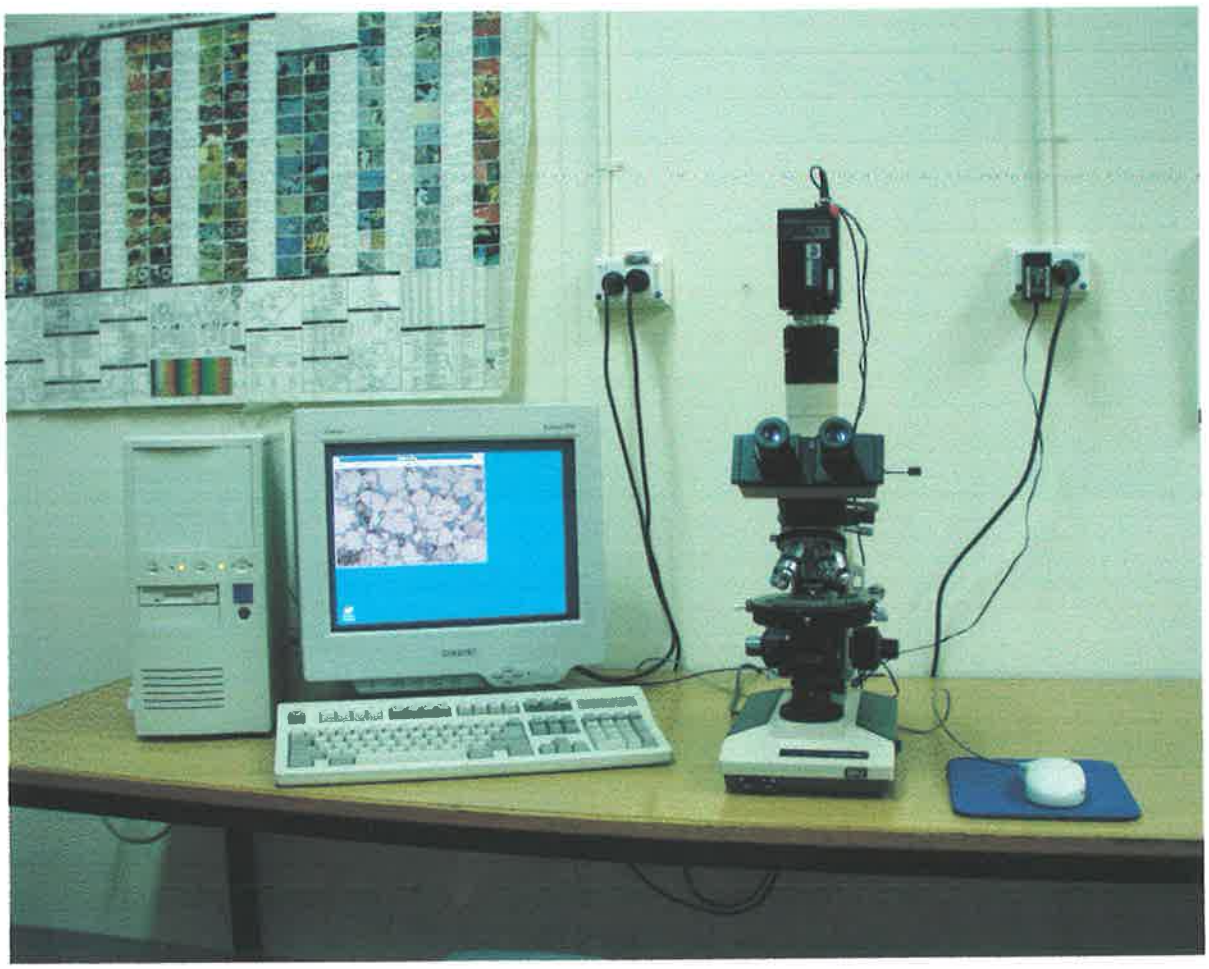

Figure 2.2: Basic set up of PIA system showing the microscope to the right with video camera mounted on top attached to the computer.

Identifying the pixels associated with a particular rock component (mineral, rock fragment, porosity etc.) permits the creation of a binary image wherein light intensities of the component pixels are discriminated from the rest of the image using a threshold colour code (red for instance). The fraction of each component in each field of view was then determined from the ratio of the number of component pixels to the total number of pixels in the field of view.

It is important to recognise however, that computer assisted PIA is simply a measurement tool and that no measurement is necessarily "correct". The resulting data can be influenced by a multitude of factors, particularly operator bias. Therefore, it is important to consider the whole image analysis system as an instrument that needs regular checking for the results to be reliable (Video Pro 32 Manual).

2.5.2 Process to determine Porosity:

The methods used to quantify porosity heterogeneity are included in Chapter 4. To determine porosity, the image analyser projects the live image of the thin section onto the screen. The steps outlined below are specific to the Video Pro 32 software used for this project but the principles are common to all image processing.

STEP 1 - Image Preparation: The image must be frozen prior to processing; this allows various parameters, not restricted solely to porosity, to be measured from the selected image field of view (e.g. mineralogy). Image freezing allows measurement of parameters even if the thin section is moved on the microscope stage. To freeze the image, the *Freeze* option from the *Image* toolbar dropdown menu (on the main screen) is selected (Figure 2.3).

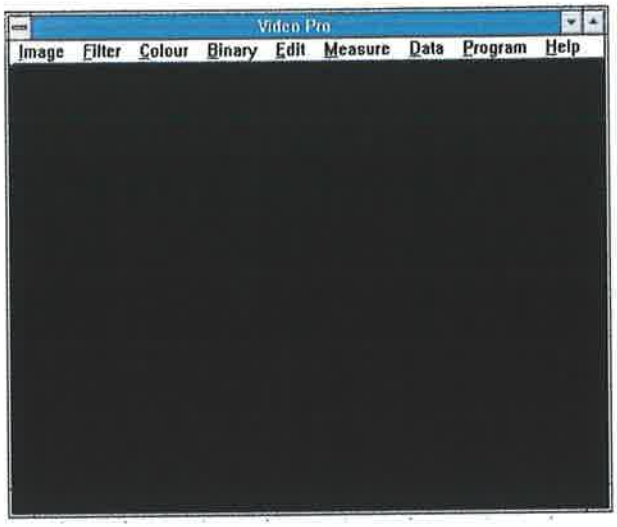

Figure 2.3: Menu screen of PIA software (Note that the Image selection is on the far left).

STEP 2 – Selection of parameters: The image analyser works by transmitted light colour or intensity recognition. By choosing *Select* from the *Colour* menu (Figure 2.4), porosity in the field of view can be sampled by using the mouse to click within the blue porosity regions on the screen image. Within the *Colour Select* box that appears, by selecting *Detect*, the porosity should then be detected and highlighted in red as an overlay.

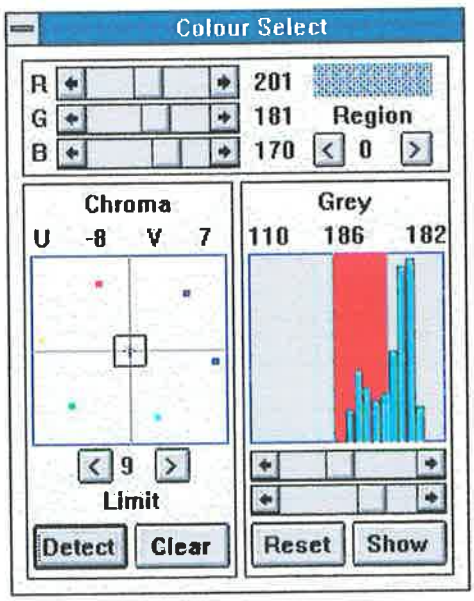

Figure 2.4: Colour Select Box. The colour indicated at the top right is the current selection the PIA is analysing. The histogram indicates what part of the spectrum that the selected colour exists in.

Errors in the porosity selection process (e.g. variations in staining of the thin section) and boundary sampling mean that all of the porosity is not always perfectly covered. This requires the image to then be processed, which is done by selecting *Process* from the *Binary* menu bar (Figure 2.5).

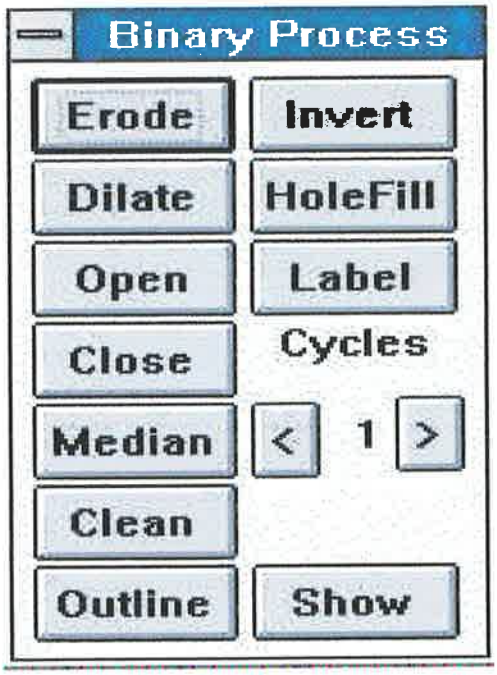

Figure 2.5: Binary Process Box with functions that permit the user to alter the overlay.

This processing method allows the selection to be altered manually. By using the *Erode* function within this same menu box, the boundary overlay is smoothed and shrunk by one pixel. Conversely, the *Dilate* function expands the overlay by one pixel. The *Close* operation closes holes and gaps by dilation to join the edges and subsequent erosion to restore the area to the original size. The result is a 'closed' version of the original overlay (Video Pro 32 manual). The *Binary Clean* function and *Binary Median* functions are similar. The difference between them is that the *Binary Clean* function only smoothes positive binary pixels, i.e. holes in the overlay do not get smoothed or filled, meaning that closely spaced features can be smoothed without being joined.

Another way of highlighting the porosity is by using the *Image Histogram* option (Figure 2.6). This enables the intensity of the image to be displayed as a histogram, thus providing an option for particular colour ranges to be chosen for observation.

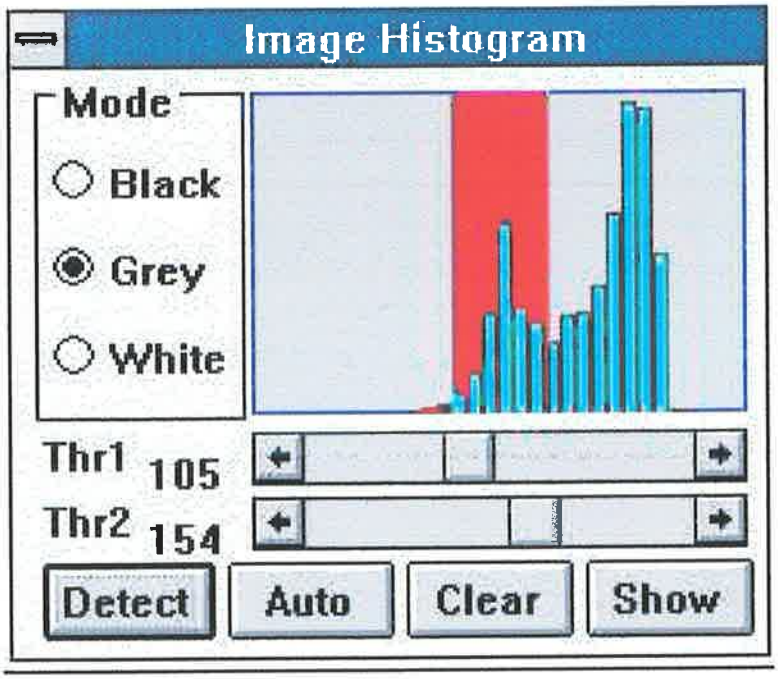

Figure 2.6: The image histogram box is another method to analyse particular colours.

STEP 3 - Measurement: To measure the porosity as a percent, the *Fraction* option from the *Data Select* menu must be chosen (Figure 2.7 (i)). This places the fraction selection as the computer's current calculation option. *View* is selected from the *Measure* menu (Figure 2.7 (ii)), and then *Fraction,* from the new box that appears. This activates the computer's ability to calculate the fraction of pixels selected compared to the total number of pixels on screen. The resultant calculation will be printed on screen once *Field* from the *Measure* menu bar (Figure 2.3) is selected.

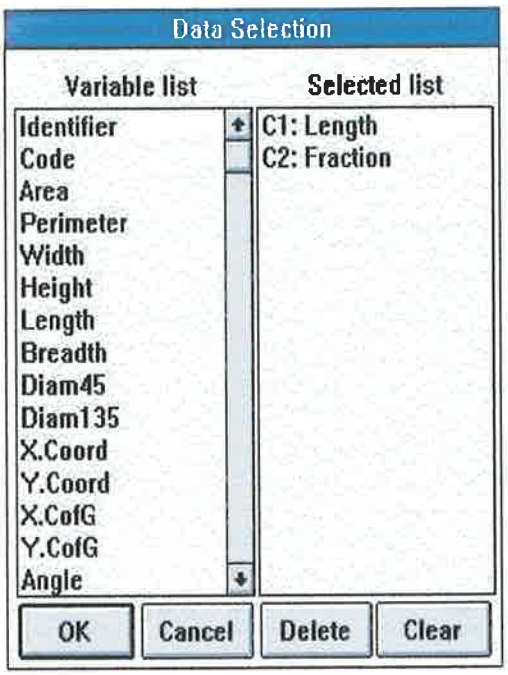

Figure 2.7(i)

Figure 2.7(ii)

Figure 2.7 (i): Data Selection box which provides the various options that might need analysing.

Figure 2.7 (ii): View Measurement box. The current selection indicates that lengths are about to be measured, which would require changing to fraction to determine porosity as a percentage.

2.5.3 Process to determine Grain size and Pore size:

The same process is used to calculate both the grain size and pore size of the samples. Although it is not essential to freeze the image to measure line lengths using PIA, it is a good habit to freeze the image before commencing calculations. This prevents any troubles if the thin section is moved accidentally resulting in that field of view being altered.

In calculating lengths using PIA, the field of view must be calibrated according to the magnification. This is done under the *Data Calibrate* tool bar (Figure 2.8). This allows both the horizontal and vertical dimensions to be calibrated for the selected magnification because the aspect ratio of the field of view changes with variation in focussing currents on the video display. Each objective lens needs to be calibrated.

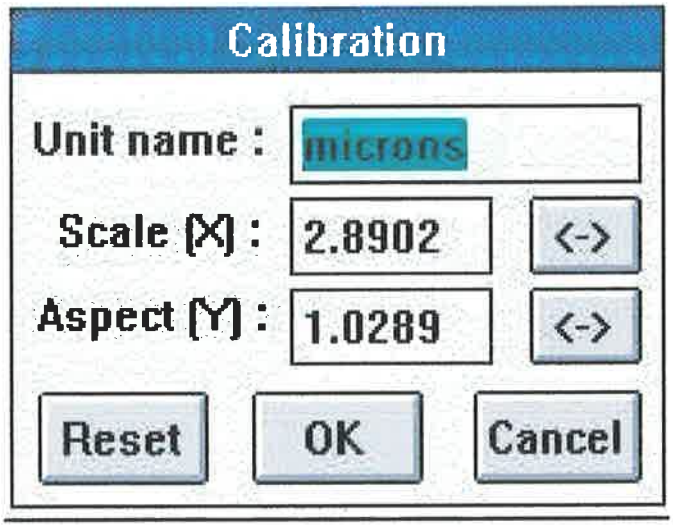

Figure 2.8: Data Calibrate Box showing that lengths will be measured in microns, while the two horizontal arrows besides X and Y allow the user to calibrate according to the magnification being used.

Following calibration of the field of view, *Length* is selected from the *Data Select* menu. Then, under the *View Measurement* menu, *Length* must again be selected as the computer's current calculation option. It is now possible, under the *Measure* menu toolbar to select *Measure Line.* Using the mouse, the *Measure Line* selection then allows lines to be drawn across individual grains or individual pores, along side of which the length is given in microns. It is then possible to store these data by using the available statistics package in conjunction with *Data New* from the menu bar (see Video Pro manual).

The image analyser was used to measure the long dimensions of approximately 200 to 250 quartz grains and 100 to 150 pores per thin section. This was done so that a more representative average of grain size and pore size was obtainable from each thin section.

2.5.4 Process to determine Quartz cement:

The PIA technique is unable to distinguish between primary quartz grains and quartz cement because they share the same colour, hence the colour recognition technique is of no assistance. Therefore, the process to estimate the amount of quartz cement in

each field of view must be done manually. Selecting the *Draw* function from the *Edit* menu allows manual drawing on the field of view (Figure 2.9), allowing an overlay to be drawn manually on screen using the mouse to control the position of the overlay. If *Cover* is selected, altering the value under the size box changes the size of the drawing instrument. Errors can be corrected, but they too must be corrected manually by using the *Erase* option.

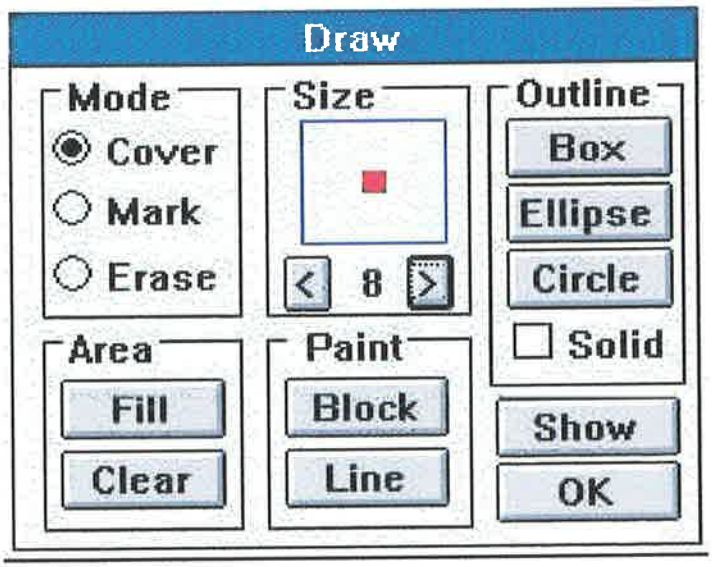

Figure 2.9: The edit draw box allows the user to manually edit the overlay of the image. The overlay can be covered further, or have inaccurate information erased.

2.5.5 Cement cluster analysis:

There were two methods employed to study the clustering of quartz cement using the image analyser.

Method 1-Evidence of clustering by pore selection:

Performing an iterative Erosion-Dilation sequence on a binary overlay (explained in Chapter 5: Cement Emplacement), results in the removal of small pores, leaving only large primary pores. This overlay discriminates between areas on the thin section that are tightly cemented and areas of large pores.

Method 2 – Evidence of clustering by total quartz selection:

The production of a binary overlay of the total quartz in the thin section (the sum of framework quartz grains and quartz cement), allows easy identification of the shape of the porosity compared to quartz arrangement. This technique is the same as Method 1, but is just a different way of highlighting the clustering, essentially producing an inverse image of that produced by Method 1. The actual process of creating the binary overlay is the same as above.

2.6 CATHODOLUMINESCENCE (CL) MICROSCOPY

Cathodoluminescence Analysis was conducted on three of the fourteen samples using a *Patco ELM-RX* Cathodoluminoscope (CL) on a *Leitz Orthomat E automatic* microscope. These three samples (G17: 1aii upper, 1fi, and 2aii) were selected because they were from parts of the core with differing porosity. CL petrography is a sophisticated technique for analysing carbonate and quartz cement stratigraphy. When minerals are excited by high-energy electrons, some of the minerals emit visible light, called Cathodoluminescence, in response to the presence of various impurities (excitors and/or enhancers) or defects in the crystal lattice (Miller 1988). CL analysis helps indicate the various cements in relation to each other and aids in the interpretation of the diagenetic sequence for the samples and the region. In this study, the primary use of CL was to identify the quartz overgrowths within the samples and compare these data with previously point counted data. Electron gun voltages and beam currents of 14 kV and 0.67 *m*A respectively were used whilst the unpolished thin sections were held under vacuum between 60 and 70 milliTorr. CL photomicrographs were taken at 2 to 4 minute exposure times in integral metering mode with *Kodak Ektapress* 1600 ASA film.

2.7 SCANNING ELECTRON MICROSCOPY (SEM)

The detailed examination of mineral morphology, grain-cement relationships and pore geometry are greatly enhanced by scanning electron microscopy. SEM studies were carried out on four of the available fourteen samples. The samples G17: 1ai upper, 1dii, 1fi and 2ai were selected because they were spread across the core and thus, are likely to reflect the range in composition of mineralogy and porosity. Samples 1ai upper and 2ai were located within cross-bed sets 1 and 2. Blocks 5mm x 5mm x 3mm

were glued to aluminium pin-type stubs then coated with carbon and gold/palladium (according to methods by (Trewin, 1991)), to study the texture, authigenic minerals and in particular for the pore casts, to study the pore types, from which stereographic images were created using the computer-assisted stereo function. A *Philips XL30* field Emission Scanning Electron Microscope (FESEM) was used at the University of Adelaide Centre for Electron Microscopy and Microanalysis (CEMMSA).

2.8 MERCURY INJECTION CAPILLARY PRESSURES (MICP)

Mercury injection capillary pressure was used primarily to obtain the pore throat size distribution for five of the available fourteen samples. The samples (G17: 1ai-low, 1ai-upper, 1dii, 1fi and 2ai) were selected because the core variation is reflected within them, and four of these same five samples were then selected for pore cast analysis. The mercury injection was conducted to constrain the pore throat diameters, which are controlled by the size and arrangement of pores and throats, which in turn, control porosity and permeability (McCreesh *et al.,* 1991). Mercury-injection capillary pressure curves provide additional information on the size distribution of pore throats. This information is related to the size of pores and throats, when measured directly from the pore casts. This technique was also used in conjunction with data obtained from pore cast analysis to calculate the recovery efficiency of the reservoir. Mercury injection capillary pressures were measured using a Micrometrics Autopore 9410 Mercury Injection Porosimeter at Amdel Corporation, South Australia.

2.9 PORECAST ANALYSIS

A rock impregnated with plastic serves the multiple purpose of providing material for thin sections, pore casts, and pore cast-thin sections (Pittman & Duschatko, 1970). Pore casts were prepared for four of the available fourteen thin sections from samples ($<1cm^3$) that were impregnated with blue dyed epoxy resin. Each sample was first impregnated within a pressure chamber. A vacuum removes the air from the pores, and then pressure is applied to allow the plastic to harden. The pore cast is then made by slowly dissolving the rock impregnated with plastic in acid. Silicate minerals require careful use of hydrofluoric acid.

Pore casts can be examined readily under binocular, petrographic and light microscopes, although they are best examined using the scanning electron microscope (SEM). The SEM is unsurpassed for illustrating pore casts because of its high resolution and depth of field. The SEM displays the secondary electrons produced via excitation from an evacuated high-energy electron source in three-dimensions. This enables the operator to effectively view the pore cast as a highly magnified specimen, focusing on the pores and pore throats.

Each pore cast was split into $1cm^3$ with the surface split perpendicular to bedding and mounted on an aluminium stub using araldite as the mounting medium. Carbon-Gold/ Palladium conductive double coating was used on the four samples prior to study under the SEM.

Paired stereo photographs taken with the SEM were ideal for the study and illustration of pore casts (Pittman & Duschatko, 1970), and as mentioned, these can now be made with ease using the SEM in-built stereo function.

2.10 GR SORT – GRAIN SIZE DETERMINATION

The grain size data obtained from thin section using the image analyser was used in a program developed at the NCPGG, called GRSORT. This program converts the 2D-grain size distribution obtained from the thin sections into the equivalent of a sieve analysis. The reason for the difference between the two distributions is that the grains in the thin section are cut at random points along their axis, and not necessarily at their maximum thickness (see Appendix 1 for theory). The data obtained from the image analyser were taken and converted to digital format. These data were then subsequently placed into the Unix system where the GRSORT program is located.

2.11 PHOTOGRAPHY

Photographs were taken of each thin section using a Minolta X300 Camera and a Tamron 90x Tele Lens with a 2:1 macro facility. The photographs were taken using low angle illumination, while photomicrographs were taken using the image analyser and stored as digital images.

Chapter 3 THE HUTTON SANDSTONE

The Jurassic Hutton Sandstone is both a major aquifer and an oil reservoir in the Eromanga Basin, which is part of the larger Great Artesian Basin. The Eromanga Basin extends over parts of South Australia, Queensland, New South Wales and the Northern Territory as shown in Figure 3.1, while Figure 3.2 shows the location of the Gidgealpa well from which the core was obtained.

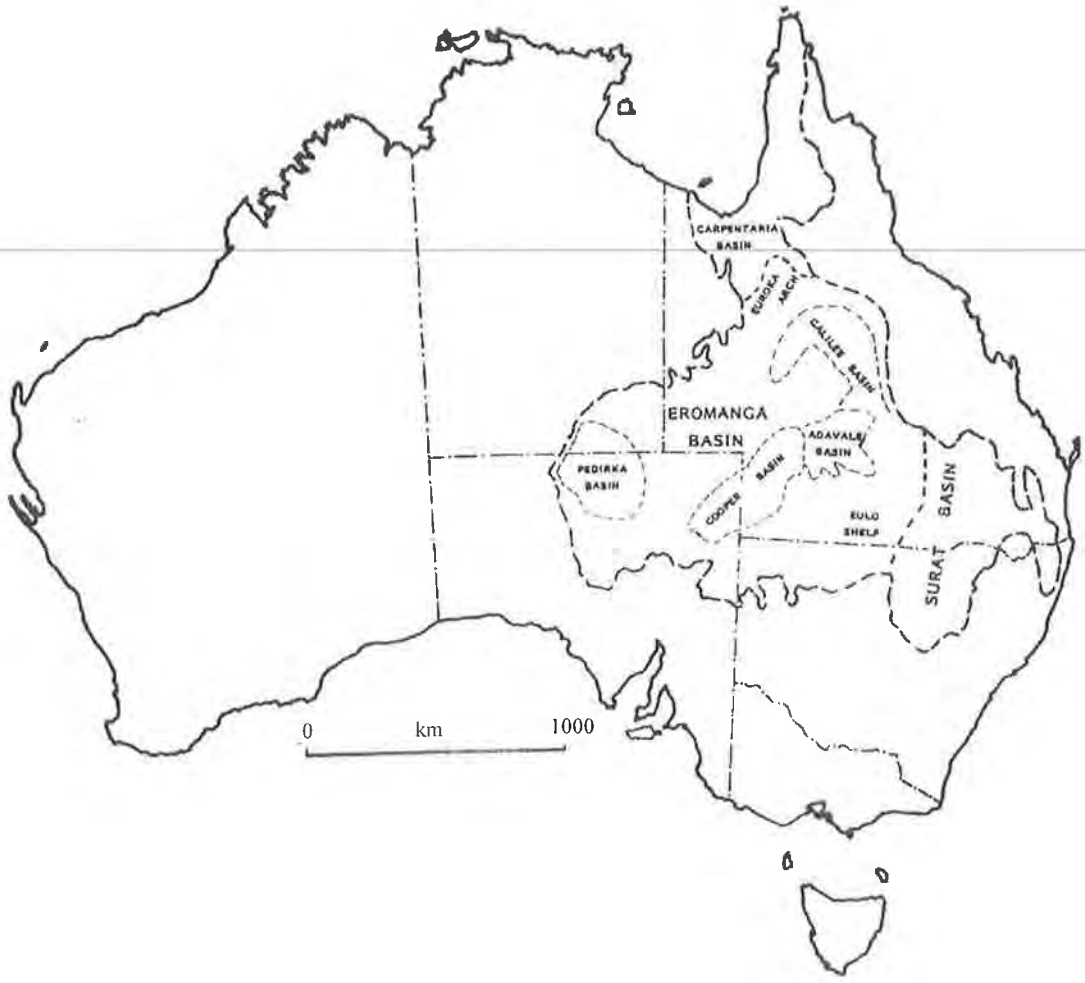

Figure 3.1: Location map showing the outline of the Eromanga Basin within Australia.

The Hutton Sandstone is predominantly a thickly bedded, relatively uniform, quartz arenite to occasionally rock-fragment-rich, pebble-dominated conglomerate. Quartz grains are usually monocrystalline with straight extinction although small amounts of polycrystalline and strained quartz may be present (Boult, 1996).

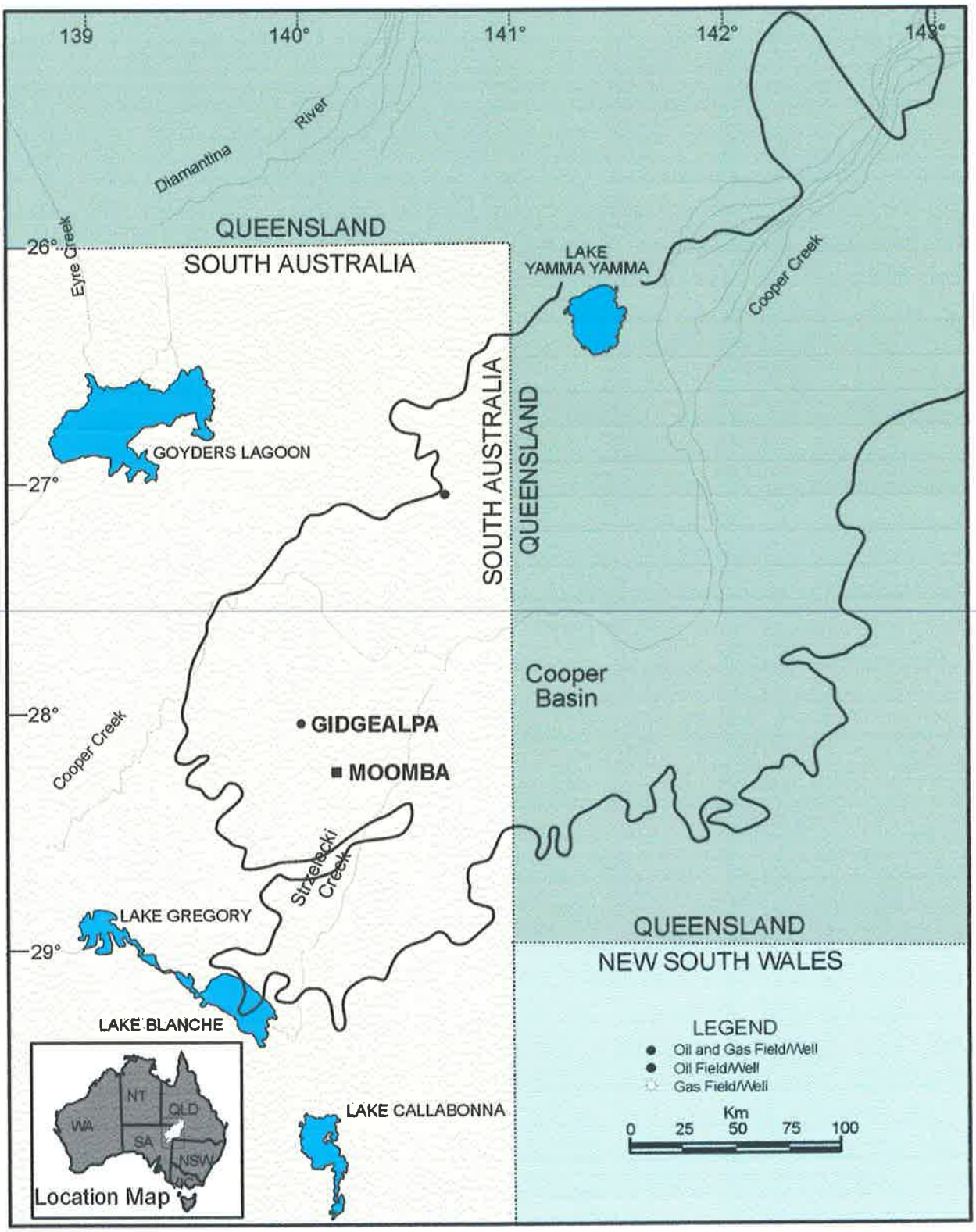

Figure 3.2: Location map of the Cooper Basin showing the position of the Gidgealpa field/well.

Reeves (1947) first used the name Hutton Sandstone for outcrop in the Surat Basin in Queensland. The Hutton Sandstone intertongues with the Poolowanna Formation in the Cooper Basin region and, where the Poolowanna Formation is absent, lies unconformably on Cooper and Warburton Basin units. The unit intertongues with and is overlain by the Birkhead Formation (Watts, 1987), and is restricted to the subsurface in South Australia (Figure 3.3).

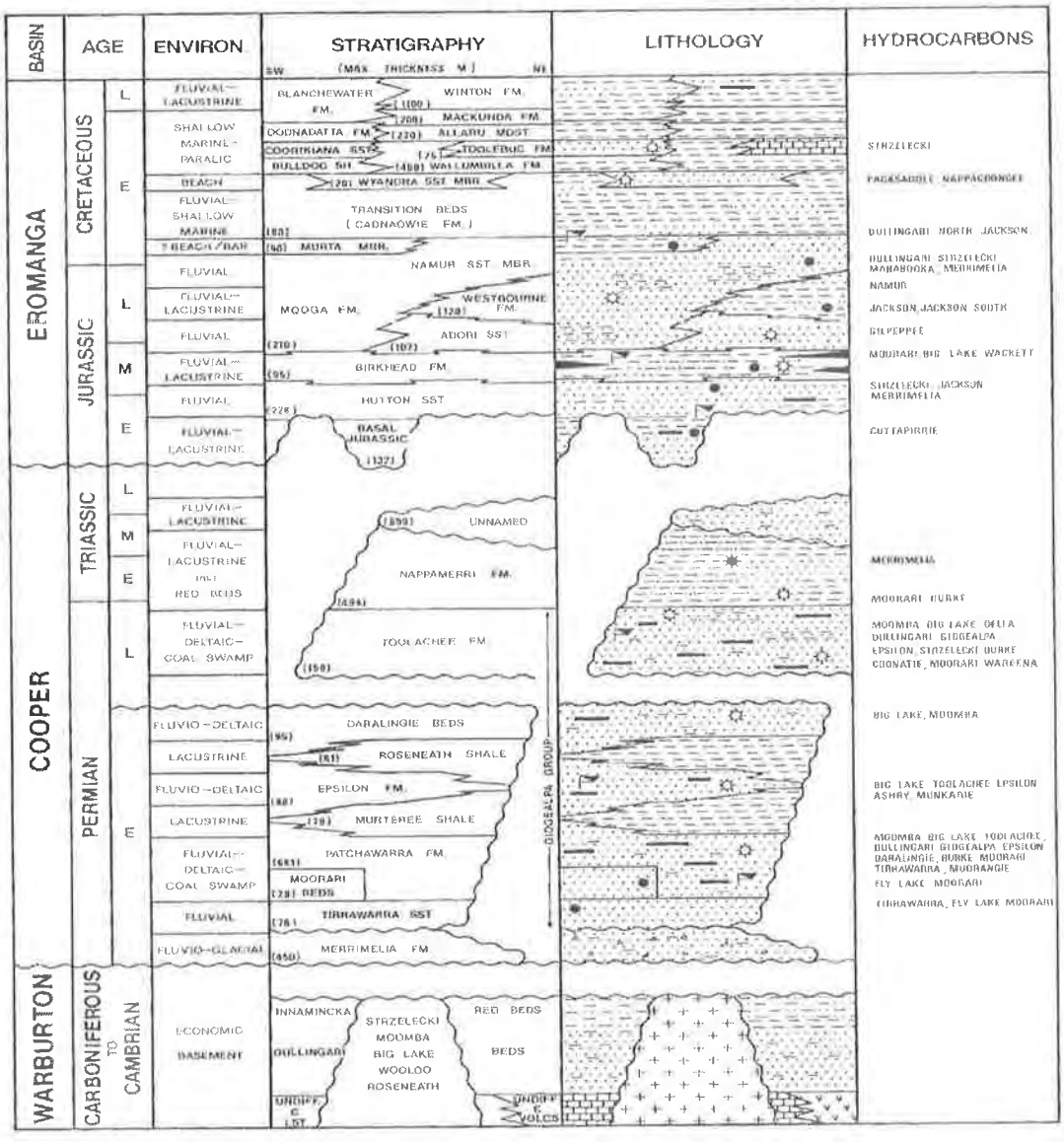

Figure 3.3: Stratigraphic column showing Eromanga Basin and the relationship with the underlying Cooper Basin (Kantsler *et al.*, 1983).

The Jurassic Hutton Sandstone is a continent-derived bed-load fluvial system as defined by Schumm (1977), but despite being dominated by medium to coarse sand, does not behave as a large, homogeneous tank in which vertical migration of oil occurs uninhibited by the aquifer.

The Hutton Sandstone is now recognised as containing numerous thin, but widespread shale units, deposited during lacustrine flooding events that periodically interrupted episodes of coarse clastic deposition (Hamilton *et al.*, 1998).

The Hutton Sandstone was deposited above a major unconformity during which time the tops of previous basins in the area were eroded and the Jurassic basins took on a new, more widespread geometry, allowing reworked sediments to be mixed with craton-derived quartz-rich sediments.

While early geological models assumed a braided fluvial system with transport to the east and northeast from westerly sediment sources (e.g. Moore *et al.,* (1986), Watts (1987)), Wiltshire (1989) pointed out that such a high-energy fluvial regime "would certainly have required a substantial drainage exit and there is no evidence of such anywhere in the eastern Eromanga Basin". As an alternative to the wholly braided fluvial model, Wiltshire (1989) proposed that braided streams transported sand into the basin. The sand was then distributed across the basin by aeolian and lacustrine processes (Wiltshire, 1989). The closest modern analogue for Hutton Sandstone deposition is suggested to be the essentially unconfined bed-load fluvial transport of the Canterbury Plain of New Zealand (Hamilton *et al.,* 1998). These authors also point out that the lateral extent and the bedding character of the Hutton Sandstone suggest that river flow was essentially unconfined across a broad alluvial plain.

Further information regarding the structure and exploration history of the Eromanga Basin is included in Appendix 2.

3.1 GIDGEALPA-17: PLUG ANALYSIS

Core plug porosity and permeability data across the chosen Hutton Sandstone interval is limited by the small interval of core used in this study. Appendix 3 displays where the core plugs were taken from the core along with their corresponding core porosity and permeability. Table 3.1 is the tabulated core plug porosity and permeability data, obtained from the PEPS Database.

Measured core porosities for the selected interval range from 20.5% through to 24.2% (Figure 3.4), with permeabilities ranging from 710md through to 1530md (Figure 3.5).

TABLE 3.1: G17 Hutton Sandstone core analysis porosity and permeability data obtained from PEPS database.

Depth (ft)	Porosity (%)	Perm (md)
6,077.50	22.3	891
6,078.50	22.2	1,400
6,079.50	21.8	714
6,081.00	23.5	1,530
6,082.00	20.7	710
6,084.00	24.2	848
6,086.50	20.5	935

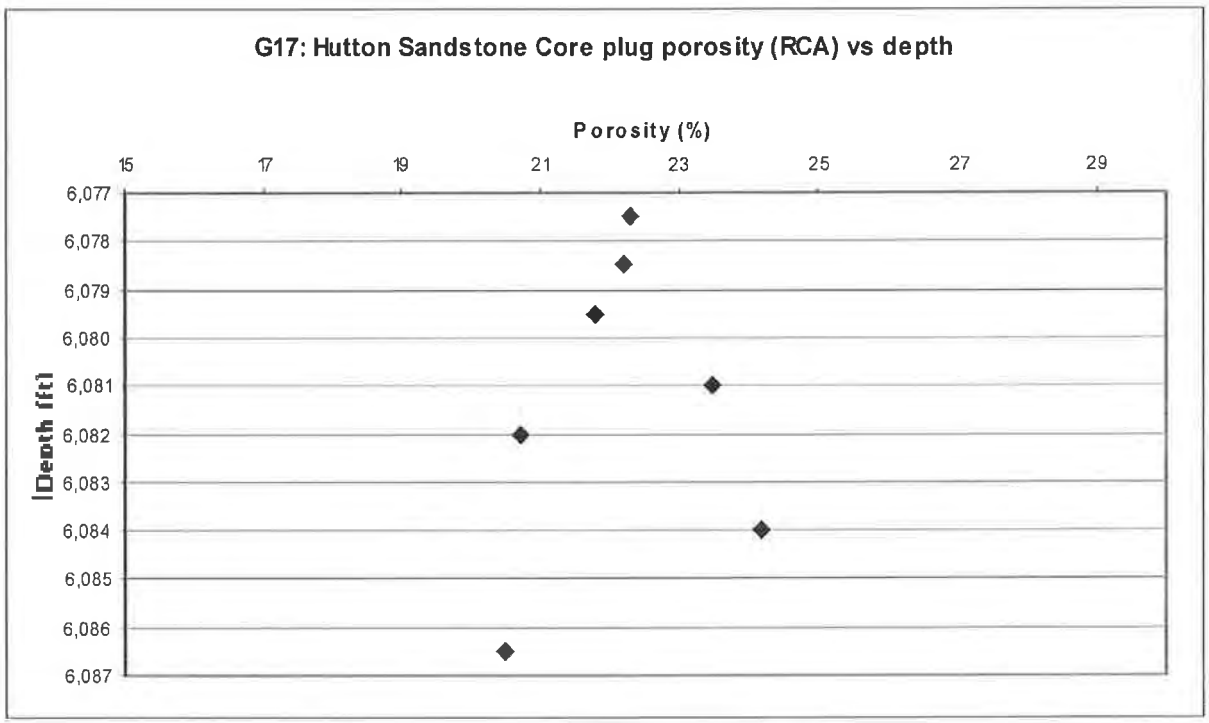

Figure 3.4: Core porosity (RCA) versus depth (PEPS database).

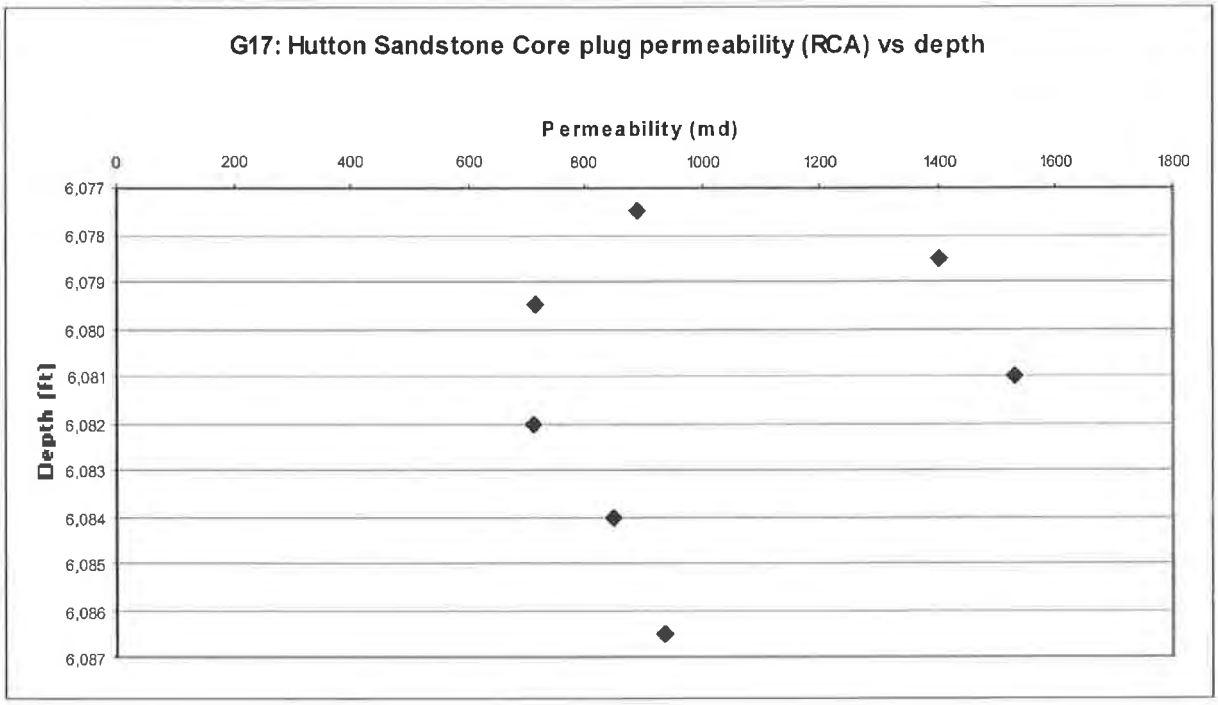

Figure 3.5: Core permeability (RCA) versus depth (PEPS database).

3.2 DIAGENETIC HISTORY

The diagenetic history of the Hutton Sandstone samples in this study is uncomplicated. After sedimentation, the only visible cements in the samples are quartz overgrowths (Figure 3.6 (a-e)) and pore-filling authigenic kaolinite (Figure 3.7 (a-e)). The quartz overgrowths are clearly visible in the photomicrographs where a dark rim exists around the framework grain, and are more pronounced under CL. Kaolinite luminesces so brightly under CL that it appears to completely occlude porosity.

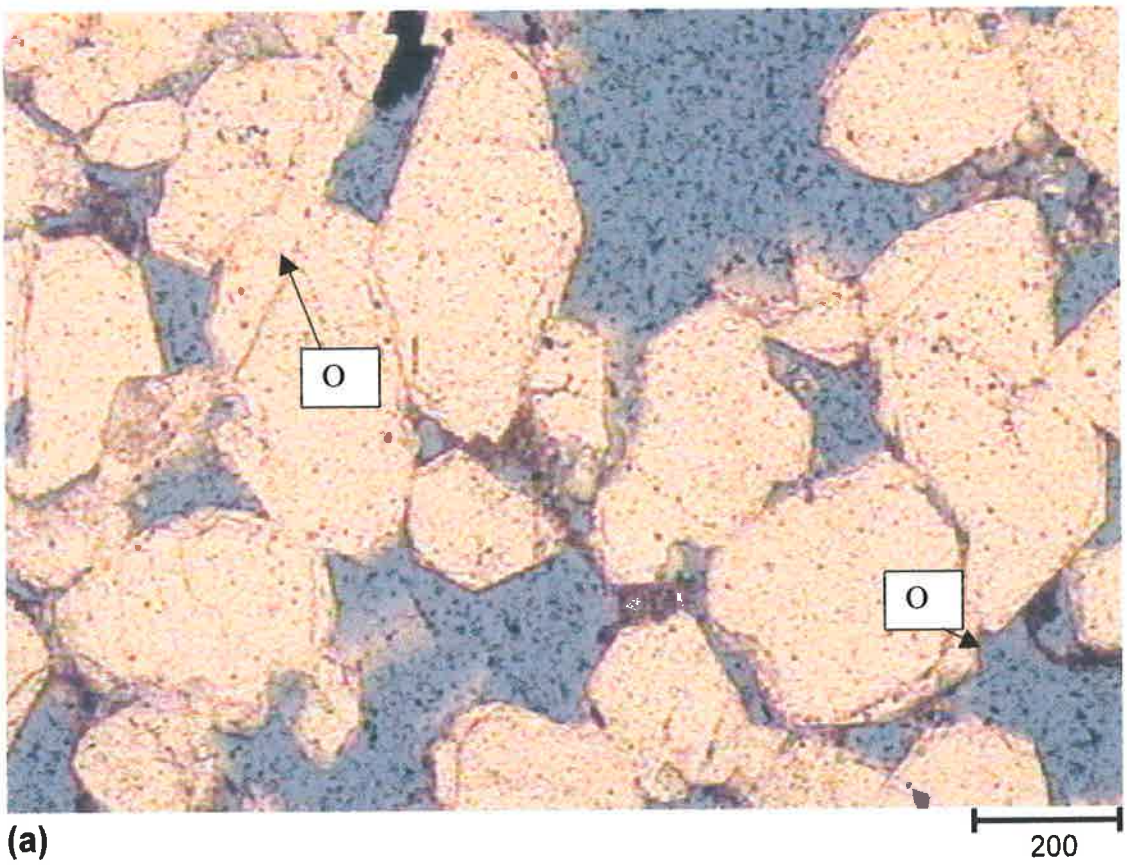

Figure 3.6 (a): Plane polarised light photomicrograph from thin section G17 1aii-upper showing polygonal primary pores between quartz overgrowths (O). The quartz overgrowths are clearly visible where a dark rim outlines the framework grain.

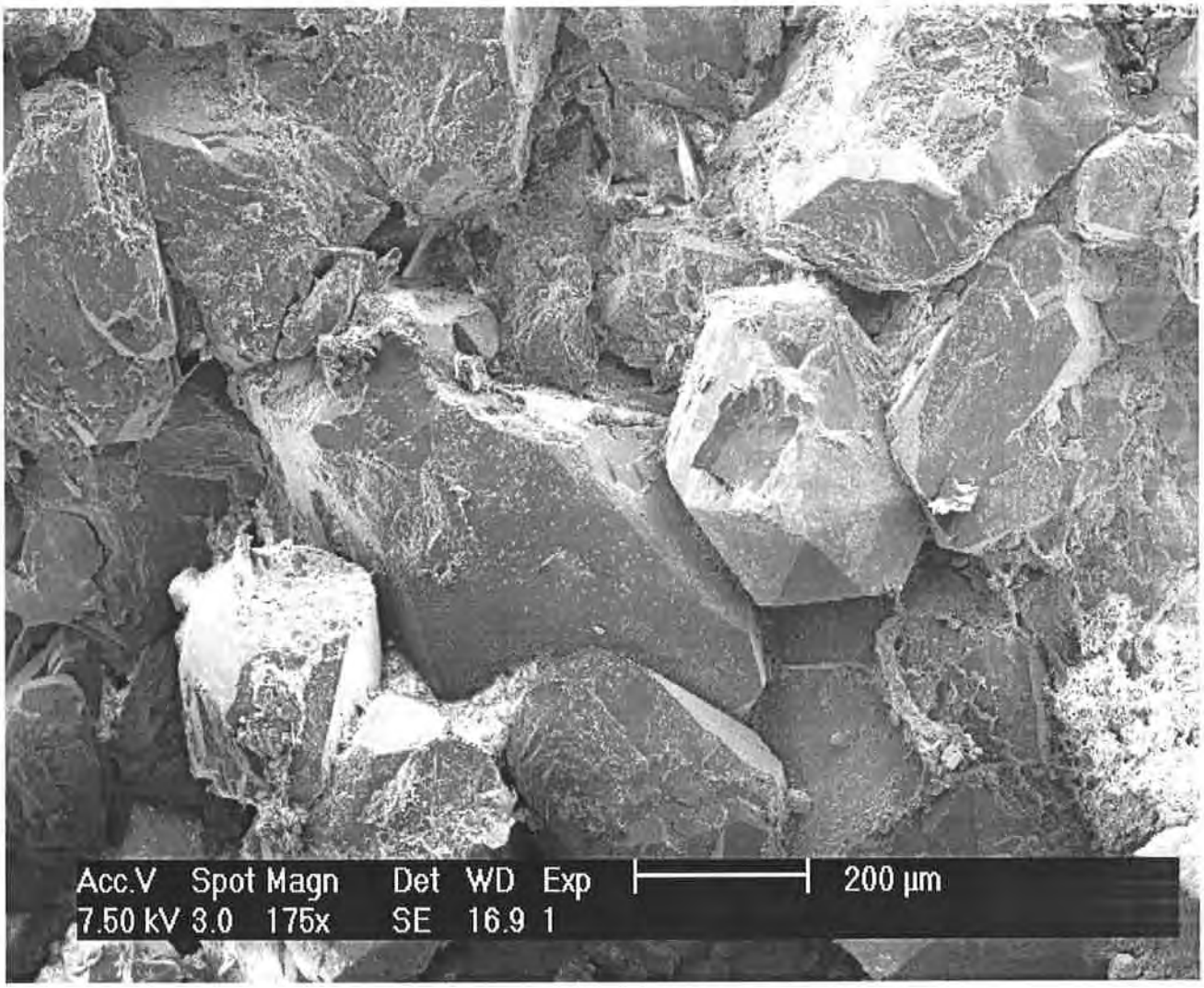

Figure 3.6 (b): SEM image from sample G17 1fi at relatively low magnification showing the crystal faces of thin authigenic overgrowths on quartz grains.

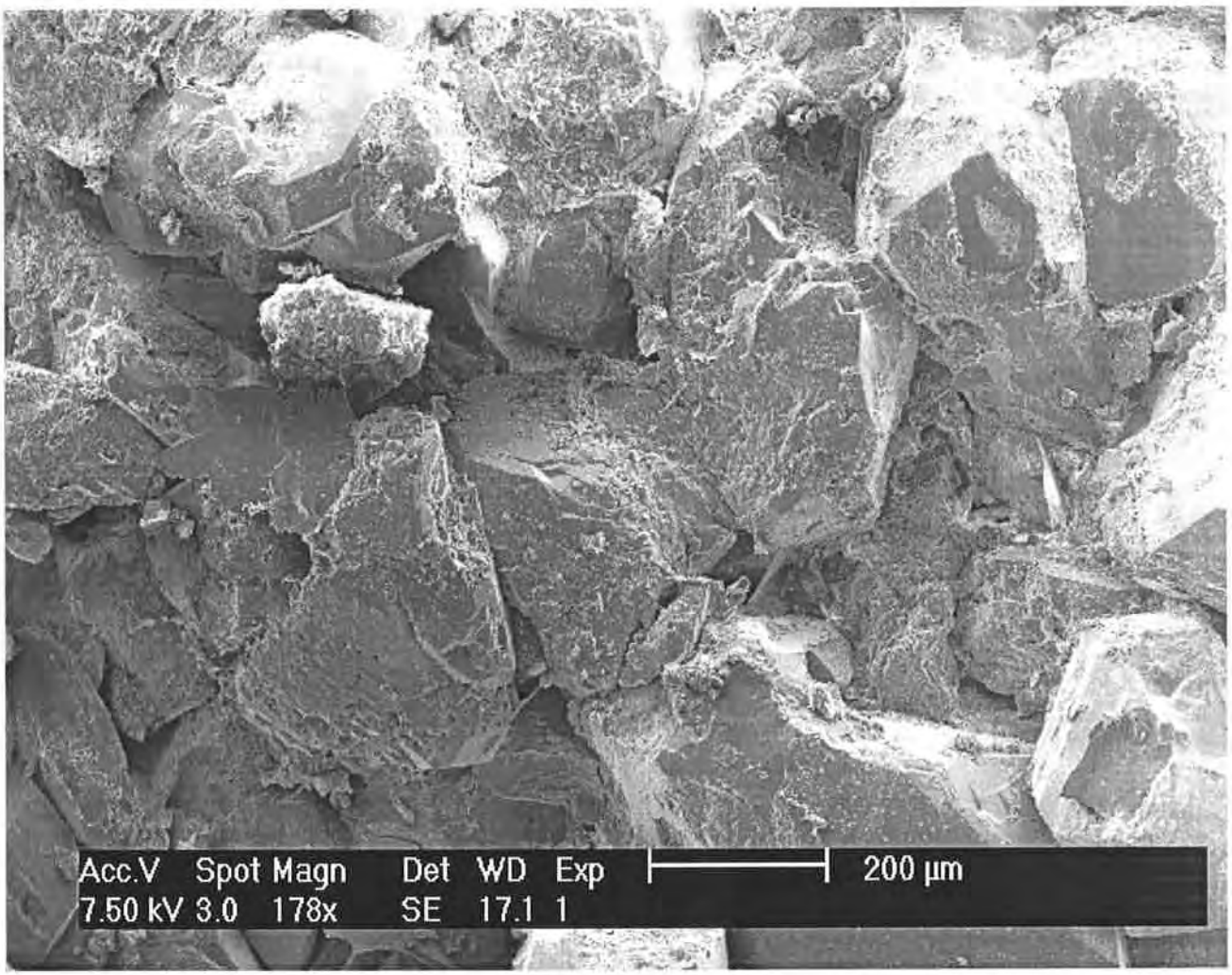

Figure 3.6 (c): SEM image from sample G17 1fi at a similar magnification as (b). Some quartz grains do not develop overgrowths. There is a light dusting of kaolinite platelets on some grains with loosely packed kaolinite booklets in some pores.

Figure 3.6 (d): CL image from thin section G17 2aii. The pastel blue and pink colours show framework quartz grains; the bright blue indicates patches of kaolin while the quartz cement is the dark rim on the framework grains.

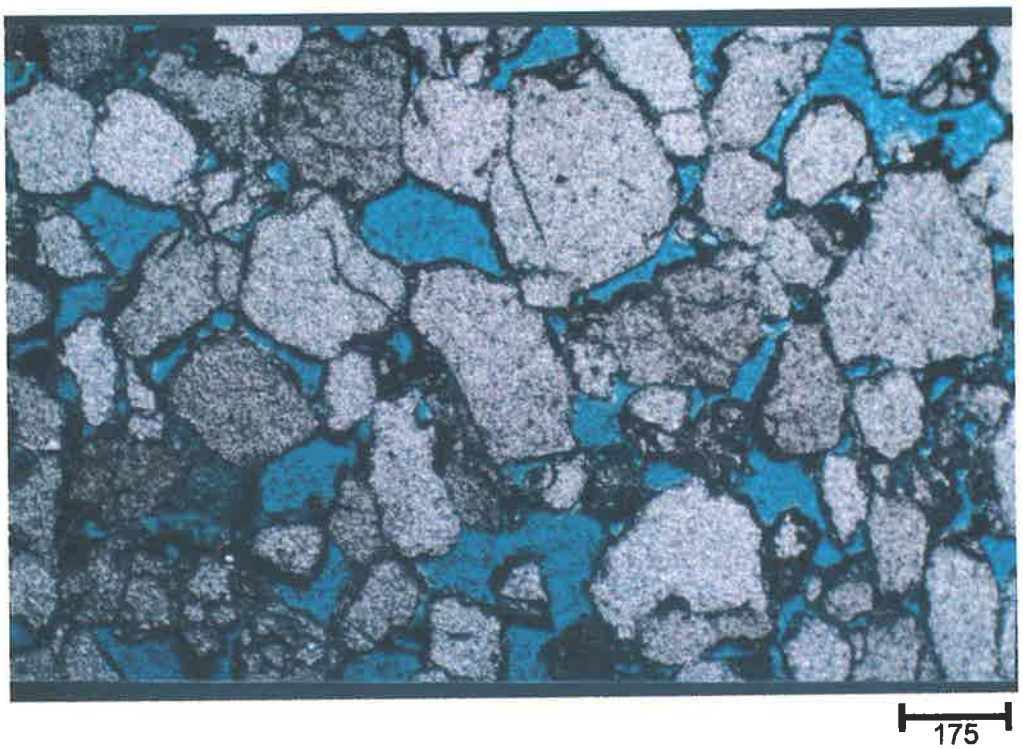

Figure 3.6 (e): Same field of view as (d) above viewed under plane polarised light. This standard presentation is used as a reference for the CL image.

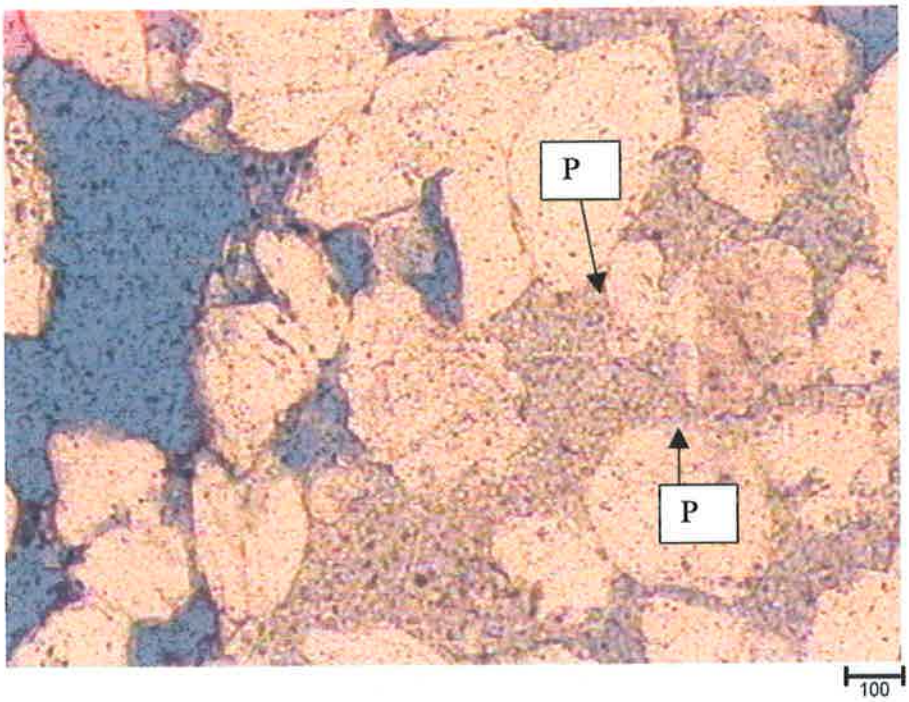

Figure 3.7 (a): Plane polarised light photomicrograph from thin section G17 1bi showing authigenic kaolinite filling primary pores. A lack of quartz cement is visible where kaolinite appears, however, often an intergrowth of kaolinite and quartz occurs (P).

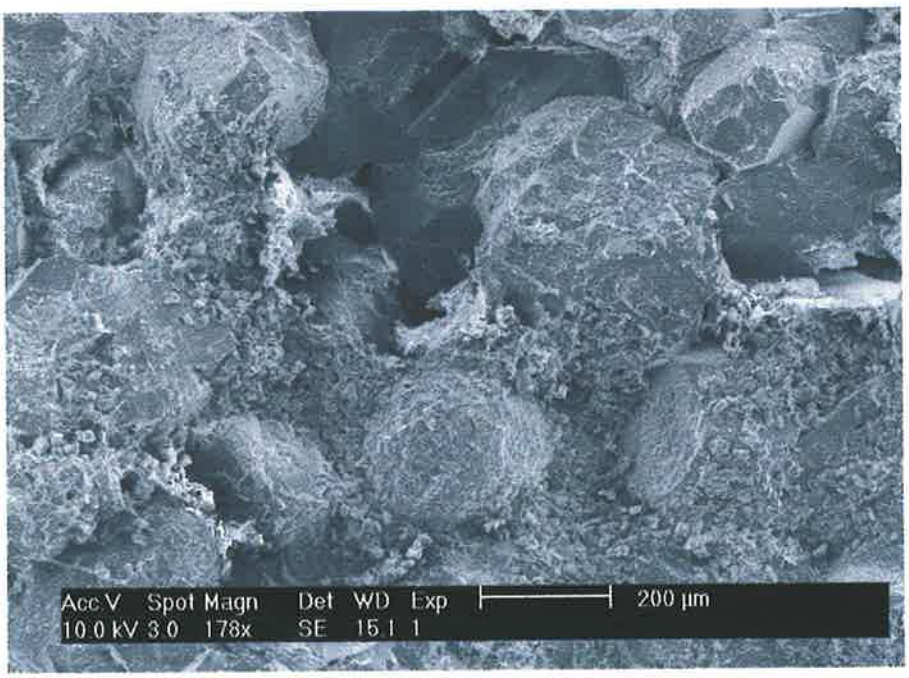

Figure 3.7 (b): SEM image from sample G17 1ai-upper showing kaolinite infilling pores and coating quartz cemented quartz grains.

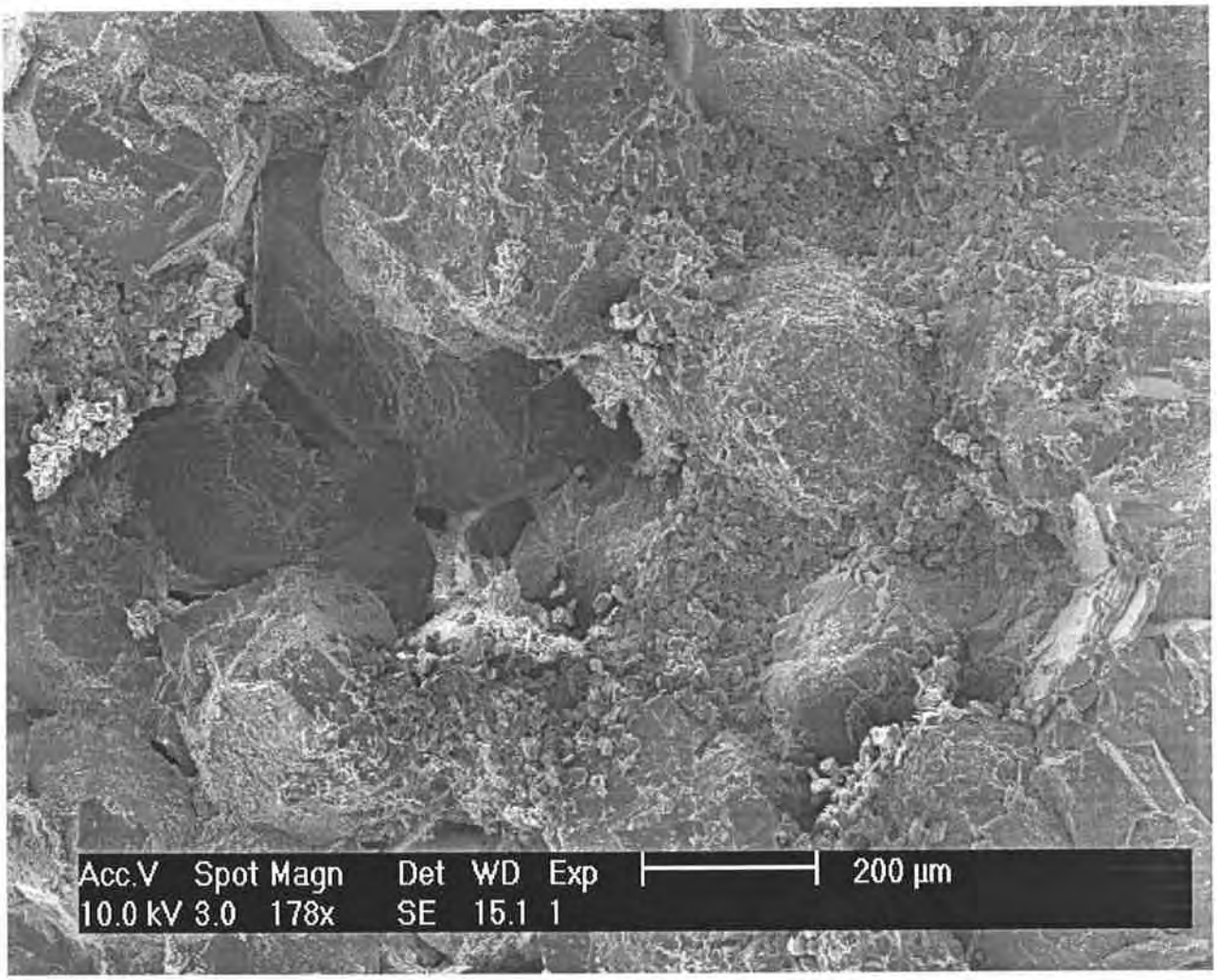

Figure 3.7 (c): SEM image from sample G17 1ai-upper at the same magnification as (b) above showing more loosely packed kaolinite filling pores and coating grains.

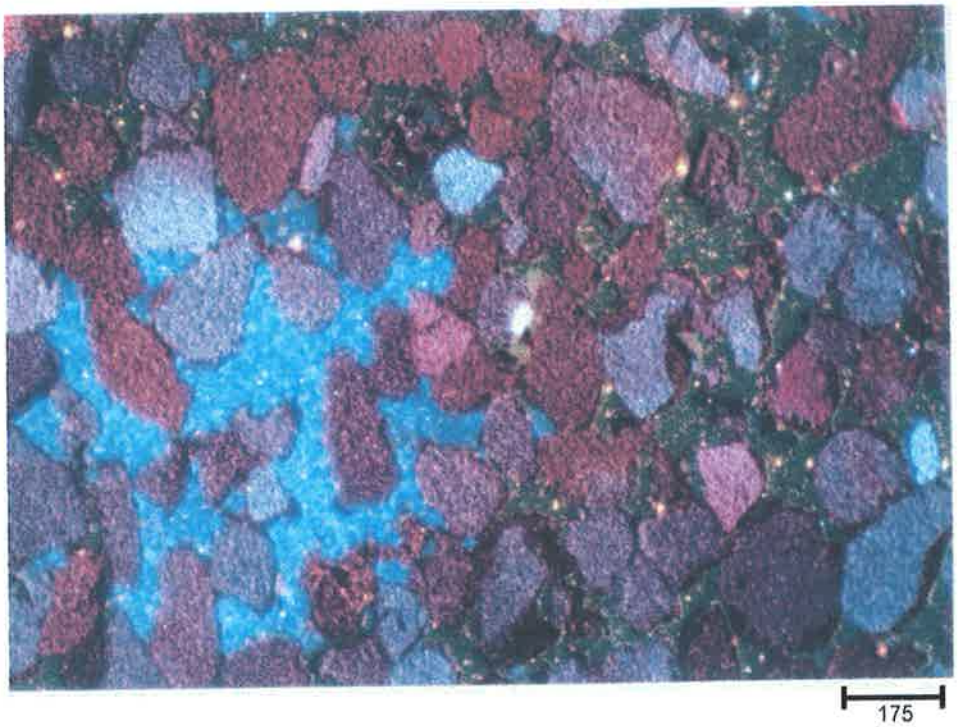

Figure 3.7 (d): CL image from thin section G17 2ai. The pastel blue and pink colours show framework quartz grains; the bright blue indicates patches of kaolinite that luminesces so brightly that it appears to occlude all porosity. Quartz cement is the dark rim on the framework grains.

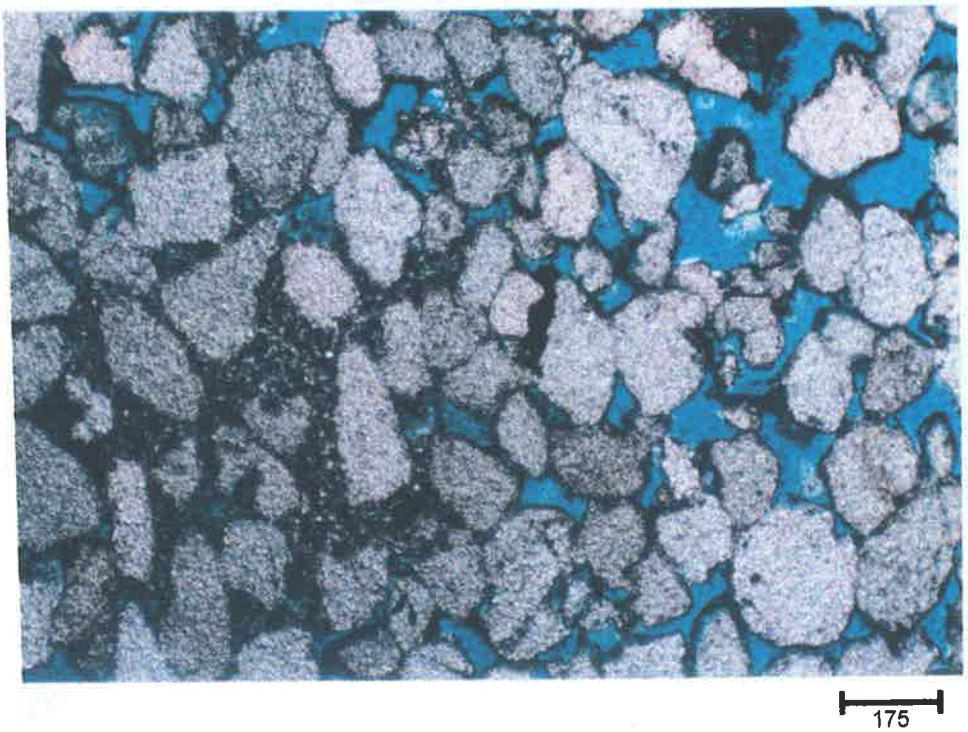

Figure 3.7 (e): Same field of view as (d) above viewed under plane polarised light. This standard presentation is used as a reference for the CL image.

From all thin sections, the average composition obtained by PIA is included in Table 3.2.

TABLE 3.2: Average composition obtained by PIA for all thin sections.

Monocrystalline quartz grains: <71%
Porosity: <21%
Kaolinite: 6%
Quartz overgrowths: <4%

3.3 PETROGRAPHY OF THE HUTTON SANDSTONE

3.3.1 TEXTURAL PETROGRAPHY

The grain size is quite consistent throughout the fourteen samples. Some larger grains are observed, as is common in fluvial sandstones. Grain size data were collected and histogram charts produced for all samples, while samples 1ai and 1aii are displayed as Figure 3.8 (a-b). The samples are medium to coarse-grained, clean quartz arenites. Histograms of the remaining samples are included in Appendix 4.

Histograms of pore sizes for samples G17 1ai upper and 1aii upper were also produced and are displayed along with the grain size charts (Figure 3.9 (a-b)). Histogram charts for the remaining samples are included in Appendix 5. To determine sorting, the grain size data were converted to the phi scale by using GRSORT (Appendix 6). Using the normal phi standard deviation sorting scale (Mcmanus, 1988), sorting ranges from moderate to moderately well sorted.

3.3.2 COMPOSITIONAL PETROGRAPHY

PIA was conducted to quantify mineral composition and thin section porosity for all samples (Appendix 7), while two of these samples (1aii upper and 2aii) were point counted using more traditional methods to check the accuracy of the PIA analysis technique (Appendix 8). The traditional point counting was also conducted on these two samples to get a more accurate estimate of the quartz cement in the rocks. This technique is required for cement calculation because PIA is unable to automatically

distinguish between primary quartz grains and quartz cement in the form of overgrowths as the technique uses colour recognition. The quartz cement values obtained by PIA were done manually (see Chapter 2 – Methods and Materials). Determining the amount of quartz cement using PIA is likely to be less accurate because the operator must not only be able to recognise and identify all the quartz cement, but must also be able to accurately highlight its shape using the mouse.

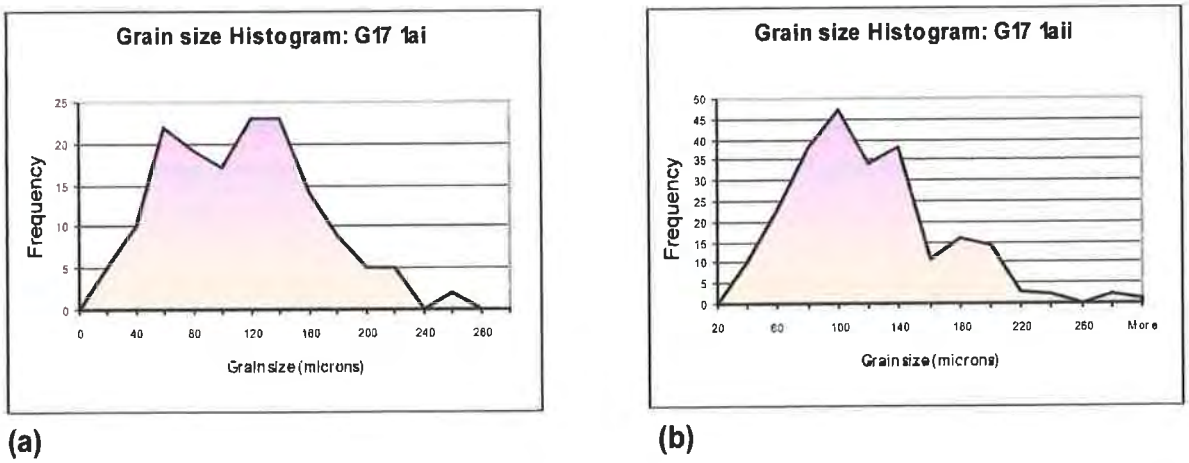

Figure 3.8 (a-b): Grain size histogram distribution charts for samples G17 1ai-upper and 1aii-upper.

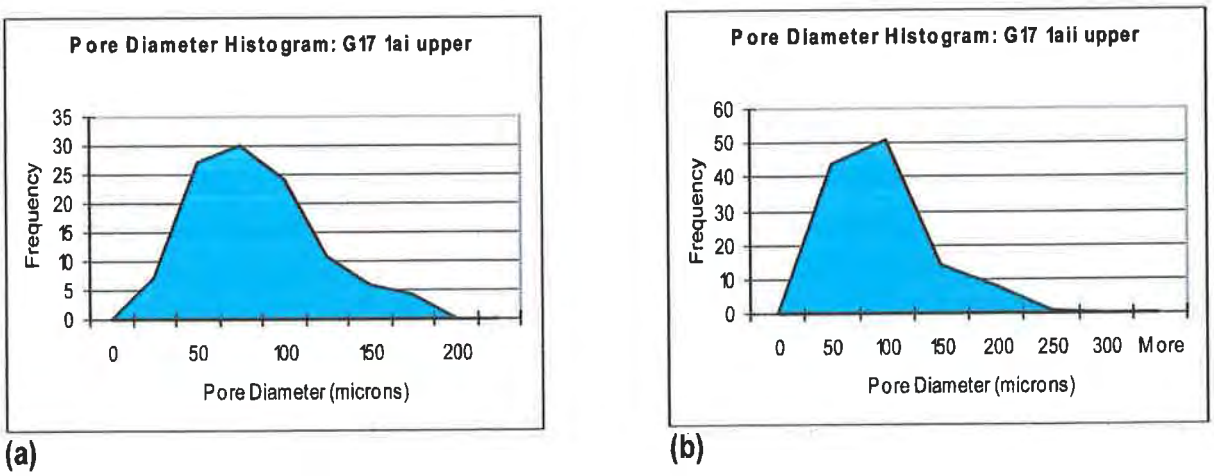

Figure 3.9 (a-b): Pore size histogram distribution charts for samples G17 1ai-upper and 1aii-upper.

The main component of the Hutton Sandstone samples is quartz. The proportion of total quartz (including quartz cement) in the samples ranges from 72% to 78%, with an average of 74.4% (Table 3.2). The next most significant component is authigenic pore-filling kaolinite, ranging from 2% to 20%, but with an average of 6%.

The remainder of each sample is predominantly porosity, with the average thin section porosity being 20.8% (Table 3.2).

3.3 HUTTON SANDSTONE POROSITY DISTRIBUTION

Three types of porosity were observed in the Hutton Sandstone samples. The most common type of porosity was primary intergranular porosity. The other types observed include secondary pores and micro pores.

Primary Intergranular Porosity was present between the euhedral faces of quartz overgrowths (Figure 3.6 (a)), but in tightly cemented regions, these pores were drastically reduced. Primary porosity usually occurs in quartz-rich sandstones where early quartz cementation has led to a strengthened framework that limits the effects of further compaction, thus preserving porosity. Sandstones that are rock-fragment rich have far less primary porosity due to greater effects of compaction on the more ductile rock fragments.

Secondary Porosity was not prominent, however it was observed as the product of unstable-grain dissolution of feldspar (Figure 3.10). The amount of secondary porosity is minimal.

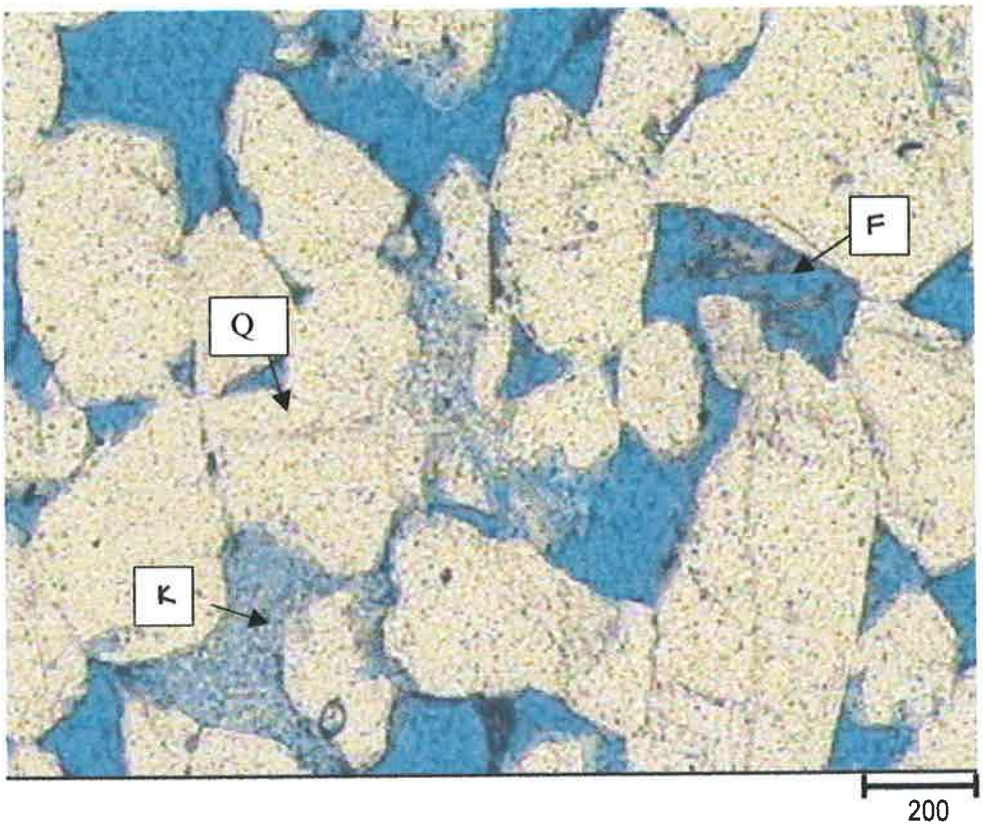

Figure 3.10: Dissolution of feldspar grain (F) produces secondary porosity. Note the authigenic kaolinite (K) and quartz overgrowths (Q) forming nearby (5x-mag, scale bar is in microns).

Micro-porosity was present in kaolinite masses (Figure 3.7 (a-e) and Figure 3.11). The concept of micro-porosity within clay minerals was introduced by Neasham (1977) and Pittman & Thomas (1978). Micro-porosity is included in calculations of porosity in this study as PIA is able to observe the presence of some porosity within the kaolinite masses, although it is acknowledged that it is not possible for all to be imaged.

Porosity within areas filled with kaolinite ranged from 10% to 30% estimated by using images produced by PIA at high magnification that were filled with kaolinite and calculating how much porosity existed within each area. A study done by Rezaee & Lemon (1997) on the Tirrawarra Sandstone calculated porosity within kaolinite masses at 20%, while Hurst & Nadeau (1995) determined, using backscattered electron micrographs, that kaolinite has average microporosity of 43%, with vermicular types ranging from 45% to 50% while blocky forms ranged from 15% to 30%.

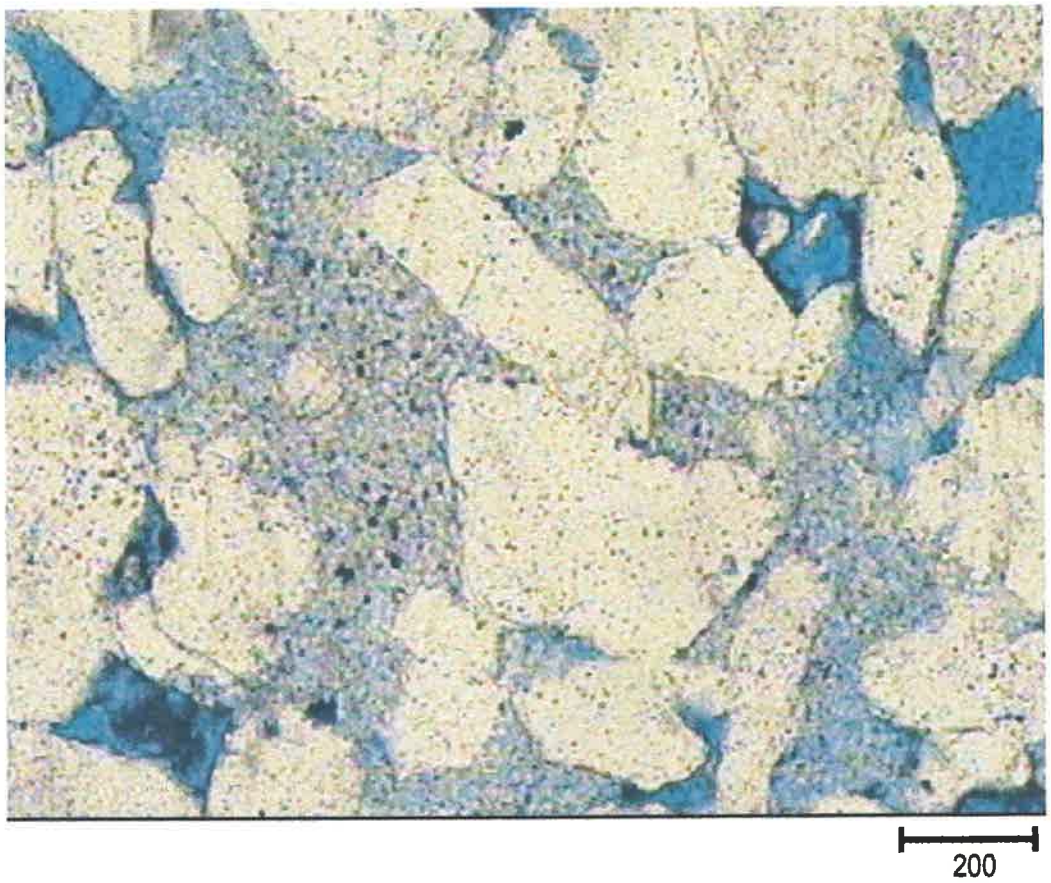

Figure 3.11: Thin section G17 1c showing tightly packed authigenic kaolinite filling primary porosity. Porosity within the kaolinite ranged from 10% to 30% of the total kaolinite area (5x-mag, scale bar in microns).

3.4 CEMENT ANALYSIS

3.4.1 ORIGIN OF CEMENT

Quartz, in the form of syntaxial rims, is the co-dominant cement in the Hutton Sandstone samples (Figure 3.12) along with kaolinite (Figure 3.13). Quartz cement grows via both homogeneous and heterogeneous nucleation mechanisms. Heterogeneous nucleation is the most common process as evidenced by the domination of syntaxial quartz overgrowths relative to crystallisation of pore-filling, discrete quartz crystals.

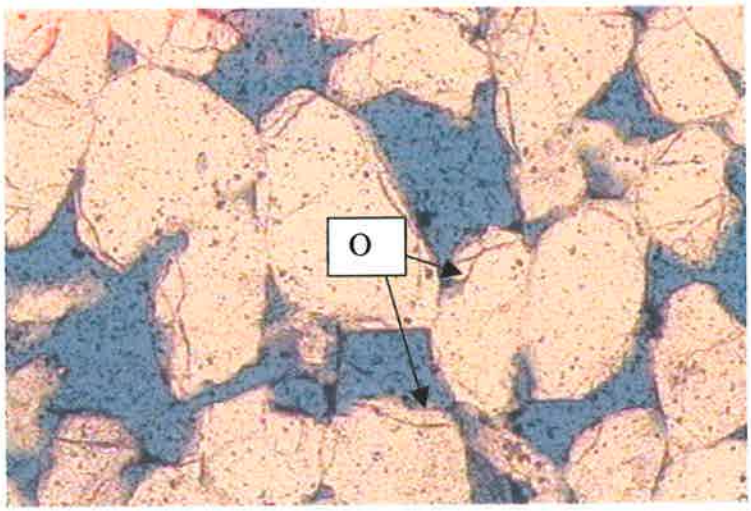

Figure 3.12: Photomicrograph from thin section G17 1ai-upper showing quartz overgrowths (O), visible by the dark rim, surrounding framework grains.

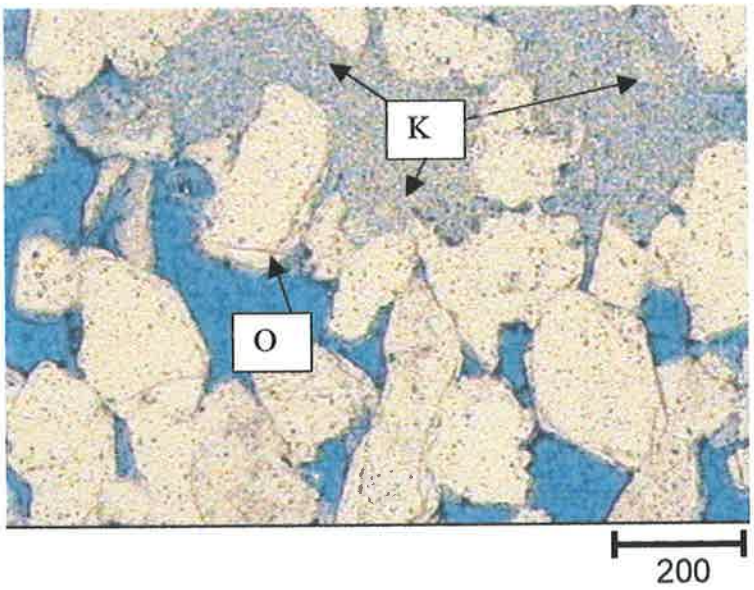

Figure 3.13: Photomicrograph from thin section G17 1dii showing authigenic kaolinite (K) filling porosity. Quartz overgrowths (O) are also visible by the dark rim surrounding the framework grains (scale bar applies to both micrographs).

Some quartz cement occurs as an isopachous overgrowth. However, some rocks have quartz outgrowths rather than overgrowths (McBride, 1989). Outgrowths are pronounced localised projections into the pore rather than rims around the majority of the detrital grain. They are also syntaxial, but they tend to occupy the adjacent pore and thus cause more damage to permeability than overgrowths (Worden & Morad, 2000).

Cathodoluminescence (CL) imaging work carried out by Hendry & Trewin (1995) and Hogg *et al.,* (1995) indicated that multiple nucleation sites might occur followed by competition for space during subsequent cement growth and dominance of one particular nucleus as the overgrowth developed.

There are two essential controls on quartz cementation. There must be a thermodynamic driving force, i.e. an overall reduction in the free energy of the system. However, for this to occur, the rate of that process must also be favourable. The overall rate of quartz cementation is related to three linked steps, which must occur in series. These are described in Figure 3.14, which is a schematic diagram from Worden and Morad (2000) that shows the geochemical controls on quartz cementation.

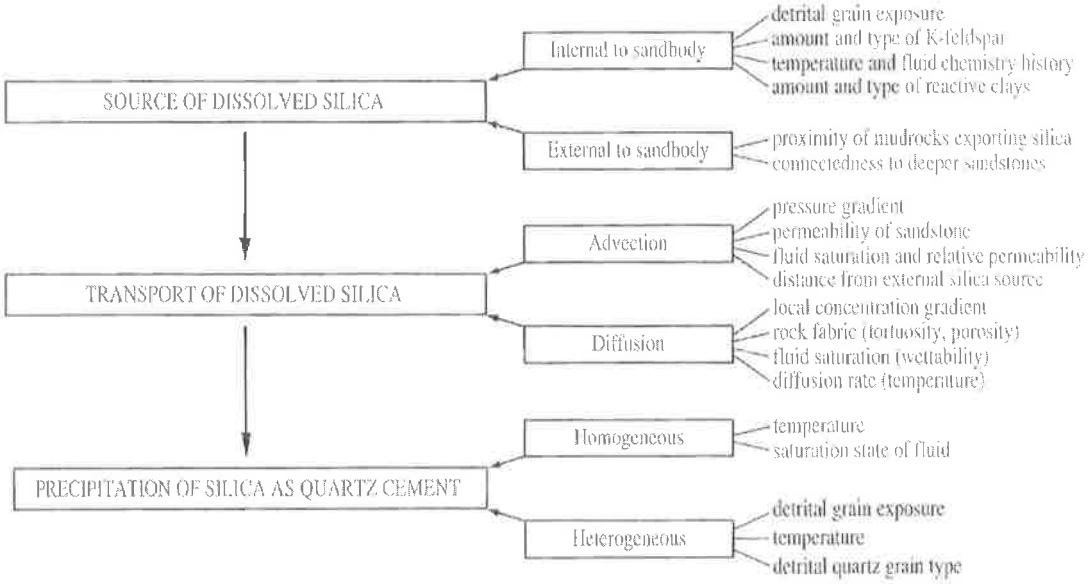

Schematic diagram for the geochemical controls on quartz cementation. The three fundamental controls are the rates of supply to aqueous solution, transport and precipitation from aqueous solution. These have been subdivided into the key secondary controls and the main influences on the rate of these key secondary controls are listed on the right of the diagram. ( )

Figure 3.14: Schematic diagram taken from Worden and Morad (2000) showing the geochemical controls on quartz cementation.

Development of quartz overgrowths involves the transfer of silica onto grain surfaces, accompanied by the displacement of fluid occupying those locations (Prince & Ehrlich, 2000).

Quartz cementation in sandstones is driven by the redistribution of silica. There can be multiple sources of SiO_2 for quartz cement in sandstones. McBride (1989) lists 23 silica sources from a literature review. Figure 3.15 is a schematic diagram taken from Worden and Morad (2000) explaining the general sources of quartz cementation.

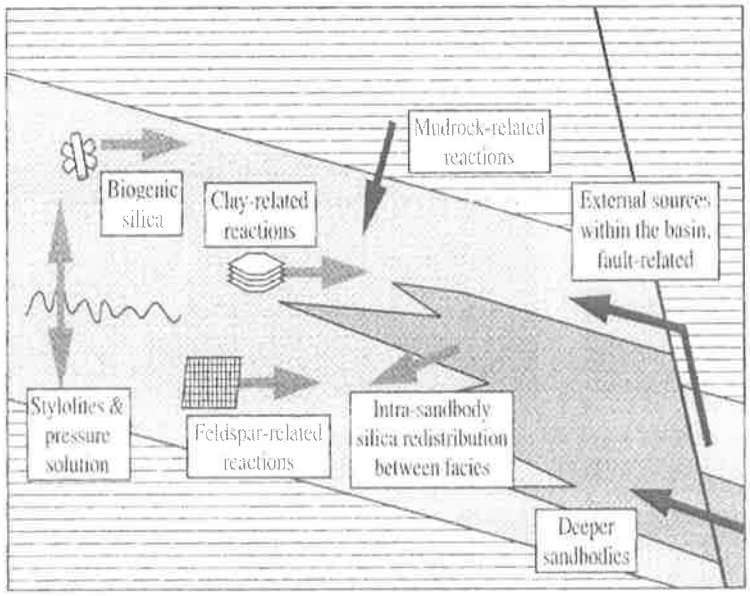

Schematic diagram for the general sources of quartz cementation. External sources are indicated by a black arrow; internal sources by a grey arrow.

Figure 3.15: Sources of silica cement modified from Worden and Morad (2000).

The most likely sources of silica for cement in the Hutton Sandstone are discussed below:

3.5 INTERNAL:

3.5.1 Alteration or Dissolution of Feldspar Grains

Dissolution of feldspar is reported as a silica source for quartz cement (Fothergill (1955), Hawkins (1978), Morad & Aldahan (1987), Siever (1957). The dissolution of

feldspar forms kaolin and an excess of silica is released during this reaction. The reaction in the case of potassium rich feldspar is:

$$2H_2CO_3 + H_20 + 2KAlSi_30_8 \rightarrow Al_2Si_20_5(OH)_4 + 4SiO_{2(aq.)} + 2K^+ + 2HCO_3^-$$

In this reaction, 1cm^3 of K-feldspar yields 0.43 cm^3 of quartz and 0.46 cm^3 of kaolinite. All reactions that involve the growth of clay minerals (such as kaolinite and illite) at the expense of feldspar lead to silica-release and thus the potential for quartz cementation (Worden & Morad 2000). There is very little feldspar seen in these samples of the Hutton Sandstone. It can be assumed from this that either they were not abundant during deposition or have been removed by alteration. The abundance of authigenic kaolinite, often clumped into areas about the size of the framework grains, suggests that during deposition, feldspar may have been an important detrital component.

3.5.2 Pressure Solution

It has been documented by various authors, including Heald (1955), Oelkers *et al.,* (1996), Waldschmidt (1941), that pressure solution of quartz grains at grain contacts can be an important source of silica. However, according to Stephan (1970), it appears to be more extensive in finer-grained sandstones.

3.6 EXTERNAL

External sources of silica include rocks adjacent to sand bodies (mudrocks encasing sand bodies) hence, transport may be on a much larger scale (tens of metres to kilometres) and may include other deeply buried sandstones, deeply buried mudrocks, granite intrusions or basement rocks (Worden & Morad, 2000).

Another poorly understood facet of quartz cementation is its duration. This issue is still unresolved, with the two arguments being that it is either **(i)** a prolonged process that occurs slowly over a very long period of time or **(ii)** an episodic process in which short bursts of activity are punctuated by long periods of quiescence (Worden & Morad 2000). According to Worden and Morad, both scenarios may occur depending upon the details of the lithology and burial -, temperature- and fluid-evolution histories.

3.7 CASE STUDIES

Work done by Giles *et al.,* (2000) showed that it is not possible to import large quantities of silica into the reservoir. They concluded that the source of silica for quartz cementation must be derived from within the sandstone or directly adjacent to it. Their work also showed that quartz cementation follows similar patterns worldwide, suggesting that quartz cementation is controlled by fundamental processes that are common to all basins.

Land & Milliken (2000) studied regional loss of SiO_2 and $CaCO_3$ and the gain of K_2O during burial diagenesis in Gulf Coast, USA, mudrocks. Their work in this area drew the conclusion that mudrock diagenesis is an open system, which raised two interesting questions. First, were the gains/losses evidenced in the mudrocks balanced by losses/gains in nearby sandstones? The answer to this question in their study appeared to be 'No', however it was noted that available data may simply be insufficient to support such a conclusion on a basinal scale. Work done by Gluyas *et al.,* (2000) on the Brae Formation sandstones of the Miller Field (UK Continental Shelf) indicated mudstones interbedded with the sandstones lost (exported) silica during diagenesis. In their study, the volume of silica exported from the mudstone matches that imported by the sandstone. The answer to Land and Millikens' second question about how the mass transfer of ions actually takes place was also unclear. Insufficient chemical gradients exist in formation waters to enable diffusive transport over the large distances that characterise the sand-mud system (Land & Milliken, 2000).

Prince and Ehrlich (2000) studied various sandstones that had been subjected to a variety of temperatures, pressures and pore-water chemistry regimes. They discovered that, in spite of the range in environmental factors, plots of these variables exhibited smooth trends over the range of studied porosity, implying that these environmental factors might not play as significant a role in quartz cementation as previously theorised (Prince & Ehrlich, 2000). Hence, there is still much debate as to the origin and movement of silica used for quartz cementation.

Within the Hutton Sandstone samples, the estimated quartz overgrowths range from 2% to 7.4% of the entire thin section, with an average of 4% (See Table 3.2). The average amount of quartz cement calculated by point counting (done manually by

indicating what is seen under the cross hairs of the microscope and then making incremental moves of 1mm) under the microscope of two samples was 7%. This is higher than the value obtained from PIA, but was expected due to a smaller chance for operator error.

Table 3.3 compares components that were measured using PIA, point counting and point counting done using a 5mm grid across a CL photomicrograph (Figure 3.16), a technique which allowed for clearer identification of quartz cement.

Sample 1a ii (upper)

COMPONENT	PIA (%)	Point Counting (%)	Point Counting using CL grid
Quartz	71	67	61
Porosity	21	18	25
Kaolln	6	5	2
Quartz cement	4	6	12
Matrix	2	3	0
Feldspar	3	1	0
Mica	1	0	0
Total	108	100	100

TABLE 3.3: A comparison of the results obtained from the three methods used to estimate rock petrology. It is evident from the data that PIA tends to overestimate each individual component because the total obtained from the 14 thin sections sums to 108%. This is a result of (a) overlap occurring when producing an overlay for quartz and porosity, and from these overlays, (b) rounding, because PIA calculates percentages including fractions.

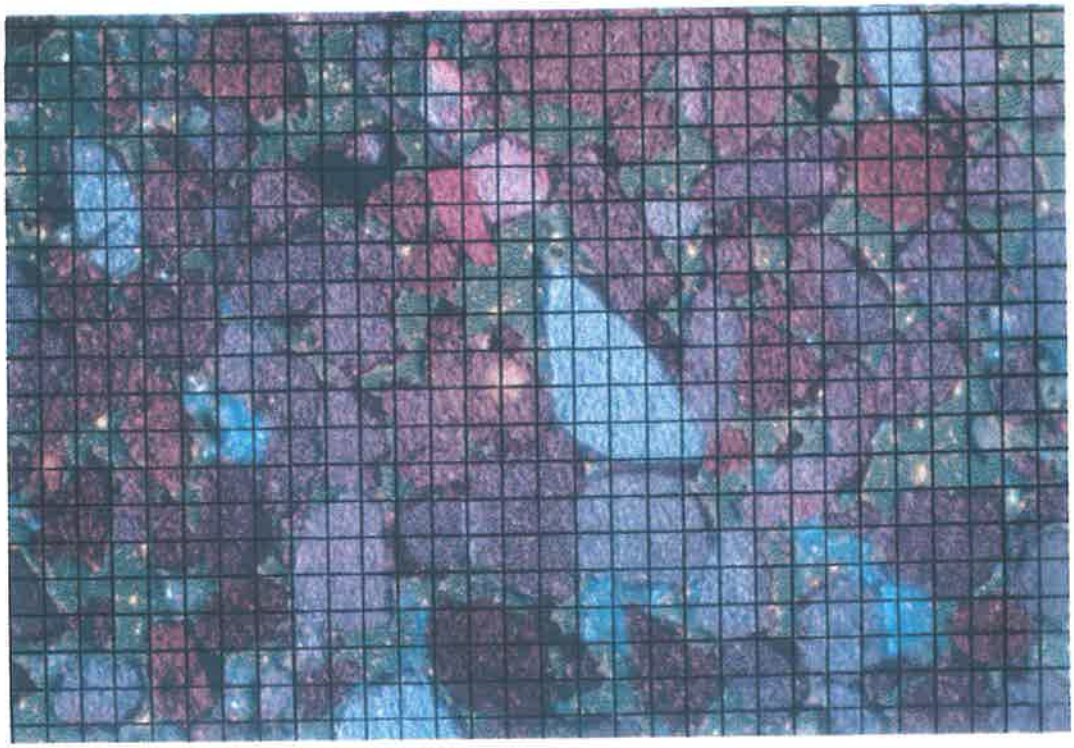

Figure 3.16: CL image showing the 5mm-overlay grid used to calculate the quartz cement by point counting. Sample 1a ii (upper)

When using the point counting technique across a CL micrograph, the values obtained matched those obtained using PIA and point counting across a plane polarized light micrograph, except for quartz cement and porosity, which were both higher. The average amount of quartz cement calculated from the two samples was 12.4%, which is considerably higher than the average taken from traditional point counting which was 7%. This difference can be understood by comparing the CL micrograph from sample 1fi (Figure 3.17 (i)) with the same micrograph but under plane polarised light (Figure 3.17 (ii)). The CL image highlights the cement within the sample that could not be distinguished under plane polarised light.

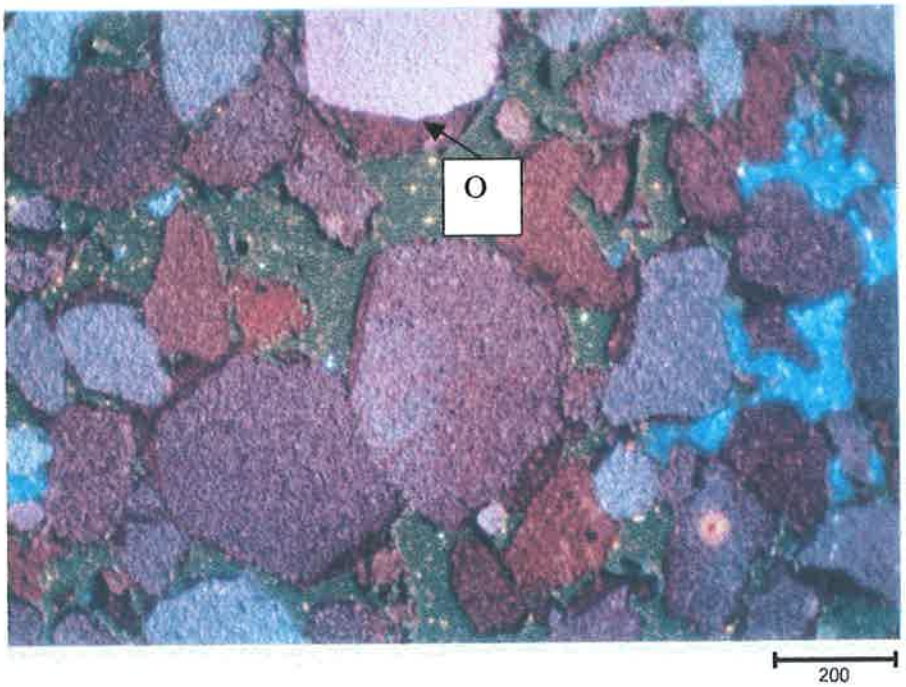

Figure 3.17 (i): Thin section G17 1fi under CL. Note the brightly luminescing kaolinite, which appears to occlude all pore space, while the quartz cement is clearly visible as overgrowths (O) surrounding many of the primary quartz grains (scale bar is in microns).

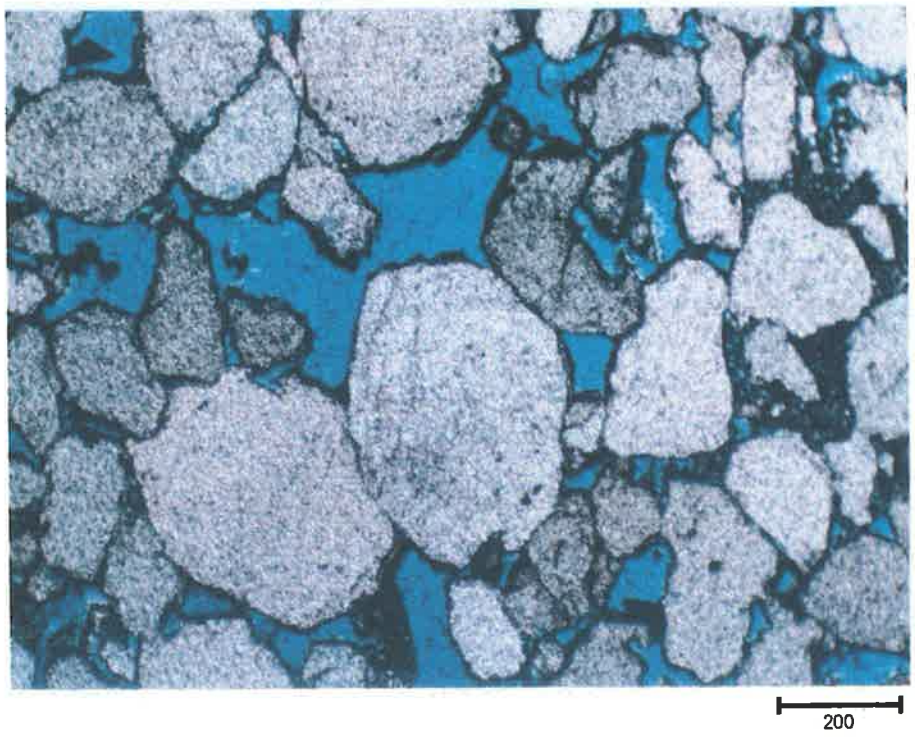

Figure 3.17 (ii): Thin section G17 1fi under plane polarised light. Where dark overgrowth rims are not pronounced is where quartz overgrowths will not be recognised (scale bar in microns).

It is suggested that the increase in calculated porosity using this technique is a result of using the CL micrograph, which does not allow for clear recognition of porosity. Any remaining variation is likely to be the result of the data being collected from different fields of view.

The cement analysis study indicated that PIA is a technique deficient for estimating the amount of quartz cement in a rock. This was due to the software's inability to distinguish between the quartz overgrowths and the primary quartz grains, which are the same colour. The results suggest that point counting a CL image provides a more accurate estimate of quartz cement. The other two methods (PIA and regular point counting) underestimate quartz cement because, when a positive identification is not made, both methods assign the point to the component with the larger percentage, i.e. framework quartz.

For rock characterisation study it is recommended that PIA be used to identify mineral composition and porosity. For cement analysis, CL micrographs used in conjunction with the PIA system would allow overlays to be created from which accurate amounts of quartz cement could be assessed. If this were not possible, then CL micrographs would require point counting.

Chapter 4 POROSITY ANALYSIS

4.1 POROSITY MEASUREMENT

Quantification of the heterogeneity (study of the porosity distribution) in the clean quartz arenite of the Hutton Sandstone reflects the measure of the change in lithology, grain size, sorting and cementation. Variation in any of these variables will be reflected by changes in porosity.

To quantify the heterogeneity of porosity in the sandstone using PIA, three separate continuous strips of porosity area measurements were taken along the length of each thin section. This was done using the 4x-magnification objective lens resulting in a field of view with dimensions of 1500 microns (horizontal) by 1025 microns (vertical).

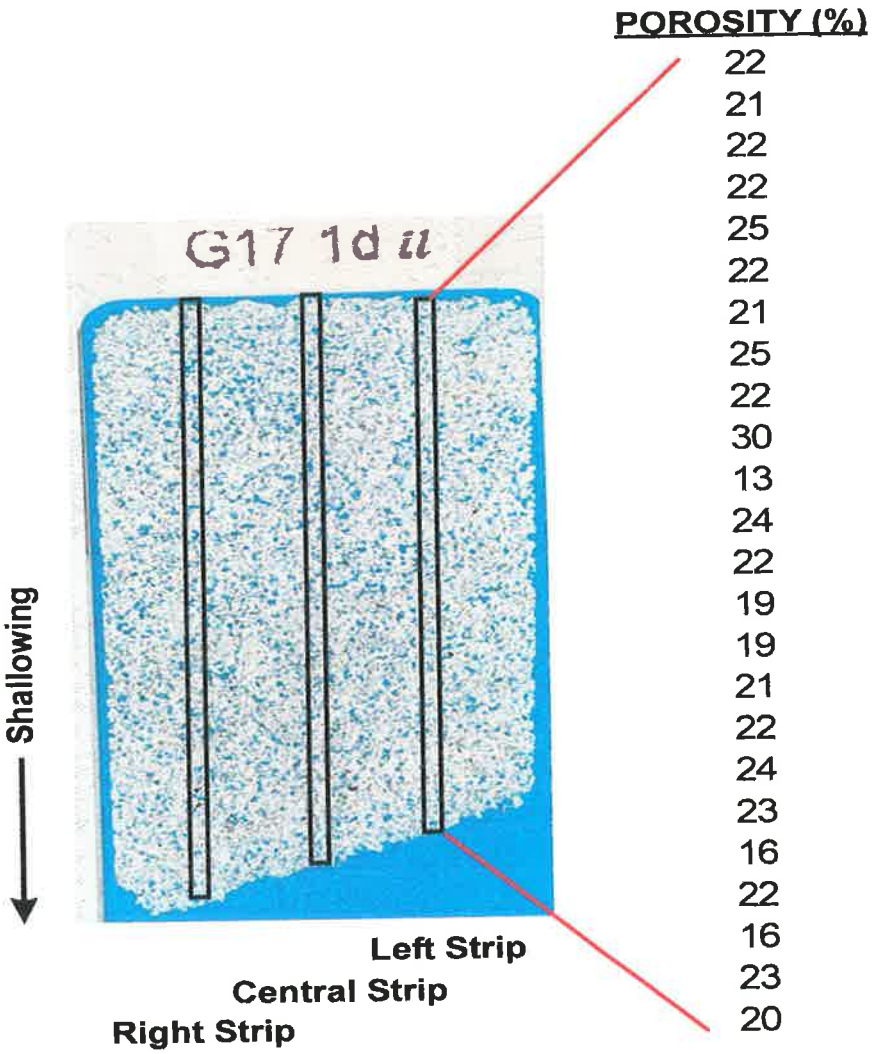

Figure 4.1: Pattern used to collect the 3-strip porosity data in thin section. Special care was taken noting the shallowing direction to keep data acquisition consistent.

Figure 4.1 shows the positioning of the three strips of values taken in thin section whilst also showing the porosity values obtained from the left strip. Note the left strip is located on the right-hand side of this thin section because the shallowing direction points down page, allowing the data to be collected consistently.

The thin section was placed horizontally on the tightened microscope rotating stage. The on-screen field of view is rectangular with the long axis parallel to the placement of the thin section on the stage (Figure 4.2)

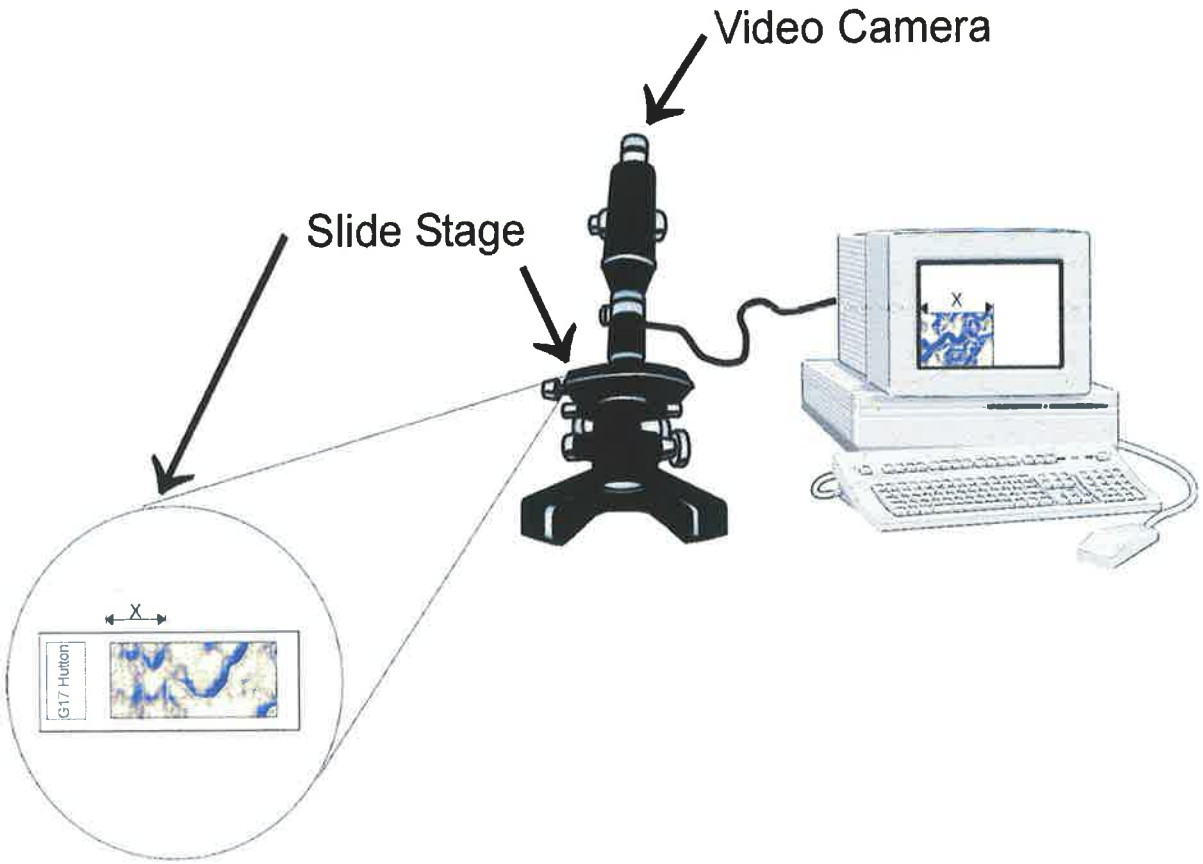

Figure 4.2: Set-up of PIA system, showing the relationship between the on-screen field of view and the thin section on the microscope stage.

Each strip of porosity data was generated by starting at one end of the thin section and then making incremental moves, with each move being the adjacent field of view, until the opposite side of the thin section was reached.

Even though the sandstone section was discontinuous (there are gaps between some thin sections, for example, a 3-foot (1-metre) gap exists between thin sections 2aiii and 1g), however, they were grouped together to highlight the variation in porosity along the available length of reservoir sandstone.

Each column was averaged and plotted separately (Figure 4.3), highlighting the interpreted cross-bed sets visible in the core. Cross-bed set one includes thin sections 2ai to 2aiii, while cross-bed set two was interpreted between 1bii to 1a lower. The thin sections between these cross-beds included the three-foot gap and the missing section from which the piece was sent for micro-CT scanning. For this reason, it has not been considered as a separate cross-bed set.

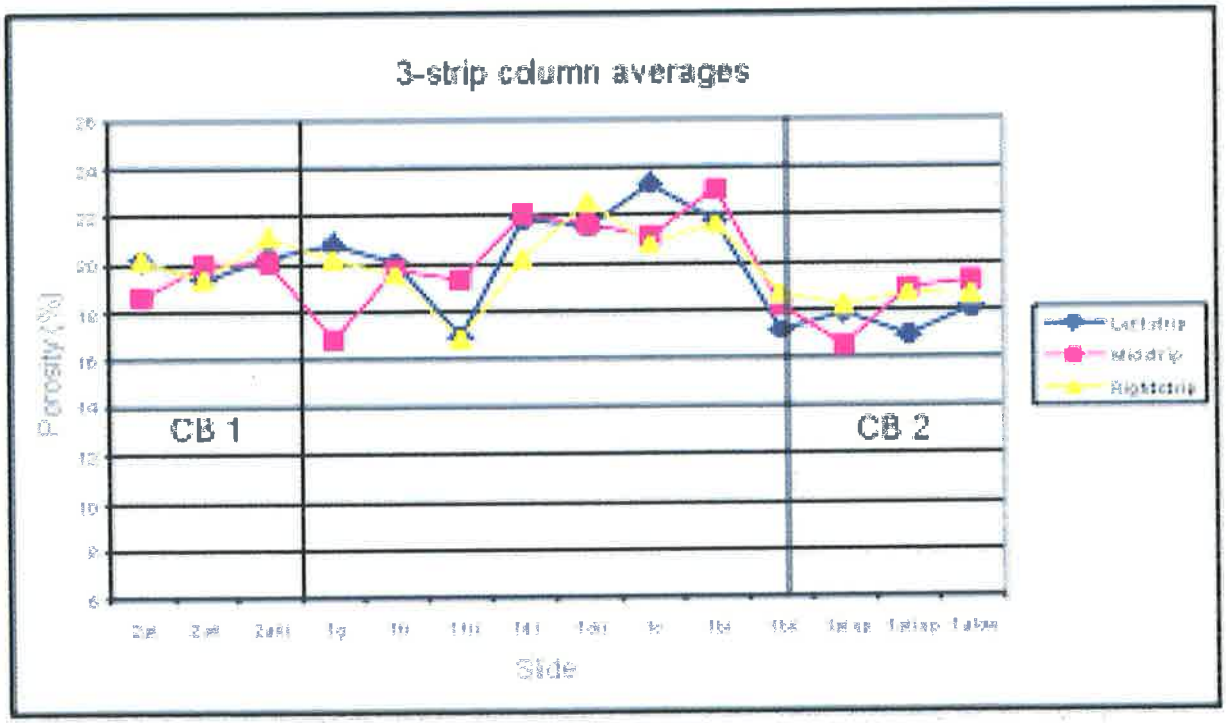

Figure 4.3: Porosity variation from thin section for the data from each of the three strips measured along the length of the vertical plug (missing core with piece sent for micro-CT scanned not included). The breaks between interpreted cross-bed set 1 and 2 (CB 1 and CB 2) are included.

The three-strip porosity data were obtained through the 4x-magnification objective lens using a specially designed program at the NCPGG. For visual assessment, the data were plotted as a spatial display where the readings were expanded across equal

areas of influence, allowing the readings to represent porosity distribution across the whole slide (Figure 4.4). Raw data can be seen in Appendix 9, while the spatial displays for samples 1aii upper and 2aii are included as Figures 4.4 (i-ii). The remaining displays are included in Appendix 10.

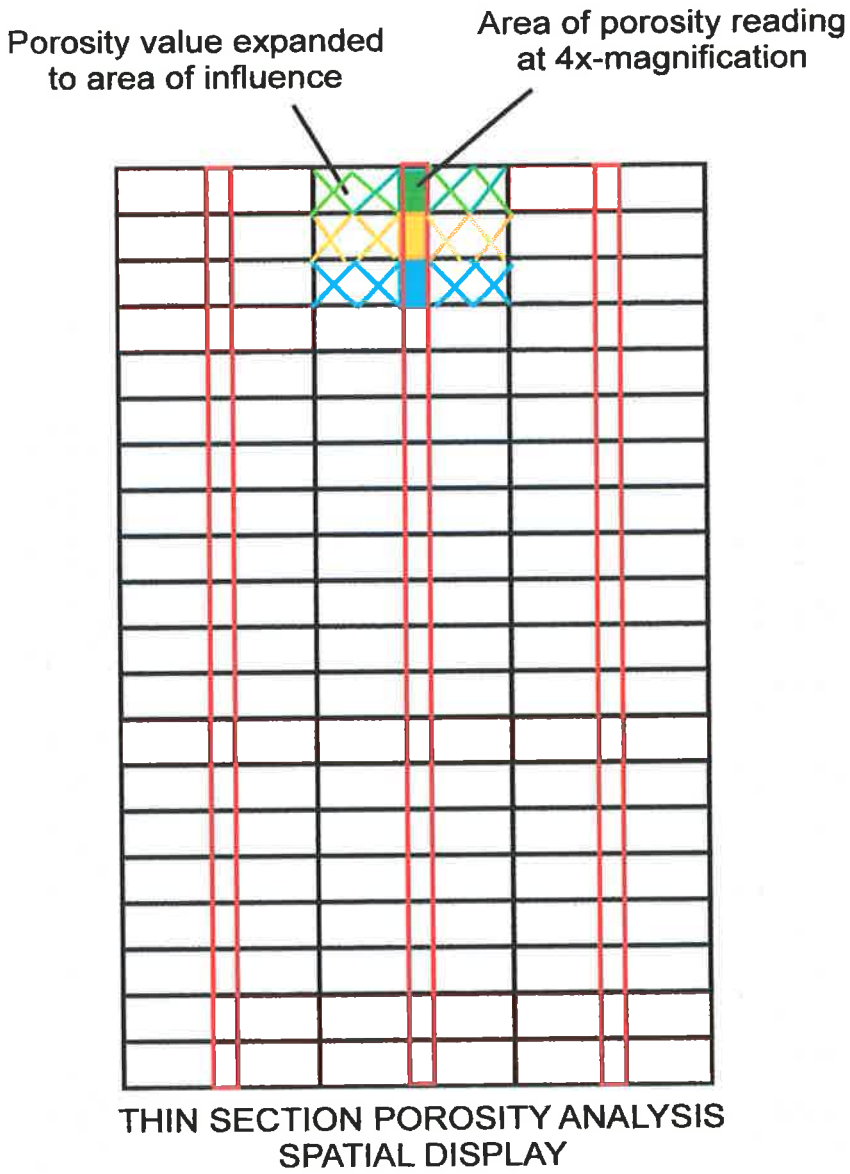

Figure 4.4: Schematic diagram of a thin section, the red columns show the areas where porosity was collected, while the cross-hatched areas shows how this data was displayed spatially.

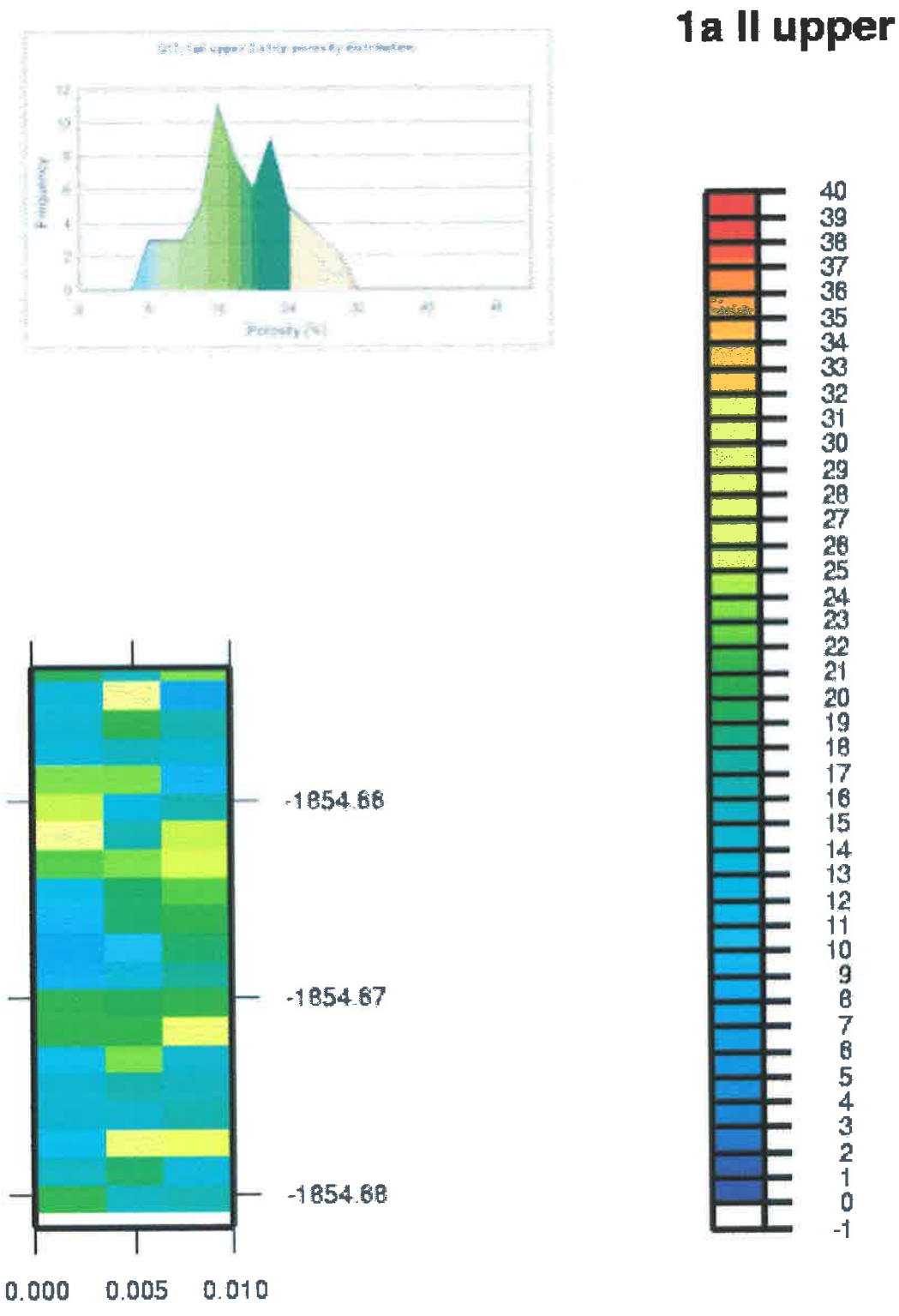

Figure 4.4 (i): 3-strip spatial display for thin section 1aii produced from 60 readings, spread across an area of influence. A low porosity area is observed in the central region of the slide, displaying heterogeneity at a microscale.

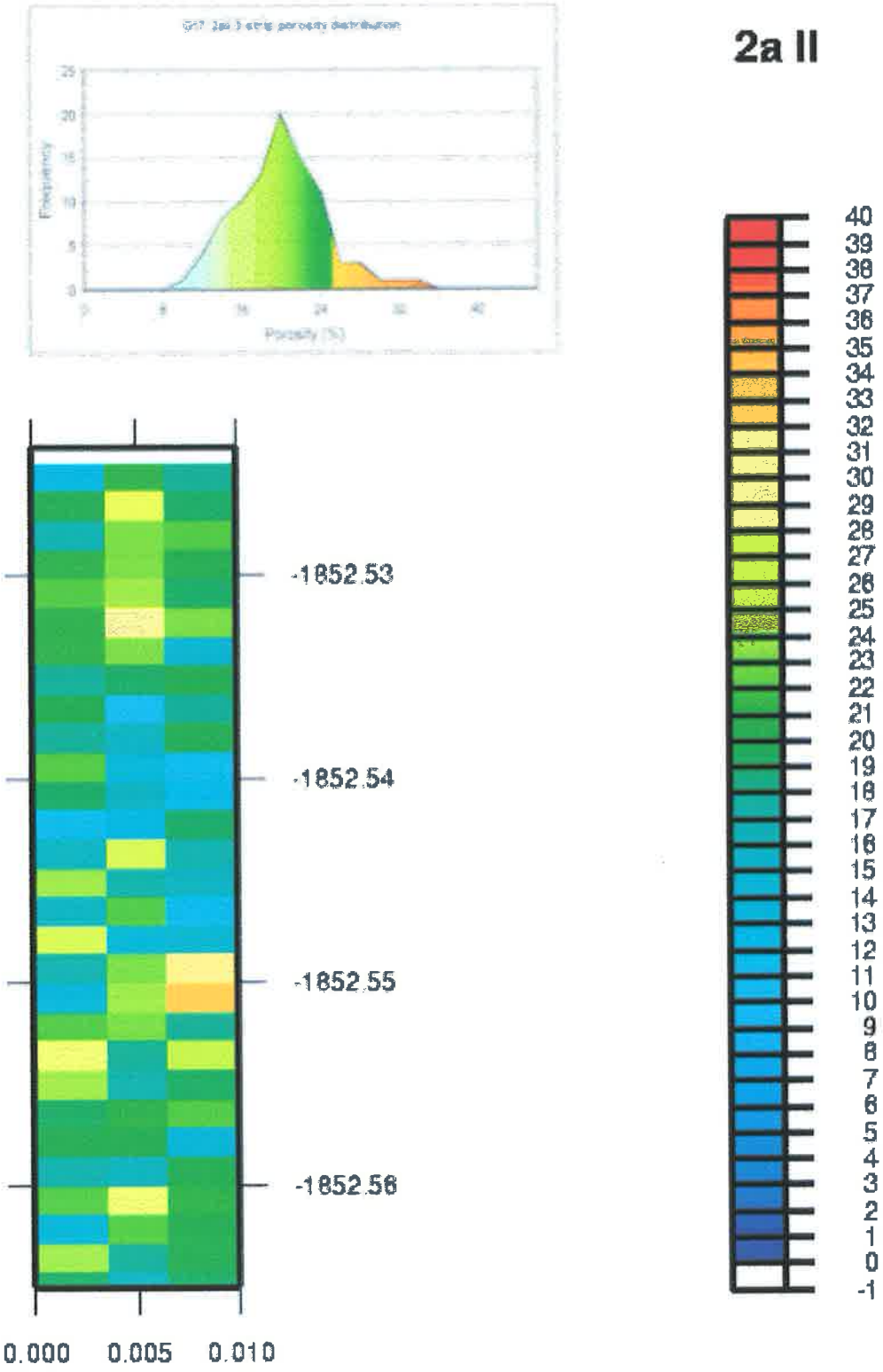

Figure 4.4 (ii): Spatial display for thin section 2aii produced from 87 readings. Interpretation of the core photo suggests some cross layering is visible across the central region, indicated by the porosity display as a low porosity zone, this being further evidence of heterogeneity at a microscale.

The 5x-magnification objective lens was then used to produce a full coverage data set across two of the fourteen samples (1aii upper and 2aii). The 5x-magnification lens was used because a different microscope was needed which allowed the use of a mechanical stage slide (which was unavailable on the microscope with the 4x lens), to provide precision for both the vertical and horizontal moves. The dimensions between the 5x- and 4x-magnificaion lens field of view are very similar (Figure 4.5).

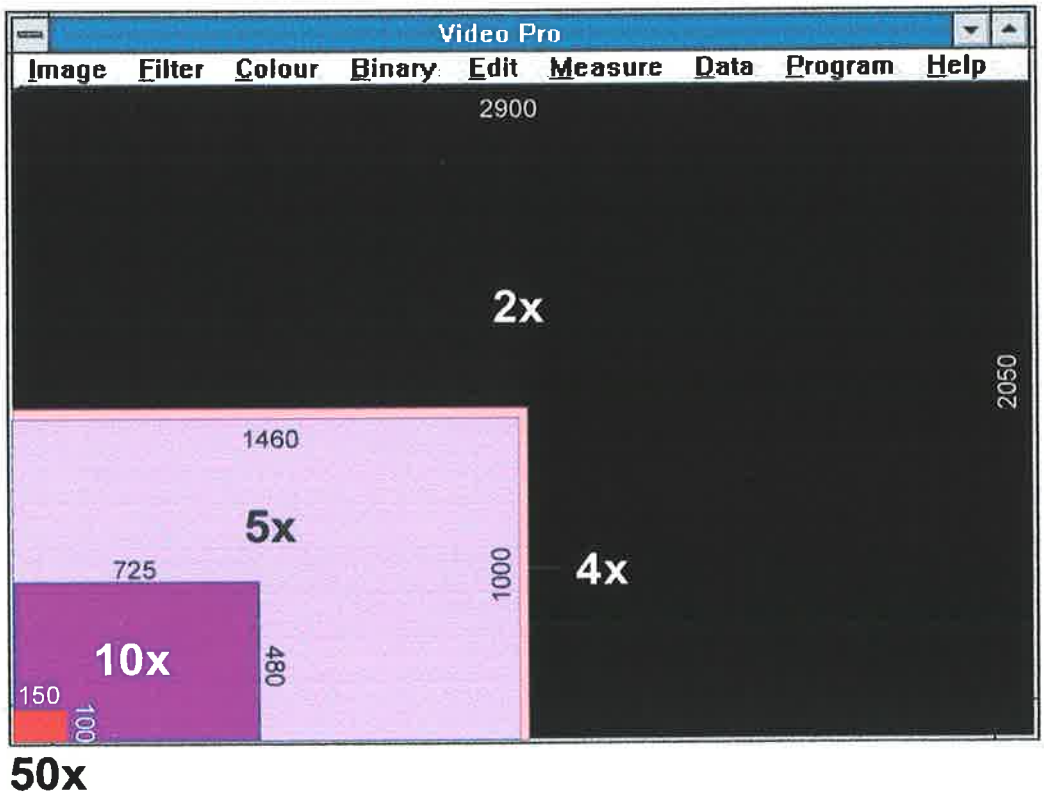

Figure 4.5: Relative coverage of a thin section at the various magnifications used to measure porosity (scale measurements are in microns and were measured using the line tool from the measure menu).

The data set was limited by the travel of the stage slide, which prevented the ends of some slides from passing under the objective. Only two samples were selected for full coverage. Selection of two samples from different cross-bed sets at opposing ends of the core increased the likelihood of variation and provided a sufficient data set to display the data and conduct a statistical analysis. Slide 2aii was selected because there was evidence of banding within the rock (see Appendix 11 for thin section photo) and it was anticipated that this banding might be reflected in the porosity distribution maps. The data from the two samples can be seen in Appendix 12, and the spatial display data are shown separately as Figures 4.6 (i) and (ii).

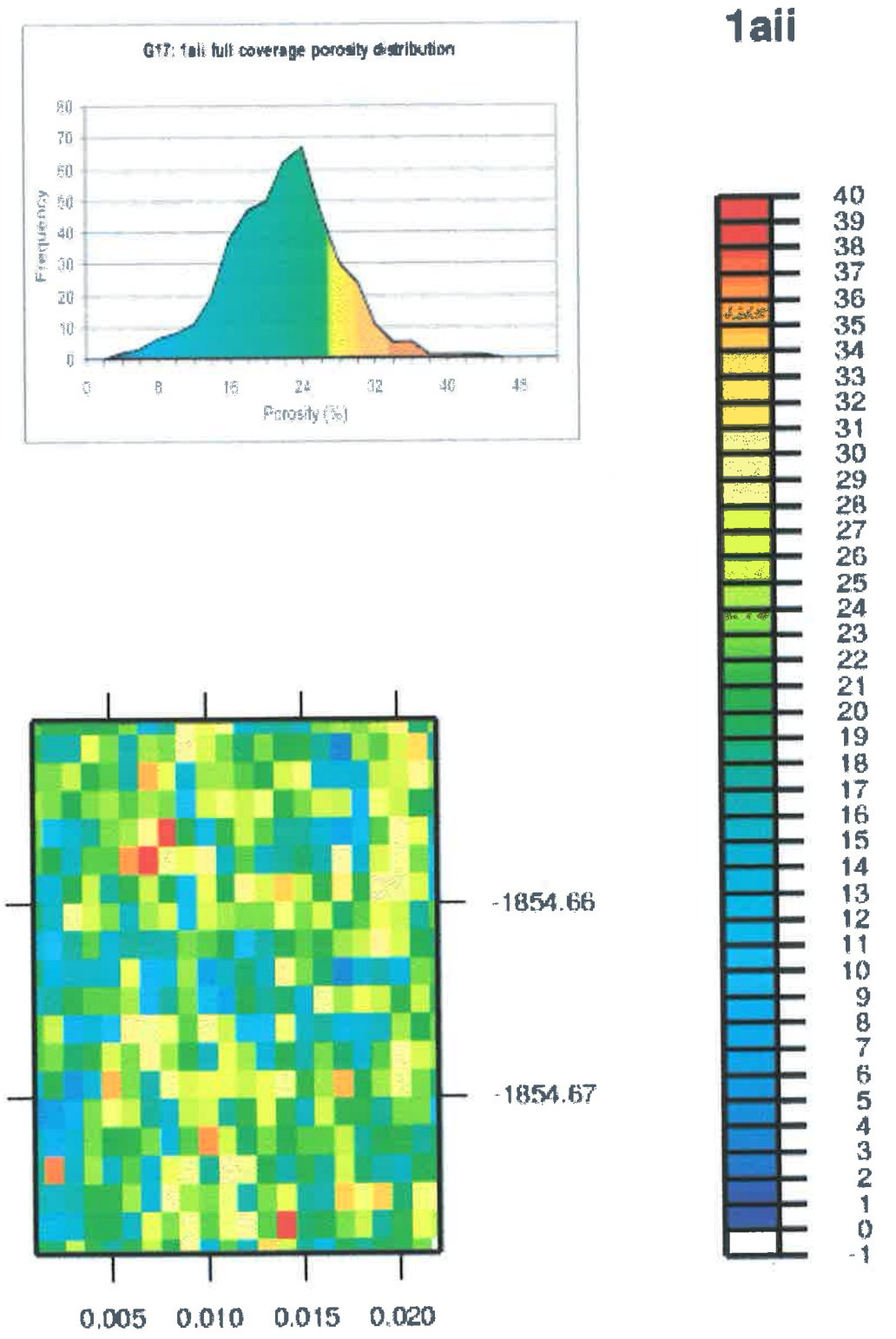

Figure 4.6 (i): Full coverage spatial display for thin section 1aii upper. No visible layerings, while patches of high and low porosity are visible throughout the sample. These areas are likely to control fluid flow.

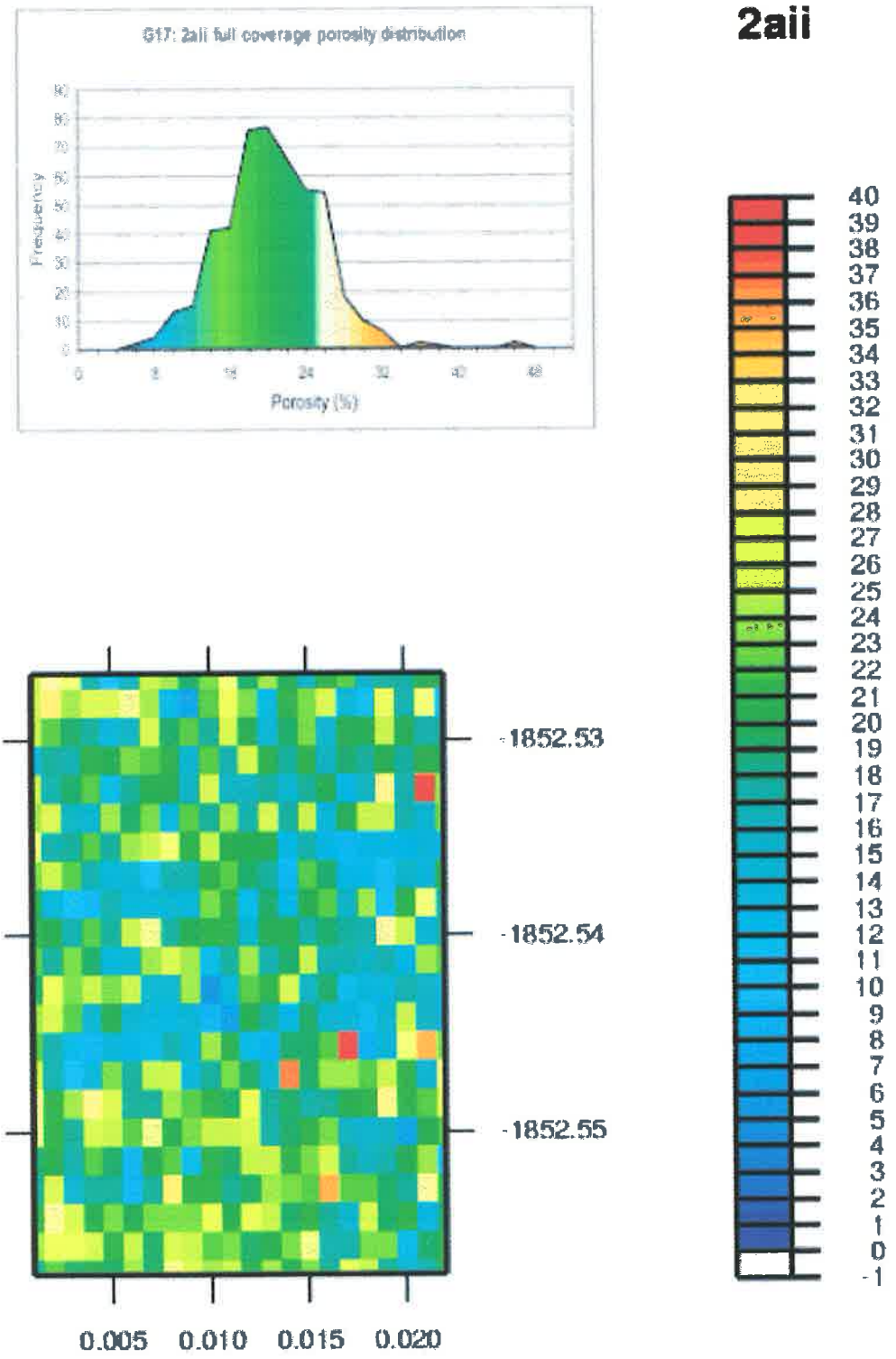

Figure 4.6 (ii): Full coverage spatial display for thin section 2aii. Two low porosity layers are interpreted through the central region of the display. The porosity histogram is included above the display.

Data from fields of view under the 5x-magnification objective were grouped at a pseudo 2.5x-magnification to assess whether a lower magnification might show the same variation (displayed within Appendix 12). The display data (Figure 4.6 (iii)) was created by averaging 4-neighbouring data points from the 5x-magnification data set, creating a pseudo 2.5x-magnification data set. The display shows the same features observed in the 5x-magnification data set, but the results are clearly smoothed. Using this type of magnification would provide similar information, however the smoothing results in significant reduction of the apparent patchiness.

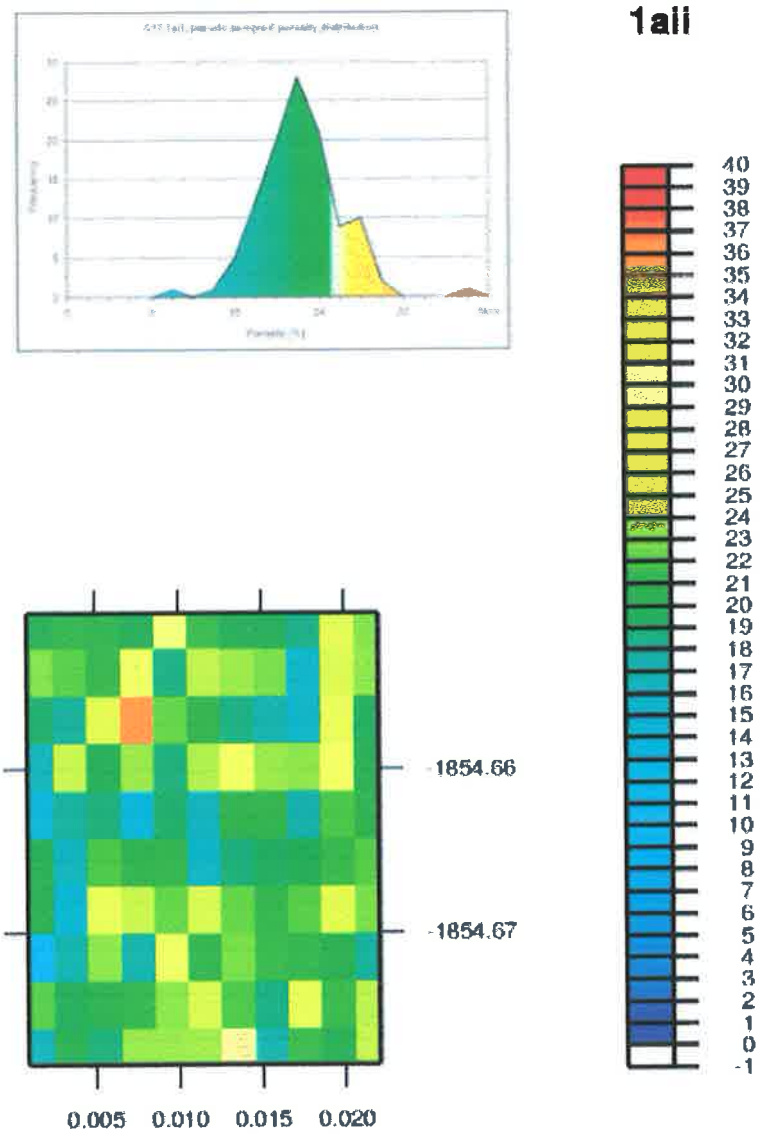

Figure 4.6 (iii): Spatial display of pseudo 2.5x-magnification porosity data for thin section 1aii upper. Areas of high and low porosity are identified with significant smoothing. The porosity histogram shows the distribution of the data within the display.

An attempt was made to emphasise this patchiness by changing the colour display scale for the 5x-magnification data. Readings with porosity less than 11% were allocated a 'low' value; readings greater than 32% were allocated a 'very high' value, while the remaining readings were cantered on the average porosity, taken to be between 20% and 22% inclusive. The displays are shown as Figures 4.7 and 4.8.

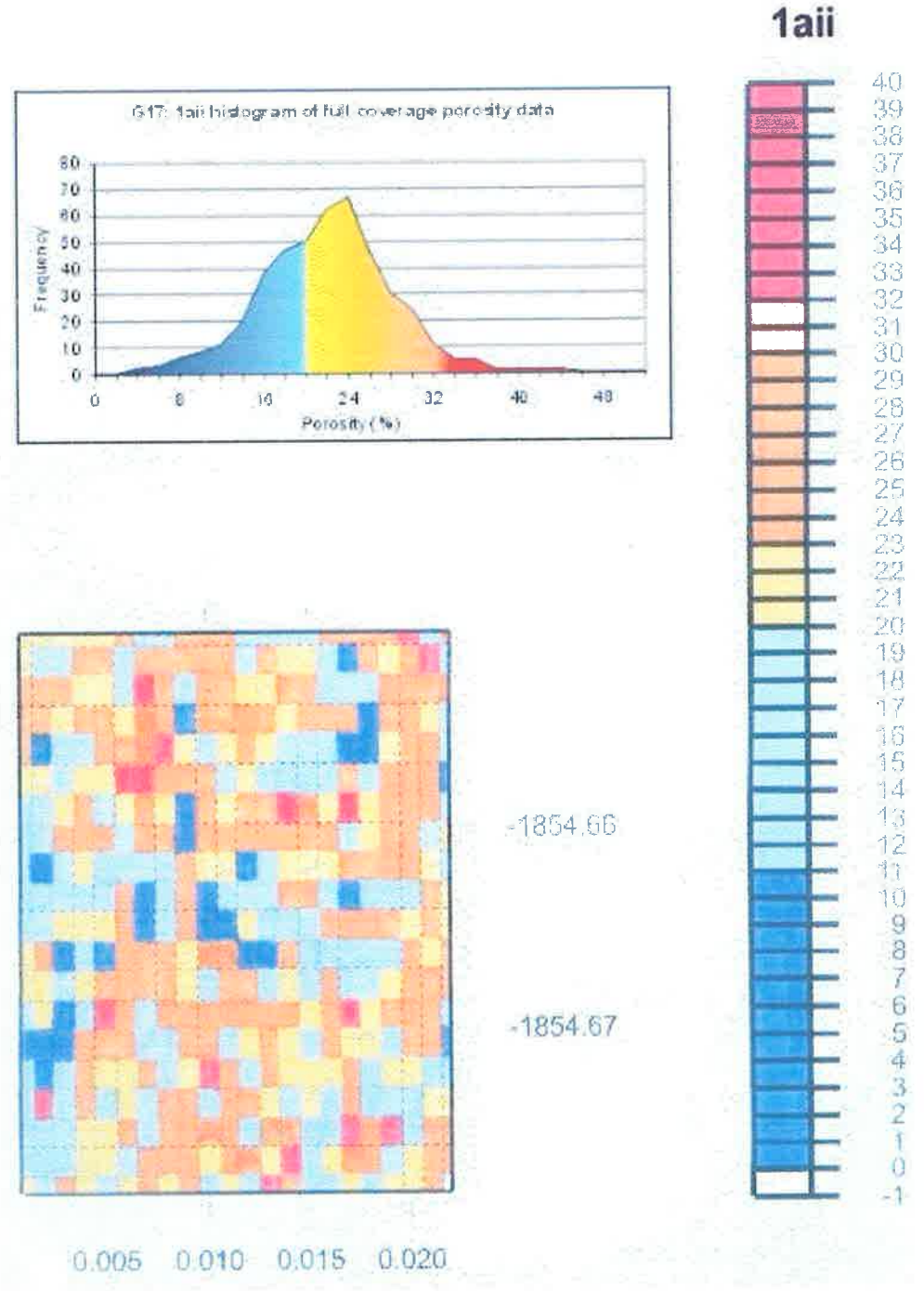

Figure 4.7: Spatial display of the full coverage porosity data for thin section 1aii upper. The colour display is altered to highlight the apparent patches within the data. The porosity histogram shows the distribution of the data within the display.

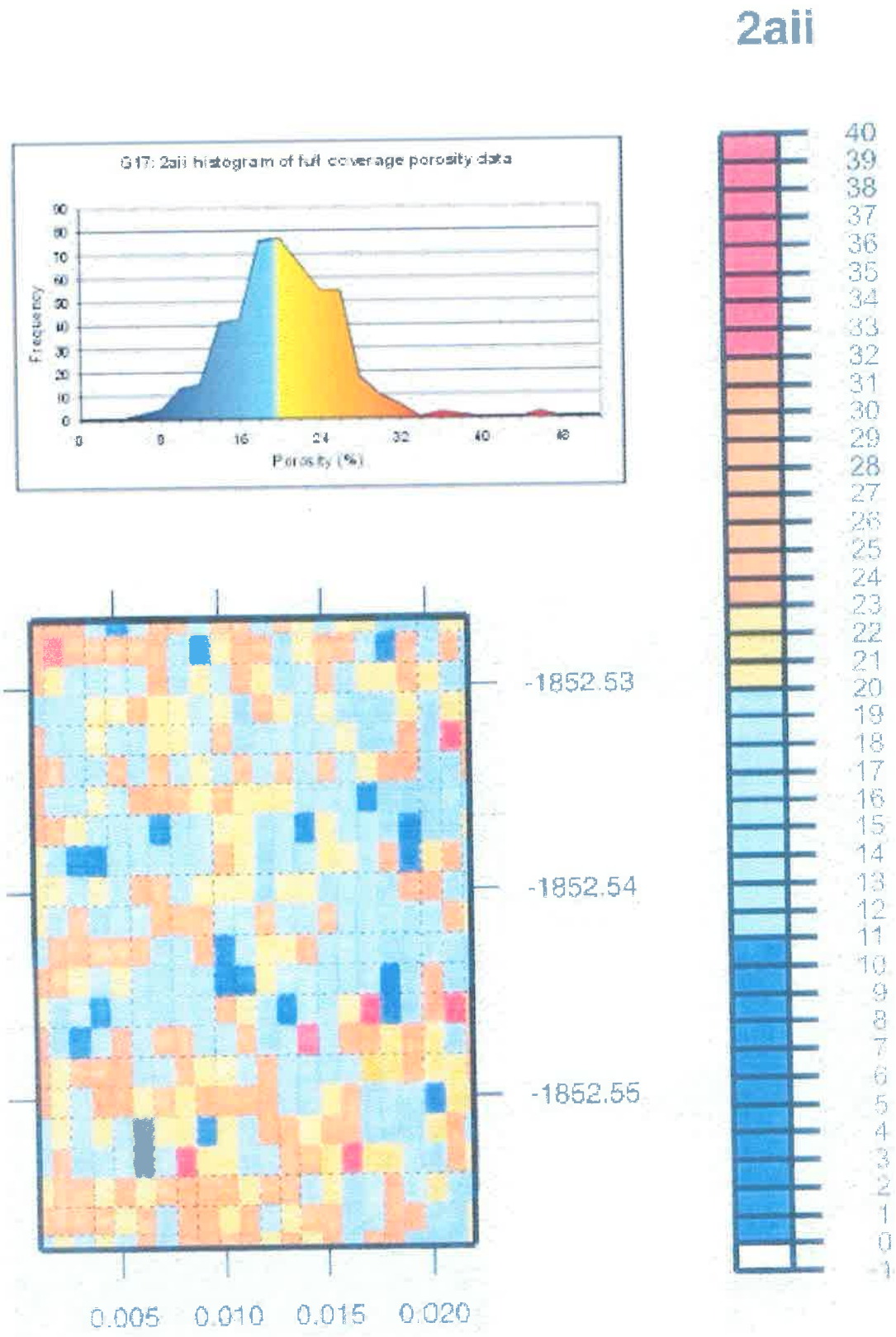

Figure 4.8: Spatial display of the full coverage porosity data for thin section 2aii. The colour display is altered to highlight the apparent patches within the data. The porosity histogram shows the distribution of the data within the display.

The 5x-magnification data from 1aii were re-sampled to determine the minimum number of readings that were needed to accurately quantify porosity in a thin section. This was done by creating a random number generator in Matlab (Appendix 13), which was designed to select sets of between 10 and 300 different readings from the available data, at increments of 10. The program repeated the sampling 100 times for each increment and then calculated the average of each. The data were then plotted to see the variance around the true mean porosity, which was taken to be the average of the entire data set (Figure 4.9 (a)).

This process was repeated with the random number generator altered to assess 500 iterations rather than 100, theoretically constraining the obtained average porosities around the true mean. The data were plotted to determine the variance and to check for differences between the two (Figures 4.10 (a)).

From this data set, it was possible to plot the standard deviation (SD) of the obtained averages as a function of the number of samples used to determine average porosity (Figures 4.9 (b) and 4.10 (b)).

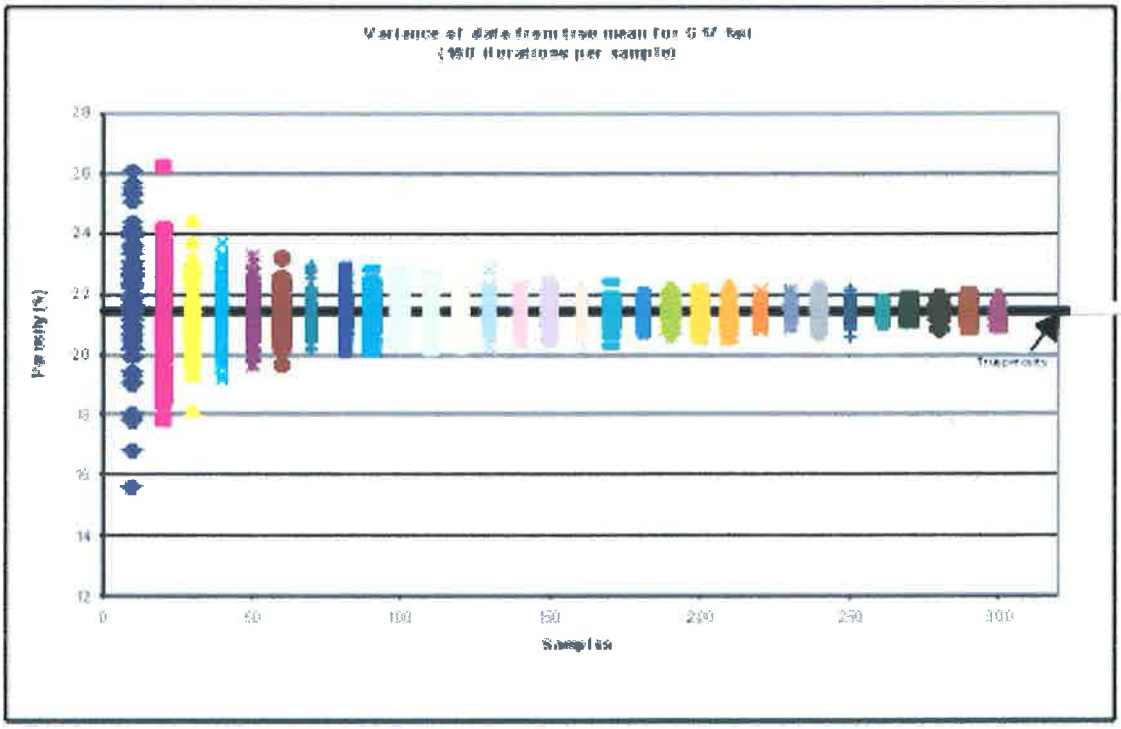

Figure 4.9 (a): Porosity variance around the true mean plotted from data obtained from a random number generator (RNG) using the 5x-mag data. The RNG chose between a group of 10-300 porosity values and did this 100 times. Using 10 samples as an example, the average obtained varied between 15.6% and 26.2%. The average when 50 samples were acquired 100 times ranged between 19.5% and 23.5%.

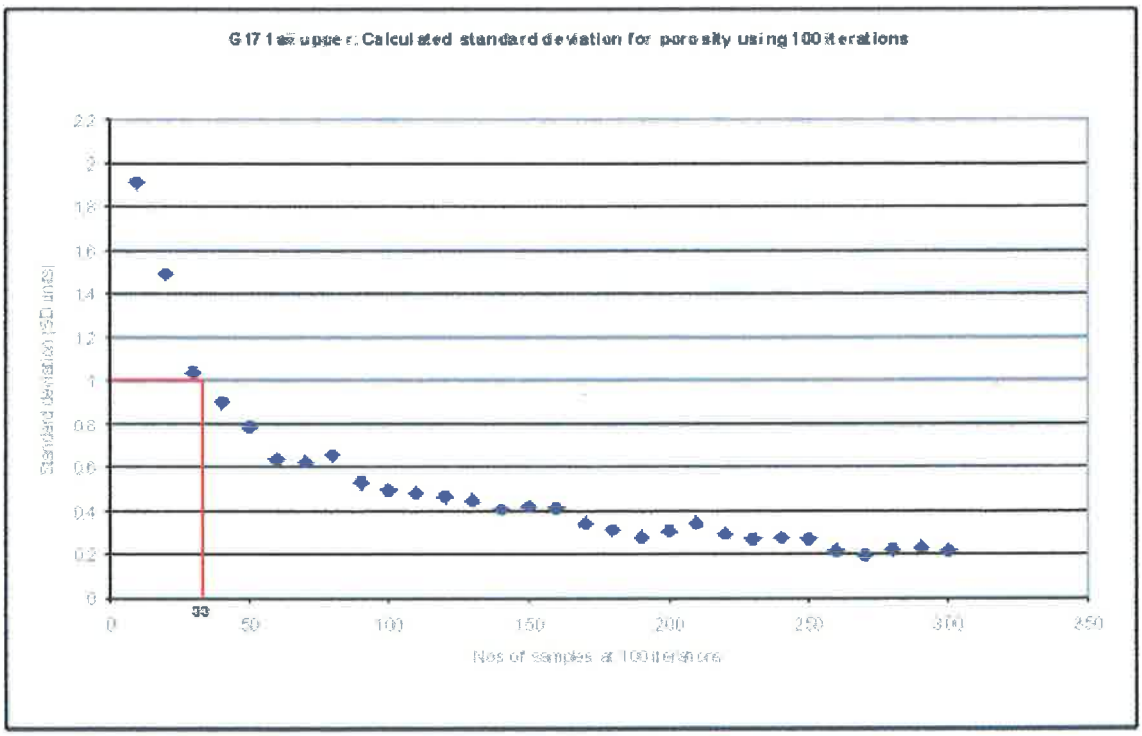

Figure 4.9 (b): The standard deviation (SD) inherent in the variation shown in the porosity data plotted in Figure 4.9 (a) above. The SD drops below one after 33 points have been sampled and the curve flattens considerably after 60 points are sampled.

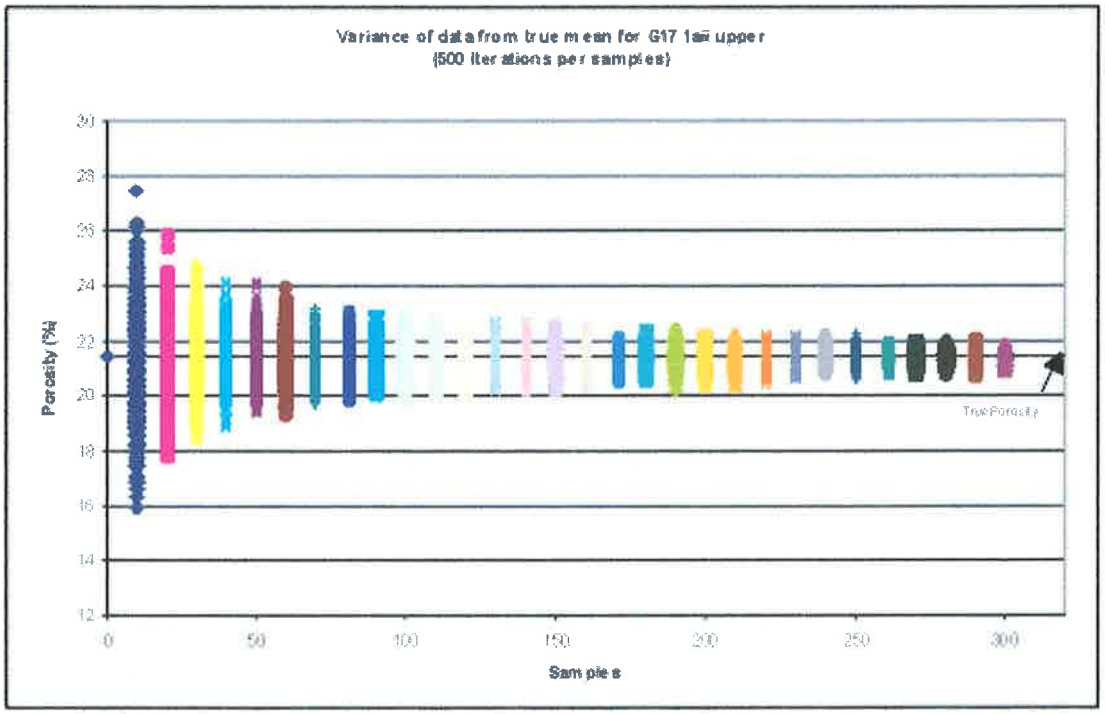

Figure 4.10 (a): Porosity variance around the true mean plotted from data obtained from a random number generator (RNG) using the 5x-mag data. The RNG chose between a group of 10-300 porosity values and did this 500 times. Using 10 samples as an example, the average obtained varied between 15.9% and 27.5%. The average when 50 samples were acquired 500 times ranged between 18.6% and 24.1%.

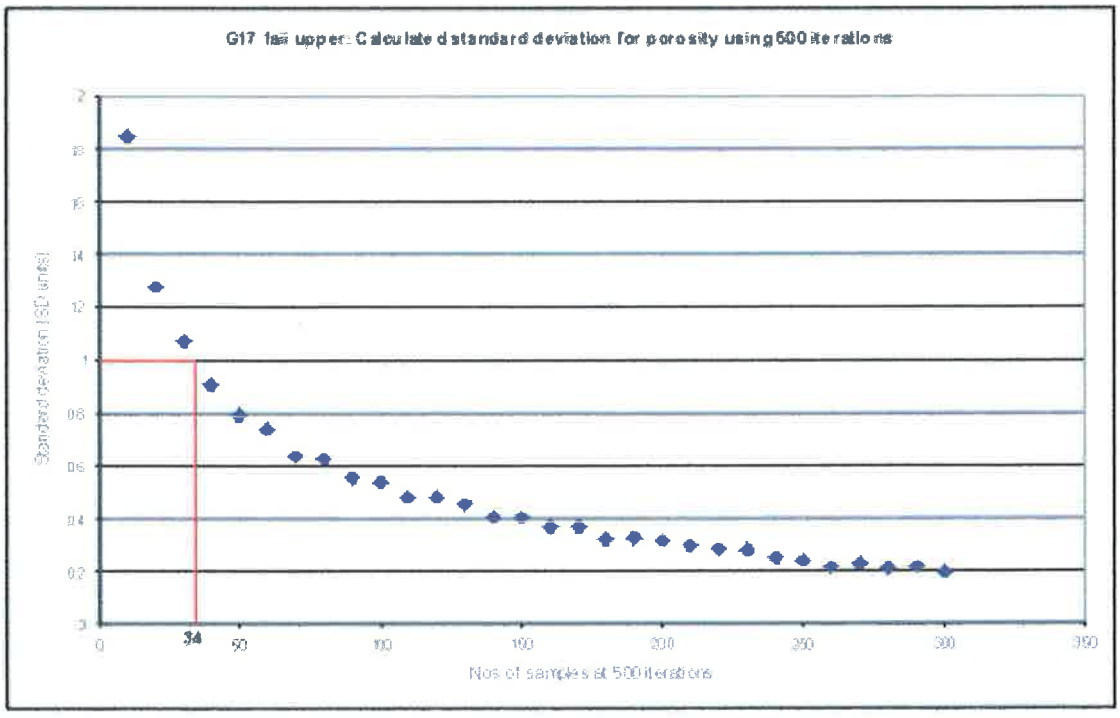

Figure 4.10 (b): The standard deviation (SD) inherent in the variation shown in the porosity data plotted in Figure 4.10 (a) above. The SD drops below one after 34 points have been sampled, and the curve flattens considerably after 70 points are sampled.

Statistics were then used on the 5x-magnification data set in an attempt to upscale porosity distribution. The aim was to create, using kriging, a representative thin section porosity distribution map, from a reduced data set. Kriging is a geostatistical interpolation technique that is a linear weighted-averaging method, similar to the inverse weighted distance method (Chambers *et al.,* 2000). However, unlike inverse distance, kriging weights depend on a model that takes into account the spatial correlation of the data points, represented by the semi-variogram. The semi-variogram is more reliable at depicting the shapes of geological features and making maps look more geologically plausible (Chambers *et al.,* 2000).

The semi-variograms created from the 5x-magnification data set for samples 1aii and 2aii-upper are below (Figure 4.11 and 4.12).

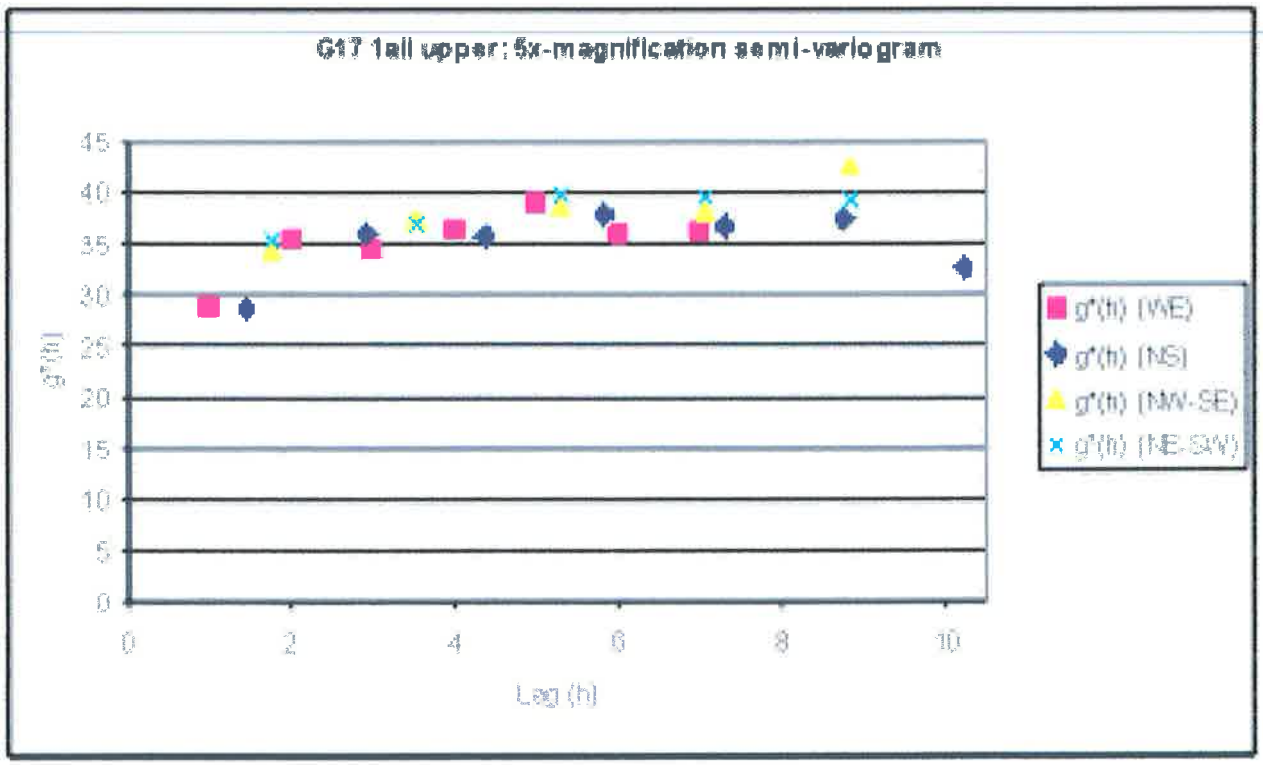

Figure 4.11: Semi-variogram of the 5x-magnification data set for thin section 1aii-upper suggesting porosity shows little correlation (nugget effect). Lag 1 corresponds to a move of 1000microns, while lag 2 corresponds to a move of 2000microns. Lags were calculated in different orientations to see if there was any directional correlation in the data set.

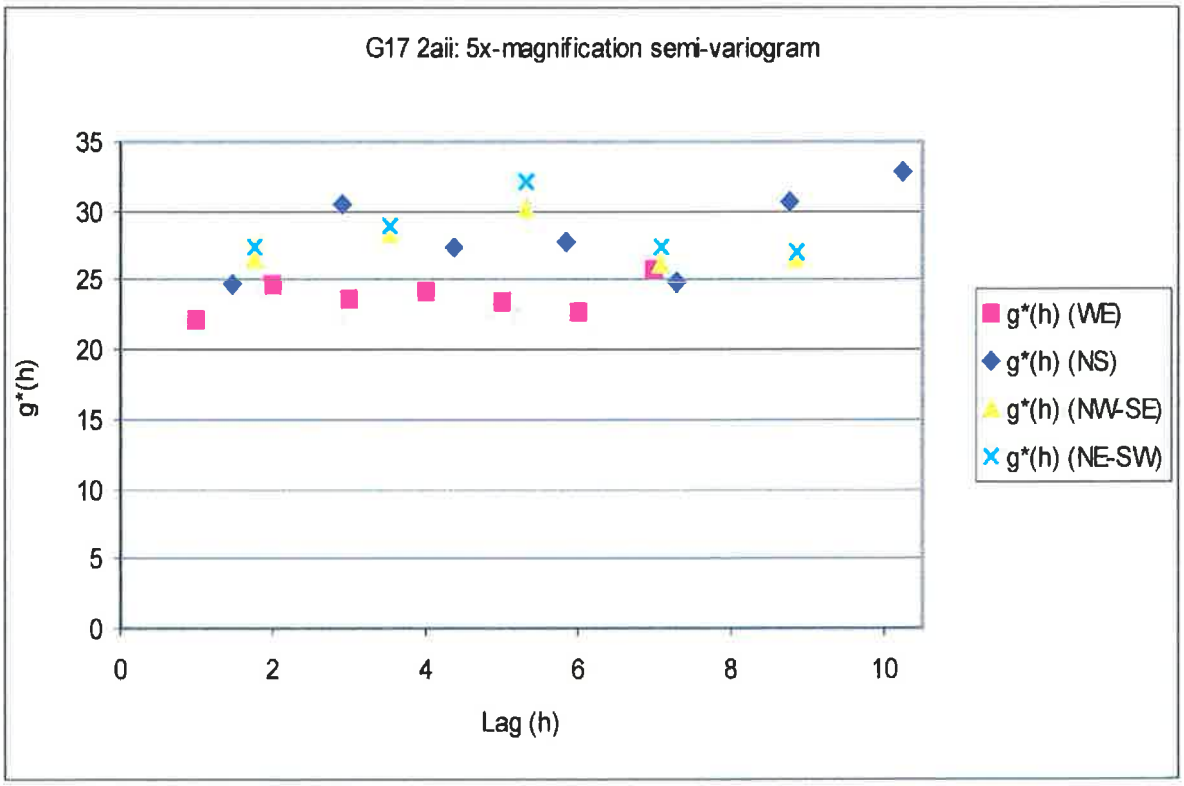

Figure 4.12: Semi-variogram of the 5x-magnification data set for thin section 2aii suggesting there is little correlation, neither distance nor direction influence correlation of porosity measurements. (Note, for direction WE, lag 1 corresponds to a move of 1000microns, while lag 2 corresponds to a move of 2000 microns).

Both semi-variograms show essentially no correlation within the porosity data for these two samples from the Hutton Sandstone. Figure 4.11 shows a slight nearest neighbour correlation, but the effect is very weak, therefore the data can be treated as having random distribution.

The data sets were run through a program, GSLIB, at the Melbourne CSIRO to check and develop the semi-variograms testing for correlation. The program tested the semi-variograms developed in Microsoft Excel 1997 ™, and provided a quick and efficient means of testing for correlation at greater separation distances or lags. The semi-variograms are included as Figures 4.13 and 4.14.

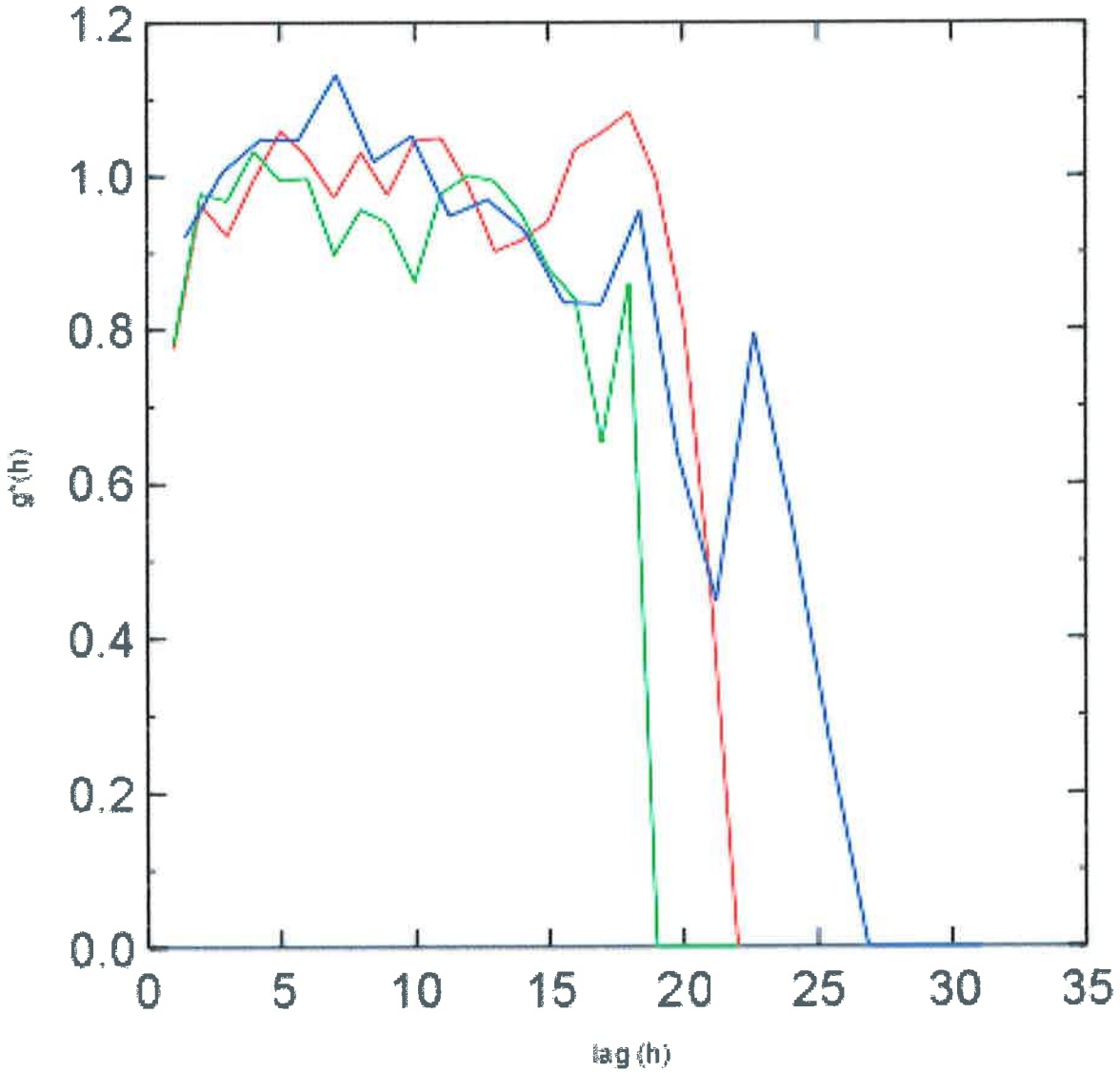

Figure 4.13: G17 1aii upper semi-variogram calculated from the program GSLIB. Colours represent directions: NS is displayed in green, WE as red, and the diagonals are averaged and displayed in blue. There is an interpreted apparent, slight short-ranged (lag 1) weak nearest neighbour correlation visible in this sample (semi-variogram produced by GSLIB at the Melbourne CSIRO).

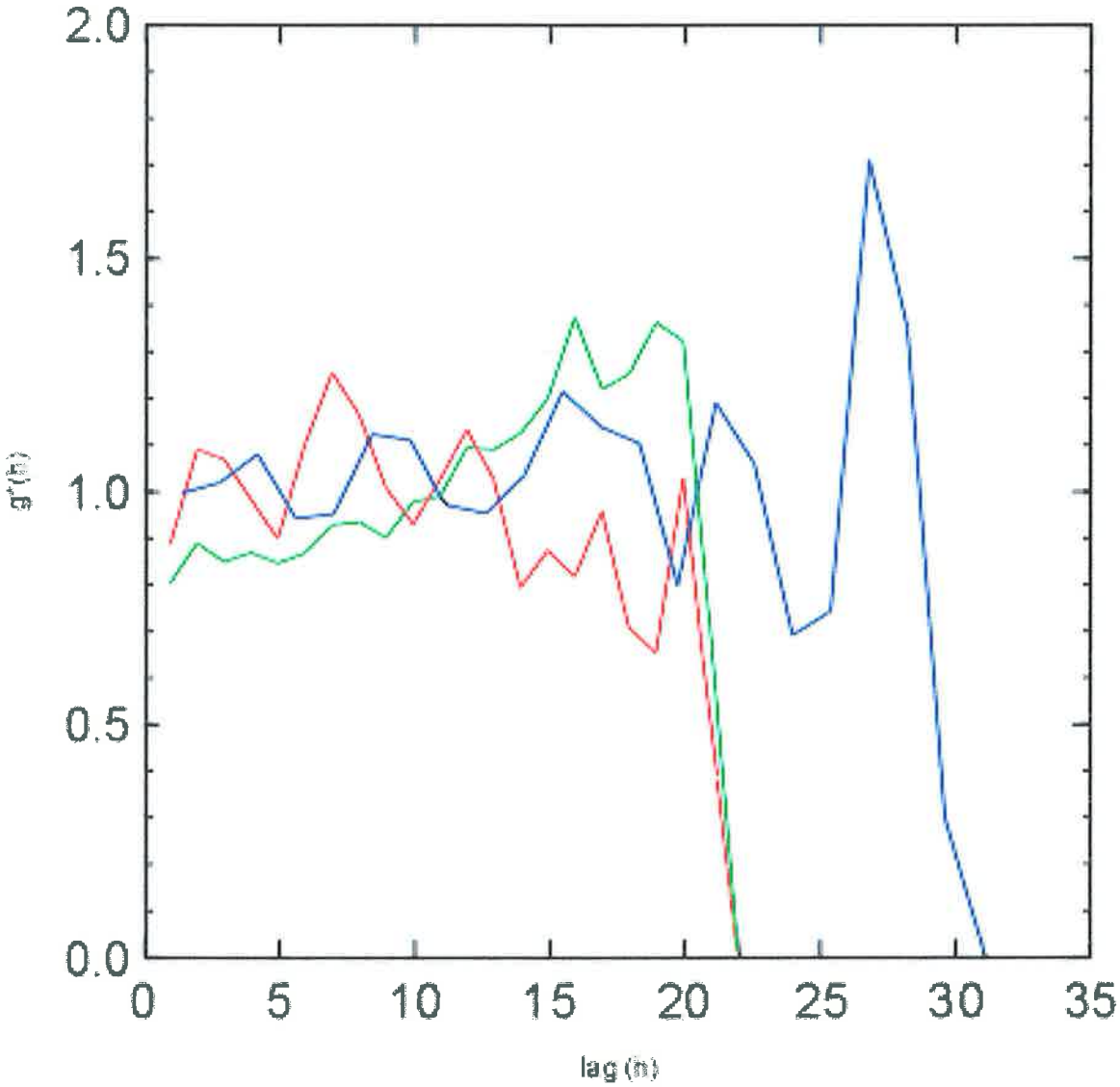

Figure 4.14: G17 2aii semi variogram calculated from the program GSLIB. Colours represent directions: NS is displayed in green; WE in red and the diagonals are averaged and displayed in blue. No correlation is seen in this sample (semi-variogram produced by GSLIB at the Melbourne CSIRO).

An attempt was made to improve definition of the semi-variograms at shorter lags. Lags are the horizontal or vertical distances between data points. It was suggested that collecting more data at increased magnifications (using the 10x and 50x objective lens (Appendix 14)) would achieve this improvement as one might expect better correlation between porosity values at shorter distances. The resultant semi-variograms are shown in Figures 4.15 and 4.16, while Figure 4.17 was an attempt made to model the 50x-magnification data for sample 1aii.

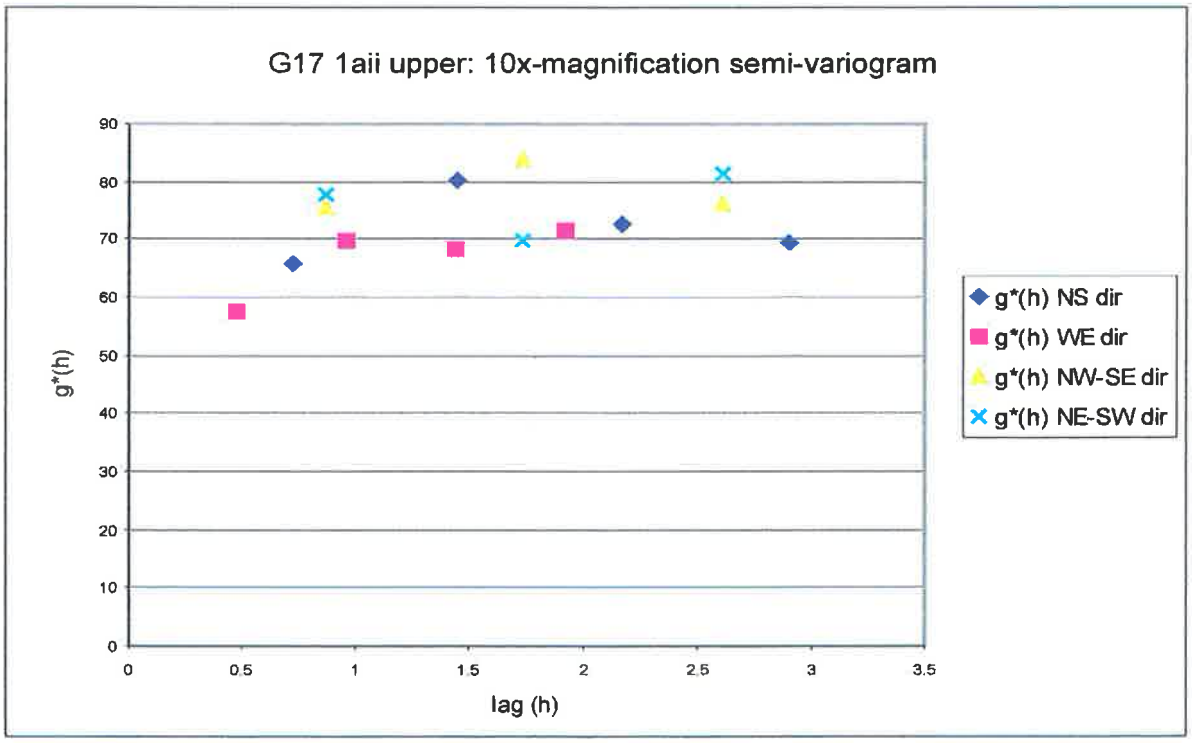

Figure 4.15: Semi-variogram from thin section 1aii-upper at 10x-magnification showing little correlation. Lag (h)= 0.5 is equivalent to a lag of 1 and corresponds to a move of 500microns, while lag (h) =1 is equivalent to a lag of 2, corresponding to a move of 2 x500 microns (1000microns).

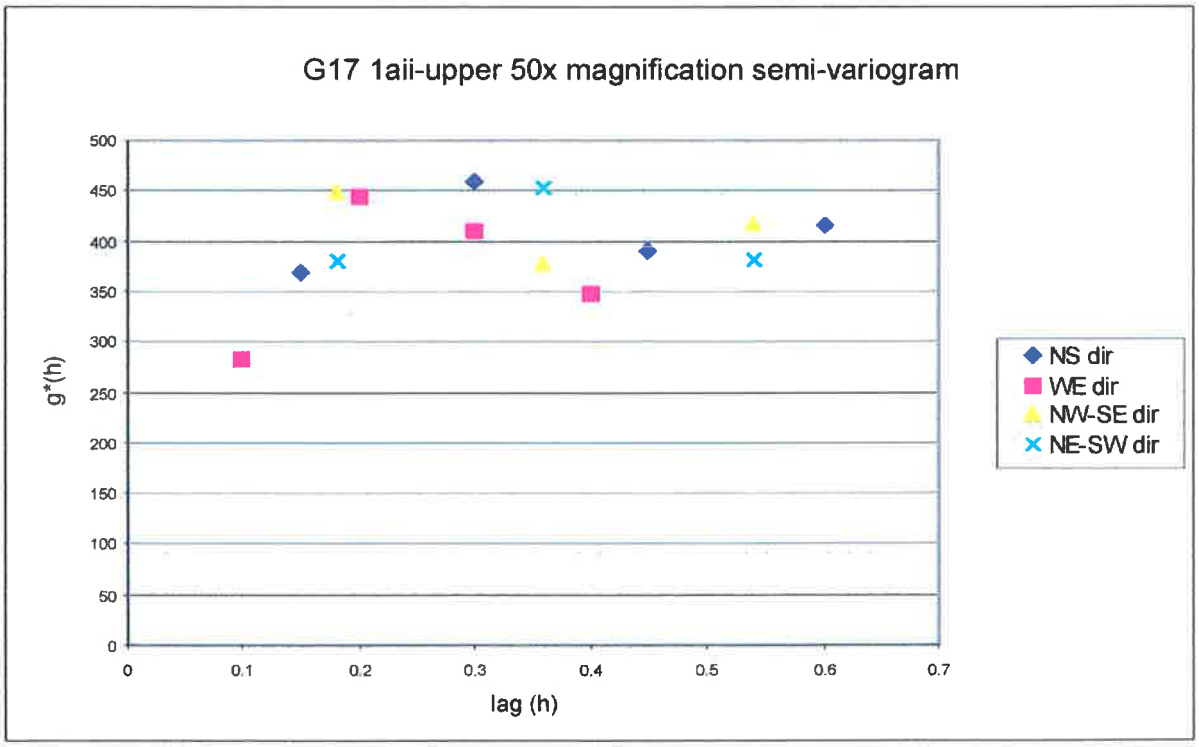

Figure 4.16: Semi-variogram from thin section 1aii-upper at 50x-magnification showing little correlation. Lag (h)= 0.1is equivalent to a lag of 1 and corresponds to a move of 100microns, while lag (h) =0.2 is equivalent to a lag of 2, corresponding to a move of 2 x100 microns (200microns).

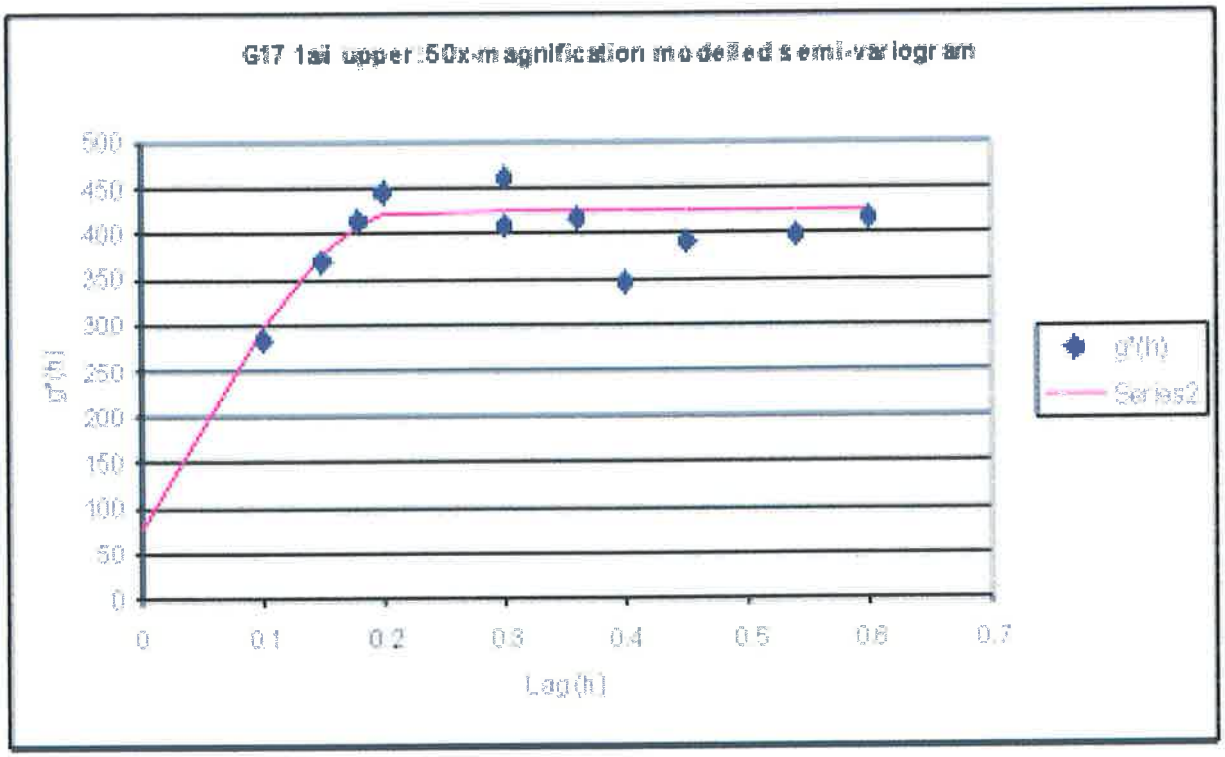

Figure 4.17: Modelled 50x-magnification data of thin section 1aii-upper. Both diagonal directions have been averaged. Model fits the first three points, however all three are still only lag 1 because of the different dimensions of the field of view when acquiring the data. At 50x-magnification, correlation exists between neighbouring porosity values and is weak.

An investigation to compare the average porosity calculated for sample 1aii for the data obtained from each individual magnification provided the results plotted in Table 4.1.

TABLE 4.1

Magnification	Average Porosity (%) (G17 1aii)	Number of readings used
4x	18.2	62
5x	21.4	439
10x	19.5	288
50x	17.7	250

Table 4.1 highlights the average porosity calculated for G17 1aii at different magnifications and the number of readings used to obtain that average.

4.2 INTERPRETATION OF DATA

As previously mentioned in Chapter 3, the porosity obtained from routine core analysis (RCA) ranged from 20% to 24% (Figure 3.3). The porosity determined from the three column strips using PIA indicates that the range is approximately 20% and 23% (Figure 4.3), and using the entire 5x-magnification data the 'true' porosity is 21.4%. Hence, PIA shows good correlation with the RCA data.

From Table 4.1, it was evident that the porosity estimate is influenced by magnification, as it shows porosity is under-estimated using a higher magnification (50x) compared with a lower magnification (5x). Further evidence of this was seen in Table 3.3 (Chapter 3) where, the total calculated summed to 108%. This suggests that the average of fourteen thin sections, with five readings used for each average at 5x-magnification over-estimated each component.

It is important to recognize the operator dependence inherent in PIA. At high magnification, the operator views a smaller area with fewer grains and pores and can distinguish grain boundaries more clearly, thus influencing the porosity estimate. Hence, there appears to be some operator bias towards the phase being analysed when producing the overlay to measure that phase.

It should be mentioned however, that higher magnifications allow the operator to see the 'thickness' of the thin section that creates the illusion of two apparent grain boundaries, one on the top surface of the thin section and one at the base. To overcome this, it is suggested that the operator should estimate the grain boundary by choosing an area between the two. At low magnification, the operator is unable to distinguish these two apparent boundaries. The porosity estimate is calculated across many grains and pores, increasing the likelihood of smoothing when the image is analysed. Figure 4.18 emphasizes the problem with PIA concerning the number of grains and pores that exist in each field of view when a porosity assessment is made.

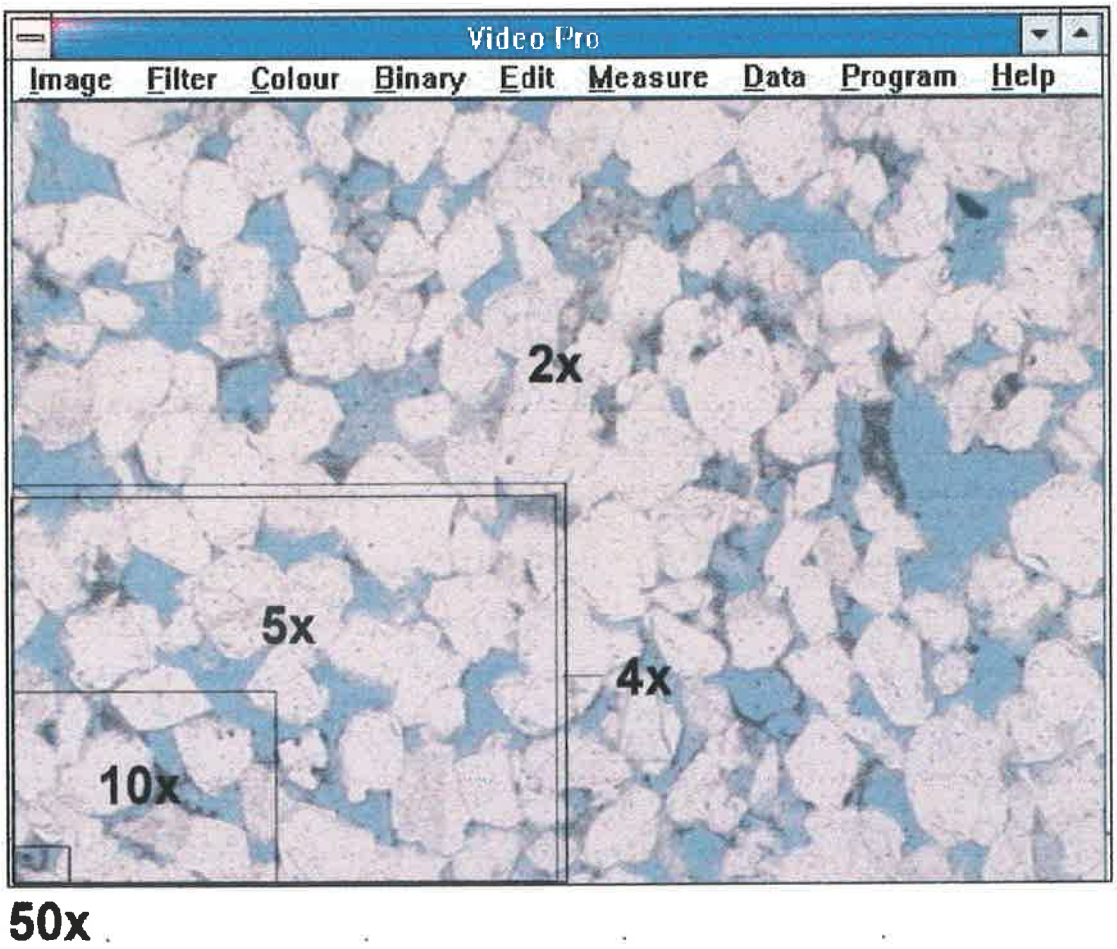

Figure 4.18: PIA image showing the problem concerning the number of grains and pores that exist in each field of view when a porosity assessment is made.

Schulz-Rojhan & Phillips (1989) stated that porosity determined from thin section may be under-estimated by up to 30%. They recognised that the under-estimation is due, in part, to the presence of authigenic kaolin that contains micro-porosity, and this is often not registered during area counting. This effect is not seen in the results of this study because an effort was made to include some porosity in parts of the thin section that were tightly packed with kaolin.

Another possible factor for under estimating porosity from thin section is that the blue dyed epoxy resin may not occupy all of the fine pore spaces. This would result in the image analyser not detecting these pores, however this effect is likely to be minimal because of the clean nature of these samples.

It was anticipated that the spatial display porosity maps would highlight bedding trends and areas of particularly high or low porosity. These areas are the primary influence on the permeability of the rock. If this technique could identify these areas, then it would prove useful for permeability estimation in reservoir simulation.

From the three-strip spatial display porosity data, the interpretation suggested there was some evidence, particularly in thin section 2aii, that bedding trends are reflected in the porosity data. The copy of the core (Appendix 3) and the photo of the thin section (Appendix 11) indicate there is some silt banding across the sandstone. This appears to be reflected in the porosity display data, but with so few readings across the slide, combined with the results from the semi-variograms (which suggest there is virtually no correlation), it is most likely to be the result of random chance. A greater sample density would be required to obtain more detail needed to reflect the porosity variation.

The 5x-magnification full coverage porosity data acquired from the same thin section (Figure 4.6 (i)) contain many more readings than the three-strip data (439 compared with 62). Thus, the abundance of data is more likely to reflect this silty banding. The results cautiously suggest two strips of low porosity can be seen across the central region of the spatial display.

The apparent patchiness of the porosity data was more pronounced when the displays were altered. Figures 4.7 and 4.8 show the porosity from thin sections 1aii and 2aii, and the altered colour display highlights areas of high and low porosity, or apparent patchiness. When looking at these plots, the reason for the semi-variogram data showing very little correlation between neighbouring data pairs became apparent because high and low readings were often coincident. Gradation between data pairs is minimal, with segments of high porosity sitting adjacent to readings of very low porosity. The data predominantly alternates between areas separated by two or three porosity units, and in some extreme cases, up to four porosity units, but rarely only one. If the porosity was spatially correlated, it is expected that the difference between areas would more often only be one porosity unit.

The plots created from the data obtained from the random number generator (Figures 4.9 (a) and 4.10 (a)) enabled visual recognition of the number of samples required (between 30 and 40) to obtain a porosity estimate in thin section that is within one standard deviation of the true average porosity.

Figures 4.9 (a) and 4.10 (a) demonstrate that there is a good chance the average porosity obtained by using only 10 random readings from a thin section at 5x-magnification will not be accurate. It is likely a porosity reading as low as 16% or as high as 26% will be attained which is a large variation that would substantially affect simulator flow results. The likelihood of obtaining an accurate value of porosity from 20 readings increases, ranging between 18% and 26%. However, once 30 readings are taken, the chances that the porosity will be accurate are much higher. The range is now only 18% to 24%, which is approximately one SD from the true porosity of 21.4%. Figure 4.7(b) demonstrates that by taking 30 random readings of porosity using PIA, the average porosity value will be close to one SD unit from the true porosity, compared with a SD of 1.92 (100 iterations) and 1.84 (500 iterations) when only 10 readings are taken. Forty readings should be included in the calculation of average porosity to be within one SD unit and the change in variance after more than 40 readings is small compared with the change in variance between 10 and 30 readings.

Figures 4.11 and 4.12, the semi-variograms for both of the 5x-magnification data sets appeared to show no correlation. Perhaps, as mentioned, there is a slight nearest neighbour correlation in the 1aii-upper semi-variogram, but the effect is very weak, and even less correlation is visible in the 2aii semi-variogram.

Removing the odd rows and columns from the existing 5x-magnification data set created a new reduced data set from which it was hoped kriging could 'recreate' another porosity distribution map that was similar to the original. A semi-variogram of this reduced data set was constructed (Figure 4.19) and showed that there is no correlation between data points (which was expected following the results obtained from the full coverage semi-variograms). The 2.5x spatial display (Figure 4.6 (iii)) suggested that, recognition of higher and lower than average porosity areas within the data set is possible, however, significant smoothing occurs as a result of using this lower magnification.

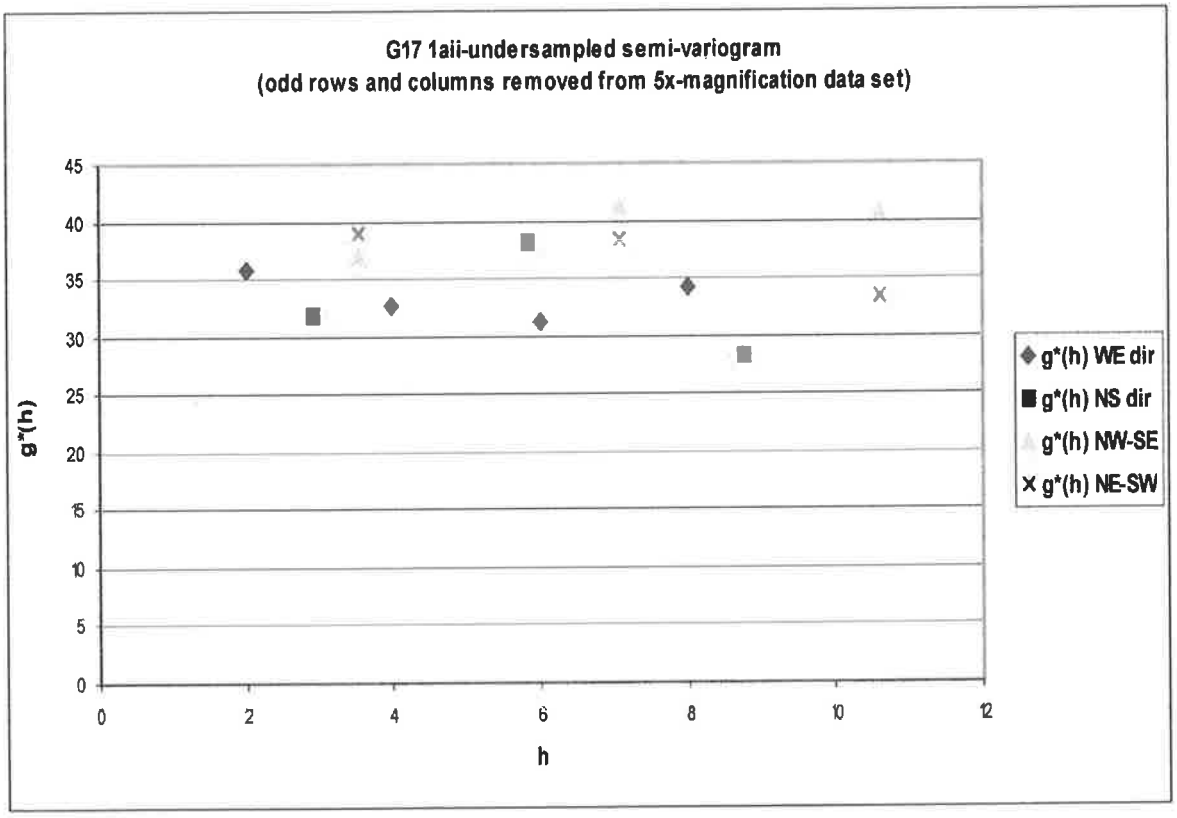

Figure 4.19: Thin section G17 1aii under-sampled semi-variogram showing no correlation (nuggett effect) between data points, that is, neither distance nor direction influence correlation. This semi-variogram was calculated with the odd rows and columns removed from the original 5x-magnification data set.

The calculation of porosity at different magnifications indicated a *fractal-like* nature to porosity. It is fractal-like because the semi-variograms at all magnifications look very similar. Figure 4.20 is a display showing the three semi-variograms on the same page. This fractal nature has limits, the lower being the pore size, and in this study, the upper limit is what can be seen under the microscope.

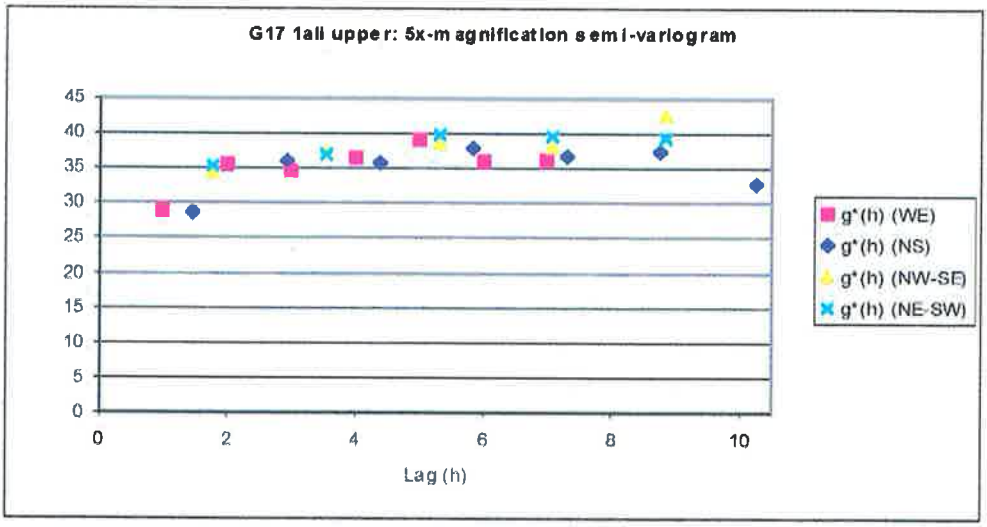

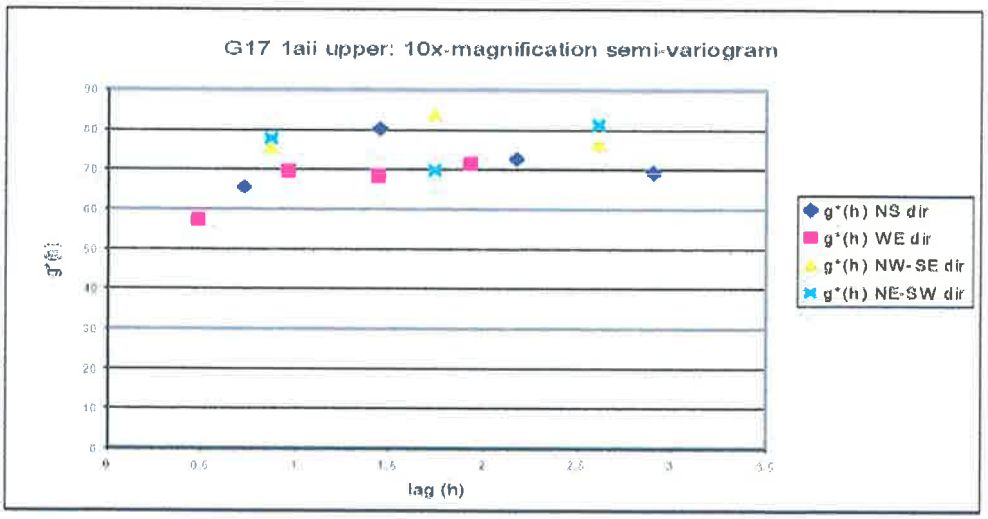

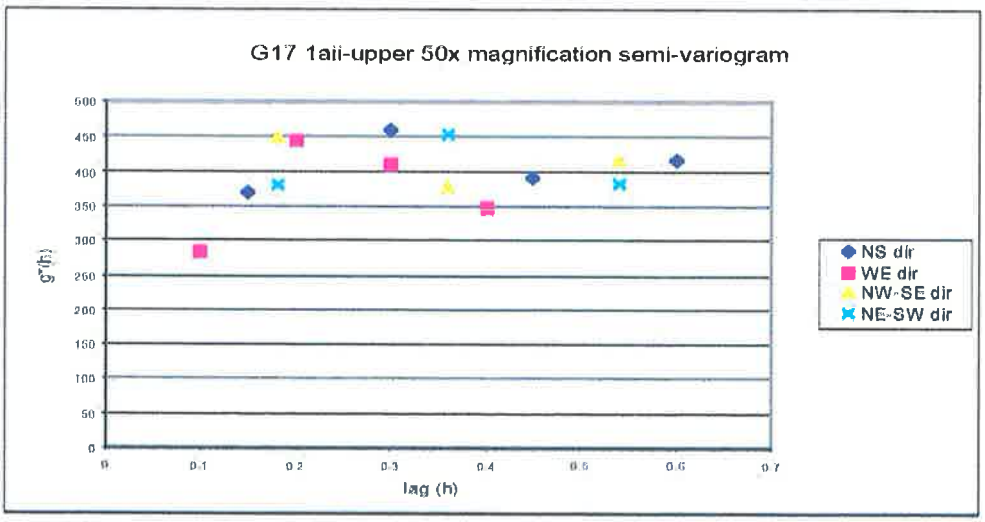

Figure 4.20: 3 semi-variograms produced at different magnifications for thin section 1aii-upper. The similar shape of each suggests a fractal nature to porosity in thin section measured using PIA.

It was anticipated that by increasing the magnifications and reducing the dimensions of the field of view from which porosity was being calculated that the semi-variograms would be better defined, particularly at short lags.

It was determined that, by increasing the magnification, Lag 1 does not change. This is because porosity is calculated across an area which only changes dimensions and can not be calculated by one point which is needed for a well defined semi-variogram to be created. While the actual distance associated with a move of lag 1 alters between 5x- and 10x-magnification (each horizontal move for 5x is 1460 microns compared with 725 microns for 10x), each move is still only a lag of 1, and the average porosity measurements remain essentially unchanged.

Some improvement can be seen in the 50x-magnification semi-variogram. Although it is acknowledged that fewer data were obtained at 50x-magnification compared with 5x, there was enough to produce a semi-variogram. An attempt was made to model this semi-variogram, but too much emphasis was placed on lags 1 and 2, making it unreliable to model confidently.

The improvement in the semi-variogram was expected because the field of view at 50x magnification is much smaller (horizontal 150 microns, vertical 100 microns) and no longer intersects as many different pores and grains to get a calculation of porosity. If it were possible to take porosity readings at 100x magnification, it is likely the correlation between adjacent readings would be greater still allowing for more accurate modelling. Correlation improves as the magnification increases, suggesting that with 100x-magnification (a miniscule field of view) a better semi-variogram will be produced.

The results of the statistical analysis suggest the data can therefore be treated as random, with no correlation between adjacent porosity measurements. This means kriging would not be required to upscale the data because kriging is a statistical tool that estimates values of neighbouring points by using the semi-variogram and the surrounding available data, applying weighting that is scaled on each data point. Since the information obtained from the semi-variograms suggests porosity shows no correlation within the individual cross-bed sets of the Hutton Sandstone, no weighting can be applied to the data points. Thus, interpolation by kriging is not possible and the

porosity data can be randomly distributed within the cross-bed set from which it was obtained.

Porosity data obtained from each cross-bed set should be treated separately. Upscaling thin section data obtained from PIA can be achieved by a) obtaining between 30 to 40 porosity readings per cross-bed set, and b) calculating average pore size. Between 30 and 40 readings provides a value of average porosity that is within one SD unit of the true porosity along with a range of values in the form of a histogram, which shows the porosity distribution. The results of this study show that, for the Hutton Sandstone, the porosity values can then be distributed randomly throughout the bed of interest.

It should be mentioned however that correlation might be observed within another sandstone deposited under different conditions. The core displays silt layering, however this is not well detected by the porosity displays. This suggests the layering was unseen by PIA within the rock. A sandstone deposited under slower flowing conditions containing more pronounced thin silt layers might allow PIA to observe and develop a model of correlation.

Chapter 5 PORE THROAT DISTRIBUTION

5.1 PORE CASTING

The data available used to study the pore throat distribution of the Hutton Sandstone samples included mercury injection capillary pressure (MICP) and the less commonly used pore casting. Pore casts, when studied under the SEM, allow detailed views of the pores and, in particular, the interconnectivity of the pore throats.

The direct study of void space in a rock is difficult. The volume of the voids is easily determined but the pores cannot be observed visually as they exist in the rock. A practical approach to this problem is the use of pore casts, that is, replicas of the void space in a rock (Pittman & Duschatko, 1970).

Paired SEM micrographs were prepared for each of the four samples so they could be used to create stereo images allowing viewing of images in three dimensions. From these images, individual pores were selected for description in terms of being *irregular*, *triangular*, *polyhedral* or *tetrahedral*, according to the shape.

The size of these individual pores was measured (using the long axis), along with the coordination number (i.e. the number of throats for each pore). The pore throat sizes were then measured and tabulated as a range, allowing calculation of the aspect ratio. Aspect ratio in this case is the ratio of pore size to throat size for each pore. A problem arose in calculating aspect ratio because the throat sizes calculated from pore casts were given as a range of sizes, and not a single value. This was overcome by summing the range of throat sizes and then dividing by the coordination number, providing a single value for throat size per pore. From this, the aspect ratio was determined and each pore was given an arrangement rating, providing a subjective way of assessing its connectivity. The pores are characterised as *poorly connected*, *moderately connected* or *interconnected* (Tables 5.1-5.4).

Sample Number (Stereo Image)	Identified measureable pore in image	Pore Shape	Pore size (long axis) (microns)	Coordination Number (throats per pore)	Min Throat size (microns)	Max Throat size (microns)	Pore size/ Throat size Ratio for each pore (aspect ratio)	Pore Arrangement
1aa_stereoedit	1	polyhedral	258	6	25	35	26	Interconnected
	2	tetrahedral	137	4	20	40	9	Interconnected
	3	tetrahedral	170	3	25	55	6	Interconnected
	4	irregular	153	5	10	40	15	Interconnected
	5	polyhedral	306	6	30	40	26	Interconnected
	6	triangular	104	3	10	30	8	Interconnected
1ab_stereoedit	1	tetrahedral	157	4	15	20	18	Interconnected
	2	tetrahedral	209	6	10	40	25	Interconnected
	3	tetrahedral	150	4	10	40	12	Interconnected
	4	tetrahedral	140	4	10	35	12	Interconnected
1ad2_stereoedit	1	irregular	208	5	12	20	33	Interconnected
	2	triangular	110	4	12	20	14	Interconnected
	3	triangular	110	3	15	20	9	Interconnected
1ae2_stereoedit	1	tetrahedral	241	5	10	15	48	Interconnected
	2	polehedral	255	7	5	15	89	Interconnected
	3	polehedral	264	4	25	50	14	Interconnected
	4	tetrahedral	250	4	15	20	29	Interconnected
	5	triangular	91	3	15	50	4	Interconnected
AVERAGE for 1a			**184.1**	**4.4**	**15.2**	**32.5**	**17.1**	

Table 5.1: Pore cast analysis data obtained from 3D images from sample 1ai upper.

The stereo images produced from the SEM must be viewed with red-green filter glasses (provided overleaf). Images from all samples were selected and are included as Plates 5.1-5.9, while the remaining images have been included in Appendix 15. Measurements for Tables 5.1 (above) and 5.2-5.4 were made from the stereo images.

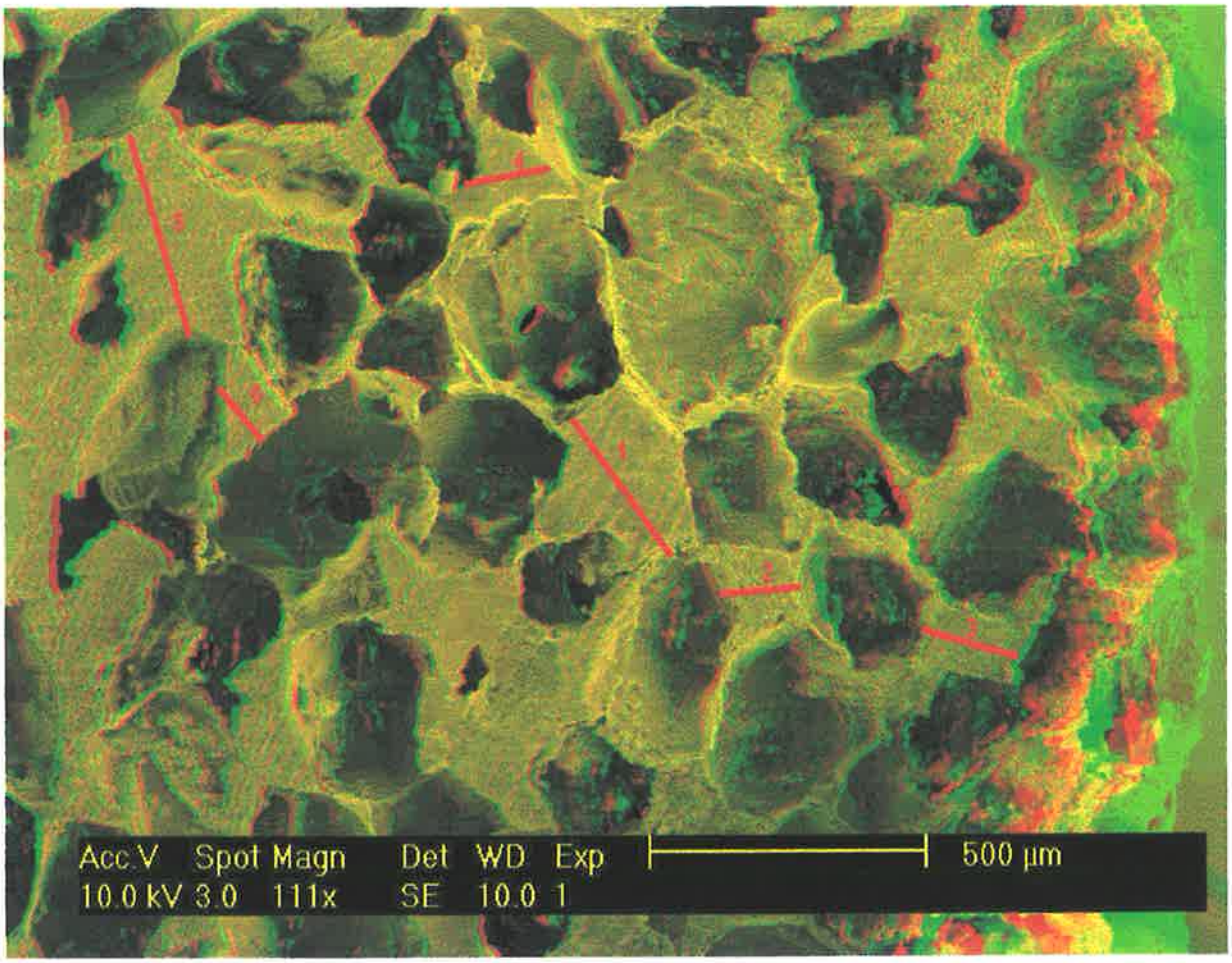

Plate 5.1: ***1aa_stereoedit.*** 6 pores were measured in this field of view (shown by labelled bars). The sample had average pore size of 188 microns, average coordination number of 4.5 with pore throats between 10 and 55 microns (use red/green filter glasses to view image in 3D).

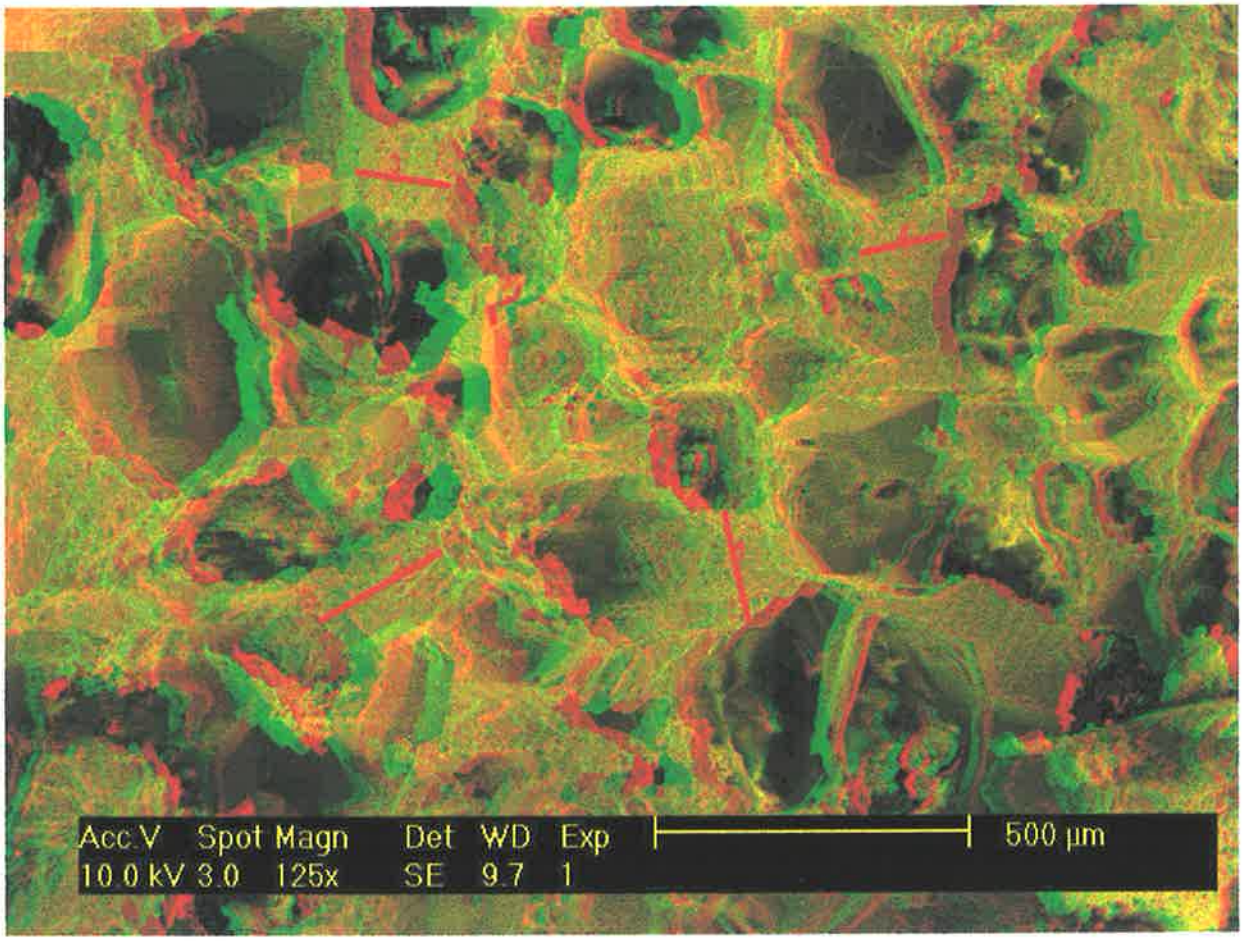

Plate 5.2: ***1ab_stereoedit.*** 4 pores were measured in this field of view (shown by labelled bars). The sample had average pore size of 164 microns, average coordination number of 4.5 with pore throats between 10 and 40 microns (use red/green filter glasses to view image in 3D).

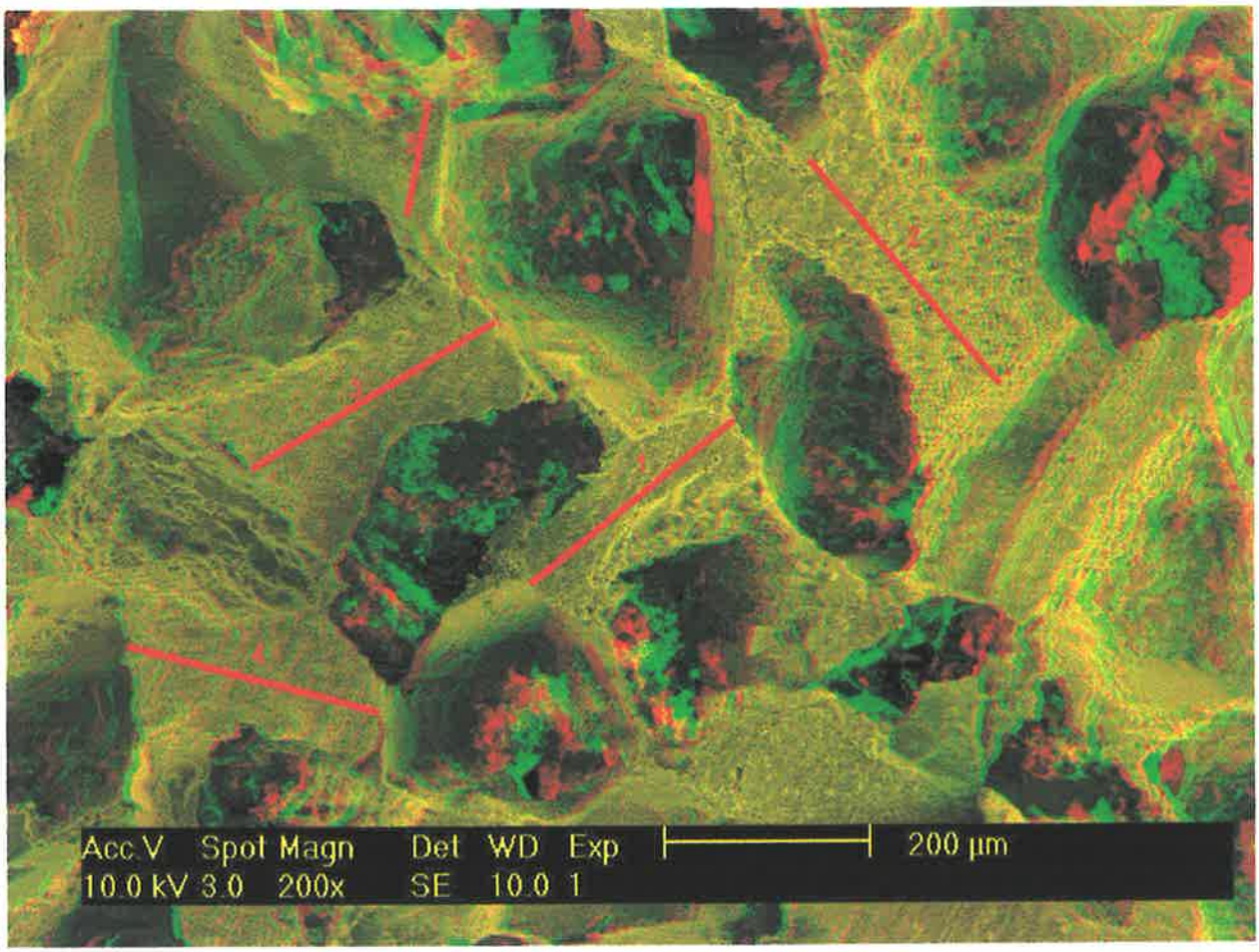

Plate 5.3: ***1ae2_stereoedit.*** 5 pores were measured in this field of view (shown by labelled bars). The sample had average pore size of 220 microns, average coordination number of 4.6 with pore throats between 15 and 50 microns (use red/green filter glasses to view image in 3D).

Sample Number (Stereo Image)	Identified measureable pore in image	Pore Shape	Pore size (long axis) (microns)	Coordination Number (throats per pore)	Min Throat size (microns)	Max Throat size (microns)	Pore size/ Throat size Ratio for each pore (aspect ratio)	Pore Arrangement
1da2_stereoedit	1	tetrahedral	183	5	15	20	26	Interconnected
	2	polyhedral	400	5	15	35	40	Interconnected
	3	tetrahedral	242	3	10	20	24	Interconnected
	4	irregular	250	5	15	30	28	Interconnected
	5	irregular	333	5	10	90	17	Interconnected
	6	irregular	325	5	20	65	19	Interconnected
	7	triangular	142	3	10	20	14	Interconnected
	8	polyhedral	167	5	10	15	33	Interconnected
	9	irregular	342	5	30	60	19	Interconnected
1db2_stereoedit	1	irregular	352	4	15	40	26	Interconnected
	2	irregular	143	3	5	15	21	Interconnected
	3	tetrahedral	187	4	15	40	14	Interconnected
	4	triangular	183	5	15	35	18	Interconnected
	5	triangular	104	2	35	45	3	Interconnected
1dc2_stereoedit	1	tetrahedral	250	4	10	75	12	Interconnected
	2	irregular	308	3	15	25	23	Interconnected
	3	tetrahedral	158	4	25	35	11	Interconnected
	4	polyhedral	225	4	15	75	10	Interconnected
	5	triangular	133	3	15	20	11	Interconnected
	6	tetrahedral	175	5	15	30	19	Interconnected
1dd2_stereoedit	1	polyhedral	336	6	10	20	67	Interconnected
	2	irregular	101	2	10	25	6	Interconnected
1de2_stereoedit	1	irregular	343	8	5	15	137	Interconnected
	2	irregular	229	4	5	10	61	Interconnected

1df2_stereoedit	1	irregular	338	8	10	25	77	Interconnected
	2	irregular	234	4	8	15	41	Interconnected
	3	irregular	148	5	10	10	37	Interconnected
	4	polyhedral	203	5	12	20	32	Interconnected
	5	triangular	156	5	10	25	22	Interconnected
	6	irregular	320	6	10	45	35	Interconnected
1dg2_stereoedit	1	irregular	123	5	15	25	15	Interconnected
	2	irregular	246	7	15	30	38	Interconnected
	3	irregular	287	4	15	25	29	Interconnected
	4	polyhedral	221	4	25	90	8	Interconnected
	5	tetrahedral	164	4	30	105	5	Interconnected
	6	tetrahedral	131	3	10	20	13	Interconnected
1dh2_stereoedit	1	tetrahedral	263	4	15	20	30	Interconnected
	2	tetrahedral	175	4	15	20	20	Interconnected
	3	irregular	630	8	45	85	39	Interconnected
	4	triangular	246	4	35	60	10	Interconnected
	5	irregular	421	7	35	70	28	Interconnected
	6	polyhedral	316	5	25	85	14	Interconnected
	7	tetrahedral	316	5	25	30	29	Interconnected
	8	polyhedral	350	6	30	70	21	Interconnected
	9	irregular	404	8	15	105	27	Interconnected
	10	polyhedral	333	5	25	85	15	Interconnected
	11	polyhedral	421	6	35	45	32	Interconnected
AVERAGE for 1d			**256.5**	**4.8**	**17.3**	**41.9**	**20.6**	

Table 5.2: Pore cast analysis data obtained from 3D images for sample 1dii.

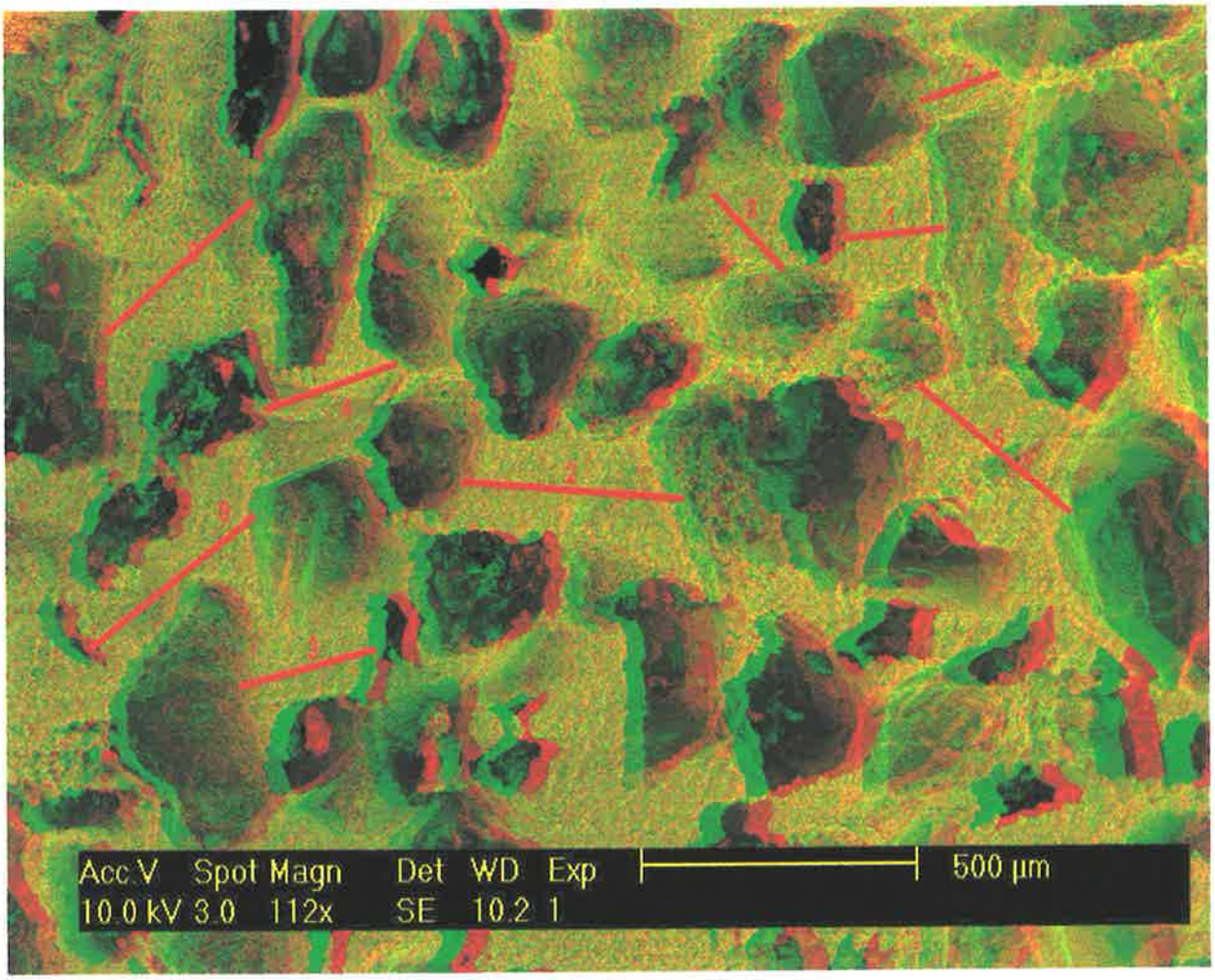

Plate 5.4: ***1da2_stereoedit.*** 9 pores were measured in this field of view (shown by labelled bars). The sample had average pore size of 265 microns, average coordination number of 4.6 with pore throats between 10 and 60 microns (use red/green filter glasses to view image in 3D).

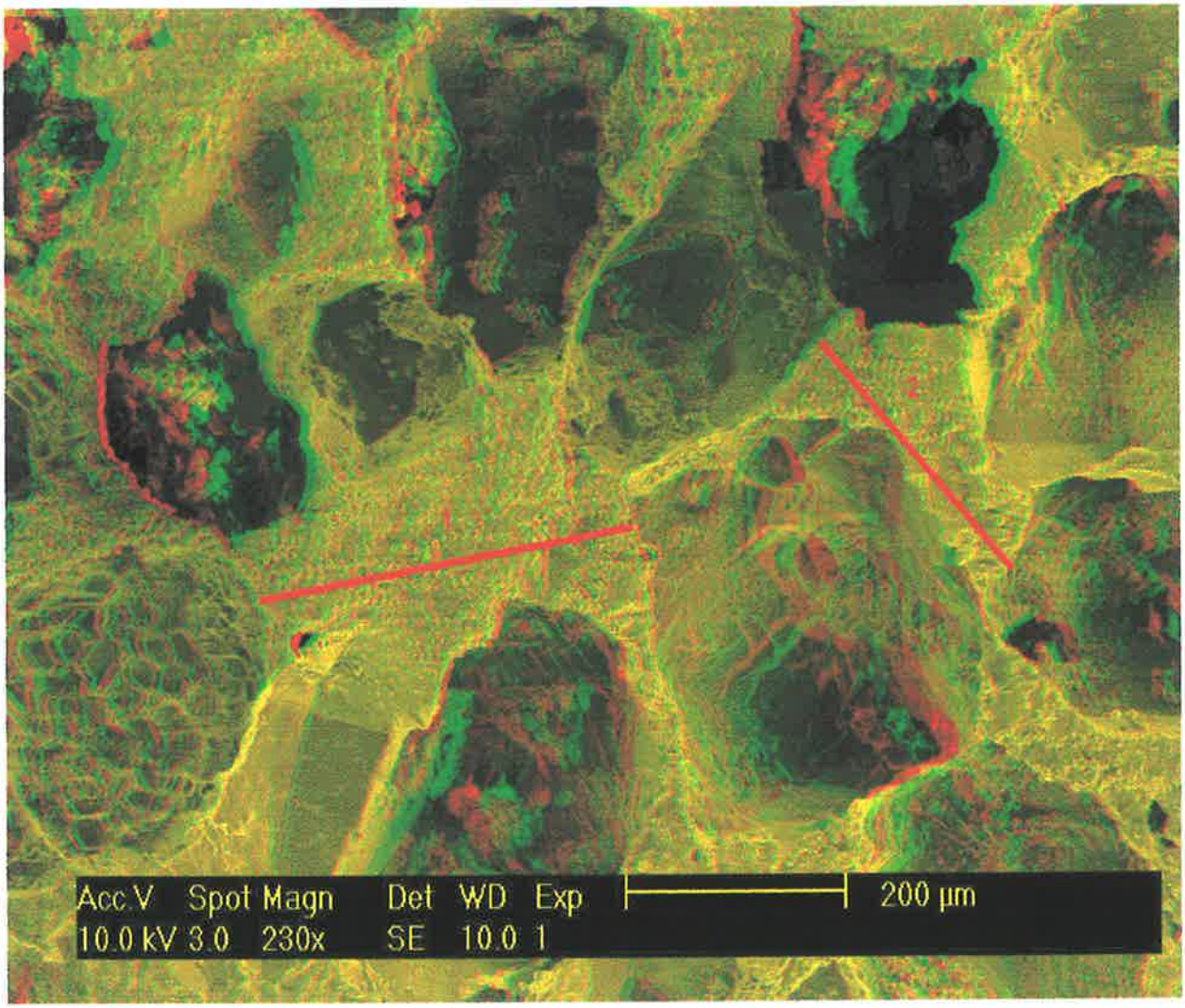

Plate 5.5: ***1de2_stereoedit.*** 2 pores were measured in this field of view (shown by labelled bars). The sample had average pore size of 286 microns, average coordination number of 6 with pore throats between 10 and 15 microns (use red/green filter glasses to view image in 3D).

Sample Number (Stereo Image)	Identified measureable pore in image	Pore Shape	Pore size (long axis) (microns)	Coordination Number (throats per pore)	Min Throat size (microns)	Max Throat size (microns)	Pore size/ Throat size Ratio for each pore (aspect ratio)	Pore Arrangement
1fb2_stereoedit	1	polyhedral	228	4	20	65	11	Interconnected
	2	irregular	327	4	5	30	37	Interconnected
	3	tetrahedral	318	4	25	65	14	Interconnected
	4	triangular	68	3	10	15	8	Interconnected
	5	triangular	68	3	5	20	8	Interconnected
1fc2_stereoedit	1	polyhedral	228	4	15	45	15	Interconnected
	2	tetrahedral	148	3	10	15	18	Interconnected
	3	polyhedral	156	4	10	30	16	Interconnected
	4	tetrahedral	124	4	15	25	12	Interconnected
1fa2_stereoedit	1	polyhedral	300	6	10	40	36	Interconnected
	2	irregular	329	4	10	90	13	Interconnected
	3	tetrahedral	235	4	15	90	9	Interconnected
	4	triangular	100	3	10	15	12	Interconnected
	5	triangular	71	3	15	25	5	Interconnected
Average for 1f			**192.9**	**3.8**	**12.5**	**40.7**	**13.7**	

Table 5.3: Pore cast analysis data obtained from 3D images for sample 1fi.

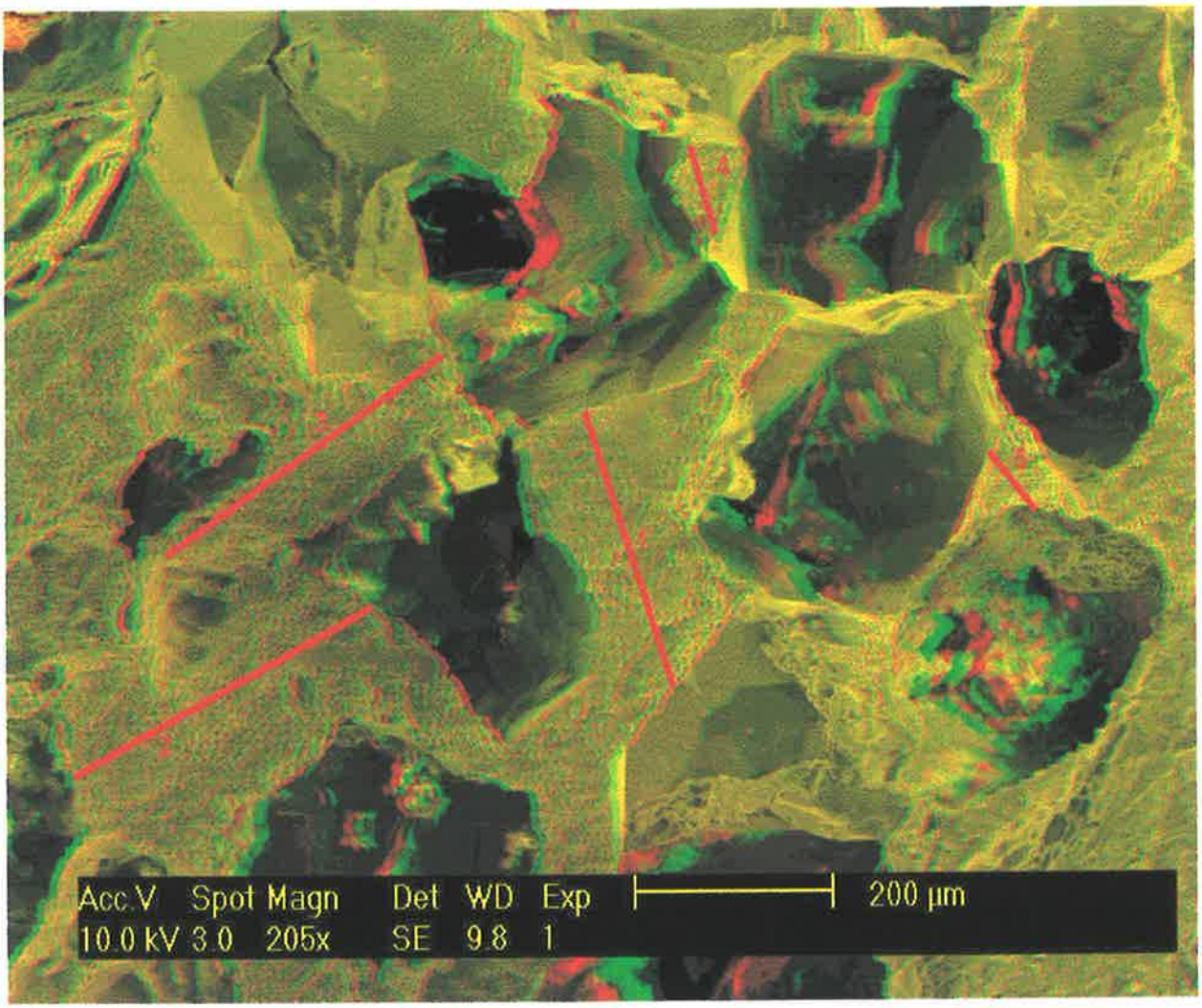

Plate 5.6: ***1fb2_stereoedit.*** 5 pores were measured in this field of view (shown by labelled bars). The sample had average pore size of 202 microns, average coordination number of 3.6 with pore throats between 5 and 65 microns (use red/green filter glasses to view image in 3D).

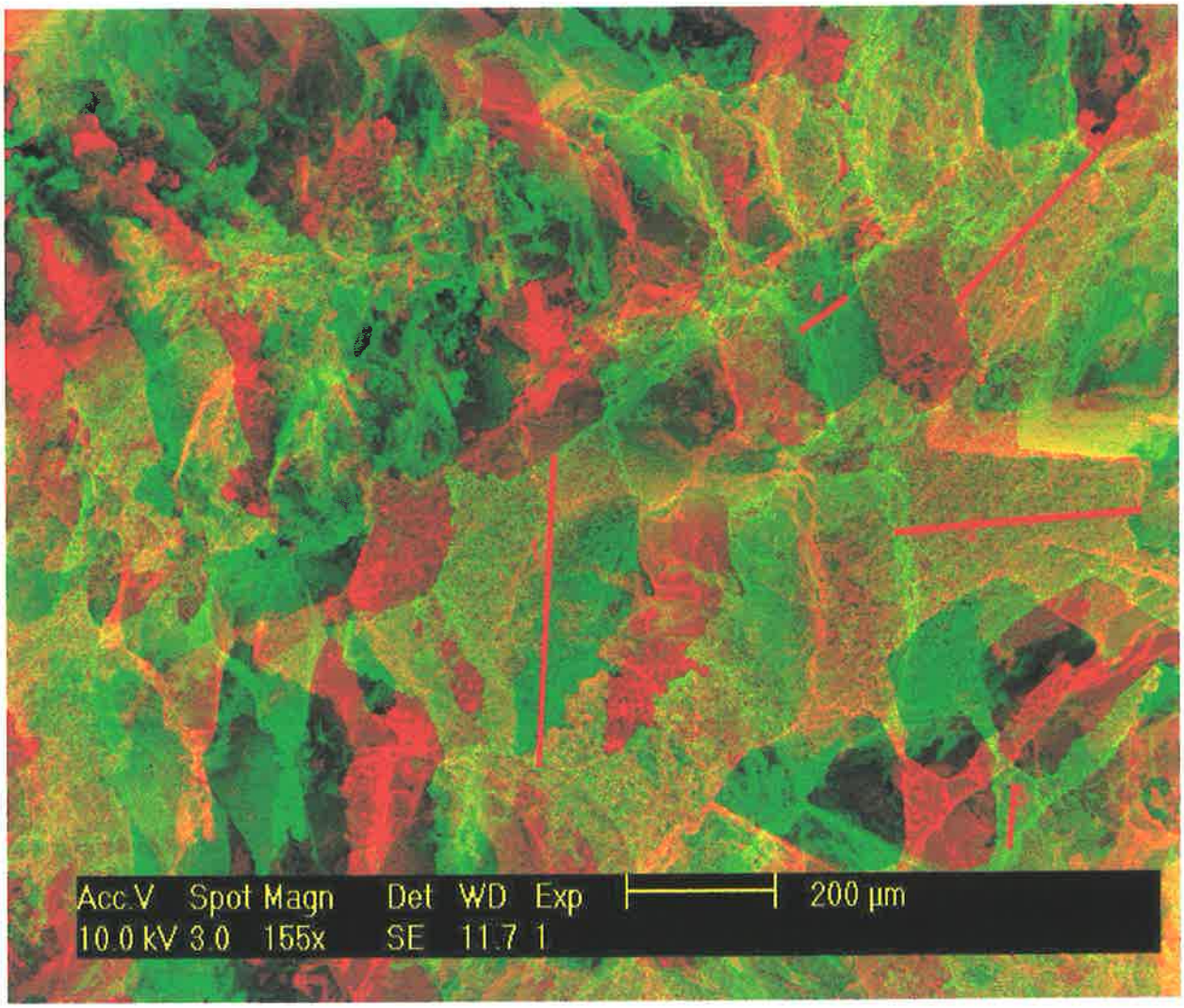

Plate 5.7: ***1fa2_stereoedit***. 5 pores were measured in this field of view (shown by labelled bars). The sample had average pore size of 207 microns, average coordination number of 4 with pore throats between 10 and 90 microns (use red/green filter glasses to view image in 3D).

Sample Number (Stereo Image)	Identified measureable pore in image	Pore Shape	Pore size (long axis) (microns)	Coordination Number (throats per pore)	Min Throat size (microns)	Max Throat size (microns)	Pore size/ Throat size Ratio for each pore (aspect ratio)	Pore Arrangement
2aa2_stereoedit	1	triangular	162	3	15	25	12	Interconnected
	2	triangular	130	4	15	30	12	Interconnected
2ab2_stereoedit	1	triangular	71	3	10	30	5	Interconnected
	2	triangular	82	3	10	20	8	Interconnected
	3	irregular	190	5	10	35	21	Interconnected
	4	tetrahedral	197	5	15	45	16	Interconnected
2ac2_stereoedit	1	tetrahedral	128	4	15	20	15	Interconnected
	2	polyhedral	410	6	15	20	70	Interconnected
	3	polyhedral	197	4	15	20	23	Interconnected
2ad2_stereoedit	1	polyhedral	201	5	15	20	29	Interconnected
	2	polyhedral	250	5	25	70	13	Interconnected
	3	tetrahedral	137	4	10	20	18	Interconnected
	4	polyhedral	328	5	25	40	25	Interconnected
2ae2_stereoedit	1	triangular	184	4	25	65	8	Interconnected
	2	tetrahedral	287	4	15	30	26	Interconnected
	3	polyhedral	368	4	20	20	37	Interconnected
2af2_stereoedit	1	tetrahedral	295	4	10	25	34	Interconnected
	2	polyhedral	311	4	30	90	10	Interconnected
	3	tetrahedral	131	4	15	30	12	Interconnected
	4	irregular	229	6	25	50	18	Interconnected
	5	polyhedral	180	6	25	30	20	Interconnected
Average for 2a			**212.8**	**4.4**	**17.1**	**35.0**	**20.6**	

Table 5.4: Pore cast analysis data obtained from 3D images for sample 2a.

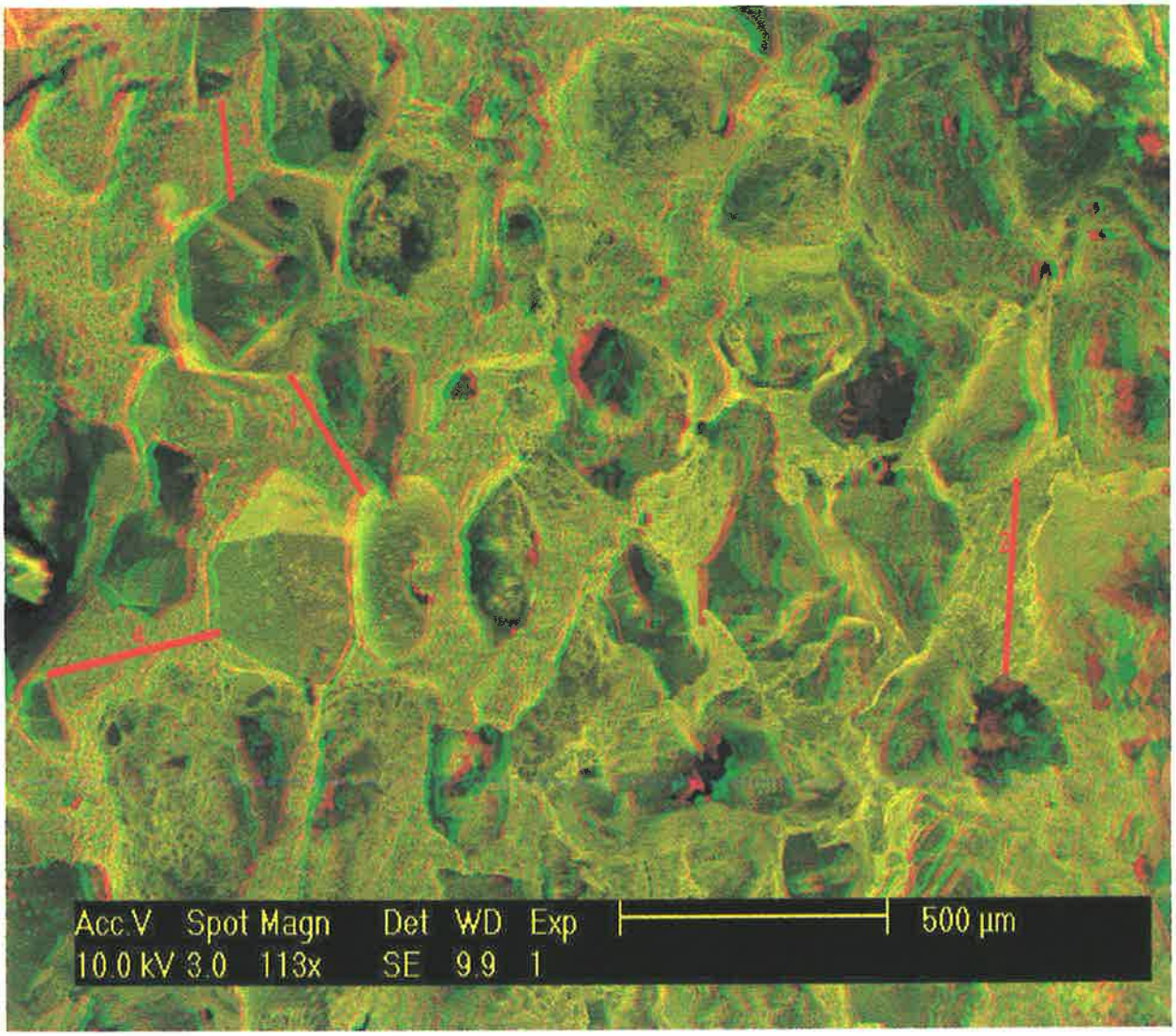

Plate 5.8: ***2ad2_stereoedit.*** 4 pores were measured in this field of view (shown by labelled bars). The sample had average pore size of 229 microns, average coordination number of 4.75 with pore throats between 10 and 70 microns (use red/green filter glasses to view image in 3D).

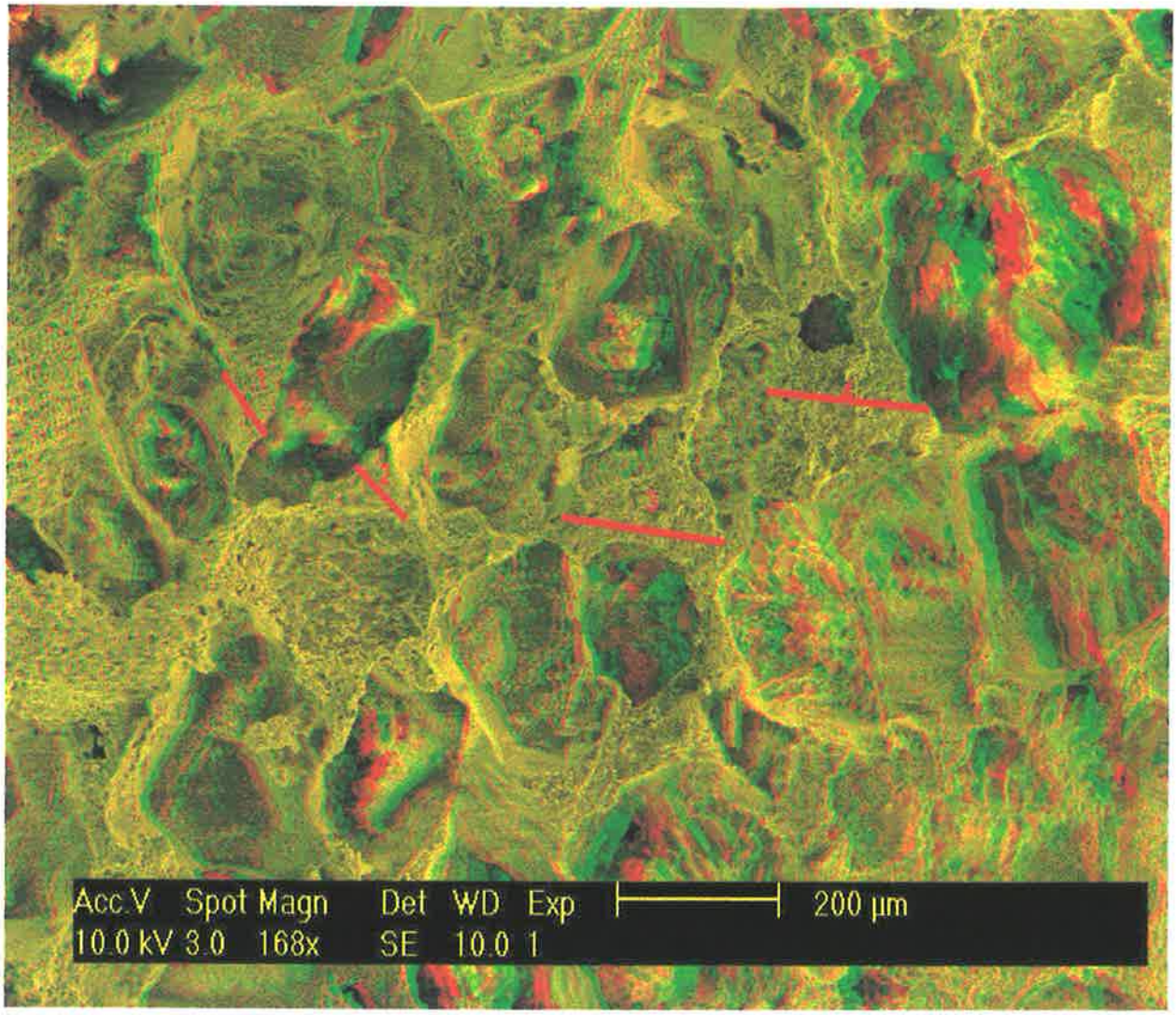

Plate 5.9: ***2ab2_stereoedit.*** 4 pores were measured in this field of view (shown by labelled bars). The sample had average pore size of 135 microns, average coordination number of 4 with pore throats between 10 and 45 microns (use red/green filter glasses to view image in 3D).

5.2 MERCURY INJECTION CAPILLARY PRESSURE (MICP)

A mercury injection curve represents the increasing saturation of mercury with pressure, i.e. as a function of pore throats of various sizes (Purcell, 1949). As mercury is a non-wetting phase, it must be forced into the pores of the sample. Pores with the largest throats will be the first entered by mercury with increasingly smaller pores entered under increased hydrostatic pressures. Pores connected with the smallest throats are the last parts of the effective porosity that may be invaded and filled by mercury at the relatively high pressures.

Mercury-ejection (imbibition) efficiency can be defined as the total volume of mercury ejected from a sample on reducing pressure from 100kg/cm^2 to 0.1kg.cm^2 expressed as a percentage of the total volume of mercury injected over the same pressure range. Ejection efficiency decreases linearly with decrease in porosity and probably results mainly from a decrease in the size of throats relative to the size of the pores (Wardlaw, 1976).

Mercury-injection and ejection tests do not provide a close analogue for an oil-water system, but may give a relative indication of the efficiency with which various rock types can expel a non-wetting phase when pressure is reduced. As ejection efficiency correlates positively with porosity, it may be possible to use porosity data to provide a factor that will indicate recovery efficiency, in so far as this is dependent on the pore geometry (Wardlaw, 1976).

MICP porosity is calculated by multiplying the maximum cumulative pore volume by 100 and dividing this by the sample volume. The results were included on the cumulative intrusion charts (Figures 5.1-5.5). These charts suggest the samples are good quality reservoir rocks because only a low pressure is required to achieve large volumes of mercury intrusion, indicating the porosity within the samples are interconnected with large pore throats. The porosity calculated by MICP ranged from 19% to 24% and is in agreement with porosity calculated for these samples by PIA from thin section.

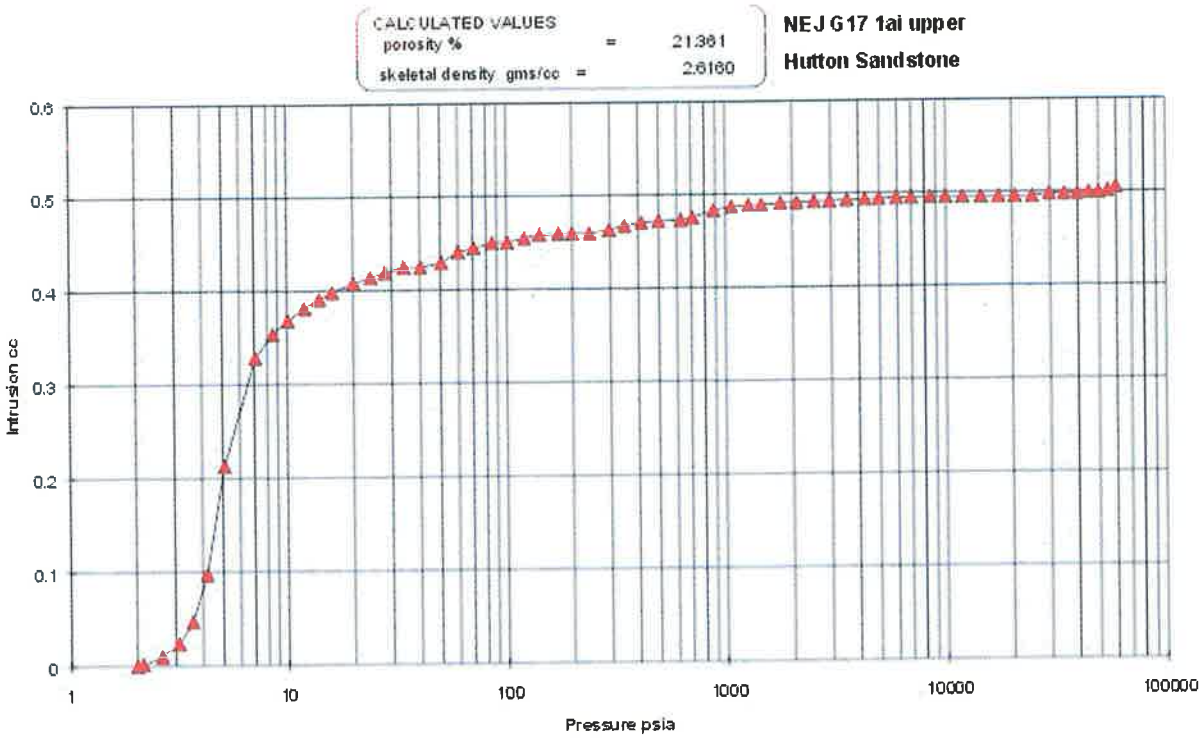

Figure 5.1: Mercury intrusion versus Pressure chart showing the intrusion of mercury with increasing pressure for sample 1ai upper. Porosity calculated by MICP for this sample is indicated above the chart while the curve suggests the sample is a good reservoir rock because low pressure is required to obtain large volumes of mercury intrusion.

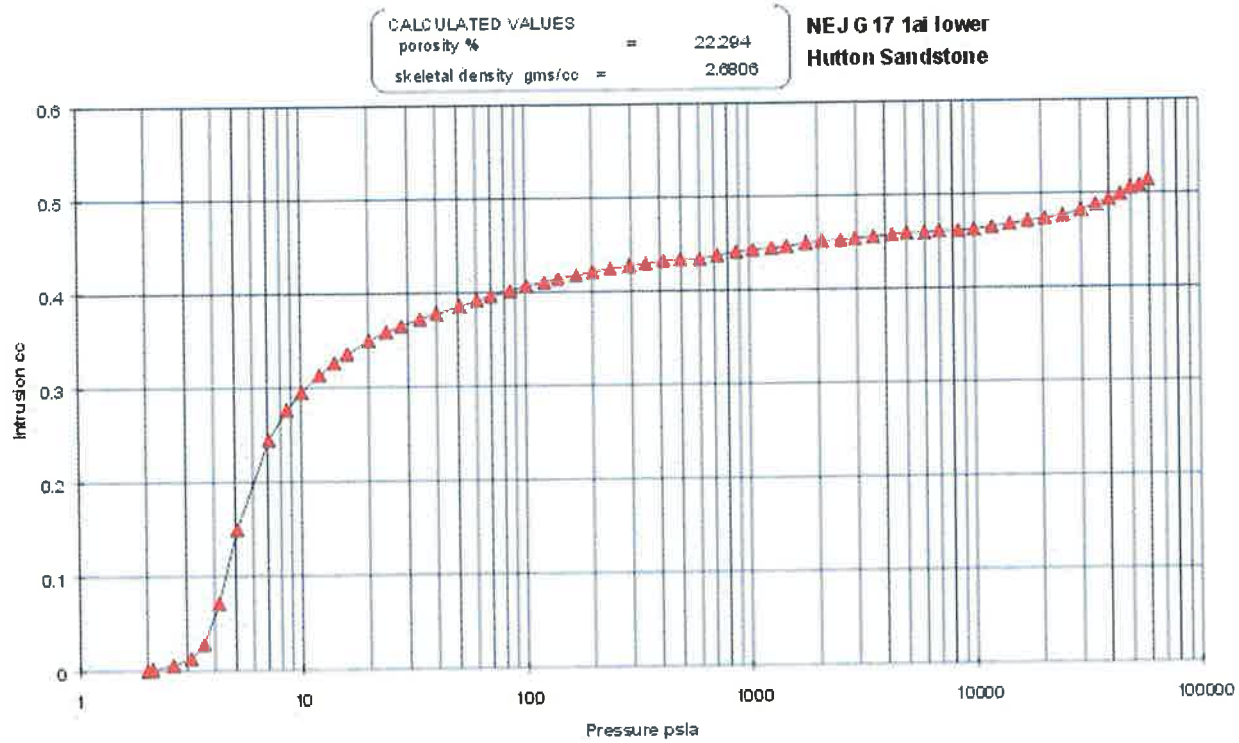

Figure 5.2: Mercury intrusion versus Pressure chart showing the intrusion of mercury with increasing pressure for sample 1a lower. Porosity calculated by MICP for this sample is indicated above the chart while the curve suggests the sample is a good reservoir rock because of the low pressure required to obtain mercury intrusion.

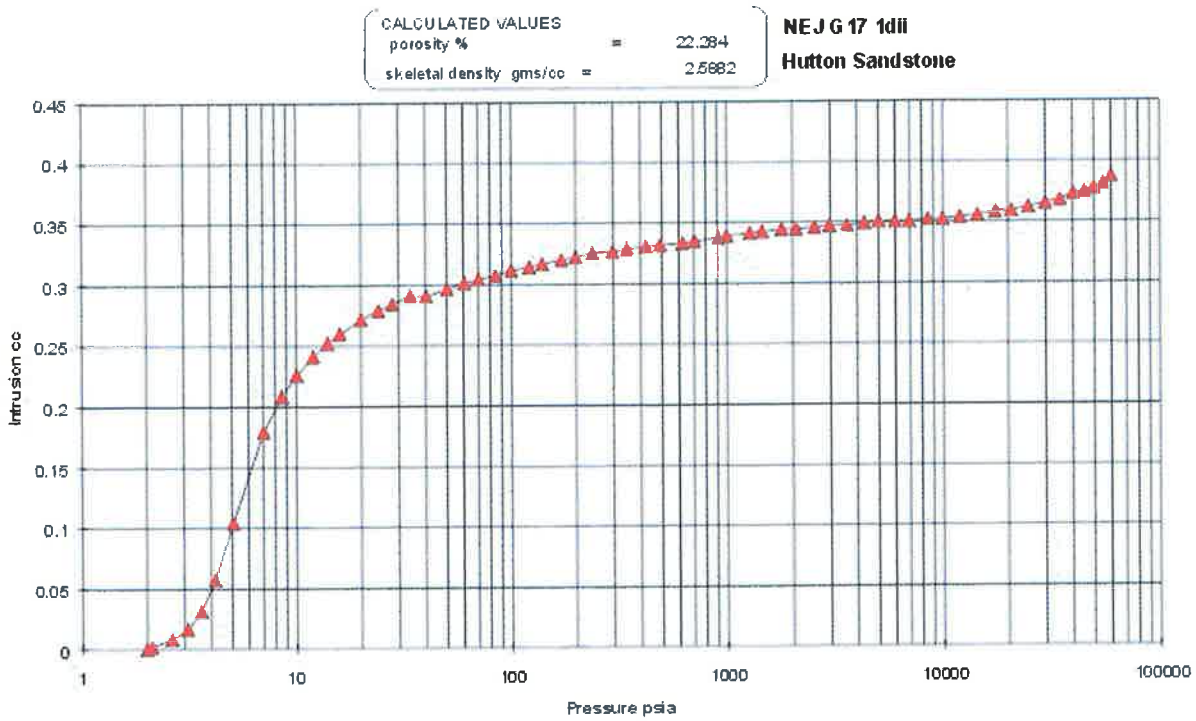

Figure 5.3: Mercury intrusion versus Pressure chart showing the intrusion of mercury with increasing pressure for sample 1dii. Porosity calculated by MICP for this sample is indicated above the chart while the curve suggests the sample is a good reservoir rock because of the low pressure required obtaining large volumes of mercury intrusion.

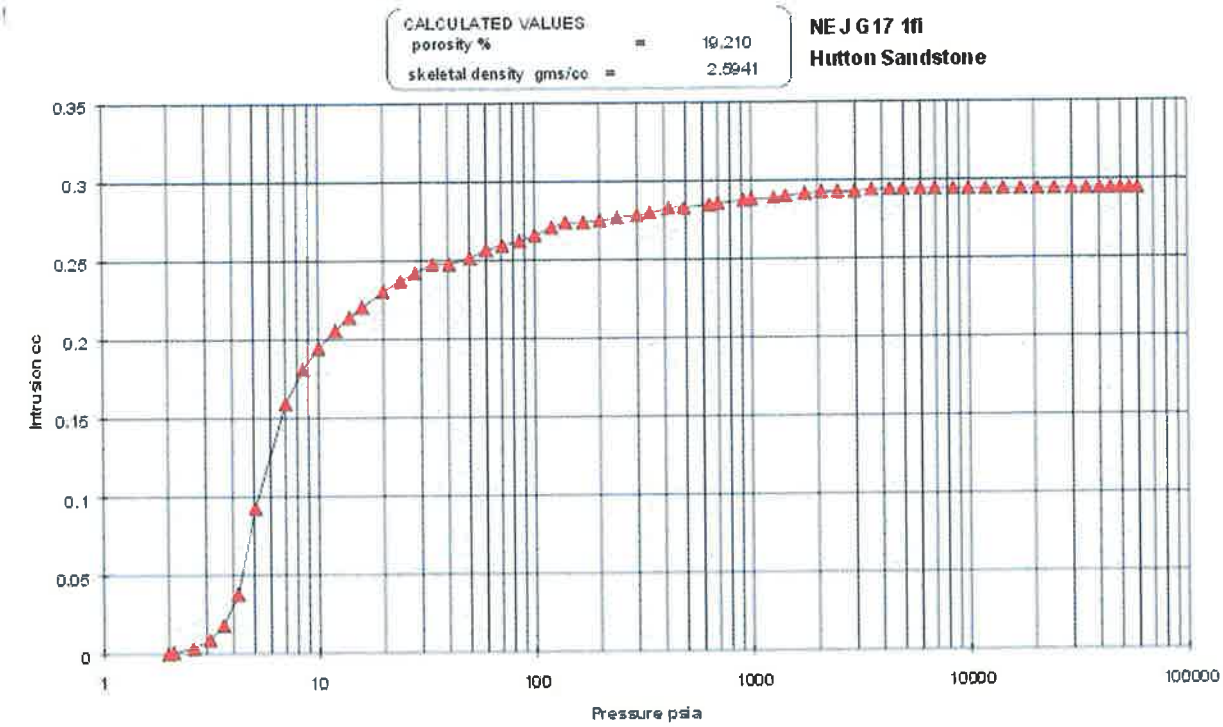

Figure 5.4: Mercury intrusion versus Pressure chart showing the intrusion of mercury with increasing pressure for sample 1fi. Porosity calculated by MICP for this sample is indicated above the chart while the curve suggests the sample is a good reservoir rock because of the low pressure required obtaining large volumes of mercury intrusion.

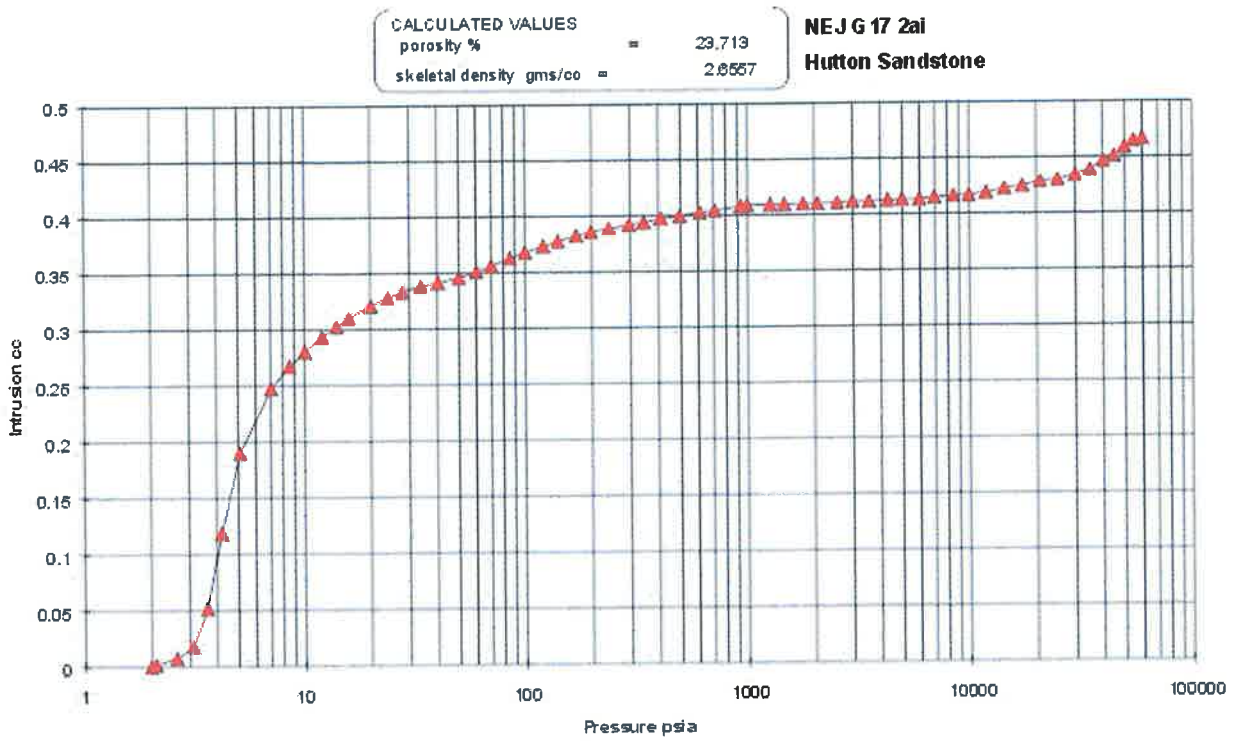

Figure 5.5: Mercury intrusion versus Pressure chart showing the intrusion of mercury with increasing pressure for sample 2a. Porosity calculated by MICP for this sample is indicated above the chart while the curve suggests the sample is a good reservoir rock because of the low pressure required obtaining large volumes of mercury intrusion

The mercury injection worksheets are included in Appendix 16, while drainage-imbibition curves (Figures 5.6-5.10), from which recovery efficiency was calculated are included below. These figures include the average aspect ratio (pore/throat size) and the coordination number (throats per pore) calculated from pore casts.

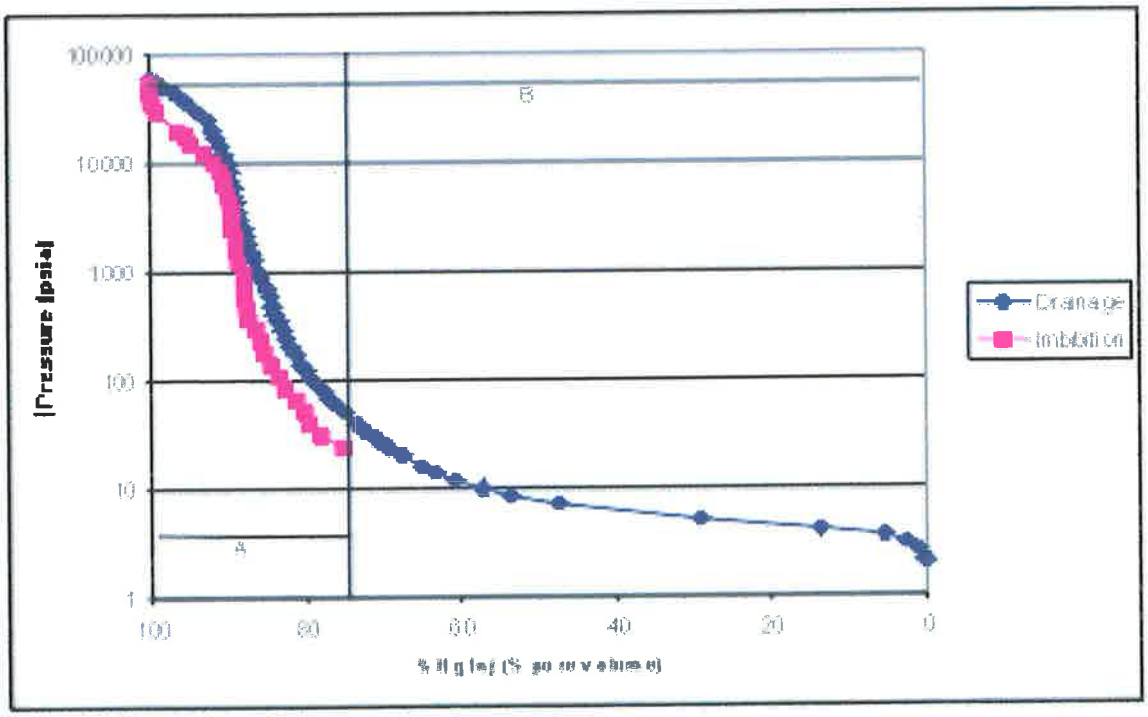

Figure 5.6: Drainage-imbibition curve for sample G17 1a-lower showing the drainage and imbibition of mercury into and from the rock.

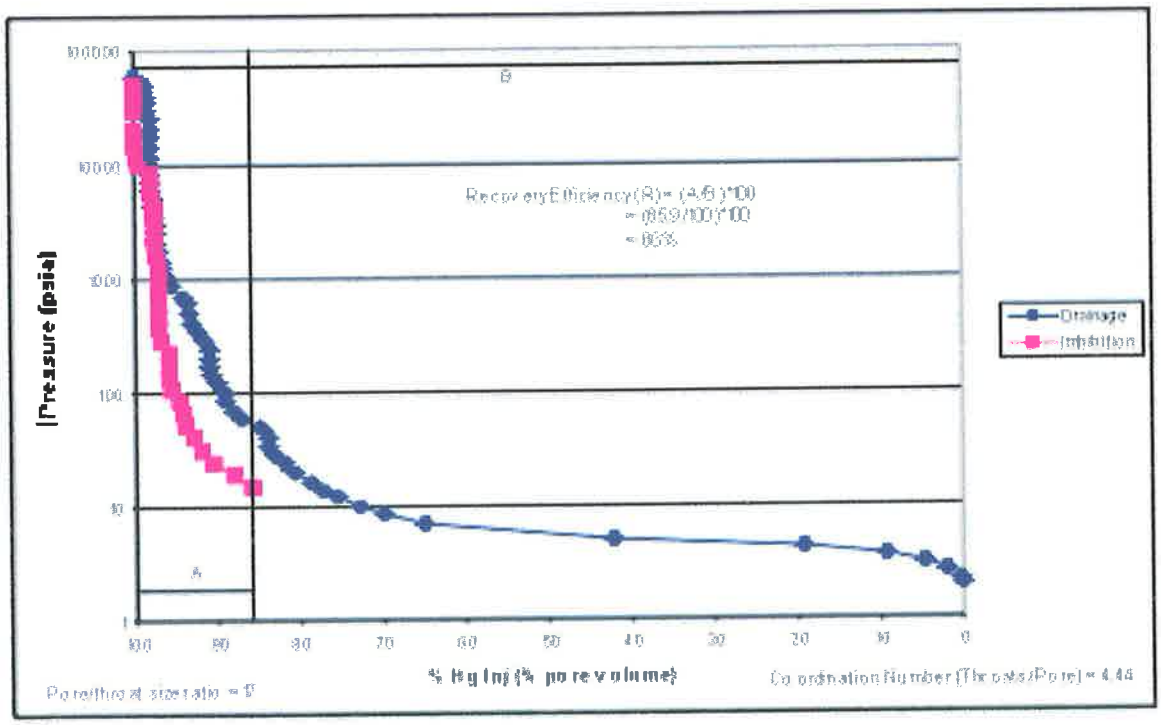

Figure 5.7: Drainage-imbibition curve for sample G17 1ai-upper showing the drainage into and imbibition of mercury from the rock. The recovery efficiency is included in the centre of the chart, calculated by the maximum imbibition divided by the drainage multiplied by 100. The coordination number and aspect ratios calculated from pore casts are included beneath the chart.

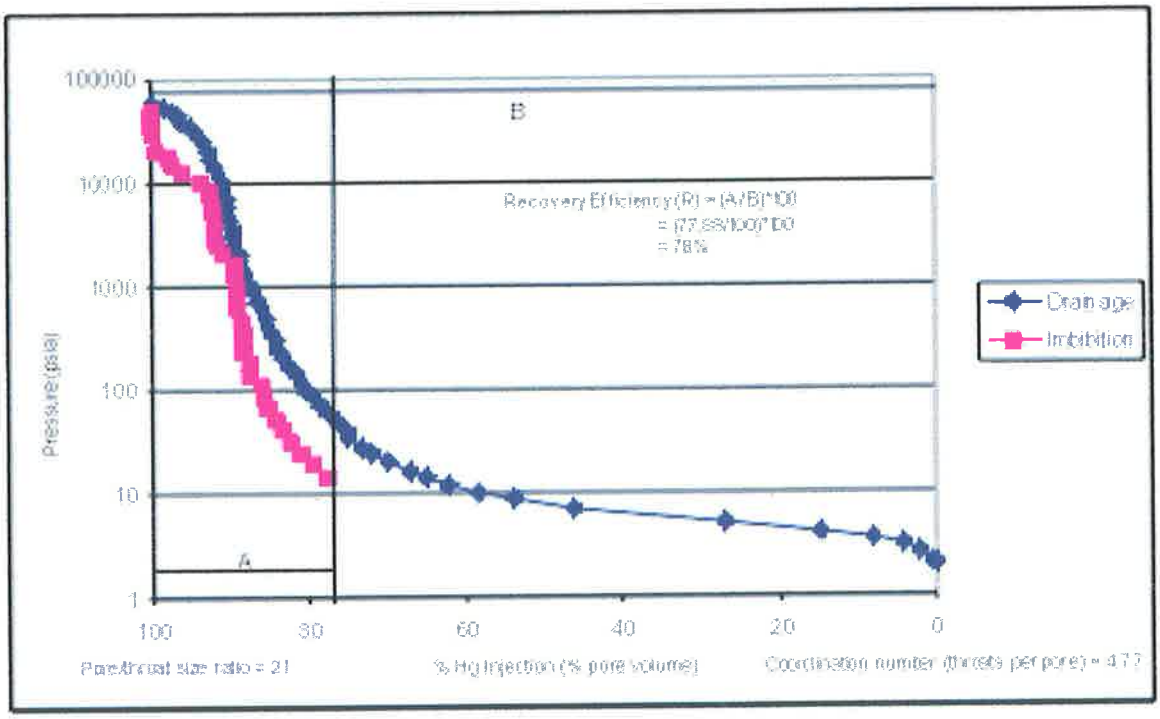

Figure 5.8: Drainage-imbibition curve for sample G17 1dii showing the drainage into and imbibition of mercury from the rock. The recovery efficiency is included in the centre of the chart, calculated by the maximum imbibition divided by the drainage multiplied by 100. The coordination number and aspect ratios calculated from pore casts are included beneath the chart

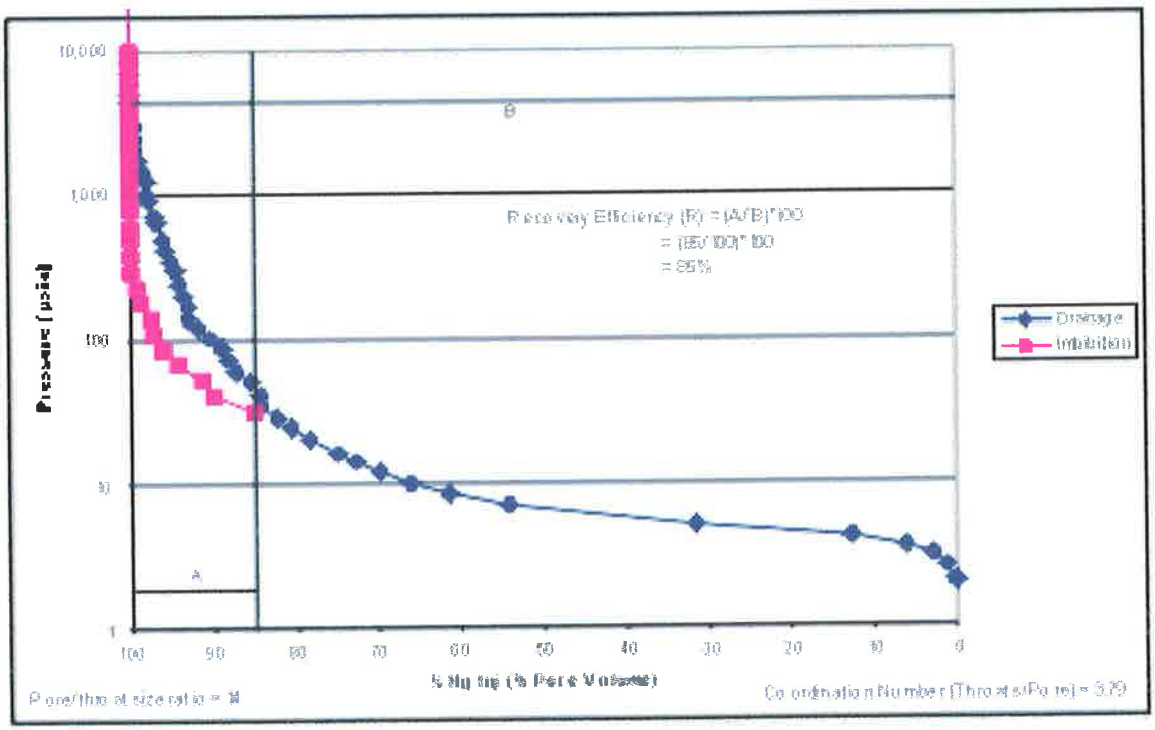

Figure 5.9: Drainage-imbibition curve for sample G17 1fi showing the drainage into and imbibition of mercury from the rock. The recovery efficiency is included in the centre of the chart, calculated by the maximum imbibition divided by the drainage multiplied by 100. The coordination number and aspect ratios calculated from pore casts are included beneath the chart.

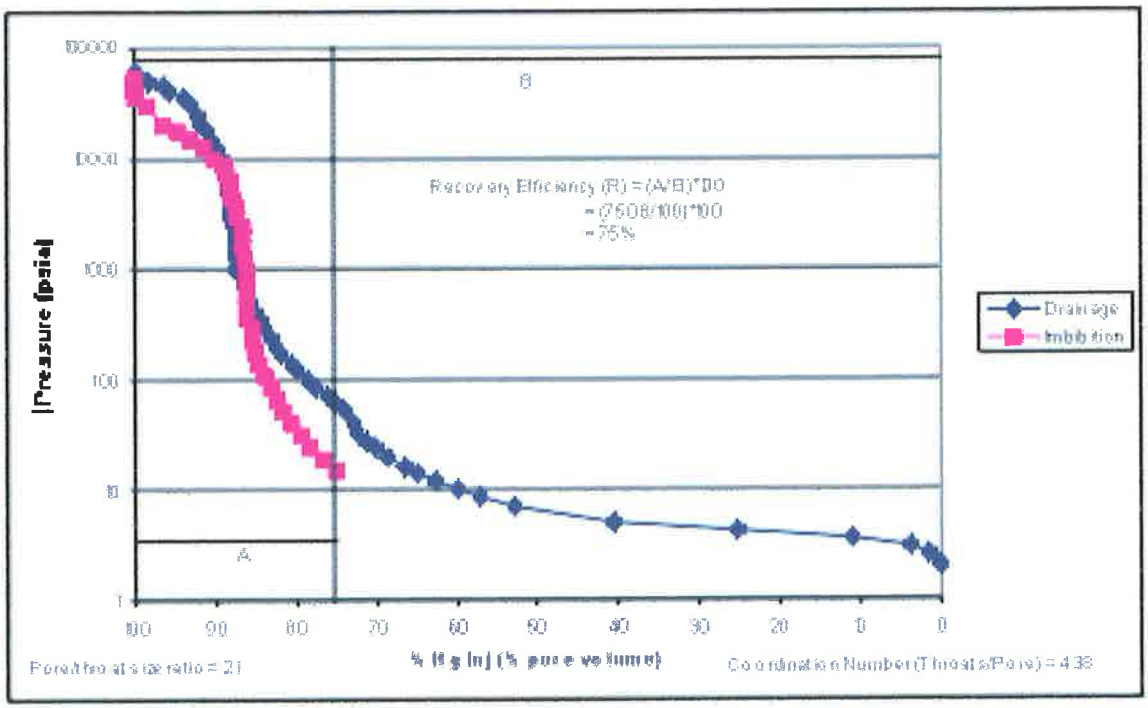

Figure 5.10: Drainage-imbibition curve for sample G17 1fi showing the drainage into and imbibition of mercury from the rock. The recovery efficiency is included in the centre of the chart, calculated by the maximum imbibition divided by the drainage multiplied by 100. The coordination number and aspect ratios calculated from pore casts are included beneath the chart.

Pore throat sizes are also calculated from MICP because the volume of mercury entering a sample between specific pressure limits is related to the fraction of the total pore volume that is connected by pore throats that are within specific size limits. Pore throat distribution charts of the five samples were calculated and are presented below as Figures 5.11-5.15.

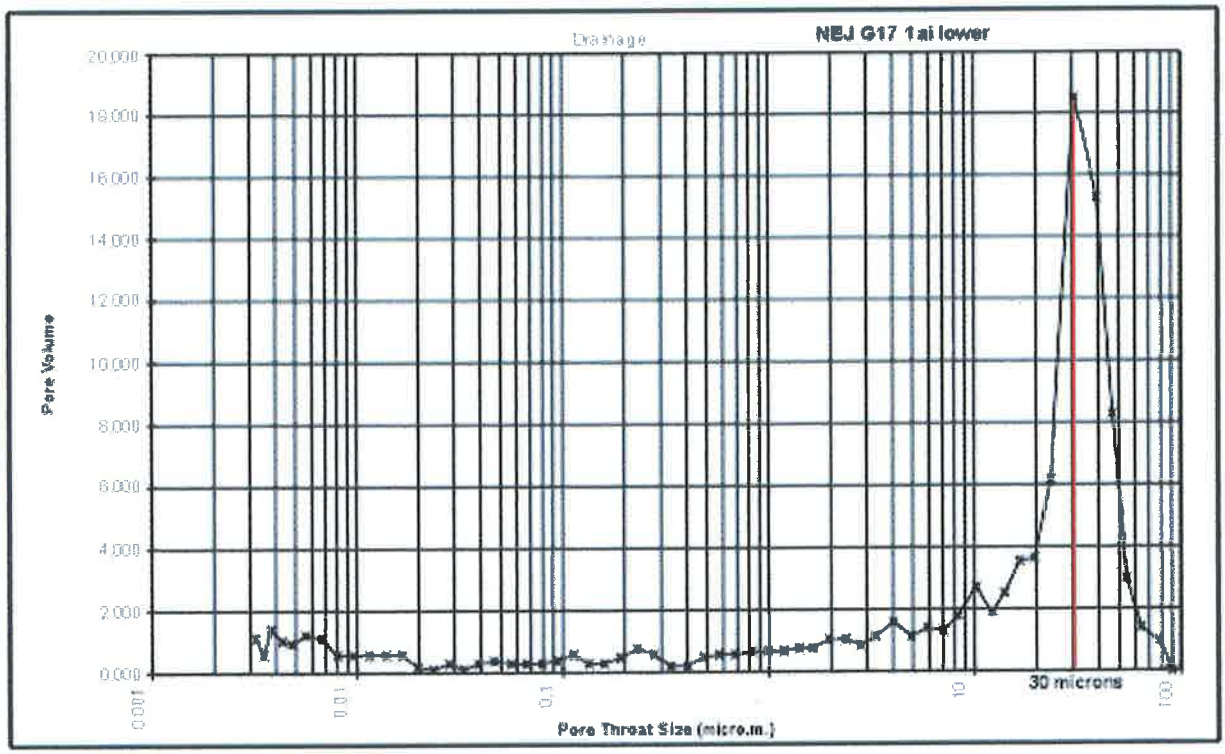

Figure 5.11: Pore throat chart calculated from MICP for sample G17 1a-lower showing that approximately 19% of the pore volume is accessed by pore throats with a size of 30 microns which is in good agreement with the range of pore throat data obtained from pore casts.

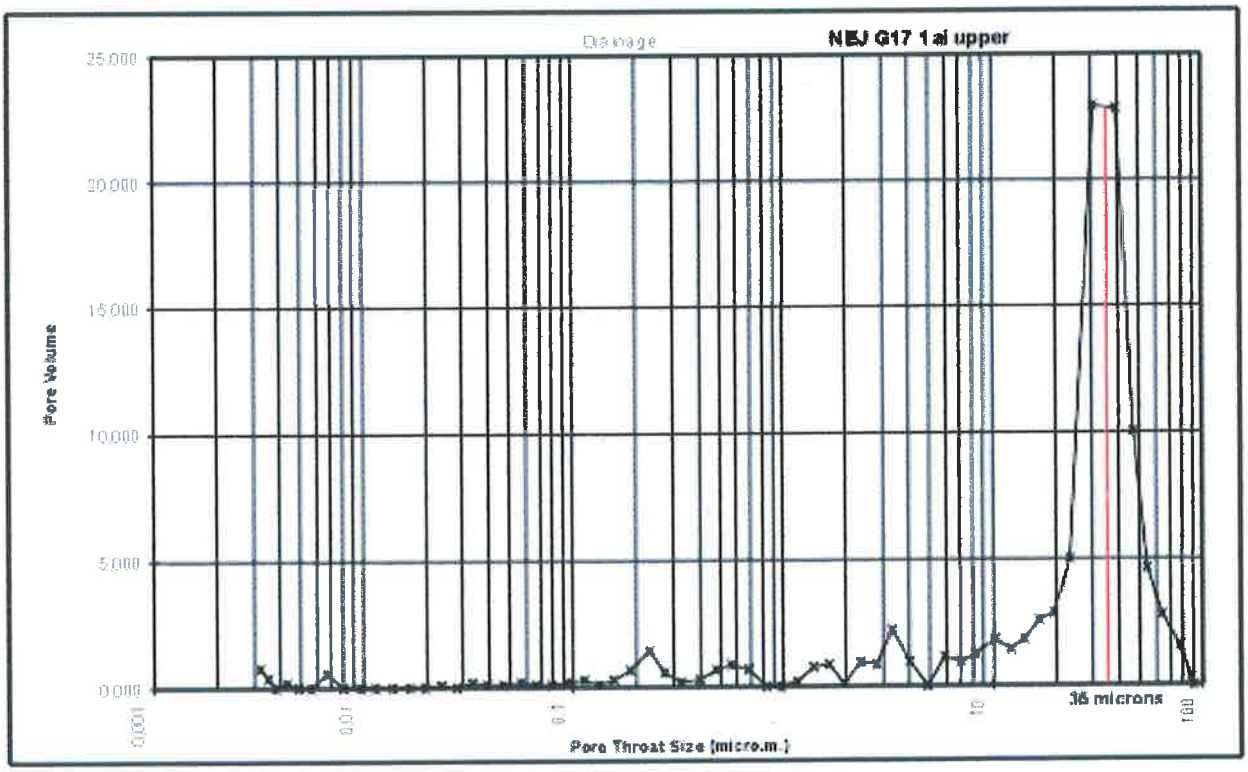

Figure 5.12: Pore throat chart calculated from MICP for sample G17 1ai upper showing that approximately 23% of the pore volume is accessed by pore throats with a size of 35 microns which is in good agreement with the range of pore throat data obtained from pore casts.

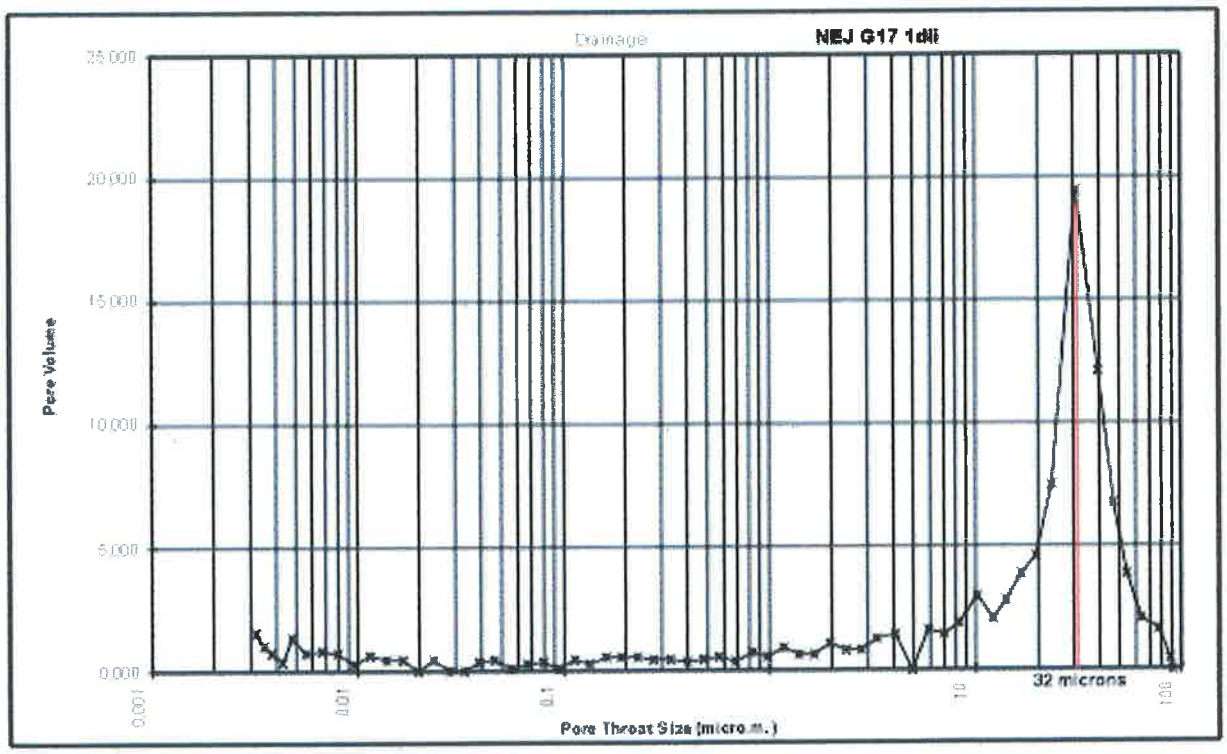

Figure 5.13: Pore throat chart calculated from MICP for sample G17 1dii showing that approximately 19% of the pore volume is accessed by pore throats with a size of 32 microns which is in good agreement with the range of pore throat data obtained from pore casts.

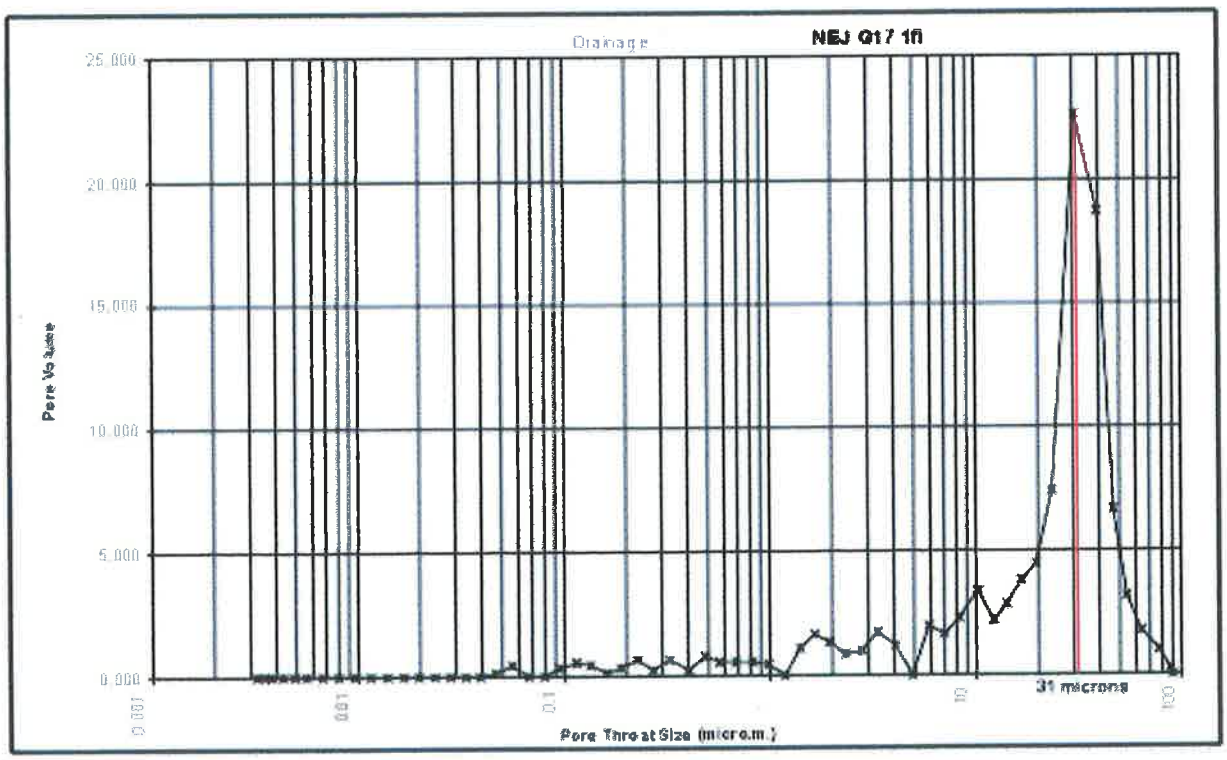

Figure 5.14: Pore throat chart calculated from MICP for sample G17 1fii showing that approximately 19% of the pore volume is accessed by pore throats with a size of 31 microns which is in good agreement with the range of pore throat data obtained from pore casts.

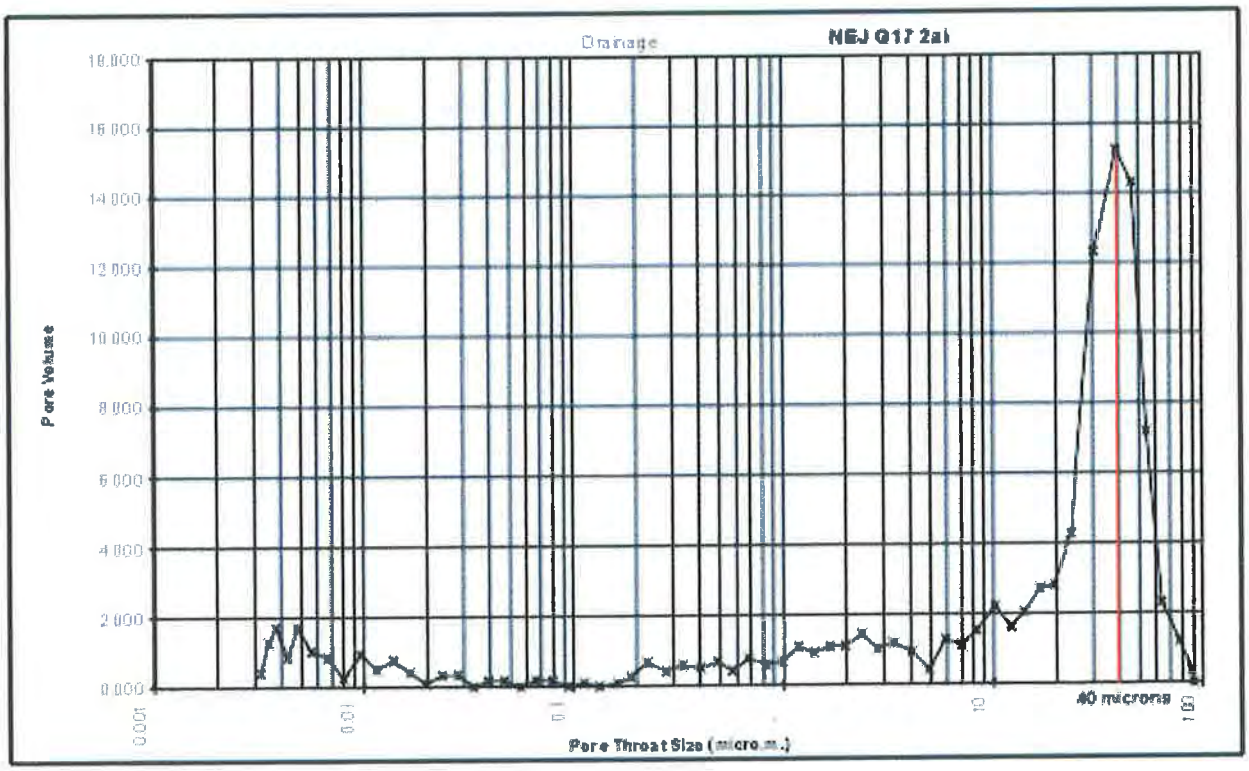

Figure 5.15: Pore throat chart calculated from MICP for sample G17 2ai showing that approximately 15% of the pore volume is accessed by pore throats with a size of 40 microns. This is in good agreement with the range of pore throat data obtained from pore casts, however there are a greater level of smaller throats suggesting the sample might be more poorly sorted.

INTERPRETATION

The porosity calculated by MICP (19% to 24%) was in agreement with porosity calculated by PIA (20% to 23%) and RCA (20% to 24%). The major width of the pore throats, as estimated from capillary pressure curves, ranges from 20 to 60 microns and is in good agreement with direct measurements made from pore casts, which indicated that measured pore throats ranged from 15 to 40 microns. Pore cast measurements are limited to the surface of the sample, thus limiting the number of possible readings, and the nature of the pore cast only allows the surface thickness of the throat to be measured. More direct measurements are likely to improve the agreement between the two. Mercury-injection capillary pressure curves provide additional information on the size distribution of pore throats, and this information is related to sizes of pores and throats when measured directly from the pore casts (Wardlaw, 1976).

Increases in the pore-to-throat-size ratio for a rock are important in influencing the ejection efficiency for a non-wetting phase. As porosity is reduced, pore-to-throat-size ratio increases and ejection efficiency is reduced (Wardlaw, 1976).

The recovery efficiencies calculated from the drainage-ejection/imbibition curves suggest that the Hutton Sandstone samples are excellent quality reservoir rocks, with recovery efficiency ranging between 75% and 90%.

According to Wardlaw (1976), mercury-injection and ejection tests do not provide a close analogue for an oil-water system, but mercury ejection-injection ratios may give a relative indication of the efficiency with which various rock types can expel a non-wetting phase when pressure is reduced. Ejection efficiency correlates positively with porosity; therefore, it may be possible to provide a factor from porosity data that will indicate recovery efficiency insofar as this is dependent on pore geometry.

Mercury injection capillary pressure is a particularly useful tool because it can be used to determine displacement threshold pressures (P_d) of mercury into a rock, which is directly related to the ability of the rock to be an effective seal. This can subsequently be used to determine the column height that can be held before it will leak. These values are not required in this study because the Hutton Sandstone is a reservoir and not a seal.

For this study, MICP was primarily used to acquire porosity and accurate pore-throat size and distribution for the five samples, and use them as a control for the pore throat sizes determined from pore cast analysis. MICP was also used to calculate the recovery efficiency of the samples, defining the reservoir quality of the Hutton Sandstone. All of the data obtained suggested there was agreement between methods (Table 5.5), however the data obtained from the pore casts is obtained from the surface of the sample and is subjected to greater operator bias. In pore casting, individual pores and pore throats are selected for examination in each image, compared with MICP, where the data is obtained from the entire rock and not just the surface.

	PORE CAST	MICP	MICP Porosity	PIA Porosity
Sample	Pore throat range (microns)	Maximum pore throat width (microns)	%	%
1ai upper	15 - 32.5	35	21	20
1a-lower	n/a	30	20	20
1dii	17 - 42	32	22	20
1fi	12.5 - 41	31	19	20
2ai	17 - 35	40	24	18

Table 5.5: Porosity and pore throat data obtained from pore casts, MICP and PIA. The data suggests that there is agreement between methods. A pore cast was not made for sample 1a-lower.

Chapter 6 CEMENT EMPLACEMENT

6.1 INTRODUCTION

During measurement of porosity in the Hutton Sandstone, it appeared that the large pores were grouped around apparent concretionary centers, which were a combination of quartz and quartz cement. These concretions were investigated using a series of image processing techniques.

The apparent concetionary cementation within the Hutton Sandstone is compared with three other examples of concretionary cement, two involving calcite (the Carizzo and Bunkers Sandstones) and one where silica is the cement (Rawnsley Quartzite).

Examples were provided explaining the origin of concretions and nodules within these other formations and these models were suggested as the method of cement emplacement within the Hutton Sandstone samples, which were examined and compared with the other formations.

6.2 CONCRETIONARY MODELS

The Eocene Carizzo Sandstone is a fluvial sand deposit that accumulated across much of the Gulf of Mexico Basin (Figure 6.1). In the East Texas Basin, on the northeast flank of the Butler salt dome (Figure 6.2) the Carizzo Sandstone shows examples of calcite cement invading clean quartz-rich sandstone as a series of overlapping concretions at different scales.

Further details pertaining to the geological structure and setting of the Gulf of Mexico Basin and other details associated with the Butler salt dome, are contained in the paper by Enos and Kyle (1998). For the purpose of this study, attention has focused on the emplacement of calcite cement within the Carizzo Sandstone as an analogue for silica cement in the Hutton Sandstone.

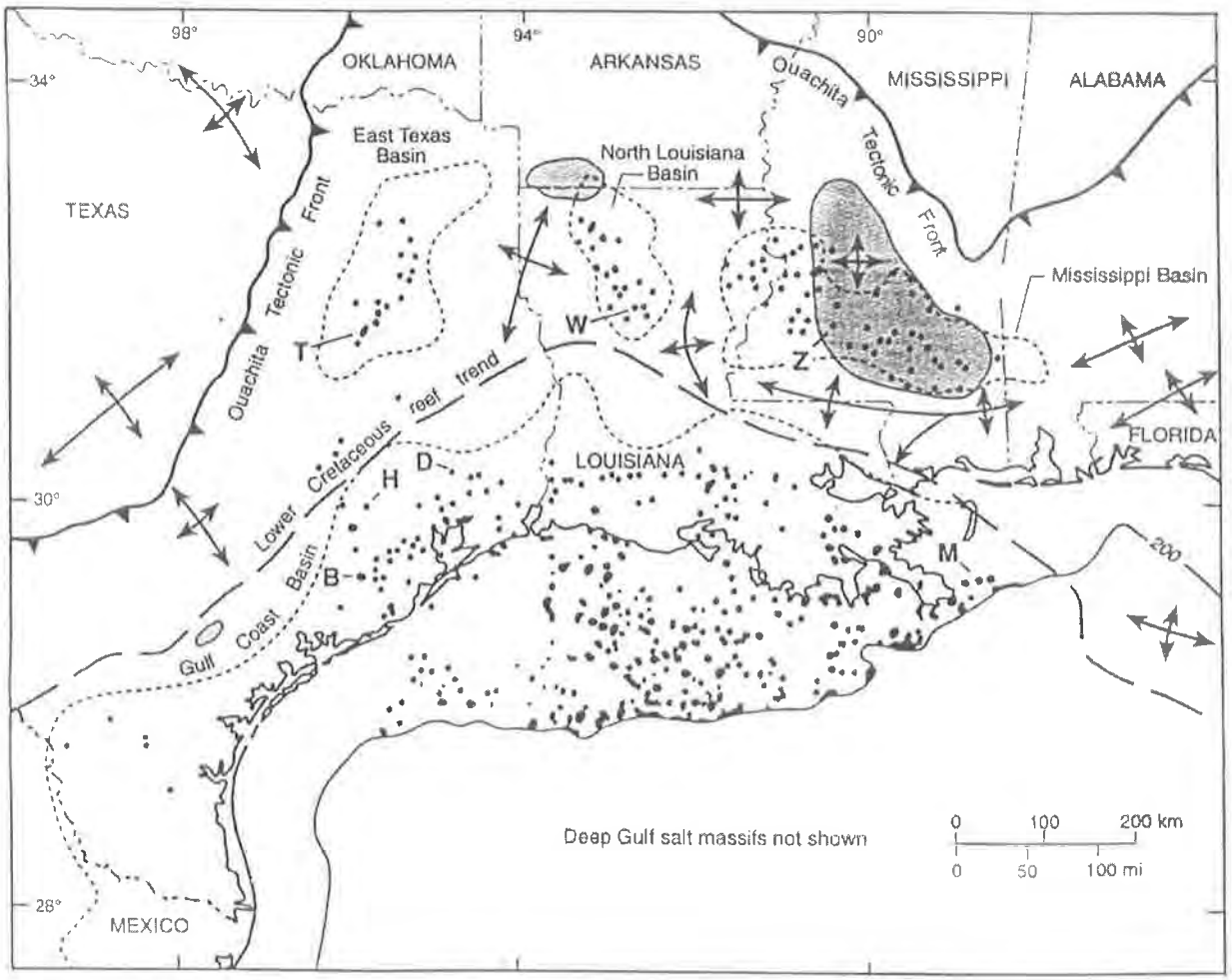

Geologic setting of the Gulf Coast Basin showing location of selected salt domes.

T = Turtle Dome [Modified from Ewing and Lopez (1990)]

Figure 6.1

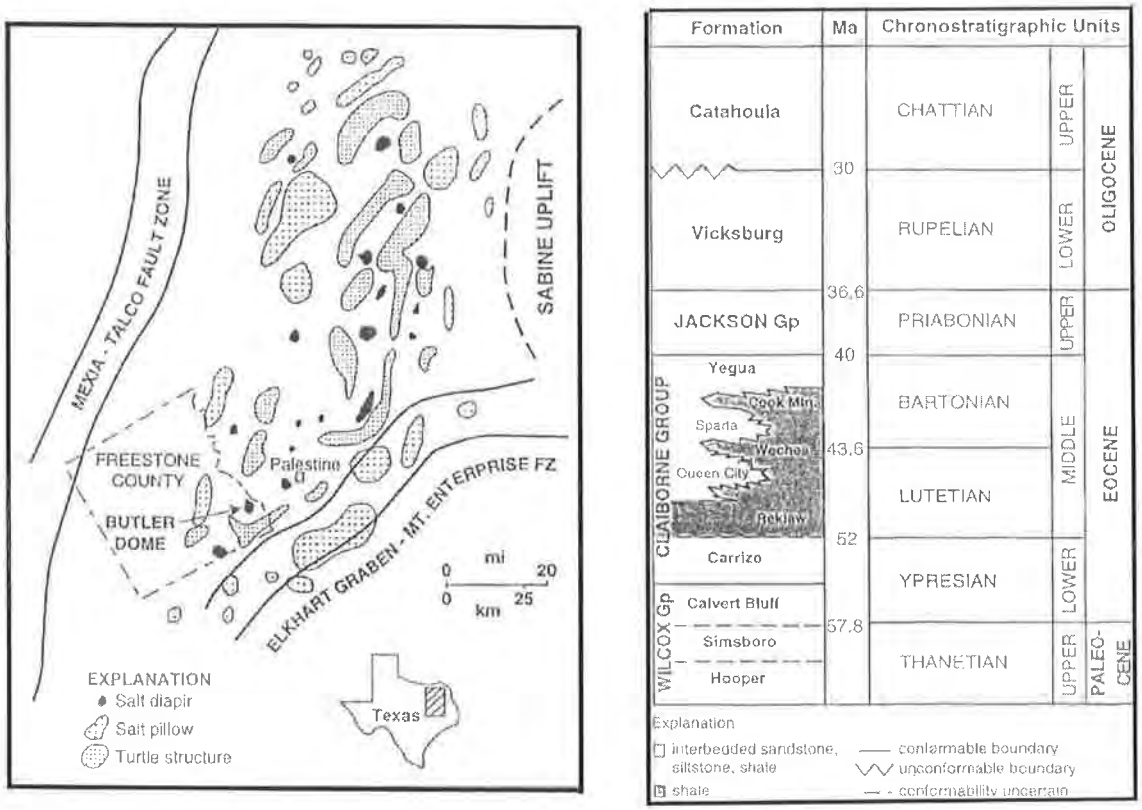

Figure 6.2: Butler Salt dome location map and Stratigraphic column.

What is unusual about the Carizzo Sandstone is that sediments are typically uncemented within the shallow Tertiary succession. However, on the northeast flank of the Butler Dome, the Carizzo Sandstone is almost completely cemented, and the study by Enos and Kyle (1998) focused on this anomalous cemented zone. It was suggested that the cementation on the northeast flank was due to processes similar to those that create salt dome calcite cap rocks throughout the Gulf Coast. Information regarding these calcite cap rocks is discussed by Kyle, (1995).

The Carizzo Sandstone is a fine-to-medium-grained quartz arenite to sublitharenite with 42% to 50% cement that is primarily poikilotopic calcite with local pyrite. The unit is massive to cross-bedded and was deposited in a distal fluvial environment. The uppermost part of the unit consists of thinly interbedded sand, silt and clay, and is interpreted as overbank or floodplain deposit (Enos & Kyle, 1998).

The study area shows a mature, well-sorted sandstone, tightly cemented with spherical calcite concretions and local spherical pyrite concretions on one side of a fault, while on the other side, the sandstone is primarily uncemented with only scattered pyrite concretions. The calcite concretions have coalesced to form thick-cemented beds (Enos & Kyle, 1998). Outcrop photographs (Lemon, pers.comm, 2000) show cementation is not complete, with uncemented zones between clusters of concretions (Figures 6.3 and 6.4).

Petrographic evidence suggests that an average of 1.8% of the framework component was feldspar, much of which was pseudomorphed by kaolinite crystals. Other feldspar grains are partially dissolved, but there are no oversized pores to indicate dissolution was a common process (Enos & Kyle, 1998).

Poikilotopic calcite is the main cement in the studied zone, comprising 64% of an average of 49% of the whole rock when all pore space is filled (Enos & Kyle, 1998). The zones with higher than average cement content show evidence for replacement of framework grains as well as possible displacement. The calcite grows in spherical concretions of all different sizes ranging from 2mm to 40cm in diameter. In outcrop, local uncemented pockets of sand are weathered from the rock (Figure 6.3) while the concretions intrude from the margins (Figures 6.4, 6.5, 6.6 and 6.7 (a and b)).

Figure 6.3: Outcrop of the calcite concreted Carizzo Sandstone showing the weathering effect of the uncemented areas.

Figure 6.4: Outcrop of the Carizzo Sandstone showing the spherical calcite concretions intruding into an uncemented zone that has washed from the outcrop.

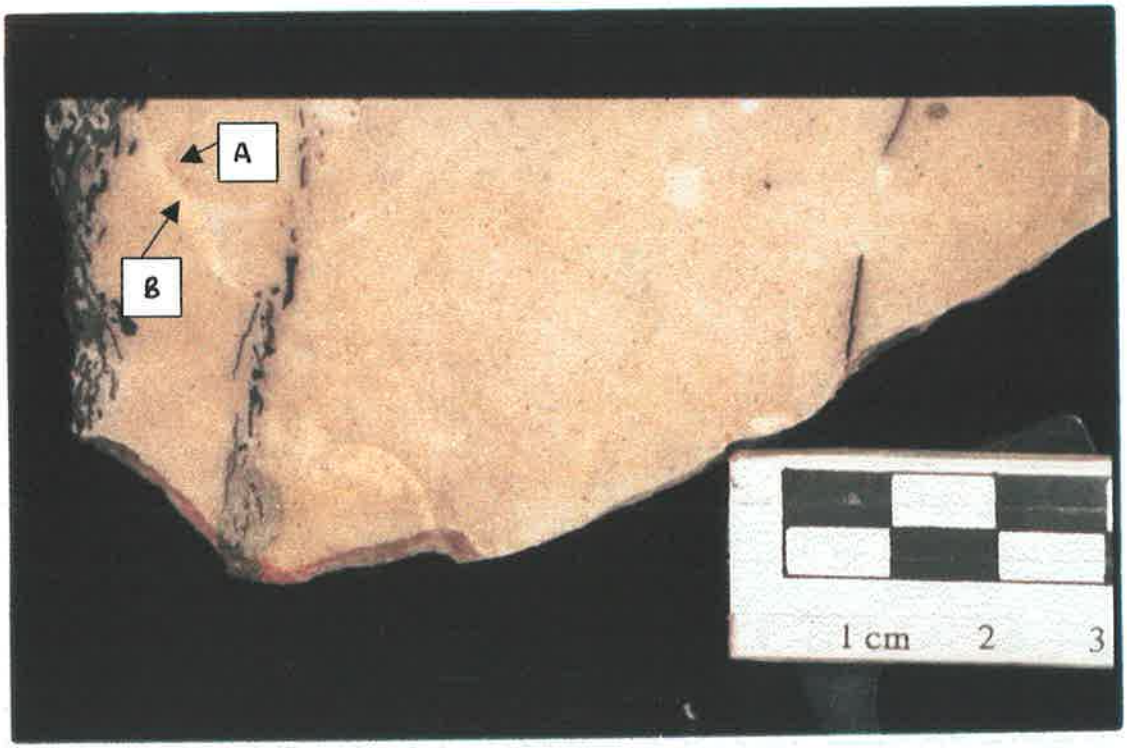

Figure 6.5: Carizzo Sandstone showing tight spherical calcite concretions (A) with areas of weakly cemented sandstone between them (B).

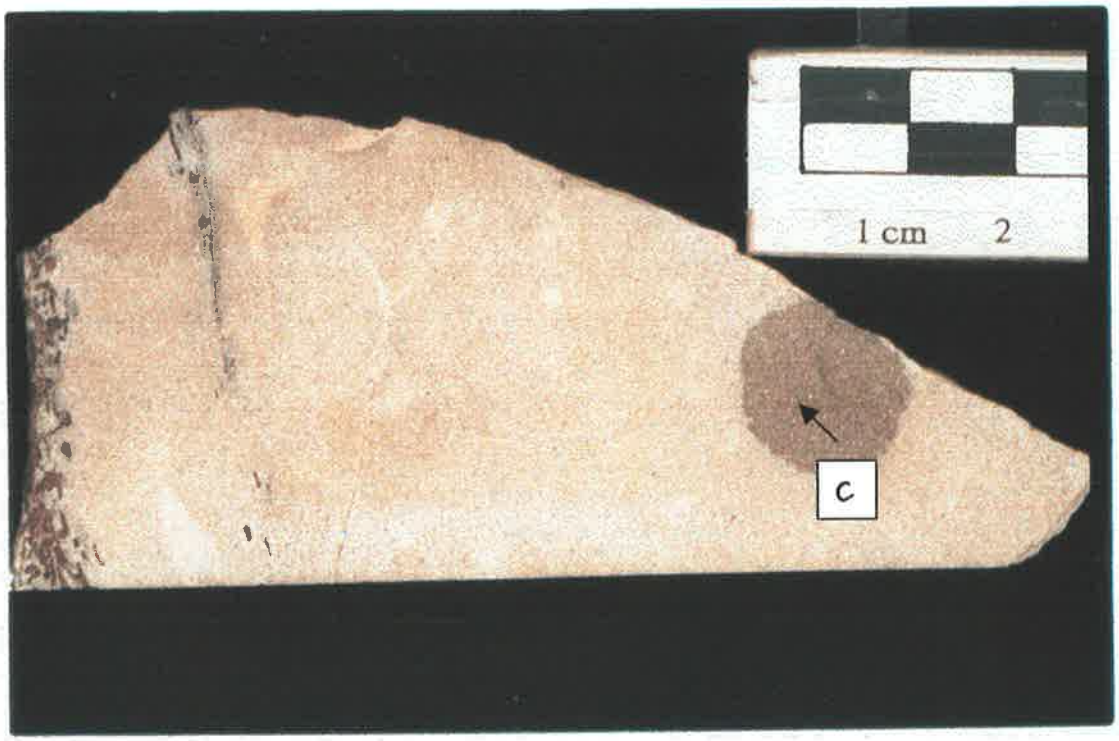

Figure 6.6 (a): Carizzo Sandstone showing more tight spherical calcite concretions indicated by the slightly darker patches along with a pyrite concretion (C). The concretions are separated by lightly coloured polygonal zones with less cement.

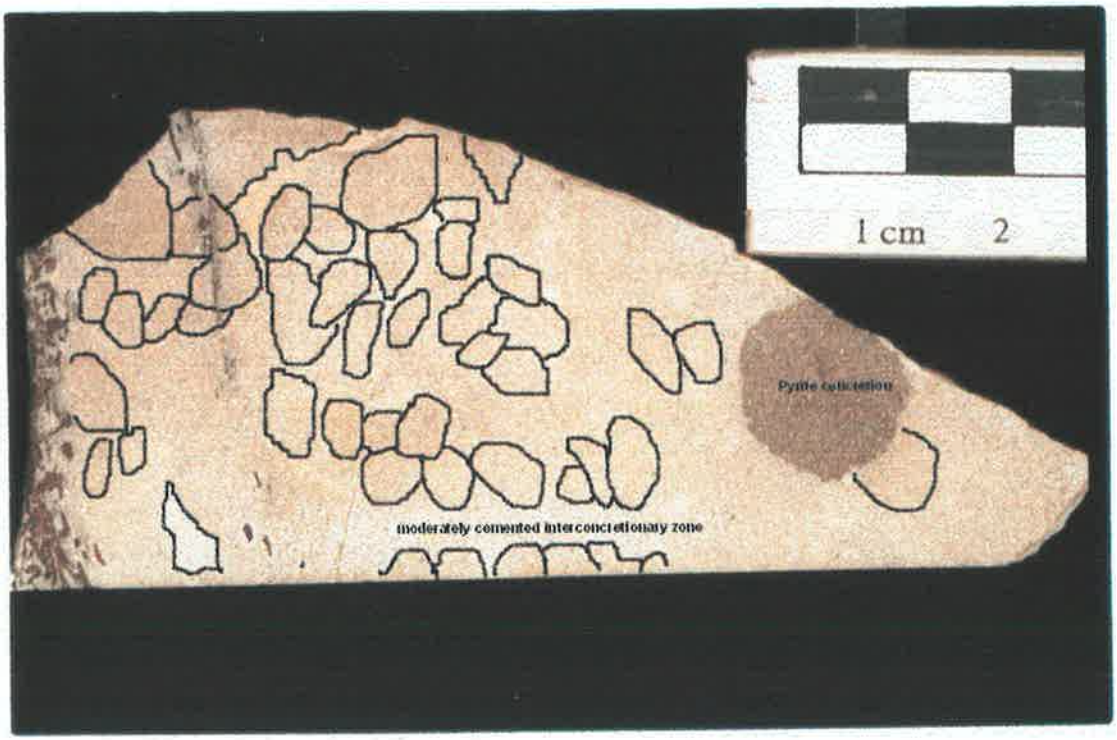

Figure 6.6 (b): Same piece of Carizzo Sandstone as above with some interpretations included showing some of the major calcite concretions that are the result of coalescing smaller concretions. This coalescing creates a concretion overprint across the rock.

Poikilotopic texture is not indicative of any particular stage of diagenesis, as it can develop at any depth of burial. The large crystals indicate a limitation of nucleation sites, which is a possible theory as to why the cement forms as concretions. Unfortunately, the factors controlling the development of nucleation sites are not understood (Enos & Kyle, 1998). Pyrite cement is present, and occurs in spherical to irregular concretions of 1mm to 3cm in diameter (Figure 6.6 (a and b)).

Other examples of sandstones that display cement emplacement by concretion include the early Cambrian Bunkers Sandstone and the Precambrian Rawnsley Quartzite, both from the Flinders Ranges in South Australia.

The Bunkers Sandstone is an early Cambrian deep-water lowstand fan sandstone that outcrops in the central Flinders Ranges of South Australia (Gravestock & Hibburt, 1991). The unit is mainly known from outcrop. Twenty to fifty centimetre thick parallel beds of massive sandstone grade upwards over 50 metres into thinner, tightly carbonate cemented beds, interbedded with dark grey, nodular silty limestones. Although there are no apparent sedimentary structures within the very clean quartz arenite units, the situation of the deposit, on the low side of a fault active during deposition and interbedded with deep-water limestones, strongly suggests that this unit was deposited as a series of proximal to mid-fan turbidites.

The thick, clean sands at the base of the unit are relatively uncemented except for bands of nodular concretions that weather from the outcrop as lumpy specimens shown in figures 6.7 and 6.8.

The Precambrian Rawnsley Quartzite is a medium-coarse grained, clean, white-pinkish-grey sandstone and quartzite, which disconformably overlies the Bonney Sandstone and is the most resistant rock unit of the Flinders Ranges (Forbes & Preiss, 1987). It contains trough cross-bedding, parallel lamination and other sedimentary features typical of shallow, tidal-shelf deposition such as a shore-face, barrier or migrating channel facies (Forbes & Preiss, 1987). The silica cementation within the unit is likely to be responsible for its resistance to weathering and sometimes forms spherical concretions as shown by Plates 6.9 and 6.10.

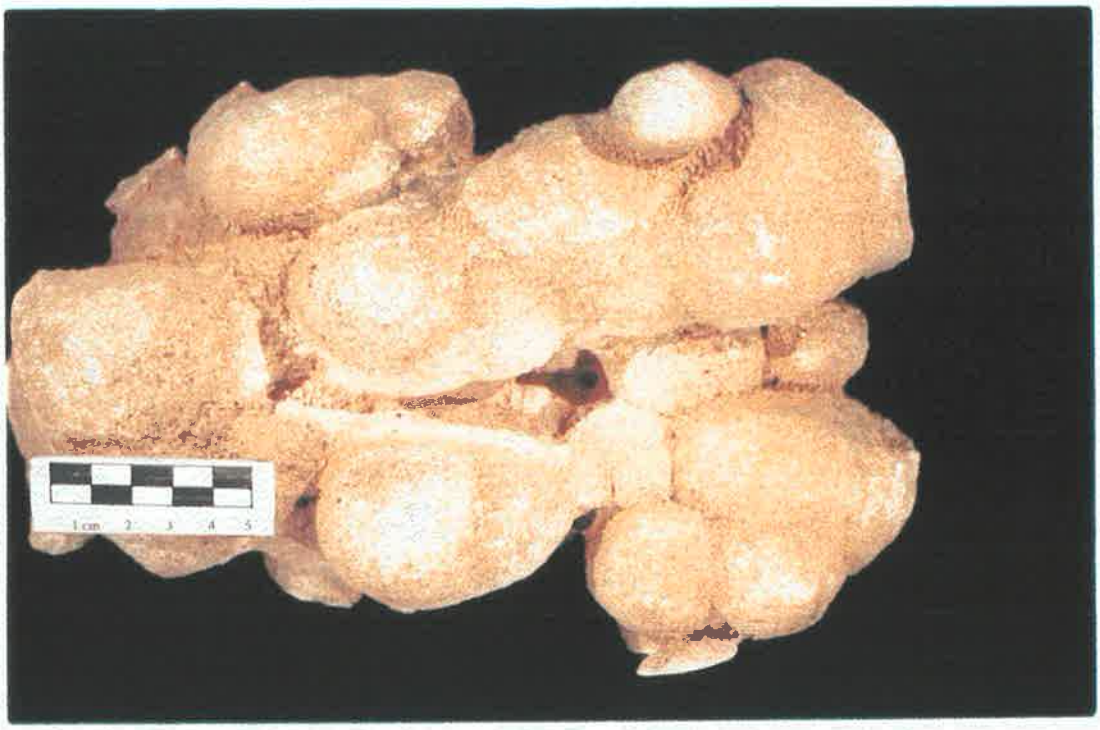

Figure 6.7: Bunkers Sandstone showing highly cemented spherical concretions clustered throughout the sample.

Figure 6.8: Bunkers Sandstone with highly cemented concretions clustered throughout the sample. Uncemented areas have been weathered away.

Figure 6.9: A highly silica cemented spherical concretion from the Rawnsley Quartzite.

Figure 6.10: A highly silica cemented spherical concretion from the Rawnsley Quartzite. The dark patch on the kidney shaped piece is resin.

Plane polarized, cross-polarized light and CL photomicrographs have been included to show what these intensely cemented concretions look like in thin section within both the Bunkers Sandstone (Figures 6.11 (a and b)) and the Rawnsley Quartzite (Figures 6.12 (a and b) and 6.13 (a and b)).

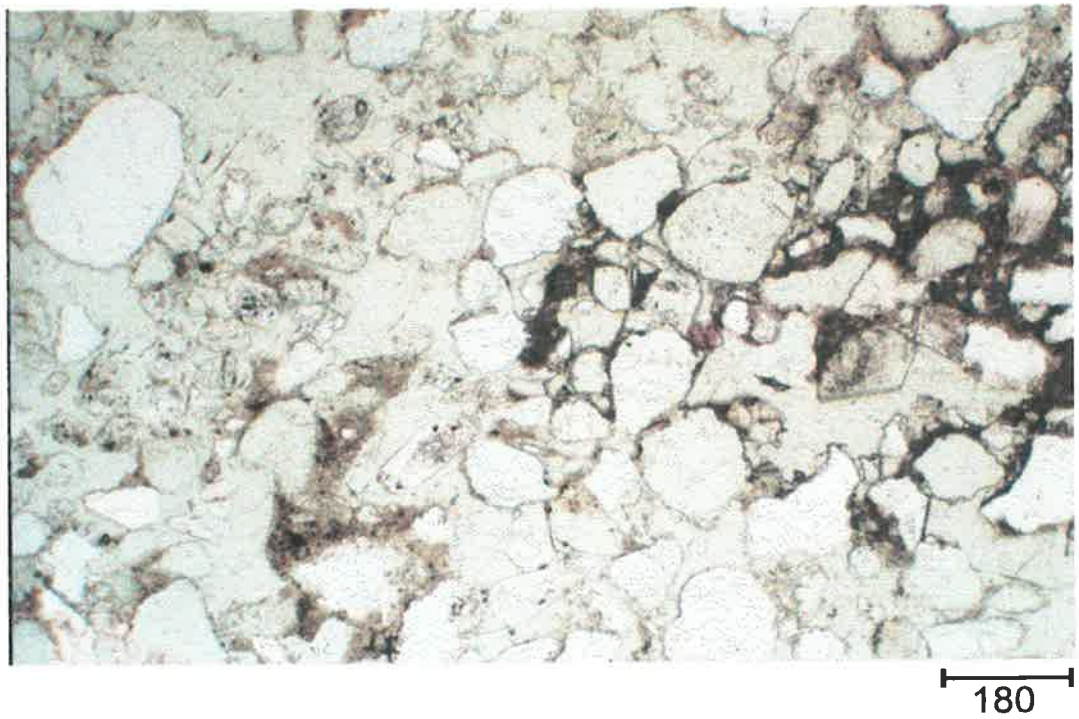

Figure 6.11 (a): Plane polarised light image within Bunkers Sandstone concretion. Cement completely occludes porosity (5x-mag, scale bar in microns).

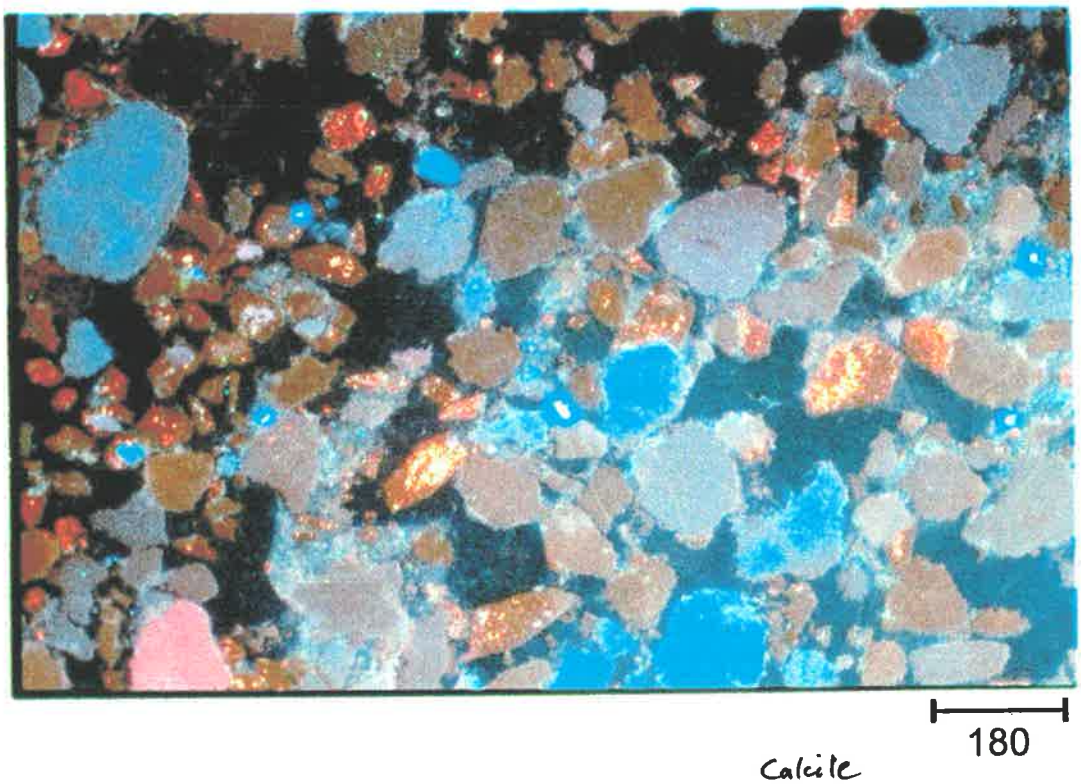

Figure 6.11 (b): CL micrograph of the Bunkers Sandstone concretion. Cement shows no luminescence (5x-mag, scale bar in microns).

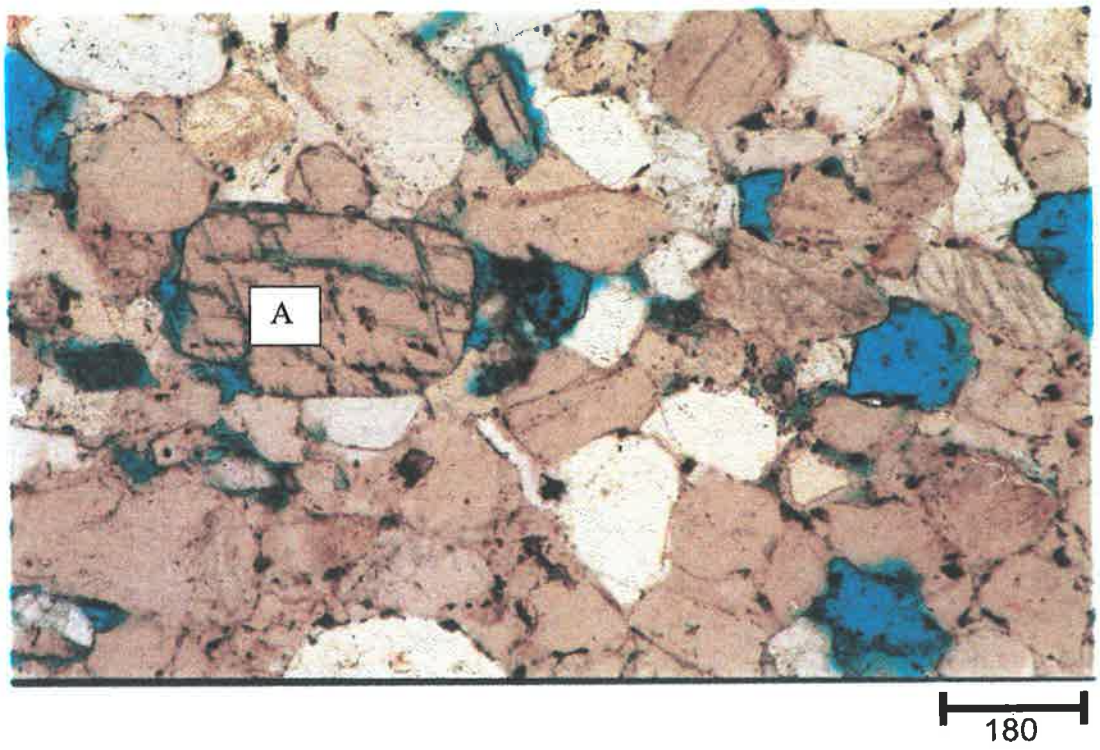

Figure 6.12 (a): Plane polarised light micrograph within a Rawnsley Quartzite concretion. Note the partially dissolved feldspar grain (A) and some primary porosity (5x-mag, scale bar in microns).

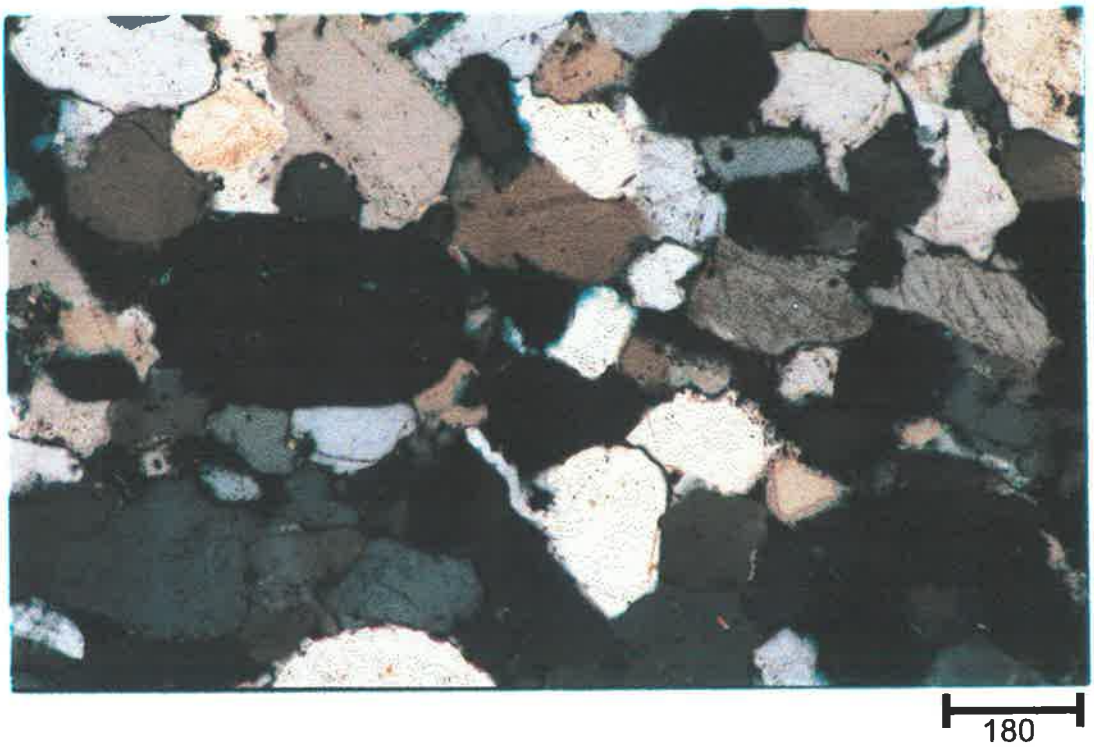

Figure 6.12 (b): Cross-polarized light micrograph of the Rawnsley Quartzite of the above image (scale bar in microns).

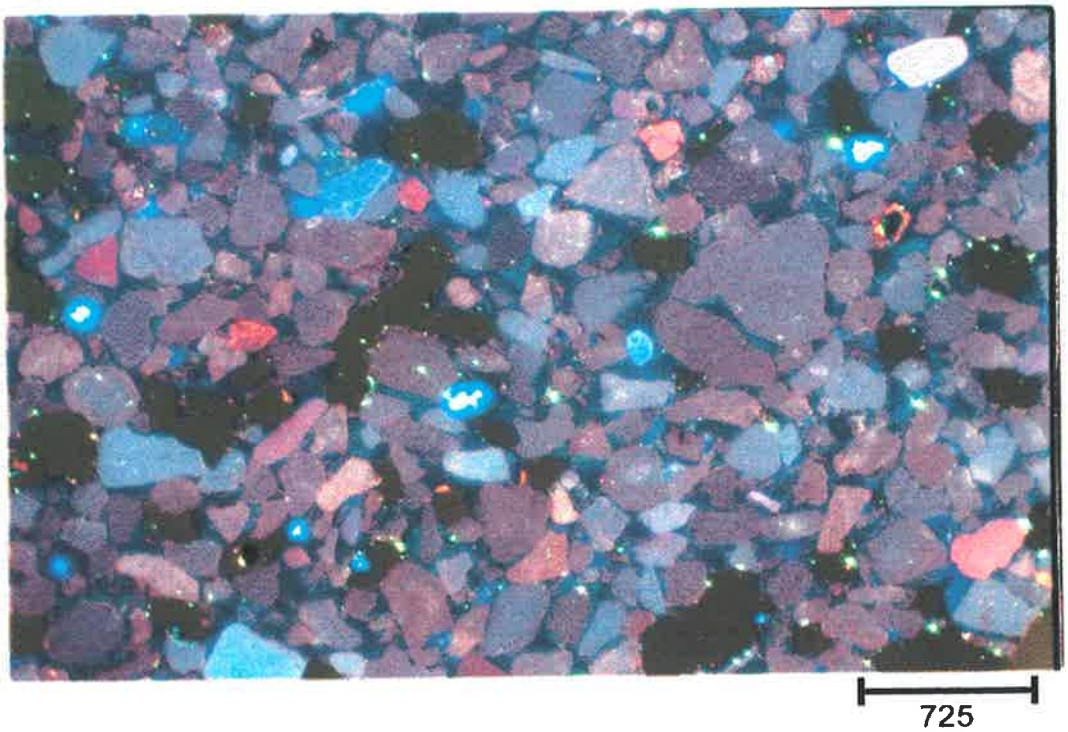

Figure 6.13 (a): CL micrograph within the Rawnsley Quartzite. Some porosity is present amongst otherwise fully cemented framework concretion (2x-mag, scale bar in microns). Quartz overgrowth is the major cement phase.

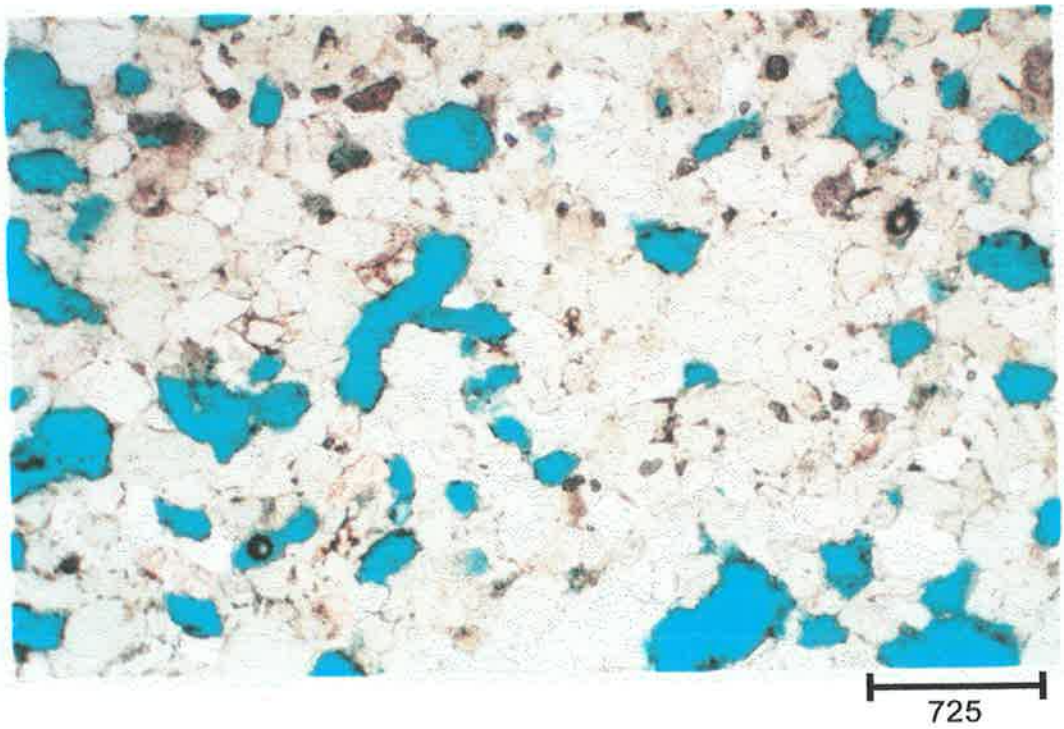

Figure 6.13 (b): Plane polarised light within the Rawnsley Quartzite. The pores are clearly visible amongst the quartz cement.

A literature search was undertaken to help build a model for nodule formation. Not all nodules appear to form the same way. Muller & Fabricus (1974) discussed an actualistic model for the formation of magnesian-calcite nodules in the Ionian deep sea, and noted that it was conceivable that a similar type of formation may account for the formation of red nodular limestones in the Mediterranean Jurassic, studied by Jenkyns (1974).

Unfortunately, Muller and Fabricus acknowledged that the triggering mechanism for the formation of the nodules is still unknown, however, they did deduce a tentative model for the formation of magnesian-calcite nodules. Magnesian calcite is precipitated as a lutite at the sediment surface. Provided the rate of cement-precipitation is higher than the sedimentation rate, the cemented lutite gradually forms concretions of increasing size. If this process is allowed to continue, nodules often coalesce to form coherent crusts (or hardgrounds) or a nodule pavement (Muller & Fabricus, 1974).

Quartz cement and kaolinite are the only visible cements within the studied Hutton Sandstone. Whilst there is no calcite cement, it is suggested the quartz cement has begun forming similar concretions that are clustered throughout the samples, although they are not nearly as pronounced as those seen in the Carizzo Sandstone or Bunkers Sandstone.

The concretions were examined using macro photos of the thin sections (Appendix 11), micrographs taken from these thin sections that showed concretions (areas of quartz cemented by quartz and kaolinite), and binary overlays created from these micrographs (Figures 6.14-6.17).

6.3 INTERPRETATION

Sample 1fii (Figure 6.14) appears relatively uniform with possible evidence of silt layering through the central region of the slide. Upon closer inspection, it appears that there are tight areas within the thin section (concretions), which are identified by larger pores surrounding them. These concretions are clustered throughout the slide. A theoretical image has been produced (Figure 6.15) highlighting what is suggested as being seen throughout these Hutton Sandstone samples.

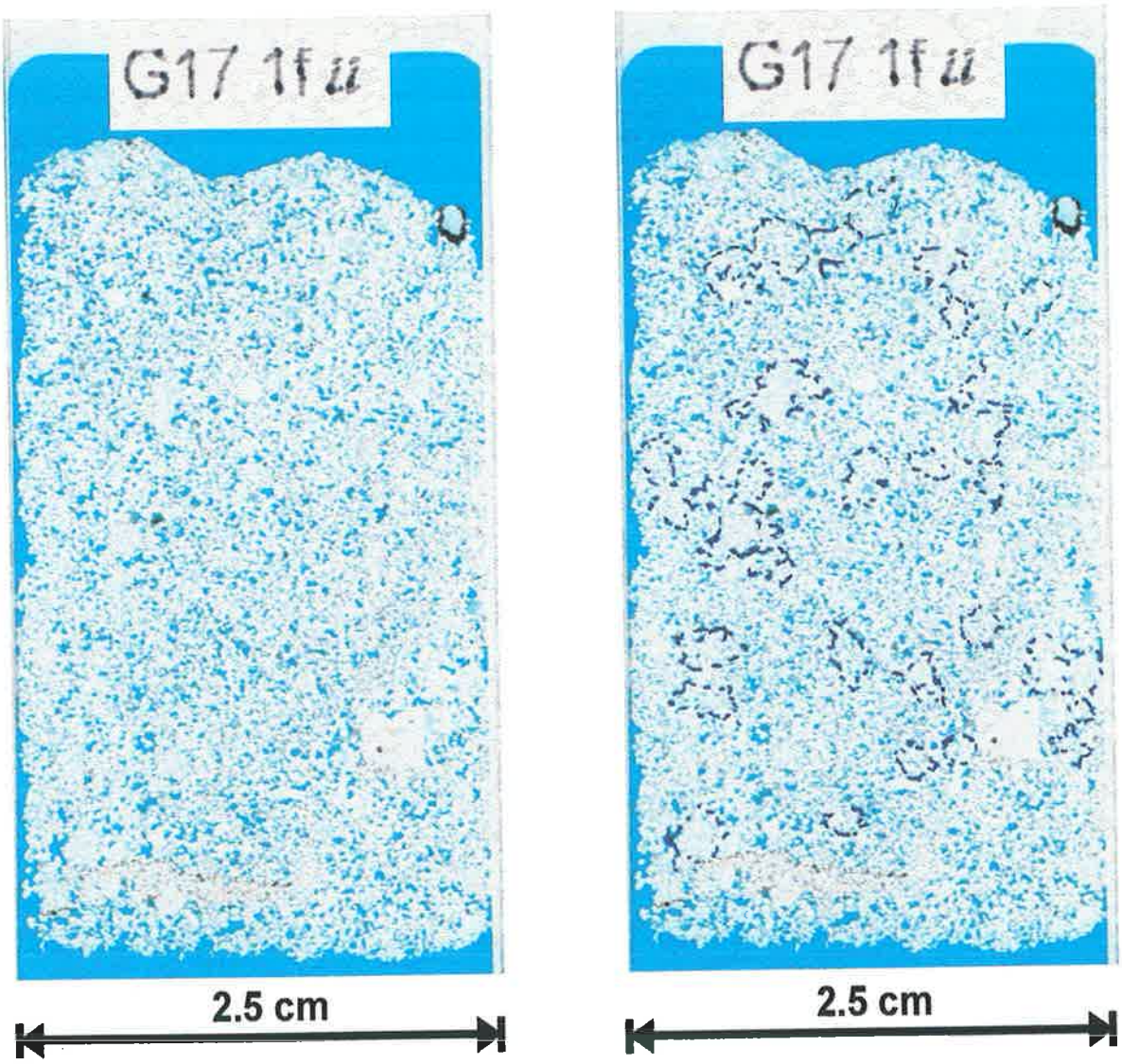

Figure 6.14: Thin section G17 1fii and the interpretation of concretions. Note some concretions are clustered together, and occur throughout the sample. The concretions are surrounded by rims of larger pores.

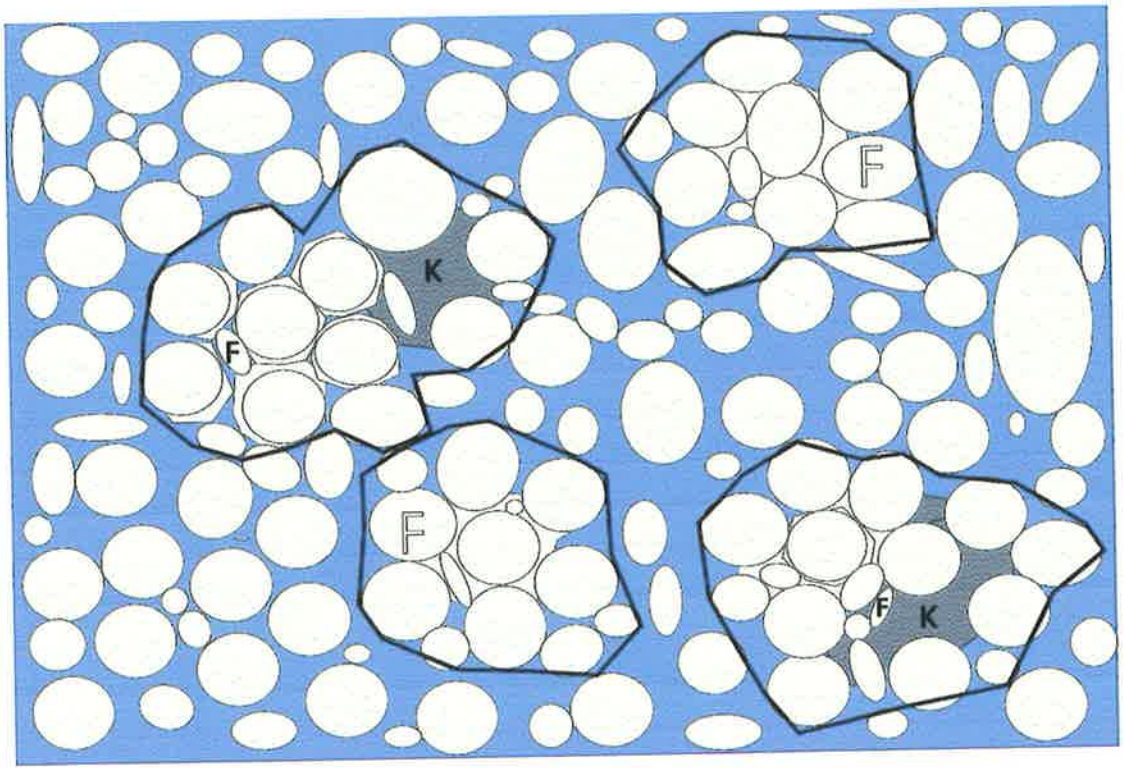

Figure 6.15: Theoretical image showing what is seen in the Hutton Sandstone samples. The clusters are highlighted with dark rings, and consist of quartz, quartz cement (in the form of overgrowths) and kaolinite (K). Some remnant feldspar grains are nearby supplying much of the silica for the quartz cement.

Figure 6.14 also contains the interpretation of these concretions alongside the original. The interpretations were produced by enlarging the images without greatly reducing the resolution by using the zoom function in Corel ™ PHOTOPAINT 9.0. The amount of enlargement is limited before resolution is reduced to a point where concretions defined by the large pores are not recognisable.

These concretions have some small pores within them. While these pores are likely to have some effect on the average porosity of the sample, they are not likely to have a pronounced effect on the permeability of the sample. Fluid flow is likely to be controlled by the connectivity of the large pores outside the concretions.

Unfortunately, the quality of images do not allow for magnification of these areas in these thin sections without loss of resolution, but it is suggested these concretions occur throughout the samples and often begin to coalesce and cluster together. One

other thin section has been included with the interpretation alongside it (Figure 6.16). The remaining thin sections are included in Appendix 11.

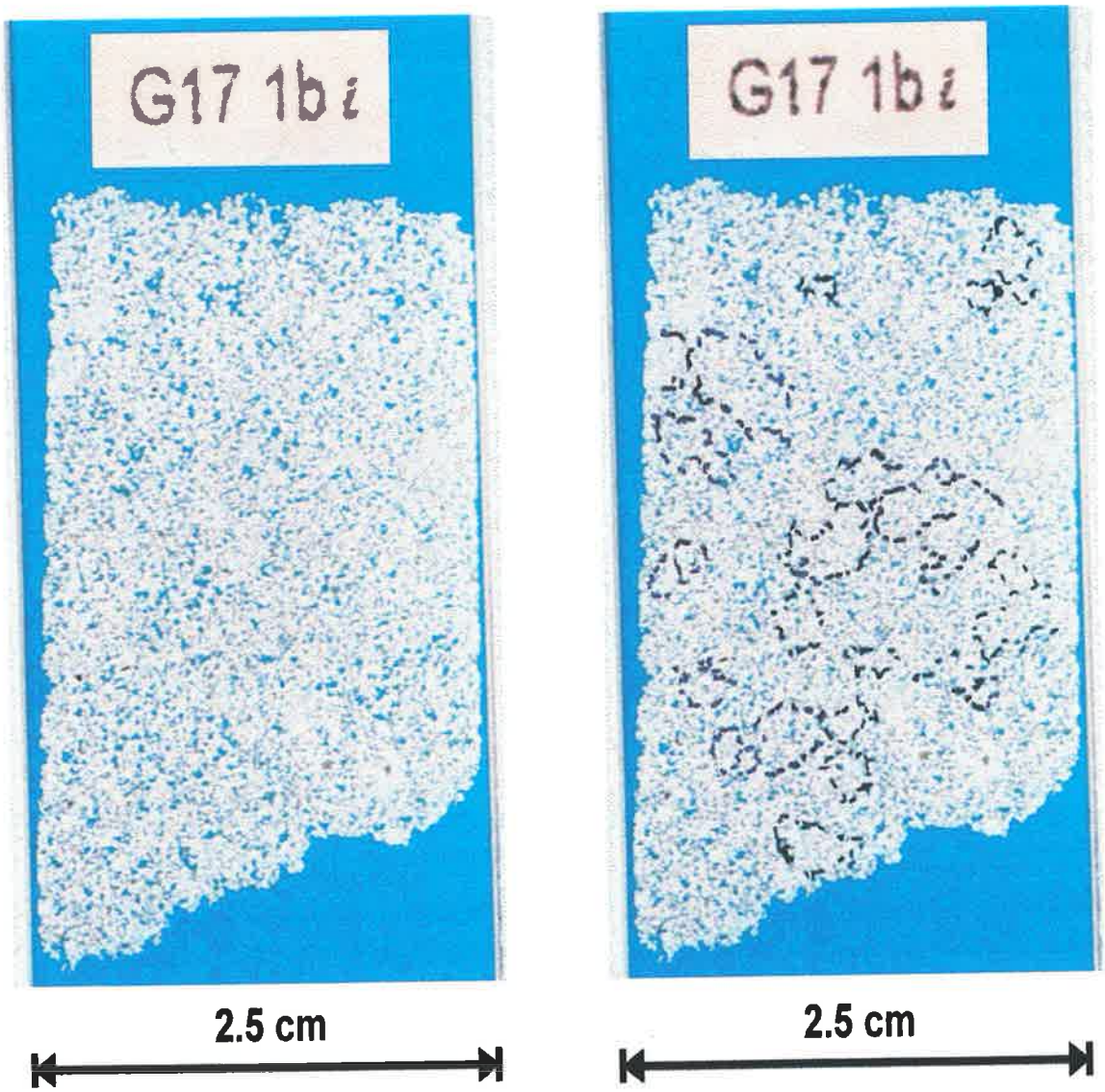

Figure 6.16: Thin section G17 1bi and the interpretation of concretions. These are also clustered throughout, however also appear to be coalescing in the central part of the thin section.

The concretions within the Hutton Sandstone range in size from 10 grains (Figures 6.17 (a-b)), to 40 grains (Figures 6.18 (a-b), and 6.19 (a-b)), although often there can be more. Larger concretions may not yet have formed to a level of cementation that makes them recognisable. Concretion size is limited by the availability of silica in the system, and the system is larger than the thin sections that have been studied.

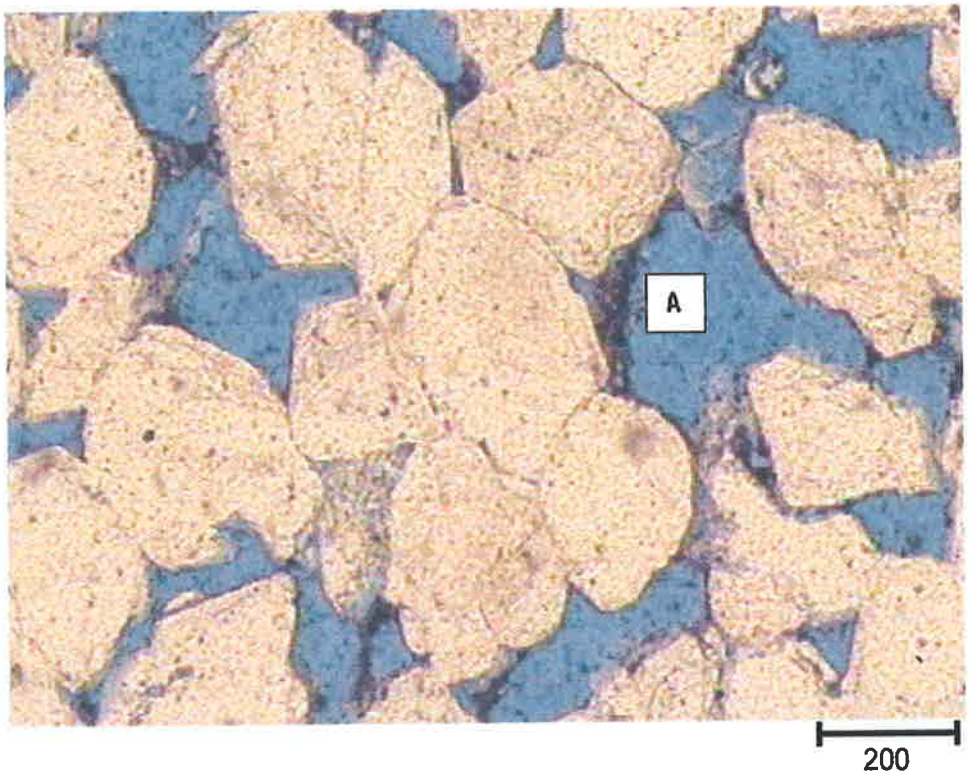

Figure 6.17 (a): Thin section G17 1ai. Small concretion defined by large primary pores and secondary pore from dissolution of feldspar (A) (5x-mag, scale bar in microns)

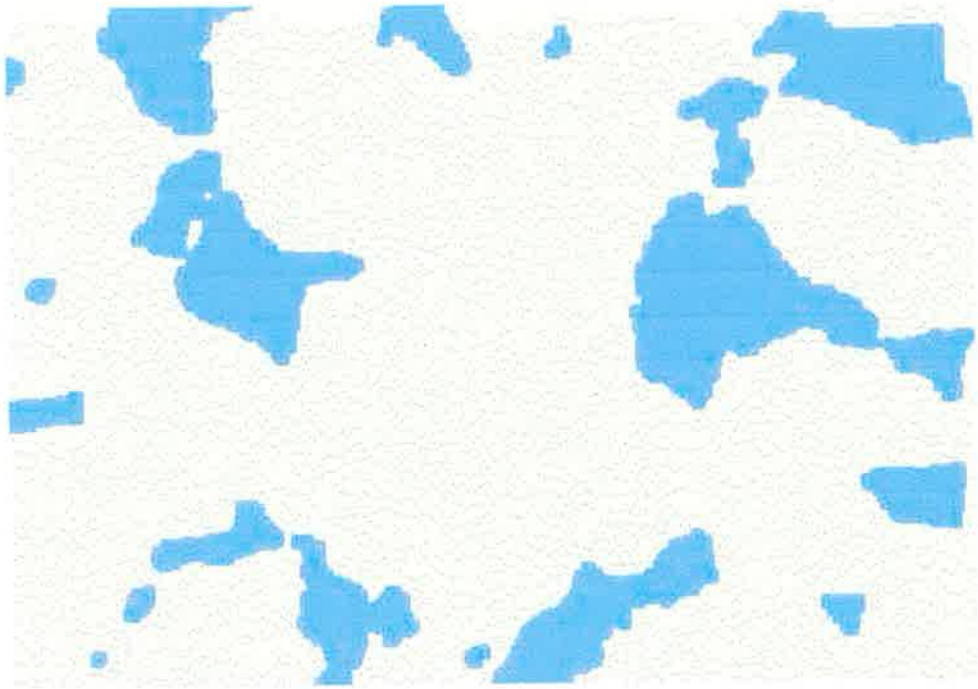

Plate 6.17 (b): Binary overlay from thin section G17 1ai. The overlay was produced by a succession of erosion and dilation iterations to purposefully eliminate the smallest pores. There is also evidence of secondary porosity forming from the dissolution of feldspar (A).

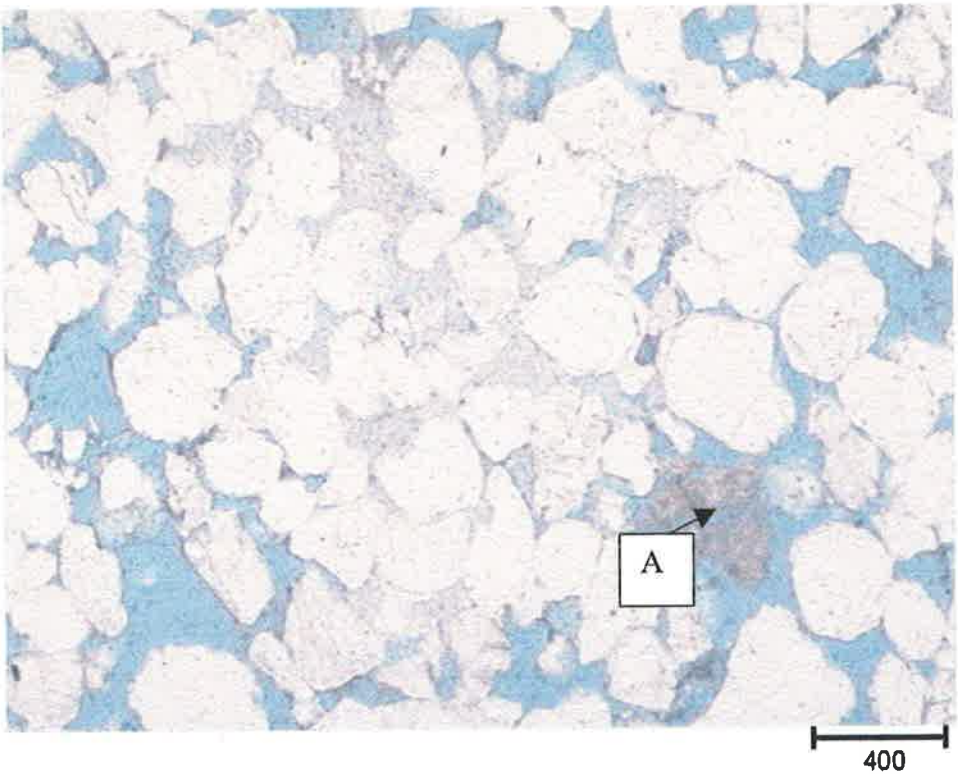

Figure 6.18 (a): Thin section G17 1fii: Dissolution of feldspar is evident (A) along with abundant kaolinite and quartz cement forming the concretion, being surrounded by large pores (2x-mag, scale bar in microns and applies to the overlay below).

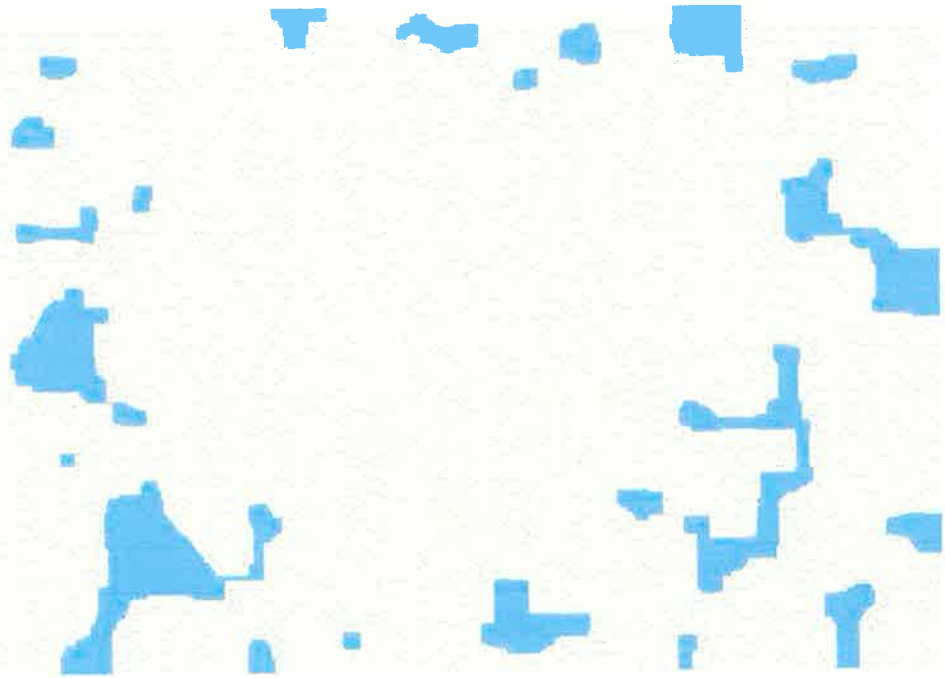

Figure 6.18 (b): G17 1fii binary overlay - the large pores surround the concretion. Image produced by erosion-dilation to eliminate the smallest pores.

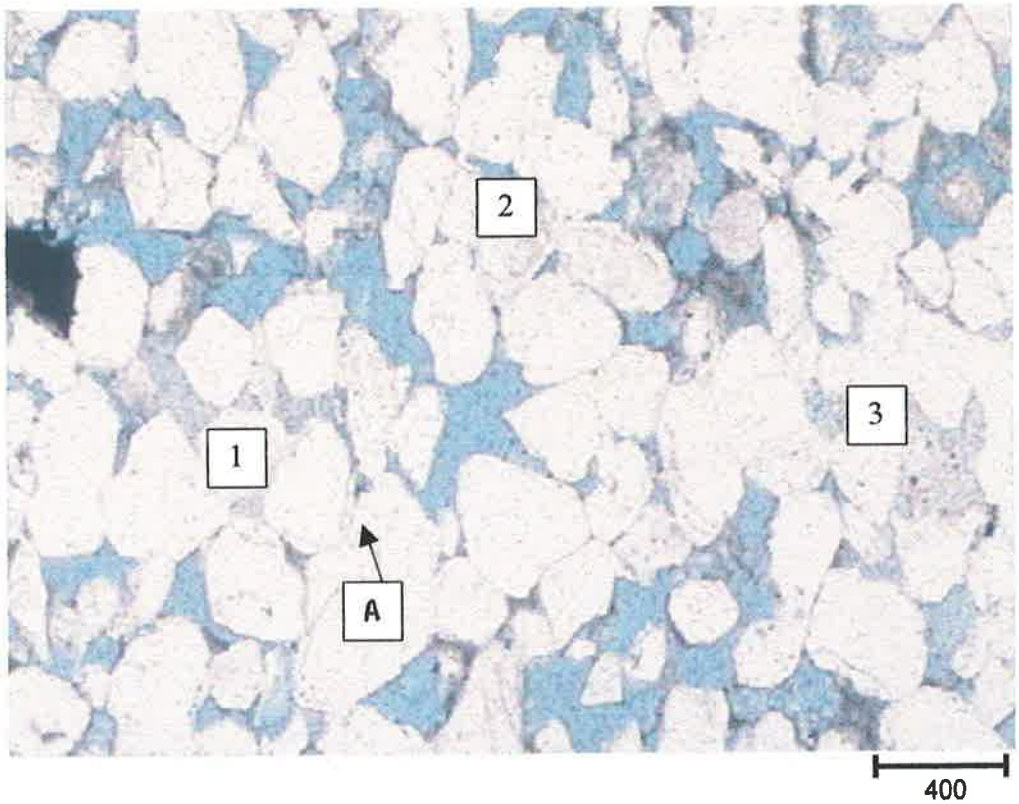

Figure 6.19 (a): Thin section G17 1a-lower. Three clusters are interpreted (1-3), surrounded by the large primary pores. Note the thick quartz cement overgrowths (A). (2x-mag, scale bar in microns and applies to the overlay below).

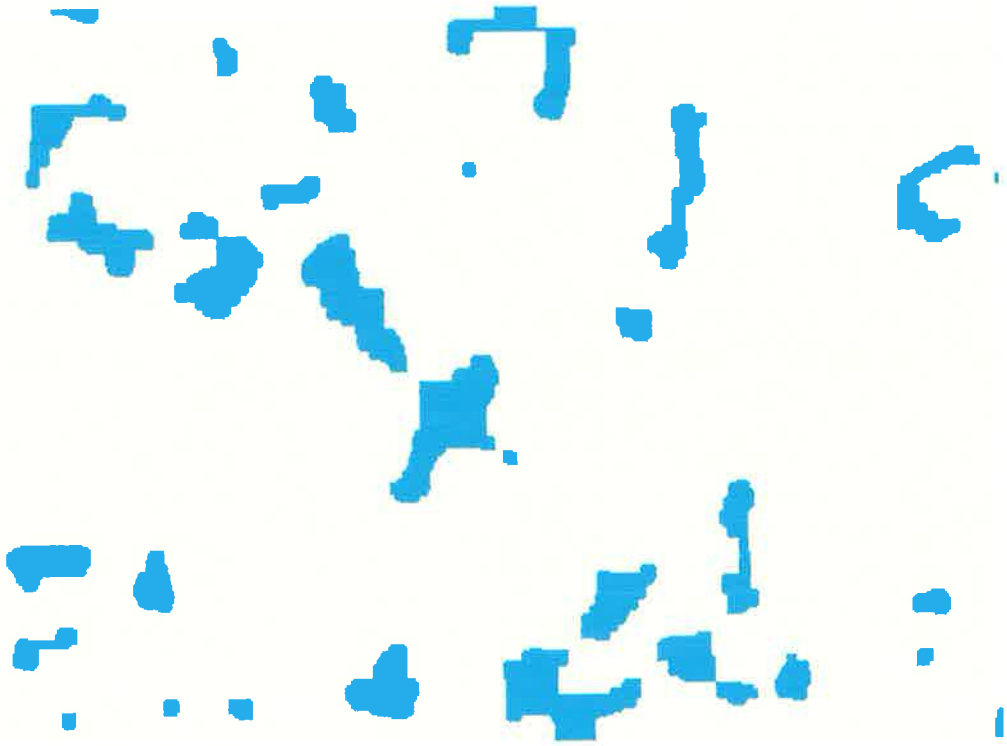

Figure 6.19 (b): Thin section G17 1a-lower binary overlay. Elimination of the smallest pores allows larger pores to highlight the three concretions.

To examine concretions that are bigger than the 2x-magnification field of view (seen in Figures 6.17 and 6.19 above), four separate adjacent micrographs and their corresponding overlays were combined and produced as a single image (Figure 6.20 (a-b)).

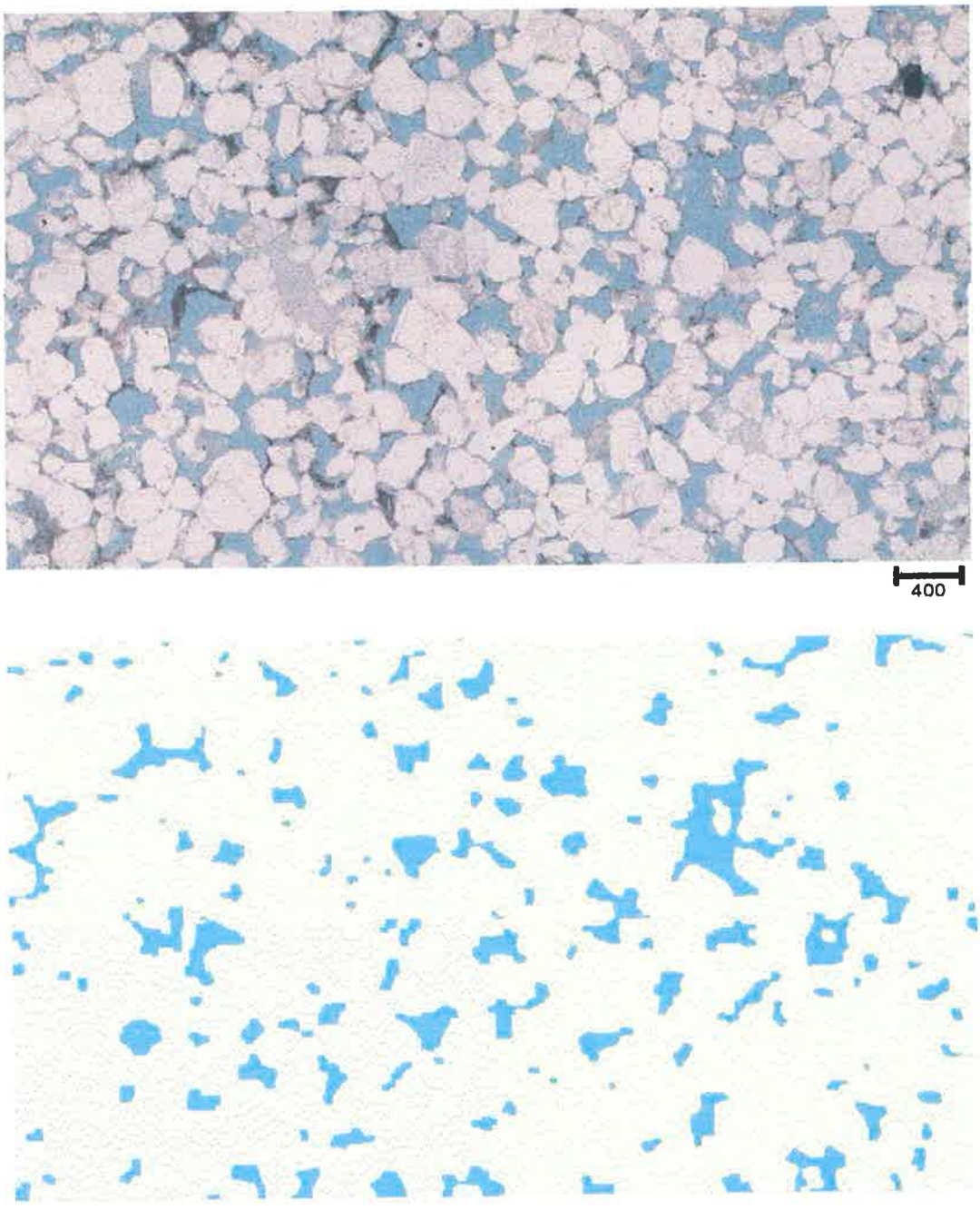

Figure 6.20 (a): Four separate adjoining images collected using the 2x-magnification objective were joined to investigate the possibility of existence of large concretions (scale bar in microns).

Figure 6.20 (b): The binary overlay produced by erosion-dilation iterations to remove the smallest pores shows that there are no large concretions in this field of view.

The erosion-dilation procedure was used to produce the overlays to highlight the larger pores that affect the connectivity within the rock and hence control the fluid flow. The erosion processing procedure is an operation that strips the outermost layer of pixels from pores, while dilation is a process that adds a layer of pixels to a pore. Erosion followed by dilation does not necessarily restore the object to its original shape (Duda & Hart, 1973), but the difference in the number of pixels before and after a cycle of erosion and dilation represents the amount of small-scale roughness elements on pores. If erosion-dilation cycles progress (three erosions followed by three dilations, etc.), the pore is progressively smoothed until a large number of successive erosions exceeds the width of the pore, which is then destroyed without any 'seed' upon which an ensuing dilation can operate.

The erosion-dilation procedure allowed overlays to be produced with small pores removed to leave the shape and distribution of the large primary pores.

6.3.1 Possible mechanisms for creation of concretions:

There are two possible mechanisms related to the likely sources of silica to explain why concretions form.

a) The first mechanism assumes concretions form in a closed or internal system. In this situation, ions are dissolved into the formation water and they must then be redistributed elsewhere nearby. When a feldspar grain within the rock undergoes dissolution, the ions released in this reaction are redistributed forming some kaolinite, while the remaining silica is redistributed as quartz cement. The clustering often forms around an area where there is a partially dissolved feldspar grain or areas of tightly packed kaolinite.

b) The alternative mechanism assumes an open or external system. In this system, the sources of silica within the formation waters are a result of reactions that occurred in other areas, possibly in surrounding mudrocks. Concretions forming in this system are likely to be a result of a limited number of poorly understood nucleation sites.

Whilst the formation of nucleation sites within a rock is poorly understood, the theory of nucleation sites suggests that the excess silica is focussed on a particular area. Depending on the availability of silica, as the site develops, increasingly more silica is drawn towards it. The factors that control the nucleation sites may be grain composition, grain size, degree of strain inherent in the quartz grains or simply random formation. Given the association of silica cement and kaolin, the closed system is the favoured mechanism for the Hutton Sandstone.

Gluyas *et al.,* (2000) discovered that the Kimmeridge Clay Formation (Miller Field, UK Continental Shelf) was capable of delivering an average of 6% quartz cement to the interbedded Brae Formation Sandstone in a period of less than 20 million years. It was determined that on average, the transport distance for the silica was little more than one metre.

It is suggested the siltstones within the Hutton Sandstone samples have contributed silica to the system, which then precipitated where nucleation sites had already been established.

6.4 IMPLICATIONS OF CONCRETIONS

It is suggested that development of a semi-variogram based on porosity distribution was unsuccessful because of **a)** the spherical arrangement of large pores around concretions along with **b)** the large field of views used in the PIA.

Kriging is a technique that studies data in a linear fashion, but it is suggested the main pores are arranged spherically. While the spherical arrangement of pores may not be the main reason kriging was unsuccessful, it is a contributing factor. The largest pores are immediately adjacent to the most tightly cemented zones, thereby enhancing the nuggett effect (lack of correlation) observed in the semi-variograms.

The concretionary nature of the cement is likely to play an important role in the fluid storage. Oil or gas is partitioned within the rock between the large intergranular porosity (primary porosity), small intergranular porosity and porosity associated with kaolinite (microporosity). Fluid flow however, is controlled by connectivity of the large pores, especially if these pores are linked throughout the entire rock framework. Permeability will be good where pore connectivity is high.

Chapter 7 SUMMARY AND CONCLUSIONS

Reservoir quality in a sandstone buried to any degree is controlled by three factors.

i. The depositional porosity and permeability, which are strongly influenced by sorting, grain size, grain morphology and the sand/mud matrix ratio,

ii. The degree of mechanical and chemical compaction; and

iii. The amount and type of pore-filling cement (Worden & Morad, 2000).

The primary aim of this study was to investigate the use of PIA in reservoir rock characterisation. There were three components of the study essentially covering part **(i)** and **(iii)** above. The first of these was to use PIA to determine the porosity distribution of the Hutton Sandstone on a microscale, ultimately, providing a set of rules for the use of PIA to effectively measure porosity using an optimum magnification and number of fields of view. The second was to determine whether a sub-set of porosity measurements could be collected which fully describe the porosity distribution and to determine the minimum number of readings required to accurately quantify porosity in thin section. The final aspect of the study (covering part **(iii)**) was to then investigate and try to understand how quartz cement is distributed in the rock.

The results of the investigation suggest PIA is particularly useful in porosity determination, especially when compared to the point counting procedure because it is less time consuming and PIA can provide multiple calculations of porosity and mineralogy per thin section, whilst point counting only provides one value of these. Also, the results suggest features such as silty layers may be recognised using PIA, provided enough readings are taken across the thin section. It is likely that the porosity distribution within these Hutton Sandstone samples was spread too evenly to recognise these features any better.

Despite the common perception that the Hutton Sandstone acts like a "homogeneous tank" (Hamilton *et al.,* 1998), it soon became apparent that the samples used in this study are in fact heterogeneous at a microscale and not homogeneous. Therefore, a problem exists with using CT-scanning to characterise a reservoir because the sample

size used is small and the results obtained would need to be placed in context of a larger reservoir interval. A major advantage of PIA is that it ties porosity distribution directly to the factors that control it. These controlling factors include grain size, grain sorting, cement type, cement distribution, clay morphology and clay distribution. Compared to micro-CT scanning, PIA is a cost effective and readily available technique to perform, whereas the CT technique is expensive and the equipment required is not readily available.

As mentioned, data obtained during the investigation suggested that PIA could be used to tentatively identify banding in thin section provided enough readings are taken to obtain full coverage of the thin section. By taking only three-strip data there was too great a chance that factors directly controlling porosity would not be recognised, however, when full coverage data was obtained at 5x-magnification, the features became more identifiable.

When the output display was altered, the patchiness within the porosity became more apparent. This patchiness was a reason why development of spatial correlation models did not work. The slight nearest neighbour correlation resulted from the patches of high and low porosity, however the data predominantly alternated from patches of high porosity to patches of low to very low porosity, exhibiting very little gradation between porosity units, expected if there was correlation. The patchiness is interpreted as being a result of the concretionary nature of the sandstone caused by the distribution of silica cement and kaolinite.

The results also indicated that whilst PIA is particularly good for porosity and mineralogy estimation, it is a technique deficient for accurate estimation of the amount of quartz cement in the rock. This was due to the software's inability to distinguish between the quartz overgrowths and the primary quartz grains, which are the same colour.

To overcome this deficiency, it is suggested that a digital image of a CL micrograph be loaded into the image analysis system, thus allowing for accurate assessment of the quartz cement by means of an overlay.

When using PIA, it was found that magnification had a direct effect on the porosity estimate. At higher magnifications, porosity tends to be under-estimated compared to lower magnifications. This is a direct result of operator error. At higher magnifications, the operator can distinguish grain boundaries more clearly. The disadvantage with choosing a high magnification far outweighs the advantage, because the porosity calculation estimate is conducted over a small area and thus may not be reflective of the overall porosity of the sample. More readings would be required to estimate porosity accurately using a high magnification (eg.50x) compared with a lower magnification (eg.5x).

It was shown by using a random number generator that to estimate porosity from only 10 readings at 5x-magnification, there is a low chance of obtaining an average porosity that is accurate. To produce an accurate average porosity reading using PIA in thin section it is recommended that, at 5x-magnification, between 30 and 40 readings be taken, thus ensuring that the standard deviation be within 1 unit from the 'true' porosity of the thin section.

Statistical analysis established that there was very little correlation within the porosity data obtained from PIA. Only the nearest neighbour porosity readings showed some correlation and even this correlation was very weak. The reason for this became apparent when the data were redisplayed using a different colour scale, which emphasised patchiness observed within the data. There was a lack of apparent gradation between the different porosity units, suggesting little correlation between neighbouring data points.

Therefore, kriging would not be required to interpolate between a reduced data set. Upscaling porosity data from the Hutton Sandstone is achievable. The method of upscaling suggests that, using PIA at 5x-magnification, between 30 to 40 porosity readings be obtained (providing a range of values), the pore sizes calculated, and then a random number generator used to conduct the upscaling. This information could be used as input into a reservoir model for reservoir simulation.

By calculating porosity across an area, PIA did not allow semi-variograms to become well defined at short lags. Changing magnification (thereby changing the size of the field of view) only changed the distance moved between neighbouring fields of view. This distance (whilst smaller when at a higher magnification) still only equated to a lag of one, therefore it was impossible to define the semi-variograms at shorter lags. A 'fractal-like' nature was observed for the porosity data in these samples of Hutton Sandstone as the semi-variograms shared the same shape and were produced from different magnifications.

The 5x-magnification display data indicated it was likely that the lower porosity areas were a result of silt layering or clustering of grains cemented with quartz cement. This, the third aspect of the study, was done visually by using PIA to highlight the areas of quartz, quartz cement and kaolinite, and by highlighting the inverse of these, the porosity. It was discovered that by focussing on the primary pores, the seemingly homogeneous quartz arenite was in fact composed of cement concretions, often clustered throughout the samples, similar to cement concretions identified in the Carizzo Sandstone. The degree of clustering in the Hutton Sandstone, however, is much lower.

Circumstantial evidence points to feldspar alteration and dissolution as the source of silica cement in the Hutton Sandstone with extra silica possibly sourced from the shales that are interbedded within the reservoir rock.

Worden and Morad (2000) concluded that silica for quartz cement has no single source that can be universally predicted in sandstones. It can be sourced on a sandbody-scale by feldspar alteration reactions, pressure dissolution at grain contacts and in stylolites, dissolution of biogenic silica and volcanic fragments and from the illitization of smectite. In principle, silica may also be sourced externally to the sandstone, including mudrock-related sources, silica transported from deep in the basin or other external sources (Worden & Morad, 2000).

Pore size histograms highlighted the average pore size within the samples, but for the purposes of this study, attention was focused on the number of larger pores because these are the primary pores that surround the cement clusters and hence strongly influence permeability.

MICP was particularly valuable because it a) provided another technique which calculated porosity, enabling a comparison and check to be made with the other techniques, b) it allowed calculation of recovery efficiency, placing a value on the reservoir quality and c) it produced distribution charts of the pore throat sizes.

Pore cast analysis provided information that was supported by MICP, but is a technique that is limited in its use because it only supplies pore throat data (which was obtained more accurately from MICP). It does however, provide a good visual aid in the study of the pore interconnectivity, particularly the 3D images produced using the stereoscope function within the SEM program which allowed calculation of reservoir parameters such as the aspect ratio and the coordination number which is valuable when assessing reservoir potential.

This study showed that the Hutton Sandstone should not just be considered as a series of sand-sized grains separating intergranular pores, but as a series of concretions separating interconnected porous zones.

Petrographic Image Analysis (PIA) proved particularly useful in determining the parameters for statistical analysis for the simple mineralogies displayed in the samples from the Hutton Sandstone. It may well be that more complex mineralogies, perhaps involving lithic rock fragments, might not allow sufficient discrimination using PIA to subdivide the framework grains from the porosity or cement. This study concentrated on establishing techniques for statistical study of data collected by PIA and used ideal samples as the base of the study. I suggest that further work could be done on a suite of more complex samples to establish if PIA is more universally applicable.

7.1 INTEGRATION WITH RESERVOIR SIMULATION

A simulation study requires a description of the reservoir's rock and fluid properties, validation of completion and production history, and extensive history matching (matching historical performance) to validate and modify these data. When history matching is complete, numerous predictions of field and well performance characteristics are calculated for various development scenarios (Laudeman, 1992).

A simulation study begins with the selection of a model type. A grid is then used which determines the resolution at which complex reservoir flow equations are solved. In general, the accuracy of results from simulation studies is greater for smaller grid block sizes because smaller grid blocks permit more detailed descriptions of reservoir heterogeneity (Laudeman, 1992).

The population of a matrix of cells to simulate the production from a hydrocarbon reservoir requires information on porosity and permeability and the distribution of those factors.

The reservoir characterisation required defining porosity and permeability for each grid block in a reservoir simulation model is stringent. Porosity and permeability data are strongly influenced by sorting, grain size, grain morphology and the sand/mud matrix ratio, the degree of mechanical and chemical compaction undergone by the reservoir and the amount and type of pore-filling cement within it (Worden & Morad, 2000). These data are supplied by the techniques used in this study (listed in Table 7.1) while the table also assesses the value of each.

TECHNIQUE	DATA	STRENGTH	LIMITATION	VALUE
PIA	Rock average porosity, mineralogy, Grain size and Pore size, diagenetic history	Speed to acquire information	Accuracy: Cement analysis, over/underestimation of parameters	Essential
POINT COUNTING	Rock porosity, mineralogy	Accuracy, magnification, 2D	Time costly	Non-essential
RCA	Rock porosity and permeability	ambient & overburden data	n/a	Essential
MICP	Pore throat sizes, recovery efficiency, Threshold pressure (Pd)	Results obtained from 3D piece of core	Destructive	Essential
SEM	Cements, cement distribution, pore surface complexities	High-magnification	availability	Essential
CL	Cements, diagenetic history	Focuses on cement		Essential for study of diagenesis
PORE CASTS	Pore geometry, aspect ratio, coordination number	Visual aid - partial 3D	Only surface readings, need SEM to view	Non-essential
PHOTOGRAPHY/ MICROGRAPHS	Images of mineral porosity relationships	n/a	n/a	Essential for all characterisation studies
MICRO CT-SCANNING	Pore geometry, permeability simulation	Accuracy, studying in 3D, non-destructive	Expensive, availability	Essential

Table 7.1: Shows various techniques used in the study which calculate, or help calculate porosity for rock characterisation, incorporated in reservoir model for simulation. The value column is a personal assessment of each technique based on the usefulness in this study.

7.2 TECHNIQUES:

1) Petrographic Image Analysis (PIA) is a fast, easy to operate technique that uses thin sections to obtain multiple average rock porosity and mineralogy readings, along with information on the rock grain and pore throat distributions. This information is likely to be more representative of the reservoir since it has greater potential of being obtained from across more of the reservoir rock. The drawback to PIA is the information obtained is only obtained from two dimensions (2D).

2) Point counting is another technique used to obtain porosity and mineralogy, however is time costly and provides only one measurement of each, making it an outdated technique which is no-longer considered essential in reservoir characterisation studies.

3) Routine core analysis (RCA) is an essential part of reservoir characterisation because porosity and permeability is obtained at both overburden and ambient conditions. A large piece of core is most likely to be representative of the reservoir, and it then provides the material for other techniques to be performed, allowing further analysis of the rock.

4) Mercury injection capillary pressure (MICP) provides information on the pore throats, along with a method of calculating reservoir recovery efficiency. This is particularly useful in simulation studies that are designed to estimate field production. The information from MICP is obtained from a 3D piece of the core, which means the results are more likely to be representative of the reservoir, because the internal area of the rock (not visible to the human eye) is being examined. The drawback to MICP is the use of mercury, which means it is a destructive technique rendering the rock unusable following analysis.

5) Scanning electron microscopy (SEM) is a high magnification, essential microscope technique required to acquire information used for reservoir characterisation studies regarding rock cement and cement distribution, while it is also useful in obtaining

information regarding rock surface complexities. SEM is the only tool with sufficient magnification to look into the pore spaces to describe the cement "decoration" within.

6) Cathodoluminescence (CL) is an essential technique in reservoir characterisation because, while it doesn't provide direct information on porosity and permeability, it does provide information on the controls of these by identifying the cements within the rock, which are then used to determine the diagenetic history. PIA, used in conjunction with CL can then be used to determine the cement distribution, highlighting areas of high or low porosity, influencing rock permeability.

7) Pore casting is a technique providing information on the pore geometry of the reservoir. This is essential for simulation studies, but the same information can be obtained from MICP, and the results from MICP are not subjected to the same operator bias present with pore casting. Due to this, and because the data obtained are only from the surface of the sample, it is considered not essential for characterisation or simulation studies. Nonetheless, used in conjunction with SEM, it can provide a useful visual aid for looking at the rock pore structure.

8) Photography and photomicrographs are essential tools used for reservoir characterisation studies, providing visual records of features such as mineral grain relationships.

9) Micro-CT scanning is a new tool used to study the pore geometry of the reservoir and then estimate permeability. The data are very accurate, obtained in three dimensions and the technique is non-destructive, making it particularly useful for simulation studies. The capability of CT to detect microfractures and to determine gas storage quantitatively makes the CT scanner tremendously important for evaluating gas reservoirs (Watson & Mudra, 1994). Unfortunately, the drawbacks include its expensive, its lack of ready availability and the sample size. The technique can only obtain data from a very small piece of rock ($<0.5cm^3$), which is not very representative of the reservoir since reservoirs can exhibit great variation across small distances.

It is important to recognise that the reservoir model in simulation studies can often be defined and then redefined by the simulation engineer because the simulator is only a set of numbers reduced to cells with groups of mathematical operators that manipulate these numbers to describe fluid flow. However, even despite the apparent plausibility of the engineers' final interpretation used to develop the model, the ultimate test of the simulation model's validity is in its reproduction of the production data (Laudeman, 1992).

REFERENCES

Boult, P. J. 1996. An investigation of reservoir/seal couplets in the Eromanga Basin; implications for petroleum entrapment & production. Development of secondary migration & seal potential theory & investigation techniques. Unpublished PhD thesis, University of South Australia.

Chambers, R. L., Yarus, J. M. & Hird, K. B. 2000. Petroleum geostatistics for nongeostaticians. *The Leading Edge*(Part 2), 592 - 599.

Duda, R. O. & Hart, P. E. 1973. *Pattern classification and scene analysis*. John Wiley, New York.

Ebanks Jr., W. J., Scheihing, M. H. & Atkinson, C. D. 1992. Flow units for reservoir characterisation. In: *Development Geology Reference Manual* (edited by Morton-Thompson, D. & Woods, A. M.) **10**. AAPG Methods in Exploration Series, Oklahoma.

Ehrlich, R. & Davis, D. K. 1989. Image analysis of pore geometry; relationship to reservoir engineering and modelling. *SPE*, 19 - 54.

Ehrlich, R., Kennedy, S. K., Crabtree, S. J. & Cannon, R. L. 1984. Petrographic image analysis 1: Analysis of reservoir pore complexes. *Journal of Sedimentary Petrology* **54**, 1365 - 1378.

Enos, J. S. & Kyle, J. R. 1998. Diagenesis of the Carizzo Sandstone at Butler Salt Dome, East Texas Basin: Evidence for the fluid-sediment interaction near halokinetic structures. *Journal of Sedimentary Research*.

Forbes, B. G. & Preiss, W. V. 1987. Stratigraphy of the Wilpena Group. In: *The Adelaide Geosyncline* (edited by Drexel, J. F.) **Bulletin 53**. Department of Mines and Energy, Adelaide.

Fothergill, C. A. 1955. The cementation of oil reservoir sands and its origin. In: *Proc. 4th World Petroleum Conference*, Rome, 301 - 314.

Giles, M. R., Indrelid, S. L., Beynon, G. V. & Amthor, J. 2000. *The origin of large-scale quartz cementation: evidence from large data sets and coupled heat-fluid mass transport modelling*. Blackwell Science.

Gluyas, J., Garland, C., Oxtoby, N. H. & Hogg, A. J. C. 2000. *Quartz cement: The Miller's Tale*. Blackwell Science.

Gravestock, D. I. & Hibburt, J. 1991. Sequence stratigraphy of the eastern Officer and Arrowie basins: a framework for cambrian oil search. *APEA Journal* **31**, 177 - 190.

Hamilton, D. S., Philip Ryles, M. H. H., Lonergan, T. & Hillyer, M. 1998. Approaches to identifying reservoir heterogeneity and reserve growth opportunities in a continental-scale bed-load fluvial system: Hutton Sandstone, Jackson field, Australia. *AAPG Bulletin* **82**(12), 2192 - 2219.

Harris, D. G. 1975. The role of geology in reservoir simulation studies. *Journal of Petroleum Technology*, 625 - 632.

Hawkins, P. J. 1978. Relationship between diagenesis, porosity reduction, and oil emplacement in late Carboniferous sandstone reservoirs, Bothamsall Oilfield, E. Midlands. *Geological Society of London Journal* **135**, 7 - 24.

Heald, M. T. 1955. Stylolites in sandstones. *Journal of Geology* **63**, 101 - 114.

Hendry, J. P. & Trewin, N. H. 1995. Authigenic quartz microfabrics in Cretaceous turbidites: evidence for silica transformation processes in sandstones. *Journal of Sedimentary Research* **65**, 380 - 392.

Hogg, A. J. C., Pearson, M. J., Fallick, A. E. & Hamilton, P. J. 1995. An integrated thermal and isotopic study of the diagenesis of the Brent Group, Alwyn-South, UK North Sea. *Applied Geochemistry* **10**, 531 - 540.

Hurst, A. & Nadeau, P. H. 1995. Clay microporosity in reservoir sandstones: an application of Quantitative Electron Microscopy in petrophysical evaluation. *AAPG Bulletin* **79**(4), 563 - 573.

Jenkyns, H. C. 1974. Origin of red nodular limestones (Ammonitico Rosso, Knollenkalke) in the Mediterranean Jurassic: a diagenetic model. In: *Pelagic sediments: on land and under the sea* (edited by Hsu, K. J. & Jenkyns, H. C.) **1**. Blackwell Scientific publications, Oxford, 249 - 271.

Kantsler, A. J., Prudence, T. J. C., Cook, A. C. & Zwigulis, M. 1983. Hydrocarbon habitat of the Cooper/Eromanga Basin, Australia. *APEA Journal* **23**, 75 - 92.

Kyle, J. R. 1995. Mineral resources of the gulf coast salt dome province. In: *Selected mineral deposits of the gulf coast and southeastern united states* (edited by Thompson, T. B.) **24**.

Land, L. S. & Milliken, K. L. 2000. *Regional loss of SiO2 and CaC03, and gain of K20 during burial diagenesis of Gulf Coast mudrocks, USA*. Blackwell Science.

Laudeman, S. K. 1992. Conducting a reservoir simulation study: an overview. In: *Development Geology Reference manual* (edited by Thompson, D. M. & Woods, A. M.) **10**. AAPG, Oklahoma.

McBride, E. F. 1989. Quartz cement in sandstones: A review. *Earth Science Review* **26**, 69 - 112.

McCreesh, C. A., Ehrlich, R. & Crabtree, S. J. 1991. Petrography and reservoir physics 2: Relating thin section porosity to capillary pressure, the association between pore types and throat size. *AAPG Bulletin* **75**(10), 1563 - 1578.

Mcmanus, J. 1988. Grain size determination and interpretation. In: *Techniques in sedimentology* (edited by Tucker, M.). Blackwell Scientific publications, Oxford.

Miller, J. 1988. Cathodoluminescence Microscopy. In: *Techniques in sedimentology* (edited by Tucker, M.). Blackwell Scientific Publications, Oxford, 174 - 190.

Moore, P. S., Pitt, G. M. & Dettman, M. E. 1986. *The early Cretaceous Coorikiana Sandstone and Toolebuc Formation: their recognition and stratigraphic relationship in the Southwestern Eromanga basin.* Geological Society of Australia, Special Publication.

Morad, S. & Aldahan, A. A. 1987 . Diagenetic replacement of feldspars by quartz in sandstones. *Journal of Sedimentary Petrology* **57**, 488 - 493.

Muller, J. & Fabricus, F. 1974. Magnesian-calcite nodules in the Ionian deep sea: an actualistic model for the formation of some nodular limestones. In: *Pelagic sediments: on land and under the sea* (edited by Hsu, K. J. & Jenkyns, H. C.) **1**. Blackwell Scientific publications, Oxford, 235 - 247.

Neasham, J. W. 1977. Application of scanning electron microscopy to the characterisation of hydrocarbon-bearing rocks. *Scanning Electron Microscopy* **1**, 523 - 552.

Posey, H. H., and Kyle, J.R, 1988, Fluid-rock interactions in the salt dome environment: an introduction and review : Chem. Geol., v. 74, p. 1-24

Oelkers, E. H., Bjørkum, P. A. & Murphy, W. M. 1996. A petrographic and computational investigation of quartz cementation and porosity reduction in North Sea sandstones. *American Journal of Science* **296**, 420 - 452.

Pittman, E. D. & Duschatko, R. W. 1970. Use of pore casts and scanning electron microscope to study pore geometry. *Journal of Sedimentary Petrology* **40**(4), 1153 - 1157.

Pittman, E. D. & Thomas, J. B. 1978. Some applications of scanning electron microscopy to the study of reservoir rock. *Paper Society of Petroleum Engineers*.

Prince, C. M. & Ehrlich, R. 2000. *A test of hypotheses regarding quartz cementation in sandstones: a quantitative image analysis approach*. Blackwell Science.

Purcell, W. R. 1949. Capillary pressure - their measurement using mercury and the calculation of permeability therefrom. *AIME Petroleum Transactions*, 39 - 48.

Reeves, F. 1947. Geology of the Roma district, Queensland, Australia. *AAPG Bulletin*, 1341 - 1371.

Rezaee, M. R. & Lemon, N. M. 1997. Estimation of effective porosity, Tirrawarra Sandstone, Cooper Basin, Australia. *Exploration Geophysics* **28**, 114 - 118.

Ruzyla, K. 1986. Characterisation of pore space by quantitative image analysis. *Society of Petroleum Engineers Formation Evaluation* **1**, 389 - 398.

Schulz-Rojhan, J. P. & Phillips, S. E. 1989. Diagenetic alteration of Permian reservoir sandstones in the Nappamerri Trough and adjacent areas, southern Cooper Basin. In: *The Cooper and Eromanga Basins, Australia* (edited by O'Neil, B. J.). Proceedings PESA/SPE/ASEG conference, Adelaide, 629 - 645.

Schumm, S. A. 1977. *The fluvial system*. Wiley, New York.

Siever, R. 1957. Pennsylvanian Sandstones of the Eastern Interior Coal Basin. *Journal of Sedimentary Petrology* **27**, 227 - 250.

Stephan, H. J. 1970. Diagenesis of the Middle Bunt sandstein in South Oldenburg, Lower Saxony: Meyniana. **20**, 39 - 82.

Trewin, N. H. 1991. Use of scanning electron microscope in sedimentology. In: *Techniques in sedimentology* (edited by Tucker, M.). Blackwell Scientific publications, 229 - 273.

Waldschmidt, W. A. 1941. Cementation materials in sandstones and their influence on the migration of oil. *Am. Assoc. Petrol. Geol. Bull.* **25**, 1839 - 1879.

Wardlaw, N. C. 1976. Pore geometry of carbonate rocks as revealed by pore casts and capillary pressure. *AAPG Bulletin* **60**(2), 245 - 257.

Watson, A. T. & Mudra, J. 1994. Characterisation of Devonian Shales with x-ray computed tomography. *Society of Petroleum Engineers Formation Evaluation* **9**, 209 - 212.

Watts, N. L. 1987. The Hutton Sandstone - Birkhead Formation transition, ATP 269, Eromanga Basin. *APEA Journal*, 215 - 228.

Weber, K. 1992. Reservoir modelling for simulation purposes. In: *Development Geology Reference Manual* (edited by Thompson, D. M. & Woods, A. M.) **10**. AAPG, Oklahoma, 531 - 540.

Wellington, S. L. & Vinegar, H. J. 1987. X-ray computerized tomography. *Journal Petroleum Technology* **39**, 885 - 930.

Wiltshire, M. J. 1989. Mesozoic stratigraphy and palaeogeography, Eastern Australia. In: *The Cooper and Eromanga Basins, Australia* (edited by O'Neil, B. J.). Proceedings of PESA, SPE, ASEG (SA Branches), Adelaide, 279 - 291.

Worden, R. H. & Morad, S. 2000. Quartz cementation in oil field sandstones: A review of the key controversies. *International Association of Sedimentologists* **29**, 1 - 20.

APPENDIX 1
GRSORT THEORY

Notes on the program GRSORT.

WHAT IS GRSORT

GRSORT converts the grainsize distribution obtained from thin sections, into the distribution actually seen in the grains. The reason for the difference between the two distributions is that the grains in the thin section are cut at random points in along their axis, and not at their maximum thickness.

THEORYGRSORT assumes all grains are spherical. Whilst this is undoubtedly a poor assumption, the actually statistics and mathematics for non-spherical grains are going to be very close to those for the spherical grains, so the overall effect will be minimal.

Consider a spherical grain. In figure 1 we see three lines A-A', B-B' and C-C'.

Imagine these lines to be cuts through the grain in an axis perpendicular to the page. If the sphere has a diameter of 1 unit, then A-A' would give a grainsize diameter of dA=1 unit, B-B' would return a value of approx dB=0.9 units and C-C' a diameter of dC=0.45 units.

You will notice that a cut resulting in a diameter of x can only occur at a certain distance from the centre of the grain. For simplicity sakes we will call this distance y. The relationship between the two is the equation for a circle.

(1) $(x/2)^2 + y^2 = (1/2)^2$

So for the line B-B' the cut would occur at a distance

$y=\text{sqrt}(1/4 - (0.9/2)^2) =\text{sqrt}(0.0475) =.2179$ units from the centre of the sphere

Imagine now that we had an infinite number of grains of equal size that were all cut at a random point along their axis (just as you would do when cutting a thin section). The percentage of the grain sizes with a cross section diameter occurring between a range of d1 and d2 where d1>d2 is

(2) P(d1-d2) = (distance d2 from centre - distance d1 from centre)/radius

$= (\text{sqrt}(r^2-(d2/2)^2) - \text{sqrt}(r^2-(d1/2)^2))/r$

where r is the radius of the grains.

So for our grain of diameter 1 (r=0.5), equation (2) gives the percentage of grains between B-B' and C-C' would be

$P(B-C)=(\text{sqrt}(0.5^2-(0.45/2)^2) - \text{sqrt}(0.5^2-(0.9/2)^2))/0.5$
$=(\text{sqrt}(0.5^2-(0.45/2)^2) - \text{sqrt}(0.5^2-(0.9/2)^2))/0.5$
$=(0.4465 - 0.2179)/0.5 \quad =0.4571$

Hence around 46% of our grains of diameter 1 unit should have a cross section diameter between 0.9 and 0.45 units.

For sieve analysis, we want to know the percentages of grains occurring in the various phi ranges
eg range phi=0 to phi =1 corresponds to the range diameter =0.5 to 1 mm.

Thus using equation (2) if we had uniform grainsize of d=2.2mm then in thin section there would be

(3) P(0->1)=(sqrt(1.1^2-(0.5/2)^2) - sqrt(1.1^2-(1/2)^2))/1.1
=(1.0712 - 0.9798)/1.1 =0.083

8% of the grain population in the phi=0 to phi =1 range.

USING THIS INFORMATION

What we have above is the method for determining the thin section grain size distribution (TSD) from the actual grain size distribution (AGD), what we need to do now is use this information for the inverse problem.

The first step is to sort your TSD into the appropriate phi classes. We may end up with a distribution like this:

phi range	number	percentage
0. to 1.	1	0.4831
1. to 2.	68	32.8502
2. to 3.	127	61.3527
3. to 4.	10	4.8309
4. to 5.	1	0.4831
TOTAL	207	100.0000

The first assumption is that the largest grainsize in the TSD is very close in size to that in the AGD. This is a reasonable assumption provided the population sample is significantly large. Using this grainsize, it is simple to calculate what percentage of the grains should fall in each category such as was done in section 3.

Imagine in the sample above, the largest grainsize was .52mm in diameter, we would expect the following distribution.

percentage in phi range 0. to 1. is 0.274670
percentage in phi range 1. to 2. is 0.602177
percentage in phi range 2. to 3. is 0.093831
percentage in phi range 3. to 4. is 0.022073
percentage in phi range 4. to 5. is 0.005442
percentage in phi range below 5. is 0.001807

In our sample we had 1 grain in the 0. to 1. range, so from the rest of the sample we would expect to see:

1 * 0.602177 / 0.274670 = 2 in the phi range 1. to 2.

Thus in our corrected sample, we would expect that 3 grains were from the 0 to 1 grainsize class.

phi range	number	
0. to 1.	3*	* = corrected value
1. to 2.	66	
2. to 3.	127	
3. to 4.	10	
4. to 5.	1	

The procedure is then repeated for the next grainsize down. Imagine that the maximum grainsize in the phi range 1. to 2. is .43mm, the corresponding distribution you would expect to see is

percentage in phi range 1. to 2. is 0.813621
percentage in phi range 2. to 3. is 0.143194
percentage in phi range 3. to 4. is 0.032566
percentage in phi range 4. to 5. is 0.007975
percentage in phi range below 5. is 0.002644

so if we have 66 grains in the 1-2 range, we can expect 12 in the 2-3 range and 3 in the 3-4 leaving the distribution as

phi range	number	
0. to 1.	3*	* = corrected value
1. to 2.	81*	
2. to 3.	115	
3. to 4.	7	
4. to 5.	1	

this process is repeated until we are left with the distribution

0. to 1.	3*	* = corrected value
1. to 2.	81*	
2. to 3.	123*	

which should be a reasonable correlation with the AGD.

One thing which hasn't been mentioned yet, is when a grain is removed from the population of a smaller class, what grain should you remove, the largest, smallest or medium sized grain.

In GRSORT, the largest grains are always removed, the reason being that statistically they are the most likely to belong to the larger phi class.

In practice, it makes little difference to the overall calculated AGD, with only a few grains difference between removing the largest or the smallest grains in each sample. Measurement error is likely to be greater than that.

Chris Dyt, NCPGG 12 October 1999.

APPENDIX 2

STRUCTURE AND EXPLORATION HISTORY OF EROMANGA BASIN

STRUCTURE OF EROMANGA

The Eromanga Basin was first defined by (Mott, 1952) as extending south of the Euroka Arch, west of the pre-Permian rocks of eastern Australia and separated from the Surat Basin by the Nebine and Eulo Ridges to the southeast. It is underlain by a number of older Palaeozoic basins (Cooper and Warburton Basins) that influenced the deposition and structural development of Eromanga sediments (Armstrong & Barr, 1986).

(Passmore 1989) described the Eromanga Basin as a broad, intracratonic basin that developed in response to continental thermal sag. This gentle downwarping was later modified by a period of regional uplift during the Late Cretaceous to Tertiary that is responsible for much of the present-day relief (Gilby & Mortimore, 1989). Rocks in the central Eromanga Basin are only mildly deformed. Folds are usually broad and of low amplitude, and faults have throws of up to 300m (Passmore & Boreham, 1989).

The eastern half of the Eromanga Basin is dominated by northeasterly trends, which are influenced by the structural features of the Permian Cooper basin. The Patchawarra and Nappamerri Troughs and the Gidgealpa-Merrimelia-Innamincka Trend is recognisable in the Eromanga section.

The western part of the Eromanga basin is dominated by the Poolawanna Trough, which is a large synclinal area separated from the Cooper basin by the north-east trending Birdsville Track Ridge. The faults and folds reflect greater deformation in the underlying basins or in basement rocks (Senior et al., 1978). Basement horst blocks uplifted during tectonics in the Devonian, Permian and Triassic. These form the major highs such as the Nappacoongee-Murteree, Gidgealpa-Merrimelia and the Wackett-Jackson trends.

The lower part of the Eromanga shows different styles of faulting to the upper. The Deep Cooper Basin faults diminish significantly at the base of the Jurassic Eromanga Basin sequence. These normal faults are however occasionally seen on seismic to extend as high as the Birkhead or even the Cadna-Owie Formation (Passmore, 1989).

Post depositional fracturing and folding of the Eromanga Basin sequence occurred during a period of compression in the Tertiary (Passmore, 1989). Major basement faulting was probably reactivated during this period, extending the lower faults up into the Jurassic sequence. Folds, some listric and keystone style faulting occurred from this tectonic activity within the upper Eromanga Basin sequence. This resulted in this sequence containing finer grained lithologies that are less compacted.

EXPLORATION HISTORY OF EROMANGA

(Sprigg 1982) has traced the history of petroleum exploration in the Eromanga Basin from its earliest days. Until the late 1970's primary exploration targets were in basins underlying the Eromanga Basin. The Eromanga Basin sandstones were commonly considered to have been water flushed and generally not prospective (Laing, 1969, Vine, 1976) despite hydrocarbon shows and porous reservoir rocks.

The Eromanga Basin has been explored for hydrocarbons since 1924 (Armstrong & Barr, 1986). The Namur 1 gas discovery in 1976 confirmed optimism, however it wasn't until substantial oil flows were obtained from Strzelecki 3 in 1978 and Dullingari North 1 in 1979 that attention was focused on the Basin. South Australian Eromanga Basin oil fields produced 3.5 million barrels of oil in 1983 following the completion of a liquids pipeline from Moomba to Port Bonython.

To date, all the economic oil discoveries have been made in the Late Jurassic to Early Cretaceous non-marine Eromanga sequences with the greatest volumes being contained in the Hutton Sandstone, the Birkhead Formation and the Namur and Murta Members of the Mooga Formation. Major Eromanga oil fields have been discovered in sandstones of all these formations.

Further details can be obtained in *The Geology of South Australia*, Bulletin 54

REFERENCES

Armstrong, J. P. & Barr, T. M. 1986. The Eromanga Basin. An overview of exploration and potential. In: *Contributions to the geology and hydrocarbon potential of the Eromanga Basin* (edited by Gravestock, D. I., Moore, P. S. & Pitt, G. M.) **12**. Geological Society of Australia, Special Publication, 12 - 38.

Gilby, A. R. & Mortimore, I. R. 1989. The prospects for Eromanga oil accumulations in the northern Cooper Basin region, Australia. In: *Proceedings of the Cooper and Eromanga Basins conference* (edited by O'Neil, B. J.), Adelaide, 391 - 403.

Laing, A. C. M. 1969. Review of geology and case history of petroleum exploration in central Eromanga sub-basin. *APEA Journal* **9**(2), 88 - 96.

Mott, W. A. 1952. Oil in Queensland. *Qld.Gov.MIn.Journ* **53**, 848 - 861.

Passmore, V. L. 1989. Petroleum accumulations of the Eromanga Basin: a comparison with other Australian Mesozoic accumulations. In: *The Cooper and Eromanga Basins, Australia* (edited by O'Neil, B. J.). Proceedings of PESA/SPE/ASEG (SA Branches), Adelaide.

Passmore, V. L. & Boreham, C. J. 1989. Source rock evaluation and maturation history of the central Eromanga Basin. *Geological Society of Australia Special Publication* **12**, 221 - 240.

Senior, B. R., Mond, A. & Harrison, P. L. 1978. Geology of the Eromanga Basin. *BMR Bulletin* **167**, 102p.

Sprigg, R. C. 1982. The long lead up to commercial oil discovery in the Mesozoic Eromanga Basin. In: *Eromanga Basin Symposium summary papers* (edited by Moore, P. S. & Mount, T. J.). Geol. Soc. Aust. & Pet. Explor. Soc. Aust, Adelaide.

Vine, R. B. 1976. Eromanga Basin. *Australian Institute of Mining and Metallurgy* **7**(3), 306 - 308.

APPENDIX 3

PHOTOCOPIES OF CORE INCLUDING RCA DATA

6079'6"

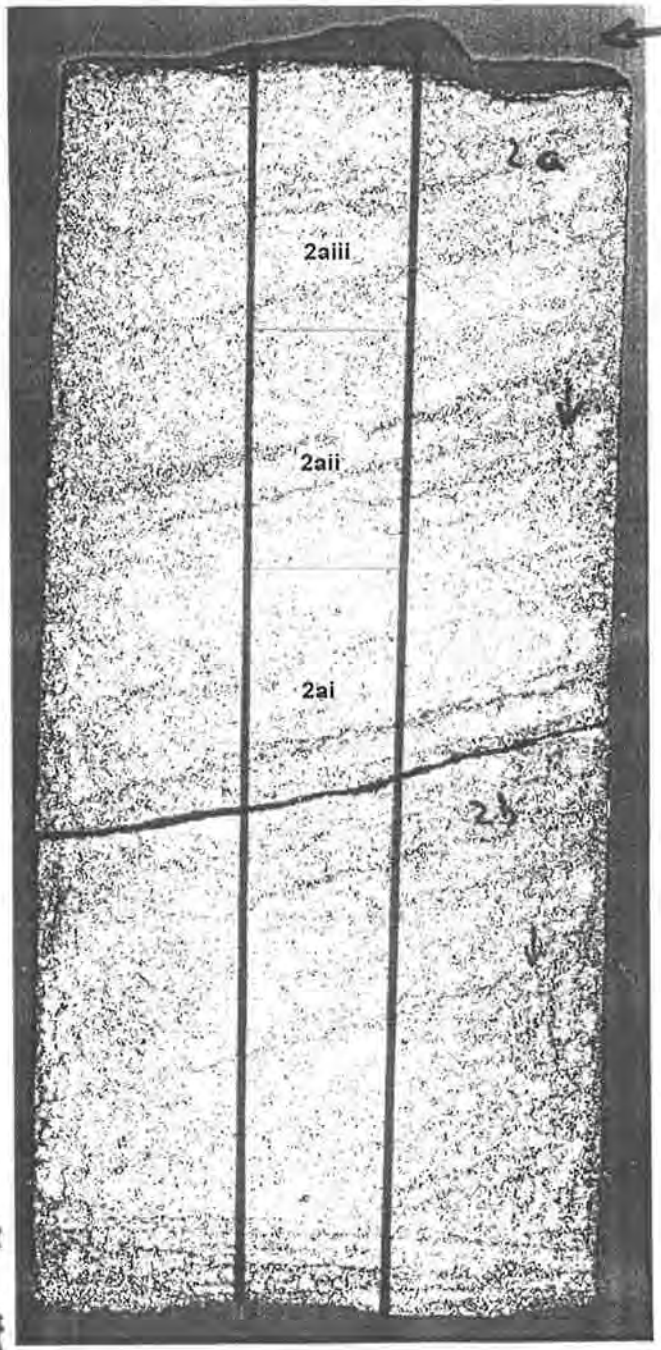

ϕ=21.8
k=714

6078'8¼"

plug
ϕ 22.2, k 1400

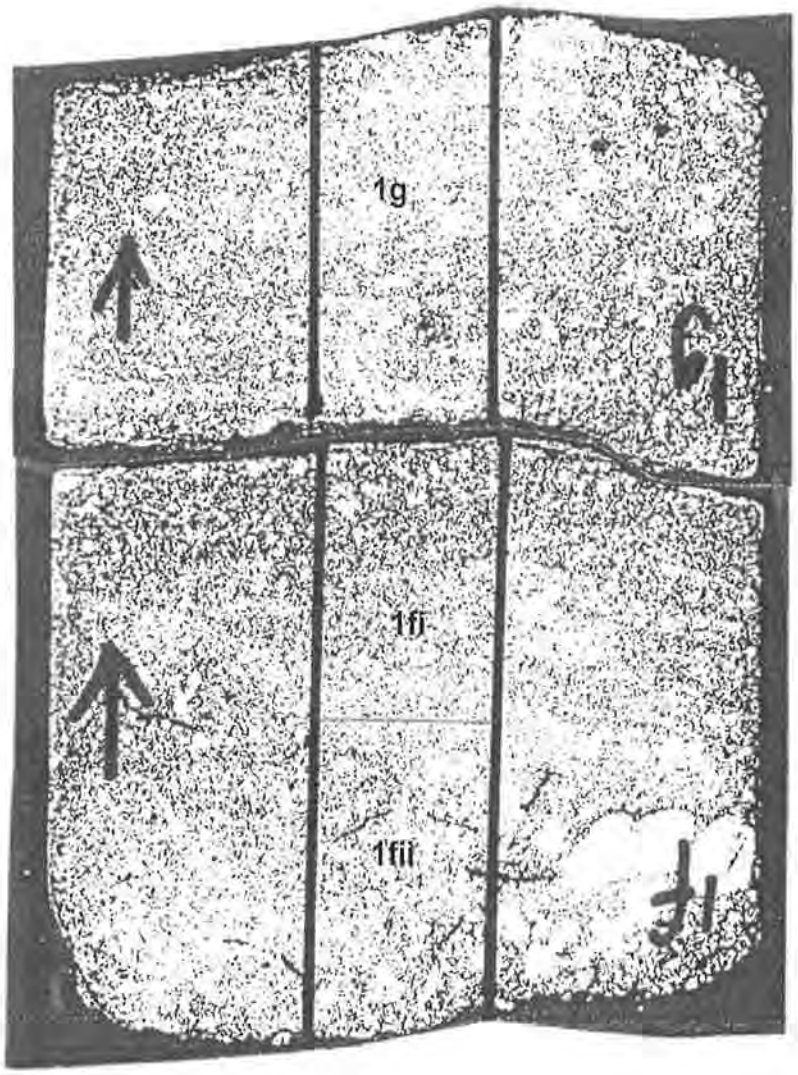

6083'
4½"

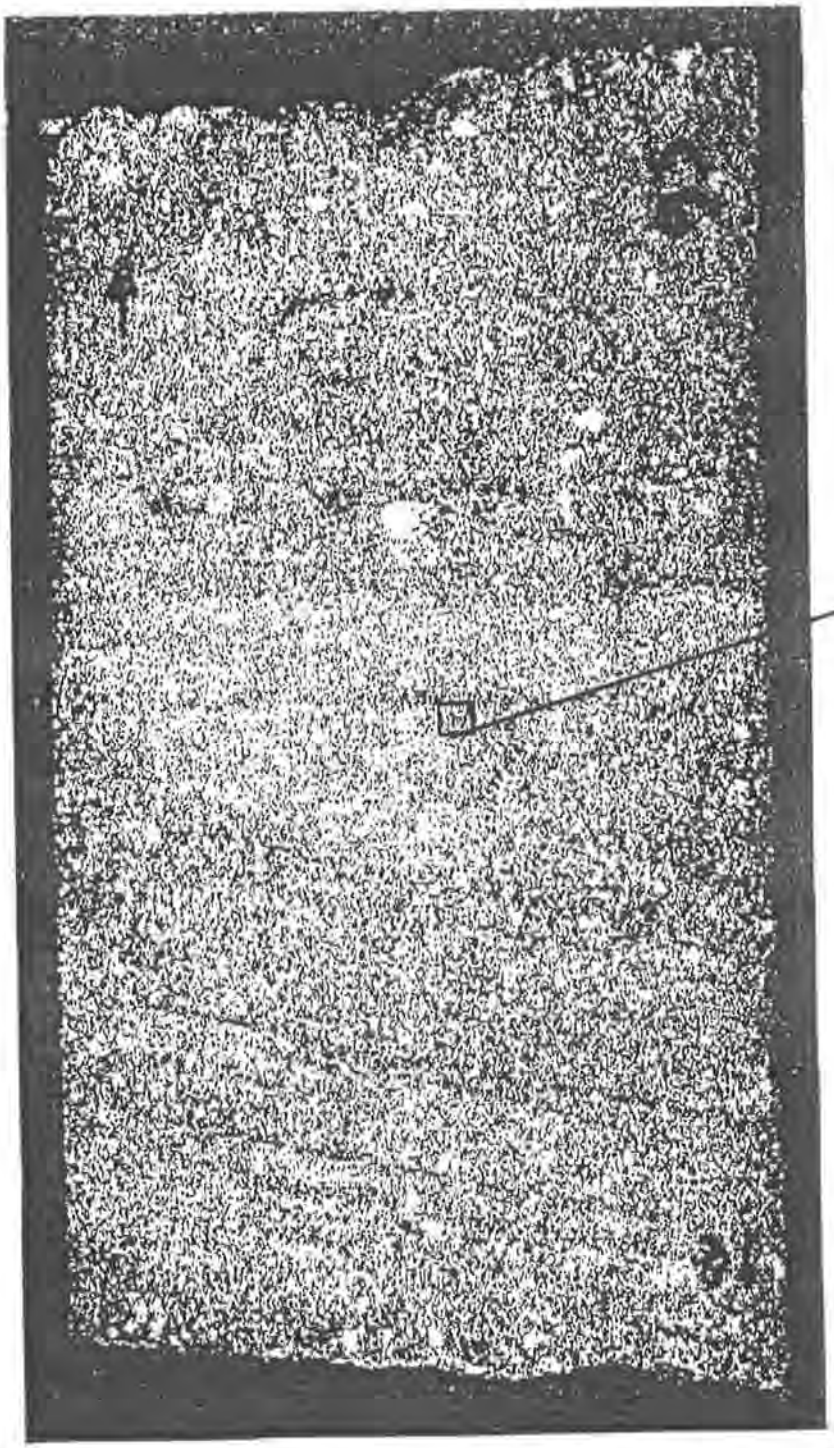
Sample analysed by
micro-CT scanning

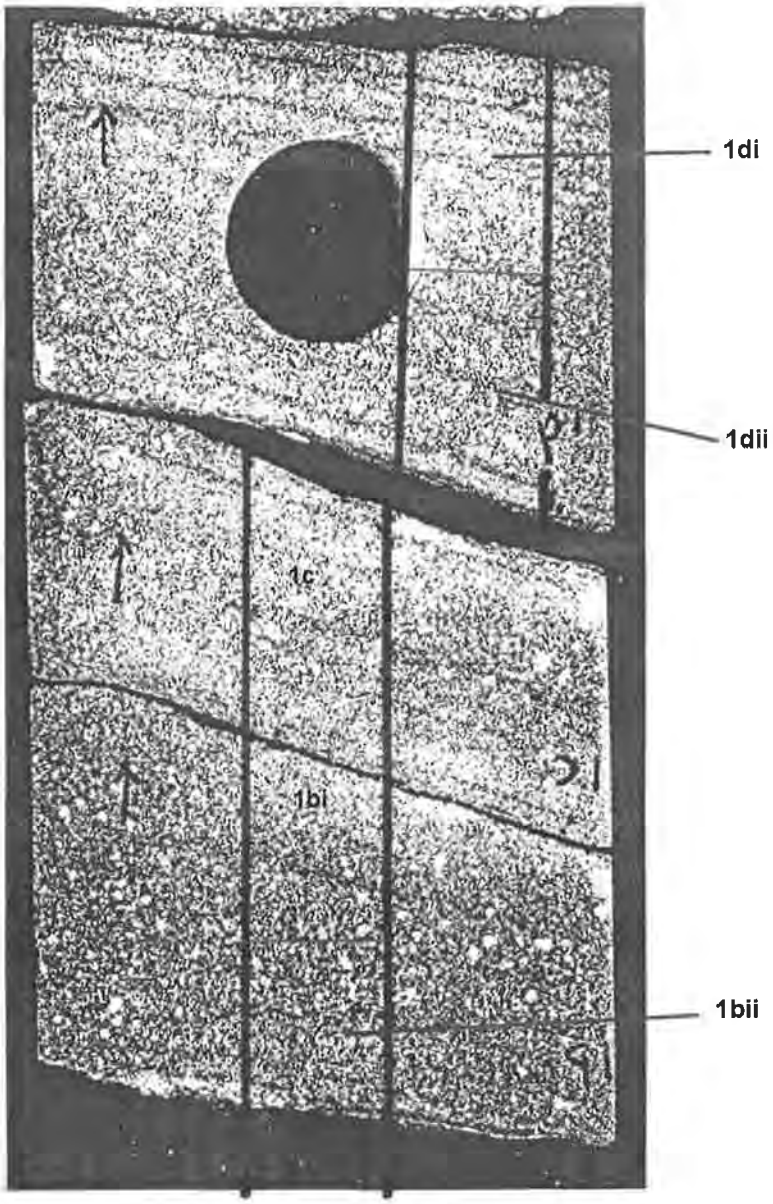
1di
1dii
1c
1bi
1bii

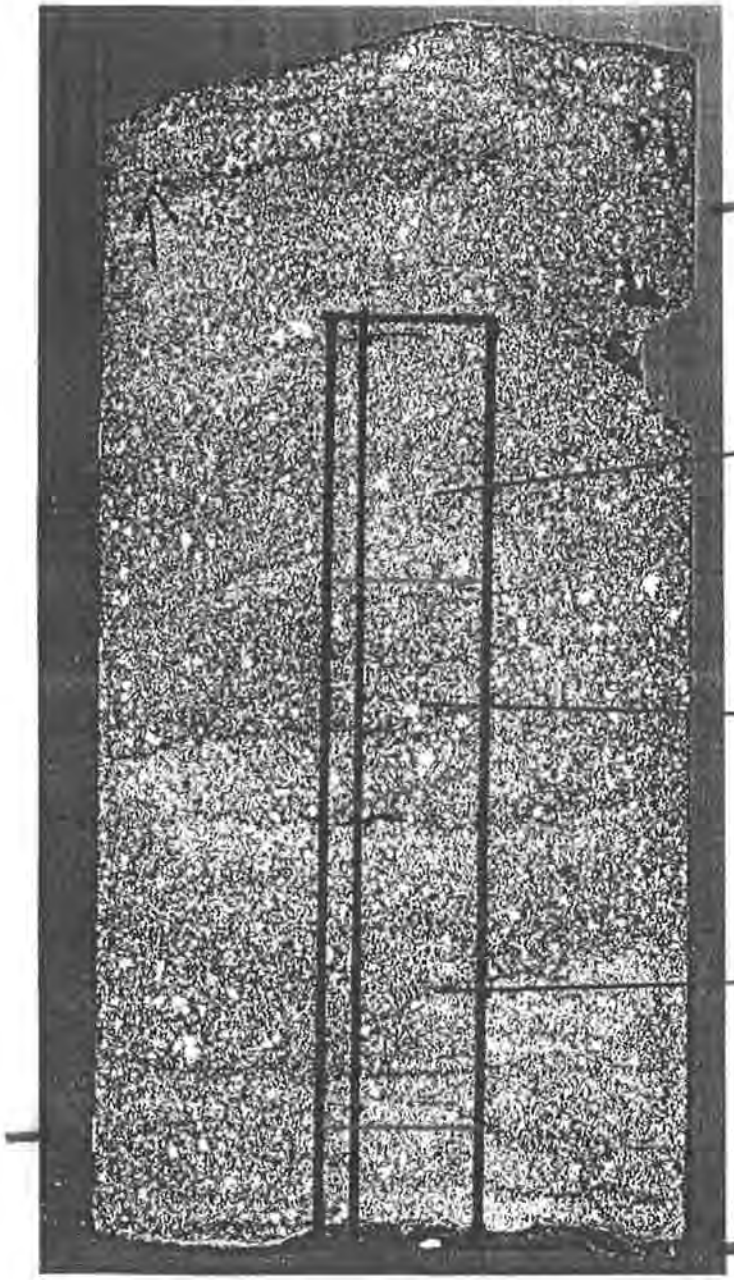
6085
1ai
1aii
1a-lower
6085' 6.5"

APPENDIX 4
GRAIN SIZE HISTOGRAM CHARTS

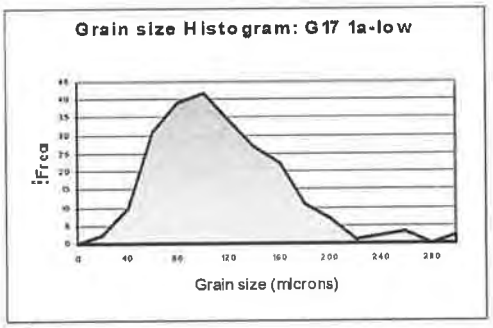
Grain size Histogram: G17 1a-low
iFreq
Grain size (microns)

(c)

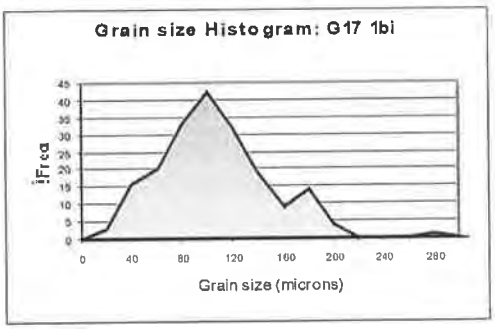
Grain size Histogram: G17 1bi
iFreq
0 40 80 120 160 200 240 280
Grain size (microns)

(d)

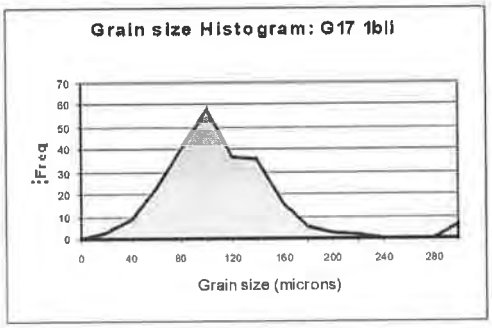
Grain size Histogram: G17 1bii
iFreq
0 10 20 30 40 50 60 70
0 40 80 120 160 200 240 280
Grain size (microns)

(e)

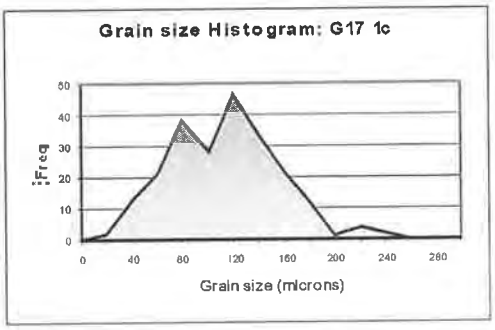
Grain size Histogram: G17 1c
iFreq
0 10 20 30 40 50
0 40 80 120 160 200 240 280
Grain size (microns)

(f)

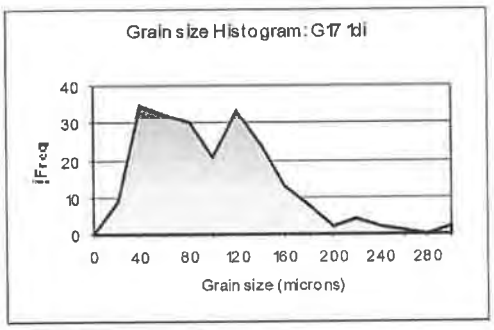
Grain size Histogram: G17 1di
iFreq
0 10 20 30 40
0 40 80 120 160 200 240 280
Grain size (microns)

(g)

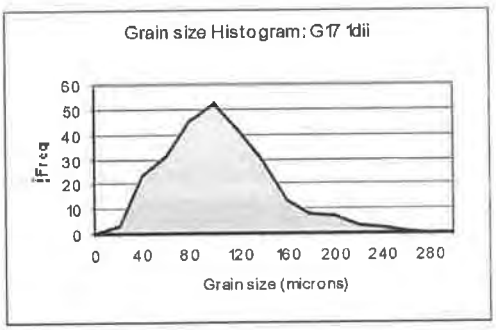
Grain size Histogram: G17 1dii
iFreq
0 10 20 30 40 50 60
0 40 80 120 160 200 240 280
Grain size (microns)

(h)

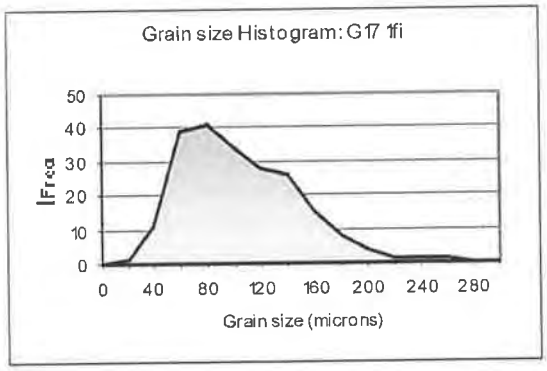
Grain size Histogram: G17 1fi
Freq
0 10 20 30 40 50
0 40 80 120 160 200 240 280
Grain size (microns)

(i)

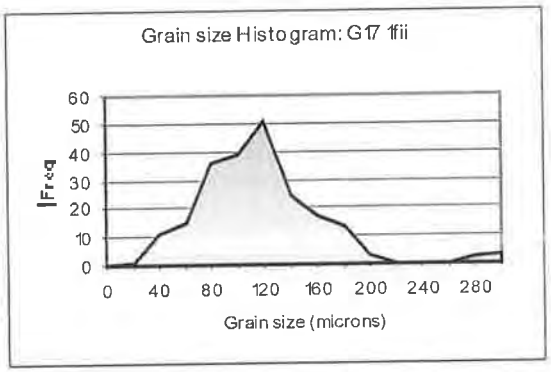
Grain size Histogram: G17 1fii
Freq
0 10 20 30 40 50 60
0 40 80 120 160 200 240 280
Grain size (microns)

(j)

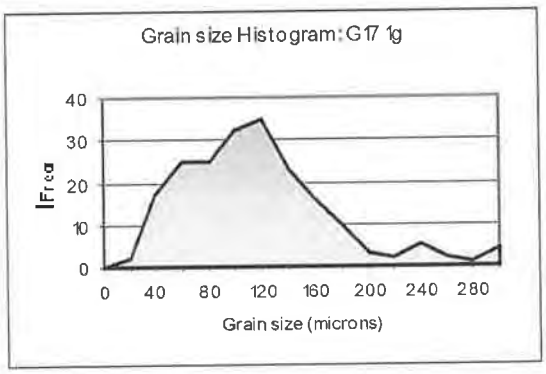
Grain size Histogram: G17 1g
Freq
0 10 20 30 40
0 40 80 120 160 200 240 280
Grain size (microns)

(k)

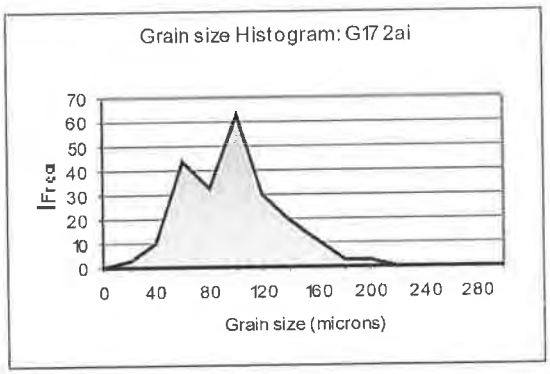
Grain size Histogram: G17 2ai
Freq
0 10 20 30 40 50 60 70
0 40 80 120 160 200 240 280
Grain size (microns)

(l)

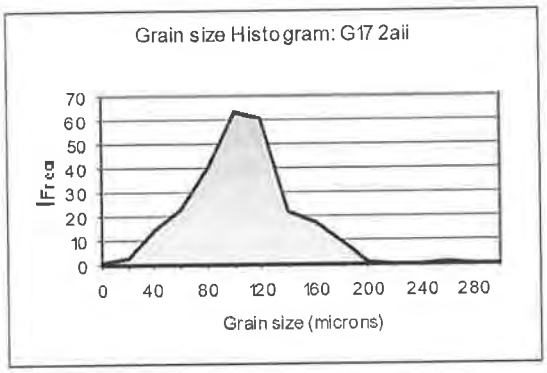
Grain size Histogram: G17 2aii
Freq
0 10 20 30 40 50 60 70
0 40 80 120 160 200 240 280
Grain size (microns)

(m)

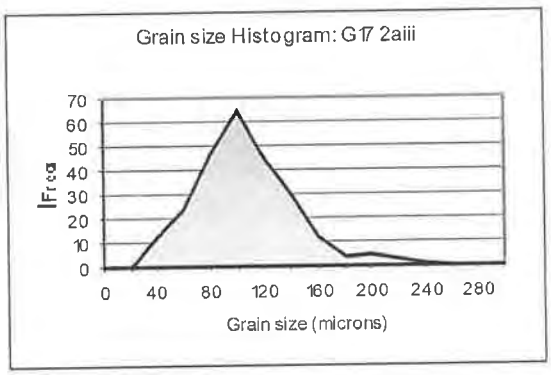
Grain size Histogram: G17 2aiii
Freq
0 10 20 30 40 50 60 70
0 40 80 120 160 200 240 280
Grain size (microns)

(n)

APPENDIX 5

PORE SIZE HISTOGRAM CHARTS

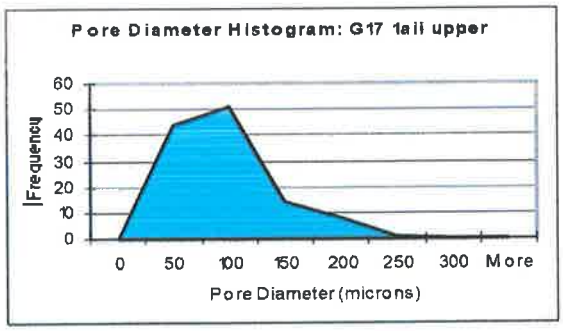
Pore Diameter Histogram: G17 1aii upper
Frequency
60
50
40
30
20
10
0
0 50 100 150 200 250 300 More
Pore Diameter (microns)

(a)

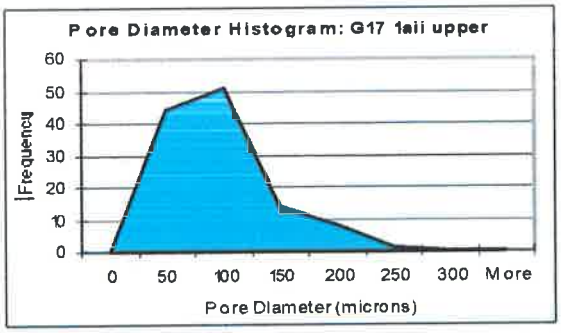
Pore Diameter Histogram: G17 1aii upper
Frequency
60
50
40
30
20
10
0
0 50 100 150 200 250 300 More
Pore Diameter (microns)

(b)

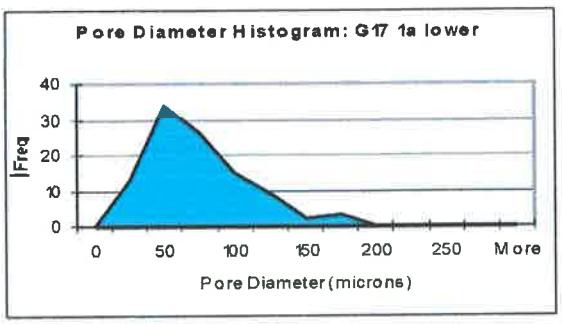
Pore Diameter Histogram: G17 1a lower
Freq
40
30
20
10
0
0 50 100 150 200 250 More
Pore Diameter (microns)

(c)

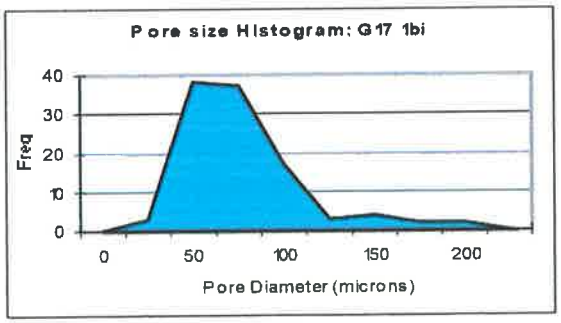
Pore size Histogram: G17 1bi
Freq
40
30
20
10
0
0 50 100 150 200
Pore Diameter (microns)

(d)

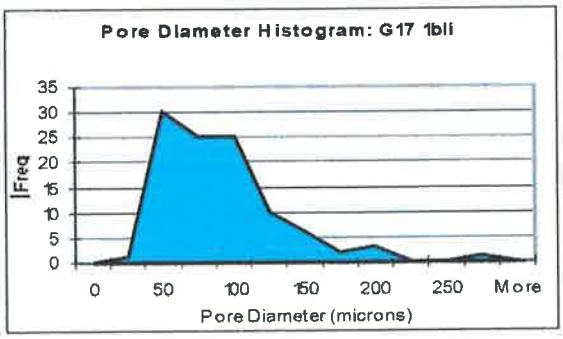
Pore Diameter Histogram: G17 1bli
Freq
35
30
25
20
15
10
5
0
0 50 100 150 200 250 More
Pore Diameter (microns)

(e)

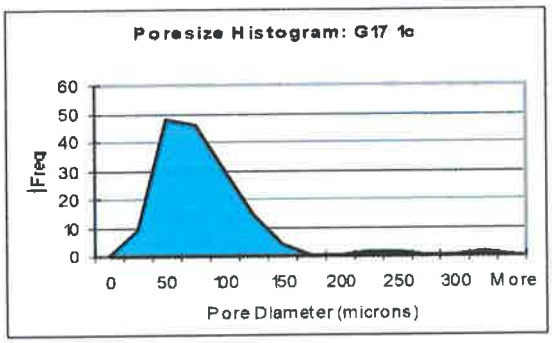
Poresize Histogram: G17 1c
Freq
60
50
40
30
20
10
0
0 50 100 150 200 250 300 More
Pore Diameter (microns)

(f)

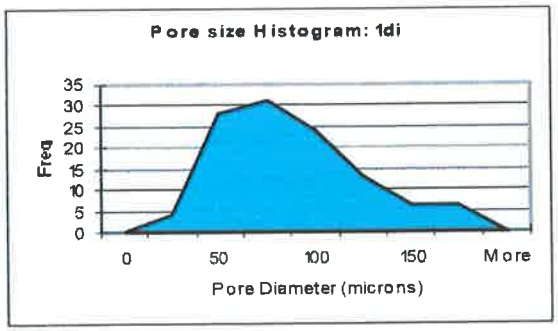
Pore size Histogram: 1di
Freq
35
30
25
20
15
10
5
0
0 50 100 150 More
Pore Diameter (microns)

(g)

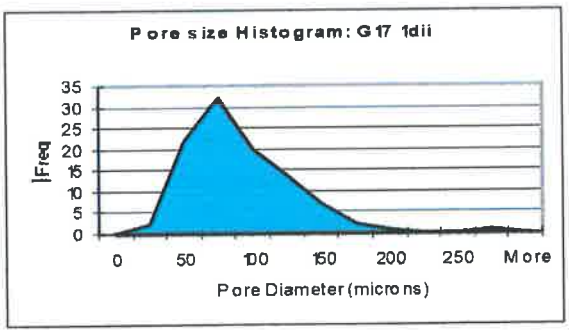
Pore size Histogram: G17 1dii
Freq
35
30
25
20
15
10
5
0
0 50 100 150 200 250 More
Pore Diameter (microns)

(h)

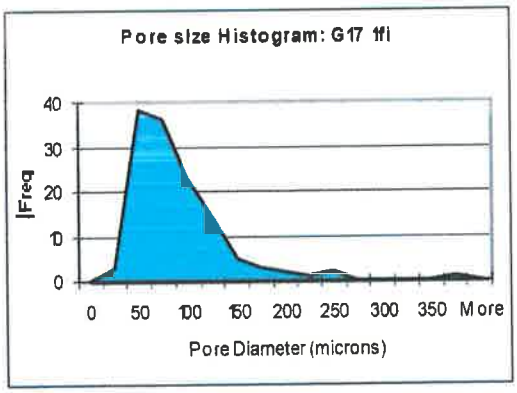
Pore size Histogram: G17 1fi
40
30
20
10
0
|Freq
0 50 100 150 200 250 300 350 More
Pore Diameter (microns)

(i)

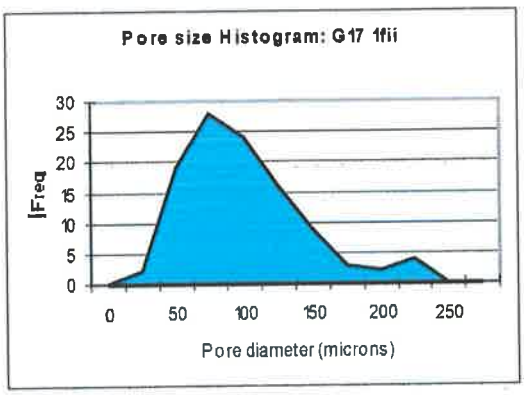
Pore size Histogram: G17 1fii
30
25
20
15
10
5
0
|Freq
0 50 100 150 200 250
Pore diameter (microns)

(j)

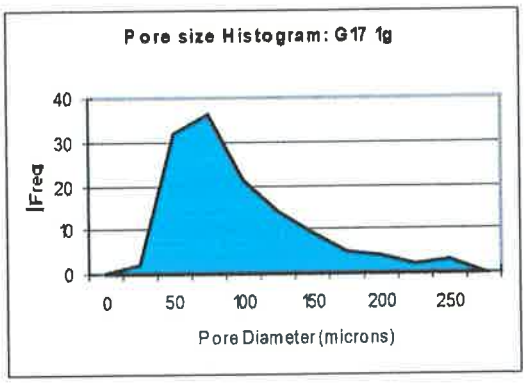
Pore size Histogram: G17 1g
40
30
20
10
0
|Freq
0 50 100 150 200 250
Pore Diameter (microns)

(k)

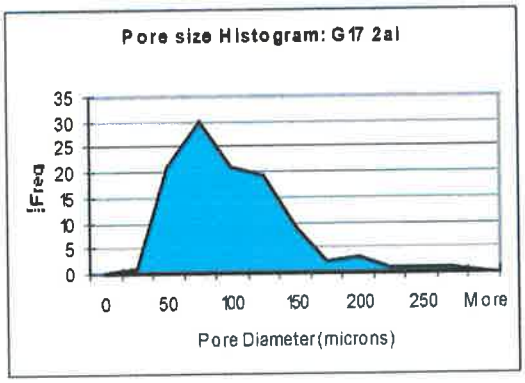
Pore size Histogram: G17 2al
35
30
25
20
15
10
5
0
|Freq
0 50 100 150 200 250 More
Pore Diameter (microns)

(l)

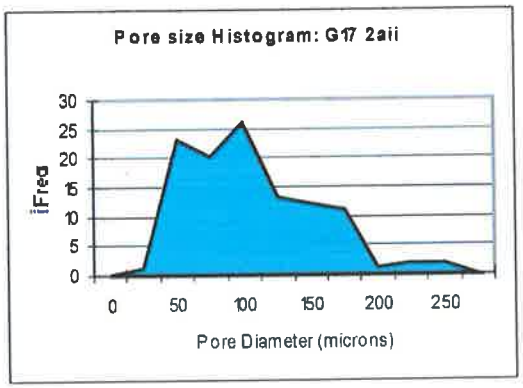
Pore size Histogram: G17 2aii
30
25
20
15
10
5
0
|Freq
0 50 100 150 200 250
Pore Diameter (microns)

(m)

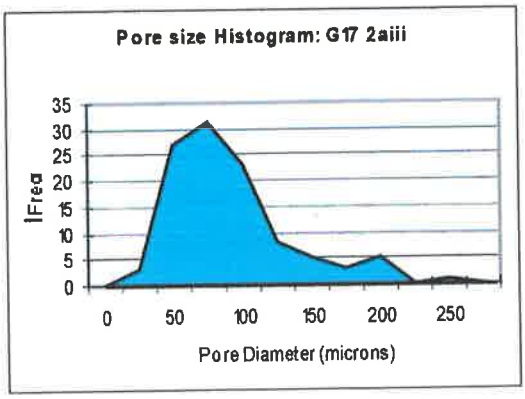
Pore size Histogram: G17 2aiii
35
30
25
20
15
10
5
0
|Freq
0 50 100 150 200 250
Pore Diameter (microns)

(n)

APPENDIX 6
GRSORT DATA

Grainsize phi classes: 2aiii

number of records = 247
number and fraction in phi range 0. to 1. is 9, 3.6437
number and fraction in phi range 1. to 2. is 129, 52.2267
number and fraction in phi range 2. to 3. is 92, 37.2470
number and fraction in phi range 3. to 4. is 16, 6.4777
number and fraction in phi range 4. to 5. is 1, 0.4049

area percent in phi range 0. to 1. is 13.4327
area percent in phi range 1. to 2. is 67.5077
area percent in phi range 2. to 3. is 18.2071
area percent in phi range 3. to 4. is 0.8362
area percent in phi range 4. to 5. is 0.0163

mass percent in phi range 0. to 1. is 21.6403
mass percent in phi range 1. to 2. is 67.0557
mass percent in phi range 2. to 3. is 11.0422
mass percent in phi range 3. to 4. is 0.2591
mass percent in phi range 4. to 5. is 0.0027

Corrected values
number and percent in phi range 0. to 1. is 15, 6.0729
number and percent in phi range 1. to 2. is 150, 60.7287
number and percent in phi range 2. to 3. is 81, 32.7935
number and percent in phi range 3. to 4. is 1, 0.4049

area percent in phi range 0. to 1. is 14.6629
area percent in phi range 1. to 2. is 74.2796
area percent in phi range 2. to 3. is 11.0442
area percent in phi range 3. to 4. is 0.0134

mass percent in phi range 0. to 1. is 20.4625
mass percent in phi range 1. to 2. is 73.7792
mass percent in phi range 2. to 3. is 5.7561
mass percent in phi range 3. to 4. is 0.0022

Grainsize phi classes: 2aii

number of records = 256
number and fraction in phi range 0. to 1. is 3, 1.1719
number and fraction in phi range 1. to 2. is 143, 55.8594
number and fraction in phi range 2. to 3. is 86, 33.5938
number and fraction in phi range 3. to 4. is 19, 7.4219
number and fraction in phi range 4. to 5. is 4, 1.5625
number and fraction in phi range below 5. is 1, 0.3906

area percent in phi range 0. to 1. is 4.7578
area percent in phi range 1. to 2. is 76.8731
area percent in phi range 2. to 3. is 17.3564
area percent in phi range 3. to 4. is 0.9607
area percent in phi range 4. to 5. is 0.0521
area percent in phi range below 5. is 0.0000

mass percent in phi range 0. to 1. is 8.3864
mass percent in phi range 1. to 2. is 80.3462
mass percent in phi range 2. to 3. is 10.9550
mass percent in phi range 3. to 4. is 0.3042
mass percent in phi range 4. to 5. is 0.0081
mass percent in phi range below 5. is 0.0000

Corrected values
number and percent in phi range 0. to 1. is 4, 1.5625
number and percent in phi range 1. to 2. is 165, 64.4531
number and percent in phi range 2. to 3. is 81, 31.6406
number and percent in phi range 3. to 4. is 6, 2.3438

area percent in phi range 0. to 1. is 4.0450
area percent in phi range 1. to 2. is 86.7211
area percent in phi range 2. to 3. is 9.1327
area percent in phi range 3. to 4. is 0.1012

mass percent in phi range 0. to 1. is 5.8096
mass percent in phi range 1. to 2. is 89.7919
mass percent in phi range 2. to 3. is 4.3797
mass percent in phi range 3. to 4. is 0.0188

Grainsize phi classes: 2ai

number of records = 219
number and fraction in phi range 0. to 1. is 4, 1.8265
number and fraction in phi range 1. to 2. is 92, 42.0091
number and fraction in phi range 2. to 3. is 105, 47.9452
number and fraction in phi range 3. to 4. is 13, 5.9361
number and fraction in phi range 4. to 5. is 5, 2.2831

area percent in phi range 0. to 1. is 7.6552
area percent in phi range 1. to 2. is 64.9021
area percent in phi range 2. to 3. is 26.4539
area percent in phi range 3. to 4. is 0.8895
area percent in phi range 4. to 5. is 0.0993

mass percent in phi range 0. to 1. is 12.9529
mass percent in phi range 1. to 2. is 69.5565
mass percent in phi range 2. to 3. is 17.1778
mass percent in phi range 3. to 4. is 0.2951
mass percent in phi range 4. to 5. is 0.0177

Corrected values
number and percent in phi range 0. to 1. is 10, 4.5662
number and percent in phi range 1. to 2. is 110, 50.2283
number and percent in phi range 2. to 3. is 98, 44.7489
number and percent in phi range 4. to 5. is 1, 0.4566

area percent in phi range 0. to 1. is 11.3274
area percent in phi range 1. to 2. is 68.8642
area percent in phi range 2. to 3. is 19.8034
area percent in phi range 4. to 5. is 0.0049

mass percent in phi range 0. to 1. is 15.9795
mass percent in phi range 1. to 2. is 72.2205
mass percent in phi range 2. to 3. is 11.7995
mass percent in phi range 4. to 5. is 0.0005

Grainsize phi classes: 1g

number of records = 202
number and fraction in phi range -1. to 0. is 2, 0.9901
number and fraction in phi range 0. to 1. is 15, 7.4257
number and fraction in phi range 1. to 2. is 102, 50.4950
number and fraction in phi range 2. to 3. is 62, 30.6931
number and fraction in phi range 3. to 4. is 17, 8.4158
number and fraction in phi range 4. to 5. is 4, 1.9802

area percent in phi range -1. to 0. is 18.9696
area percent in phi range 0. to 1. is 24.4407
area percent in phi range 1. to 2. is 47.5254
area percent in phi range 2. to 3. is 8.4104
area percent in phi range 3. to 4. is 0.6124
area percent in phi range 4. to 5. is 0.0416

mass percent in phi range -1. to 0. is 45.4577
mass percent in phi range 0. to 1. is 25.2673
mass percent in phi range 1. to 2. is 26.6263
mass percent in phi range 2. to 3. is 2.5521
mass percent in phi range 3. to 4. is 0.0932
mass percent in phi range 4. to 5. is 0.0035

Corrected values
number and percent in phi range -1. to 0. is 2, 0.9901
number and percent in phi range 0. to 1. is 17, 8.4158
number and percent in phi range 1. to 2. is 116, 57.4257
number and percent in phi range 2. to 3. is 59, 29.2079
number and percent in phi range 3. to 4. is 8, 3.9604

area percent in phi range -1. to 0. is 10.5497
area percent in phi range 0. to 1. is 28.8029
area percent in phi range 1. to 2. is 54.3907
area percent in phi range 2. to 3. is 6.1153
area percent in phi range 3. to 4. is 0.1414

mass percent in phi range -1. to 0. is 24.0008
mass percent in phi range 0. to 1. is 37.1376
mass percent in phi range 1. to 2. is 36.8928
mass percent in phi range 2. to 3. is 1.9502
mass percent in phi range 3. to 4. is 0.0186

Grainsize phi classes: 1fii

number of records = 215
number and fraction in phi range -1. to 0. is 2, 0.9302
number and fraction in phi range 0. to 1. is 6, 2.7907
number and fraction in phi range 1. to 2. is 126, 58.6047
number and fraction in phi range 2. to 3. is 63, 29.3023
number and fraction in phi range 3. to 4. is 15, 6.9767
number and fraction in phi range 4. to 5. is 3, 1.3953

area percent in phi range -1. to 0. is 22.1840
area percent in phi range 0. to 1. is 10.2952
area percent in phi range 1. to 2. is 57.2027
area percent in phi range 2. to 3. is 9.6772
area percent in phi range 3. to 4. is 0.6086
area percent in phi range 4. to 5. is 0.0323

mass percent in phi range -1. to 0. is 55.6150
mass percent in phi range 0. to 1. is 10.7133
mass percent in phi range 1. to 2. is 30.6307
mass percent in phi range 2. to 3. is 2.9425
mass percent in phi range 3. to 4. is 0.0959
mass percent in phi range 4. to 5. is 0.0026

Corrected values
number and percent in phi range -1. to 0. is 2, 0.9302
number and percent in phi range 0. to 1. is 7, 3.2558
number and percent in phi range 1. to 2. is 145, 67.4419
number and percent in phi range 2. to 3. is 57, 26.5116
number and percent in phi range 3. to 4. is 4, 1.8605

area percent in phi range -1. to 0. is 12.0158
area percent in phi range 0. to 1. is 10.6068
area percent in phi range 1. to 2. is 71.2898
area percent in phi range 2. to 3. is 6.0231
area percent in phi range 3. to 4. is 0.0646

mass percent in phi range -1. to 0. is 31.1788
mass percent in phi range 0. to 1. is 13.8220
mass percent in phi range 1. to 2. is 52.9179
mass percent in phi range 2. to 3. is 2.0727
mass percent in phi range 3. to 4. is 0.0087

Grainsize phi classes: 1fi

number of records = 210
number and fraction in phi range 0. to 1. is 7, 3.3333
number and fraction in phi range 1. to 2. is 90, 42.8571
number and fraction in phi range 2. to 3. is 88, 41.9048
number and fraction in phi range 3. to 4. is 23, 10.9524
number and fraction in phi range 4. to 5. is 2, 0.9524

area percent in phi range 0. to 1. is 13.5350
area percent in phi range 1. to 2. is 65.6431
area percent in phi range 2. to 3. is 19.2579
area percent in phi range 3. to 4. is 1.5368
area percent in phi range 4. to 5. is 0.0272

mass percent in phi range 0. to 1. is 21.7562
mass percent in phi range 1. to 2. is 67.0100
mass percent in phi range 2. to 3. is 10.7563
mass percent in phi range 3. to 4. is 0.4737
mass percent in phi range 4. to 5. is 0.0039

Corrected values
number and percent in phi range 0. to 1. is 11, 5.2381
number and percent in phi range 1. to 2. is 103, 49.0476
number and percent in phi range 2. to 3. is 87, 41.4286
number and percent in phi range 3. to 4. is 9, 4.2857

area percent in phi range 0. to 1. is 15.5910
area percent in phi range 1. to 2. is 70.0583
area percent in phi range 2. to 3. is 14.0369
area percent in phi range 3. to 4. is 0.3138

mass percent in phi range 0. to 1. is 22.6258
mass percent in phi range 1. to 2. is 70.4300
mass percent in phi range 2. to 3. is 6.8728
mass percent in phi range 3. to 4. is 0.0714

Grainsize phi classes: 1dii

number of records = 259
number and fraction in phi range 0. to 1. is 13, 5.0193
number and fraction in phi range 1. to 2. is 119, 45.9459
number and fraction in phi range 2. to 3. is 98, 37.8378
number and fraction in phi range 3. to 4. is 24, 9.2664
number and fraction in phi range 4. to 5. is 5, 1.9305

area percent in phi range 0. to 1. is 19.1004
area percent in phi range 1. to 2. is 62.8945
area percent in phi range 2. to 3. is 16.9521
area percent in phi range 3. to 4. is 0.9982
area percent in phi range 4. to 5. is 0.0547

mass percent in phi range 0. to 1. is 29.6566
mass percent in phi range 1. to 2. is 60.7037
mass percent in phi range 2. to 3. is 9.3658
mass percent in phi range 3. to 4. is 0.2664
mass percent in phi range 4. to 5. is 0.0075

Corrected values
number and percent in phi range 0. to 1. is 19, 7.3359
number and percent in phi range 1. to 2. is 135, 52.1236
number and percent in phi range 2. to 3. is 95, 36.6795
number and percent in phi range 3. to 4. is 10, 3.8610

area percent in phi range 0. to 1. is 20.7904
area percent in phi range 1. to 2. is 66.8981
area percent in phi range 2. to 3. is 12.1452
area percent in phi range 3. to 4. is 0.1663

mass percent in phi range 0. to 1. is 29.7083
mass percent in phi range 1. to 2. is 64.3303
mass percent in phi range 2. to 3. is 5.9321
mass percent in phi range 3. to 4. is 0.0293

Grainsize phi classes: 1di

number of records = 216
number and fraction in phi range -1. to 0. is 2, 0.9259
number and fraction in phi range 0. to 1. is 9, 4.1667
number and fraction in phi range 1. to 2. is 89, 41.2037
number and fraction in phi range 2. to 3. is 64, 29.6296
number and fraction in phi range 3. to 4. is 35, 16.2037
number and fraction in phi range 4. to 5. is 15, 6.9444
number and fraction in phi range below 5. is 2, 0.9259

area percent in phi range -1. to 0. is 24.9845
area percent in phi range 0. to 1. is 14.7541
area percent in phi range 1. to 2. is 48.7902
area percent in phi range 2. to 3. is 9.8508
area percent in phi range 3. to 4. is 1.4204
area percent in phi range 4. to 5. is 0.1934
area percent in phi range below 5. is 0.0066

mass percent in phi range -1. to 0. is 58.9792
mass percent in phi range 0. to 1. is 12.7488
mass percent in phi range 1. to 2. is 25.3391
mass percent in phi range 2. to 3. is 2.7148
mass percent in phi range 3. to 4. is 0.2027
mass percent in phi range 4. to 5. is 0.0151
mass percent in phi range below 5. is 0.0003

Corrected values
number and percent in phi range -1. to 0. is 2, 0.9259
number and percent in phi range 0. to 1. is 13, 6.0185
number and percent in phi range 1. to 2. is 100, 46.2963
number and percent in phi range 2. to 3. is 65, 30.0926
number and percent in phi range 3. to 4. is 29, 13.4259
number and percent in phi range 4. to 5. is 7, 3.2407

area percent in phi range -1. to 0. is 14.7976
area percent in phi range 0. to 1. is 16.5985
area percent in phi range 1. to 2. is 60.8807
area percent in phi range 2. to 3. is 6.9750
area percent in phi range 3. to 4. is 0.6984
area percent in phi range 4. to 5. is 0.0498

mass percent in phi range -1. to 0. is 36.9589
mass percent in phi range 0. to 1. is 17.2217
mass percent in phi range 1. to 2. is 43.6180
mass percent in phi range 2. to 3. is 2.0980
mass percent in phi range 3. to 4. is 0.0995
mass percent in phi range 4. to 5. is 0.0039

Grainsize phi classes: 1c

number of records = 222
number and fraction in phi range 0. to 1. is 7, 3.1532
number and fraction in phi range 1. to 2. is 130, 58.5586
number and fraction in phi range 2. to 3. is 62, 27.9279
number and fraction in phi range 3. to 4. is 20, 9.0090
number and fraction in phi range 4. to 5. is 3, 1.3514

area percent in phi range 0. to 1. is 11.0732
area percent in phi range 1. to 2. is 76.3926
area percent in phi range 2. to 3. is 11.4720
area percent in phi range 3. to 4. is 1.0283
area percent in phi range 4. to 5. is 0.0340

mass percent in phi range 0. to 1. is 17.3657
mass percent in phi range 1. to 2. is 76.0035
mass percent in phi range 2. to 3. is 6.3294
mass percent in phi range 3. to 4. is 0.2967
mass percent in phi range 4. to 5. is 0.0046

Corrected values
number and percent in phi range 0. to 1. is 11, 4.9550
number and percent in phi range 1. to 2. is 148, 66.6667
number and percent in phi range 2. to 3. is 55, 24.7748
number and percent in phi range 3. to 4. is 8, 3.6036

area percent in phi range 0. to 1. is 10.6644
area percent in phi range 1. to 2. is 83.1126
area percent in phi range 2. to 3. is 6.0278
area percent in phi range 3. to 4. is 0.1952

mass percent in phi range 0. to 1. is 14.0363
mass percent in phi range 1. to 2. is 83.2555
mass percent in phi range 2. to 3. is 2.6675
mass percent in phi range 3. to 4. is 0.0408

Grainsize phi classes: 1bii

number of records = 238
number and fraction in phi range -1. to 0. is 5, 2.1008
number and fraction in phi range 0. to 1. is 6, 2.5210
number and fraction in phi range 1. to 2. is 129, 54.2017
number and fraction in phi range 2. to 3. is 79, 33.1933
number and fraction in phi range 3. to 4. is 15, 6.3025
number and fraction in phi range 4. to 5. is 4, 1.6807

area percent in phi range -1. to 0. is 39.9859
area percent in phi range 0. to 1. is 6.5024
area percent in phi range 1. to 2. is 43.1685
area percent in phi range 2. to 3. is 9.8440
area percent in phi range 3. to 4. is 0.4675
area percent in phi range 4. to 5. is 0.0317

mass percent in phi range -1. to 0. is 75.5192
mass percent in phi range 0. to 1. is 4.6992
mass percent in phi range 1. to 2. is 17.3333
mass percent in phi range 2. to 3. is 2.3892
mass percent in phi range 3. to 4. is 0.0572
mass percent in phi range 4. to 5. is 0.0019

Corrected values
number and percent in phi range -1. to 0. is 6, 2.5210
number and percent in phi range 0. to 1. is 9, 3.7815
number and percent in phi range 1. to 2. is 152, 63.8655
number and percent in phi range 2. to 3. is 69, 28.9916
number and percent in phi range 3. to 4. is 2, 0.8403

area percent in phi range -1. to 0. is 32.3926
area percent in phi range 0. to 1. is 5.9653
area percent in phi range 1. to 2. is 55.3261
area percent in phi range 2. to 3. is 6.2968
area percent in phi range 3. to 4. is 0.0193

mass percent in phi range -1. to 0. is 65.2183
mass percent in phi range 0. to 1. is 4.2082
mass percent in phi range 1. to 2. is 28.9235
mass percent in phi range 2. to 3. is 1.6483
mass percent in phi range 3. to 4. is 0.0016

Grainsize phi classes: 1bi

number of records = 193
number and fraction in phi range 0. to 1. is 5, 2.5907
number and fraction in phi range 1. to 2. is 99, 51.2953
number and fraction in phi range 2. to 3. is 67, 34.7150
number and fraction in phi range 3. to 4. is 19, 9.8446
number and fraction in phi range 4. to 5. is 3, 1.5544

area percent in phi range 0. to 1. is 10.1096
area percent in phi range 1. to 2. is 73.0134
area percent in phi range 2. to 3. is 15.8723
area percent in phi range 3. to 4. is 0.9694
area percent in phi range 4. to 5. is 0.0354

mass percent in phi range 0. to 1. is 16.5398
mass percent in phi range 1. to 2. is 74.3248
mass percent in phi range 2. to 3. is 8.8755
mass percent in phi range 3. to 4. is 0.2555
mass percent in phi range 4. to 5. is 0.0044

Corrected values
number and percent in phi range 0. to 1. is 6, 3.1088
number and percent in phi range 1. to 2. is 114, 59.0674
number and percent in phi range 2. to 3. is 65, 33.6788
number and percent in phi range 3. to 4. is 8, 4.1451

area percent in phi range 0. to 1. is 9.6261
area percent in phi range 1. to 2. is 80.5411
area percent in phi range 2. to 3. is 9.6738
area percent in phi range 3. to 4. is 0.1590

mass percent in phi range 0. to 1. is 14.5767
mass percent in phi range 1. to 2. is 80.9348
mass percent in phi range 2. to 3. is 4.4617
mass percent in phi range 3. to 4. is 0.0268

Grainsize phi classes: 1alow

number of records = 233
number and fraction in phi range 0. to 1. is 15, 6.4378
number and fraction in phi range 1. to 2. is 115, 49.3562
number and fraction in phi range 2. to 3. is 85, 36.4807
number and fraction in phi range 3. to 4. is 15, 6.4378
number and fraction in phi range 4. to 5. is 3, 1.2876

area percent in phi range 0. to 1. is 25.8515
area percent in phi range 1. to 2. is 60.0853
area percent in phi range 2. to 3. is 13.3656
area percent in phi range 3. to 4. is 0.6624
area percent in phi range 4. to 5. is 0.0352

mass percent in phi range 0. to 1. is 41.3369
mass percent in phi range 1. to 2. is 52.1442
mass percent in phi range 2. to 3. is 6.3496
mass percent in phi range 3. to 4. is 0.1648
mass percent in phi range 4. to 5. is 0.0045

Corrected values
number and percent in phi range 0. to 1. is 18, 7.7253
number and percent in phi range 1. to 2. is 133, 57.0815
number and percent in phi range 2. to 3. is 81, 34.7639
number and percent in phi range 3. to 4. is 1, 0.4292

area percent in phi range 0. to 1. is 30.6488
area percent in phi range 1. to 2. is 60.7737
area percent in phi range 2. to 3. is 8.5654
area percent in phi range 3. to 4. is 0.0120

mass percent in phi range 0. to 1. is 47.6895
mass percent in phi range 1. to 2. is 48.9876
mass percent in phi range 2. to 3. is 3.3214
mass percent in phi range 3. to 4. is 0.0016

Grainsize phi classes: 1aii

number of records = 239
number and fraction in phi range -1. to 0. is 1, 0.4184
number and fraction in phi range 0. to 1. is 21, 8.7866
number and fraction in phi range 1. to 2. is 118, 49.3724
number and fraction in phi range 2. to 3. is 86, 35.9833
number and fraction in phi range 3. to 4. is 12, 5.0209
number and fraction in phi range 4. to 5. is 1, 0.4184

area percent in phi range -1. to 0. is 9.4317
area percent in phi range 0. to 1. is 24.3512
area percent in phi range 1. to 2. is 53.2314
area percent in phi range 2. to 3. is 12.5352
area percent in phi range 3. to 4. is 0.4371
area percent in phi range 4. to 5. is 0.0134

mass percent in phi range -1. to 0. is 29.3584
mass percent in phi range 0. to 1. is 27.2669
mass percent in phi range 1. to 2. is 38.2554
mass percent in phi range 2. to 3. is 5.0307
mass percent in phi range 3. to 4. is 0.0869
mass percent in phi range 4. to 5. is 0.0016

Corrected values
number and percent in phi range -1. to 0. is 1, 0.4184
number and percent in phi range 0. to 1. is 27, 11.2971
number and percent in phi range 1. to 2. is 132, 55.2301
number and percent in phi range 2. to 3. is 79, 33.0544

area percent in phi range -1. to 0. is 5.0177
area percent in phi range 0. to 1. is 29.5840
area percent in phi range 1. to 2. is 57.2888
area percent in phi range 2. to 3. is 8.1096

mass percent in phi range -1. to 0. is 13.6161
mass percent in phi range 0. to 1. is 37.5150
mass percent in phi range 1. to 2. is 45.7213
mass percent in phi range 2. to 3. is 3.1476

Grainsize phi classes: 1ai

number of records = 154
number and fraction in phi range 0. to 1. is 12, 7.7922
number and fraction in phi range 1. to 2. is 80, 51.9481
number and fraction in phi range 2. to 3. is 36, 23.3766
number and fraction in phi range 3. to 4. is 19, 12.3377
number and fraction in phi range 4. to 5. is 6, 3.8961
number and fraction in phi range below 5. is 1, 0.6494

area percent in phi range 0. to 1. is 25.8675
area percent in phi range 1. to 2. is 64.5580
area percent in phi range 2. to 3. is 8.0813
area percent in phi range 3. to 4. is 1.3880
area percent in phi range 4. to 5. is 0.1020
area percent in phi range below 5. is 0.0033

mass percent in phi range 0. to 1. is 37.2257
mass percent in phi range 1. to 2. is 58.5148
mass percent in phi range 2. to 3. is 3.8761
mass percent in phi range 3. to 4. is 0.3701
mass percent in phi range 4. to 5. is 0.0131
mass percent in phi range below 5. is 0.0002

Corrected values
number and percent in phi range 0. to 1. is 17, 11.0390
number and percent in phi range 1. to 2. is 89, 57.7922
number and percent in phi range 2. to 3. is 31, 20.1299
number and percent in phi range 3. to 4. is 15, 9.7403
number and percent in phi range 4. to 5. is 2, 1.2987

area percent in phi range 0. to 1. is 29.4219
area percent in phi range 1. to 2. is 65.5969
area percent in phi range 2. to 3. is 4.2992
area percent in phi range 3. to 4. is 0.6651
area percent in phi range 4. to 5. is 0.0169

mass percent in phi range 0. to 1. is 40.0004
mass percent in phi range 1. to 2. is 58.1986
mass percent in phi range 2. to 3. is 1.6546
mass percent in phi range 3. to 4. is 0.1447
mass percent in phi range 4. to 5. is 0.0016

APPENDIX 7
PIA AREA COUNTS

SAMPLE	Reading 1	2	3	4	5	Average
1ai						
tot qz	67	78	72	65	68	**70**
porosity	24	15	16	25	21	**20**
kaolin	3	1	1			**2**
qz o/g	7	5	8	9	8	**7**
gunk'		1	1	1	1	**1**
feld						
mica						
total	101	100	98	100	98	**99**

SAMPLE	Reading 1	2	3	4	5	Average
1aii upp						
tot qz	70	69	69	74	65	**69**
porosity	21	28	26	15	31	**24**
kaolin			2	5		**4**
qz o/g	4	3	3	4	4	**4**
gunk'	1					**1**
feld						
mica						
total	96	100	100	98	100	**99**

SAMPLE	Reading 1	2	3	4	5	Average
1a low						
tot qz	76	73	72	74	66	**72**
porosity	24	13	22	16	26	**20**
kaolin		13				**13**
qz o/g		2	3	5	3	**3**
gunk'				2	5	**4**
feld						
mica						
total	100	101	97	97	100	**99**

SAMPLE	Reading 1	2	3	4	5	Average
1bi						
tot qz	68	70	71	74	63	**69**
porosity	26	24	24	18	12	**21**
kaolin					21	**21**
qz o/g	4	4	3	2	2	**3**
gunk'				2	1	**2**
feld						
mica						
total	98	98	98	96	99	**98**

SAMPLE	Reading 1	2	3	4	5	Average
1bii						
tot qz	80	78	66	72	71	**73**
porosity	14	17	30	16	27	**21**
kaolin						
qz o/g	3	2	3	6	3	**3**
gunk'	1	1	1	2		**1**
feld						
mica						
total	98	98	100	96	101	**99**

SAMPLE	Reading 1	2	3	4	5	Average
1c						
tot qz	65	72	66	66	79	**70**
porosity	33	20	30	26	19	**26**
kaolin		5		1		**3**
qz o/g	3	4	2	4	3	**3**
gunk'	1	2	2		1	**2**
feld						
mica						
total	102	103	100	97	102	**101**

SAMPLE	Reading 1	2	3	4	5	Average
1di						
tot qz	70	70	72	66	61	**68**
porosity	16	22	24	26	13	**20**
kaolin	2				19	**11**
qz o/g	4	6	3	5	5	**5**
gunk'	5	1	1		1	**2**
feld						
mica						
total	97	99	100	97	99	**98**

SAMPLE	Reading 1	2	3	4	5	Average
1dii						
tot qz	74	81	70	74	65	**73**
porosity	20	13	23	17	27	**20**
kaolin	1	1	1	5	1	**2**
qz o/g	3	2	2		5	**3**
gunk'	1	4	1		1	**2**
feld			1	2		**2**
mica						
total	99	101	97	96	99	**98**

a	Reading					
SAMPLE	**1**	**2**	**3**	**4**	**5**	**Average**
1fi						
tot qz	72	76	68	68	75	**72**
porosity	18	21	22	24	15	**20**
kaolin					4	**4**
qz o/g	4	3	2	5	5	**4**
gunk'	6		5	3		**5**
feld						
mica						
total	100	100	97	100	99	**99**

	Reading					
SAMPLE	**1**	**2**	**3**	**4**	**5**	**Average**
1fii						
tot qz	70	71	71	63	67	**68**
porosity	22	24	22	19	17	**21**
kaolin				10	11	**11**
qz o/g	2	3	3	4	1	**3**
gunk'	3	1				**2**
feld			5			**5**
mica						
total	97	99	101	96	96	**98**

	Reading					
SAMPLE	**1**	**2**	**3**	**4**	**5**	**Average**
1g						
tot qz	79	64	81	69	64	**71**
porosity	13	33	16	14	23	**20**
kaolin	1		1	12	5	**5**
qz o/g	6	3	3	4	2	**4**
gunk'	1	1		1	4	**2**
feld						
mica						
total	100	101	101	100	98	**100**

	Reading					
SAMPLE	**1**	**2**	**3**	**4**	**5**	**Average**
2ai						
tot qz	76	68	77	71	65	**71**
porosity	12	18	17	21	24	**18**
kaolin	6	2	5	1		**4**
qz o/g	4	4			3	**4**
gunk'		3	1	5	4	**3**
feld						
mica	1					**1**
total	99	95	100	98	96	**98**

SAMPLE	Reading 1	2	3	4	5	Average
2aii						
tot qz	69	73	80	69	67	**72**
porosity	25	19	21	13	21	**20**
kaolin	3	5		9		**6**
qz o/g	3	2		6	6	**4**
gunk'				2	3	**3**
feld						
mica						
total	100	99	101	99	97	**99**

SAMPLE	Reading 1	2	3	4	5	Average
2aiii						
tot qz	73	75	68	75	71	**72**
porosity	21	14	25	21	24	**21**
kaolin		2		1		**2**
qz o/g	6	4	5	3	4	**4**
gunk'			1		1	**1**
feld						
mica						
total	100	95	99	100	100	**99**

APPENDIX 8
TRADITIONAL POINT COUNTING
AND CL POINT COUNTING

APPENDIX 8

(Traditional Point Count for 1aii upper)

Start position	Quartz	Porosity	Feldspar	Matrix	Kaolin	Qz o/g	Heavy	other	total per strip (should equal 28)
70/26	16	7		2		3			28
25	19	4		1	1	3			28
24	20	6			1	1			28
23	17	6		1	4				28
22	24	2		2					28
21	21	3		1	2	1			28
20	15	11			1	1			28
19	18	4			2	4			28
18	20	7		1					28
17	19	5			2	2			28
16	21	3		1	1	2			28
15	18	7		2	1				28
14	20	4			2	2			28
13	15	7		1	1	4			28
12	20	2		2	2	2			28
11	19	5	2		1	1			28
10	20	4	1	2		1			28
9	17	4			2	5			28
8	20	3			2	3			28
7	17	7			3	1			28
total	376	101	3	16	28	36	0	0	**560**
%	67.14286	18.03571	0.535714	2.857143	5	6.428571	0	0	**100**

(Traditional Point Count for 2aii)

Start position	Quartz	Porosity	Feldspar	Matrix	Kaolin	Qz o/g	Heavy	other	total per strip (should equal 28)
70/27	17	6	1	1		2	1		28
26	18	4		1	3	2			28
25	16	5		2	2	3			28
24	20	6				2			28
23	14	9			4	1			28
22	22	5				1			28
21	20	6			1	1			28
20	18	7		2	1				28
19	17	7		1	1	2			28
18	21	4		1	1	1			28
17	14	5		2	1	6			28
16	15	10			1	2			28
15	14	7		3	1	3			28
14	15	7		3		3			28
13	20	2		1	2	3			28
12	18	5			1	4			28
11	15	7		2	1	3			28
10	18	3			3	3		1	28
9	18	8			1	1			28
8	17	5		2	2	2			28
7	20	6		2					28
total	367	124	1	23	26	45	1	1	**588**
%	62.41497	21.08844	0.170068	3.911565	4.421769	7.653061	0.170068	0.170068	**100**

APPENDIX 8

(Point Count using CL micrograph – 1aii-upper)

Start position	Quartz	Porosity	Feldspar	Matrix	Kaolin	Qz o/g	Heavy	other	total per strip (should equal 30)
1	20	7			1	2			30
2	22	4				4			30
3	23	5				2			30
4	22	5				3			30
5	21	3				6			30
6	14	9				7			30
7	19	8				3			30
8	23	4				3			30
9	25	3				2			30
10	19	5			1	5			30
11	16	6		1		7			30
12	20	6			1	3			30
13	18	8			1	3			30
14	16	9			3	2			30
15	13	8			4	5			30
16	15	9		1	1	4			30
17	18	8				4			30
18	13	5				12			30
19	15	8			1	6			30
20	14	8		1	1	6			30
total	366	128	0	3	14	89	0	0	**600**
%	61	21.33333	0	0.5	2.333333	14.83333	0	0	**100**

(Point Count using CL micrograph – 2aii-upper)

Start position	Quartz	Porosity	Feldspar	Matrix	Kaolin	Qz o/g	Heavy	other	total per strip (should equal 30)
1	16	9				5			30
2	21	6		1		2			30
3	16	11			2	1			30
4	17	9			3	1			30
5	17	8			2	3			30
6	22	4			1	3			30
7	19	8				3			30
8	20	7				3			30
9	19	10			1				30
10	26	3				1			30
11	20	6				4			30
12	20	6				4			30
13	18	7				5			30
14	14	12				4			30
15	21	5				4			30
16	19	8				3			30
17	8	18				4			30
18	18	9				3			30
19	16	10				4			30
20	16	11				3			30
total	363	167	0	1	9	60	0	0	**600**
%	60.5	27.83333	0	0.166667	1.5	10	0	0	**100**

APPENDIX 9
3-STRIP POROSITY DATA

APPENDIX 9

3-Strip porosity data

2a l				Depth (m)	Depth (ft)
		28	**26**	1852.483999	6078
		15	18	1852.485419	6078.004659
	23	21	20	1852.486839	6078.009318
	17	19	14	1852.488259	6078.013977
	18	11	28	1852.489679	6078.018636
	25	16	18	1852.491099	6078.023295
	20	10	28	1852.492519	6078.027954
	8	24	15	1852.493939	6078.032613
	13	22	17	1852.495359	6078.037272
	21	10	19	1852.496779	6078.041931
	19	16	23	1852.498199	6078.04659
	21	18	17	1852.499619	6078.051249
	12	10	19	1852.501039	6078.055908
	24	21	22	1852.502459	6078.060567
	17	28	21	1852.503879	6078.065226
	25	23	23	1852.505299	6078.069885
	25	22	21	1852.506719	6078.074544
	19	27	19	1852.508139	6078.079203
	13	15	23	1852.509559	6078.083862
	15	8	19	1852.510979	6078.088521
	17	22	22	1852.512399	6078.09318
	25	10	24	1852.513819	6078.097839
	19	19	17	1852.515239	6078.102498
	26	25	24	1852.516659	6078.107157
	19	20	10	1852.518079	6078.111816
	31	16	20	1852.519499	6078.116476
	26	22	17	1852.520919	6078.121135
	27	22	21	1852.522339	6078.125794

2a ii	14	15	22	1852.520919	6078.121135
	13	21	18	1852.522339	6078.125794
	20	27	19	1852.523759	6078.130453
	17	23	22	1852.525179	6078.135112
	21	23	20	1852.526599	6078.139771
	22	24	19	1852.528019	6078.14443
	21	30	23	1852.529439	6078.149089
	21	23	15	1852.530859	6078.153748
	18	19	20	1852.532279	6078.158407
	20	10	18	1852.533699	6078.163066
	18	16	20	1852.535119	6078.167725
	22	14	11	1852.536539	6078.172384
	19	16	12	1852.537959	6078.177043
	11	13	19	1852.539379	6078.181702
	16	26	17	1852.540799	6078.186361
	24	17	16	1852.542219	6078.19102
	16	22	11	1852.543639	6078.195679
	26	14	15	1852.545059	6078.200338
	17	23	31	1852.546479	6078.204997
	14	24	34	1852.547899	6078.209656
	22	23	18	1852.549319	6078.214315
	28	18	25	1852.550739	6078.218974
	24	17	19	1852.552159	6078.223633
	19	21	22	1852.553579	6078.228292
	20	20	14	1852.554999	6078.232951
	17	16	20	1852.556419	6078.23761
	22	28	21	1852.557839	6078.242269
	14	22	20	1852.559259	6078.246928
	24	18	20	1852.560679	6078.251587
	19	16	19	1852.562099	6078.256246

2a iii	18	14	19	1852.566359	6078.270223
	23	18	20	1852.567779	6078.274882
	17	27	24	1852.569199	6078.279541
	14	22	25	1852.570619	6078.2842
	16	16	24	1852.572039	6078.288859
	10	14	16	1852.573459	6078.293518
	19	16	21	1852.574879	6078.298177
	18	22	23	1852.576299	6078.302836
	29	22	17	1852.577719	6078.307495
	20	20	22	1852.579139	6078.312154
	24	24	25	1852.580559	6078.316813
	16	21	23	1852.581979	6078.321472
	25	20	22	1852.583399	6078.326131
	32	23	23	1852.584819	6078.33079
	29	23	27	1852.586239	6078.335449
	18	18	32	1852.587659	6078.340108
	16	21	23	1852.589079	6078.344767
	17	24	16	1852.590499	6078.349427
	19	18	11	1852.591919	6078.354086
	6	6	14	1852.593339	6078.358745
	13	25	17	1852.594759	6078.363404
	24	18	27	1852.596179	6078.368063
	25	26	20	1852.597599	6078.372722
	21	18	22	1852.599019	6078.377381
	34	23	24	1852.600439	6078.38204
	24	28	23	1852.601859	6078.386699
	21	22	16	1852.603279	6078.391358
	23	19	24	1852.604699	6078.396017
	22	22	24	1852.606119	6078.400676
	16	17	12	1852.607539	6078.405335
	20	16	20	1852.608959	6078.409994
			19	1852.610379	6078.414653

1g	**26**	**18**	**27**	1854.122224	6083.375018
	27	10	15	1854.123644	6083.379677
	14	18	38	1854.125064	6083.384336
	16	18	24	1854.126484	6083.388995
	18	16	22	1854.127904	6083.393654
	19	14	31	1854.129324	6083.398313
	23	13	14	1854.130744	6083.402972
	17	18	23	1854.132164	6083.407631
	21	19	23	1854.133584	6083.41229
	18	18	19	1854.135004	6083.416949
	50	17	17	1854.136424	6083.421609
	35	11	24	1854.137844	6083.426268
	20	20	22	1854.139264	6083.430927
	13	17	14	1854.140684	6083.435586
	30	24	2	1854.142104	6083.440245
	22	19	23	1854.143524	6083.444904
	23	18	23	1854.144944	6083.449563
	17	23	20	1854.146364	6083.454222
	23	3	19	1854.147784	6083.458881
	26	17	13	1854.149204	6083.46354
	25	11	14	1854.150624	6083.468199
	17	15	14	1854.152044	6083.472858
	16	23	16	1854.153464	6083.477517
	14	10	16	1854.154884	6083.482176
	13	21	14	1854.156304	6083.486835
	11	26	30	1854.157724	6083.491494
	17	13	25	1854.159144	6083.496153
	19	15	14	1854.160564	6083.500812
	16	22	19	1854.161984	6083.505471
	26	17	23	1854.163404	6083.51013
	17	19	15	1854.164824	6083.514789
	16	17	33	1854.166244	6083.519448

1f I	**16**	**24**	**20**	1854.167664	6083.524107
	10	22	16	1854.169084	6083.528766
	16	15	27	1854.170504	6083.533425
	24	21	25	1854.171924	6083.538084
	19	9	30	1854.173344	6083.542743
	30	17	38	1854.174764	6083.547402
	29	23	21	1854.176184	6083.552061
	20	27	29	1854.177604	6083.55672
	18	17	13	1854.179024	6083.561379
	15	19	23	1854.180444	6083.566038
	14	9	12	1854.181864	6083.570697
	18	22	27	1854.183284	6083.575356
	21	16	12	1854.184704	6083.580015
	20	20	22	1854.186124	6083.584674
	18	21	17	1854.187544	6083.589333
	16	17	18	1854.188964	6083.593992
	22	25	21	1854.190384	6083.598651
	14	14	23	1854.191804	6083.60331
	22	28	30	1854.193224	6083.607969
	19	21	2	1854.194644	6083.612628
	35	21	0	1854.196064	6083.617287
	21	20	13	1854.197484	6083.621946
	25	20	16	1854.198904	6083.626605
		29	14	1854.200324	6083.631264
1f ii					
	23	**26**	**26**	1854.200324	6083.631264
	29	12	7	1854.201744	6083.635923
	23	13	7	1854.203164	6083.640582
	14	26	18	1854.204584	6083.645241
	12	36	21	1854.206004	6083.6499
	12	19	13	1854.207424	6083.65456
	5	18	22	1854.208844	6083.659219
	8	15	23	1854.210264	6083.663878
	11	21	19	1854.211684	6083.668537
	21	19	10	1854.213104	6083.673196
	12	17	19	1854.214524	6083.677855
	15	21	21	1854.215944	6083.682514
	9	24	24	1854.217364	6083.687173
	22	21	27	1854.218784	6083.691832
	18	26	19	1854.220204	6083.696491
	19	18	22	1854.221624	6083.70115
	22	17	18	1854.223044	6083.705809
	26	15	2	1854.224464	6083.710468
	21	16	16	1854.225884	6083.715127
	23	22	15	1854.227304	6083.719786
	21	17	16	1854.228724	6083.724445
	14	19	16	1854.230144	6083.729104
	15	20	11	1854.231564	6083.733763
	15	13	14	1854.232984	6083.738422
	13	13	16	1854.234404	6083.743081

1di	**23**	**26**	**20**	1854.402244	6084.293764
	25	22	22	1854.403664	6084.298423
	21	15	26	1854.405084	6084.303082
	16	21	19	1854.406504	6084.307741
	26	17	19	1854.407924	6084.3124
	20	23	23	1854.409344	6084.317059
	21	19	15	1854.410764	6084.321718
	10	24	17	1854.412184	6084.326377
	25	27	19	1854.413604	6084.331036
	17	23	21	1854.415024	6084.335695
	25	23	31	1854.416444	6084.340354
	28	13	21	1854.417864	6084.345013
	37	23	22	1854.419284	6084.349672
	24	25	7	1854.420704	6084.354331
	27	18	23	1854.422124	6084.35899
	10	20	34	1854.423544	6084.363649
	19	12	29	1854.424964	6084.368308
	27	27	27	1854.426384	6084.372967
	22	31	12	1854.427804	6084.377626
	25	21	26	1854.429224	6084.382285
	19	24	16	1854.430644	6084.386944
	14	25	14	1854.432064	6084.391603
	16	22	9	1854.433484	6084.396262
	22	21	8	1854.434904	6084.400921
	21	22	19	1854.436324	6084.40558
	27	30	24	1854.437744	6084.410239
1dii	**22**	**20**	**20**	1854.439164	6084.414898
	21	25	30	1854.440584	6084.419557
	22	27	27	1854.442004	6084.424216
	22	28	36	1854.443424	6084.428876
	25	25	33	1854.444844	6084.433535
	22	20	20	1854.446264	6084.438194
	21	10	10	1854.447684	6084.442853
	25	28	20	1854.449104	6084.447512
	22	26	25	1854.450524	6084.452171
	30	26	28	1854.451944	6084.45683
	13	22	29	1854.453364	6084.461489
	24	19	25	1854.454784	6084.466148
	22	28	37	1854.456204	6084.470807
	19	27	26	1854.457624	6084.475466
	19	17	18	1854.459044	6084.480125
	21	25	10	1854.460464	6084.484784
	22	20	17	1854.461884	6084.489443
	24	21	18	1854.463304	6084.494102
	23	23	16	1854.464724	6084.498761
	16	18	21	1854.466144	6084.50342
	22	19	22	1854.467564	6084.508079
	16	15	21	1854.468984	6084.512738
	23	13	17	1854.470404	6084.517397
	20	14	13	1854.471824	6084.522056

1c	**16**			1854.473244	6084.526715
	23	**14**		1854.474664	6084.531374
	33.6	12	**12**	1854.476084	6084.536033
	24.5	16	17	1854.477504	6084.540692
	35	23	14	1854.478924	6084.545351
	23.7	25	19	1854.480344	6084.55001
	20.2	19	22	1854.481764	6084.554669
	31	15	25	1854.483184	6084.559328
	27	29	21	1854.484604	6084.563987
	22	23	25	1854.486024	6084.568646
	22	21	20	1854.487444	6084.573305
	21	35	21	1854.488864	6084.577964
	25	26	14	1854.490284	6084.582623
	23	11	19	1854.491704	6084.587282
	22	19	19	1854.493124	6084.591941
	22	8	24	1854.494544	6084.5966
	20	19	20	1854.495964	6084.601259
	30	27	25	1854.497384	6084.605918
	19	21	15	1854.498804	6084.610577
	22	14	16	1854.500224	6084.615236
	25	23	31	1854.501644	6084.619895
	20	24	26	1854.503064	6084.624554
	20	22	17	1854.504484	6084.629213
	26	30	19	1854.505904	6084.633872
	21	24	28	1854.507324	6084.638531
	21	25	31	1854.508744	6084.64319
	16	21	15	1854.510164	6084.647849
	20	22	16	1854.511584	6084.652508
		23	30	1854.513004	6084.657167
1bi	**19**			1854.513004	6084.657167
	26	**30**		1854.514424	6084.661827
	22	21	**25**	1854.515844	6084.666486
	23	18	17	1854.517264	6084.671145
	21	19	26	1854.518684	6084.675804
	21	22	30	1854.520104	6084.680463
	24	19	20	1854.521524	6084.685122
	22	30	23	1854.522944	6084.689781
	22	15	22	1854.524364	6084.69444
	20	20	24	1854.525784	6084.699099
	29	27	23	1854.527204	6084.703758
	18	25	22	1854.528624	6084.708417
	29	26	20	1854.530044	6084.713076
	25	24	18	1854.531464	6084.717735
	33	36	18	1854.532884	6084.722394
	23	18	21	1854.534304	6084.727053
	16	27	22	1854.535724	6084.731712
	12	14	27	1854.537144	6084.736371
	13	21	19	1854.538564	6084.74103
	17	27	13	1854.539984	6084.745689

	29	**26**	**27**	1854.539984	6084.745689
1bii	31	26	9	1854.541404	6084.750348
	18	22	13	1854.542824	6084.755007
	18	22	23	1854.544244	6084.759666
	15	17	26	1854.545664	6084.764325
	16	21	20	1854.547084	6084.768984
	7	23	23	1854.548504	6084.773643
	11	18	31	1854.549924	6084.778302
	19	20	5	1854.551344	6084.782961
	12	9	9	1854.552764	6084.78762
	16	14	14	1854.554184	6084.792279
	25	12	13	1854.555604	6084.796938
	22	20	14	1854.557024	6084.801597
	6	21	14	1854.558444	6084.806256
	17	14	25	1854.559864	6084.810915
	16	19	21	1854.561284	6084.815574
	18	18	9	1854.562704	6084.820233
	24	16	33	1854.564124	6084.824892
	16	16	14	1854.565544	6084.829551
	16	9	24	1854.566964	6084.83421
	9	16	16	1854.568384	6084.838869
	16	22	23	1854.569804	6084.843528
1ai upper	**15**	**14**	**24**	1854.623444	6085.019521
	20	17	21	1854.624864	6085.02418
	20	23	18	1854.626284	6085.028839
	19	16	21	1854.627704	6085.033498
	26	12	17	1854.629124	6085.038157
	17	10	9	1854.630544	6085.042816
	9	15	11	1854.631964	6085.047475
	12	14	13	1854.633384	6085.052134
	23	11	18	1854.634804	6085.056793
	14	19	25	1854.636224	6085.061452
	20	14	20	1854.637644	6085.066111
	19	22	22	1854.639064	6085.07077
	18	29	15	1854.640484	6085.075429
	12	19	22	1854.641904	6085.080088
	16	18	21	1854.643324	6085.084747
	18	20	21	1854.644744	6085.089406
	23	21	14	1854.646164	6085.094065
	14	14	19	1854.647584	6085.098724
	24	13	17	1854.649004	6085.103383
	14	7	15	1854.650424	6085.108043

1a ii upper	**20**	**16**	**23**	1854.650424	6085.108043
	14	29	7	1854.651844	6085.112702
	15	21	17	1854.653264	6085.117361
	14	16	15	1854.654684	6085.12202
	23	23	9	1854.656104	6085.126679
	25	13	17	1854.657524	6085.131338
	29	17	25	1854.658944	6085.135997
	22	23	26	1854.660364	6085.140656
	12	19	22	1854.661784	6085.145315
	9	19	21	1854.663204	6085.149974
	7	10	19	1854.664624	6085.154633
	8	14	18	1854.666044	6085.159292
	21	20	21	1854.667464	6085.163951
	21	21	28	1854.668884	6085.16861
	12	23	15	1854.670304	6085.173269
	15	17	16	1854.671724	6085.177928
	15	15	17	1854.673144	6085.182587
	12	28	27	1854.674564	6085.187246
	16	19	14	1854.675984	6085.191905
	21	16	17	1854.677404	6085.196564
1a lower					
			30	1854.681664	6085.210541
	18	**17**	31	1854.683084	6085.2152
	6	23	23	1854.684504	6085.219859
	27	18	13	1854.685924	6085.224518
	12	24	21	1854.687344	6085.229177
	15	28	27	1854.688764	6085.233836
	20	30	24	1854.690184	6085.238495
	30	18	22	1854.691604	6085.243154
	20	21	20	1854.693024	6085.247813
	26	16	14	1854.694444	6085.252472
	21	17	11	1854.695864	6085.257131
	17	22	20	1854.697284	6085.26179
	22	18	12	1854.698704	6085.266449
	17	15	14	1854.700124	6085.271108
	12	12	14	1854.701544	6085.275767
	12	8	26	1854.702964	6085.280426
	8	16	23	1854.704384	6085.285085
	17	13	18	1854.705804	6085.289744
	19	18	15	1854.707224	6085.294403
	19	21	19	1854.708644	6085.299062
	21	20	23	1854.710064	6085.303721
	14	26	18	1854.711484	6085.30838
	18	19	5	1854.712904	6085.313039
	23	19	12	1854.714324	6085.317698
	17	16	12	1854.715744	6085.322357
	26	18	11	1854.717164	6085.327016
	21	19	25	1854.718584	6085.331675
	11	18	21	1854.720004	6085.336334
	16	14	19	1854.721424	6085.340994
	20	19	17	1854.722844	6085.345653
	12	20	16	1854.724264	6085.350312
	11	27	19	1854.725684	6085.354971
	21	25		1854.727104	6085.35963

APPENDIX 10
3-STRIP SPATIAL DISPLAYS

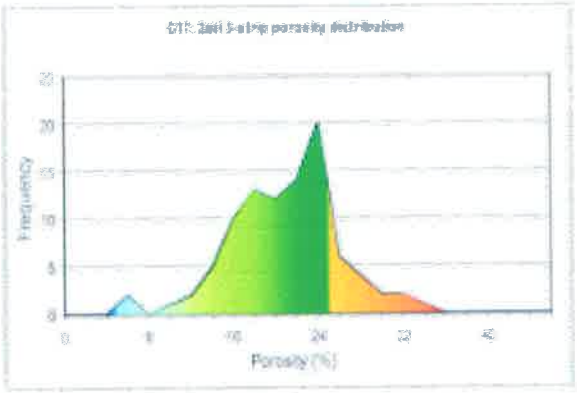
Frequency
Porosity (%)

2a III

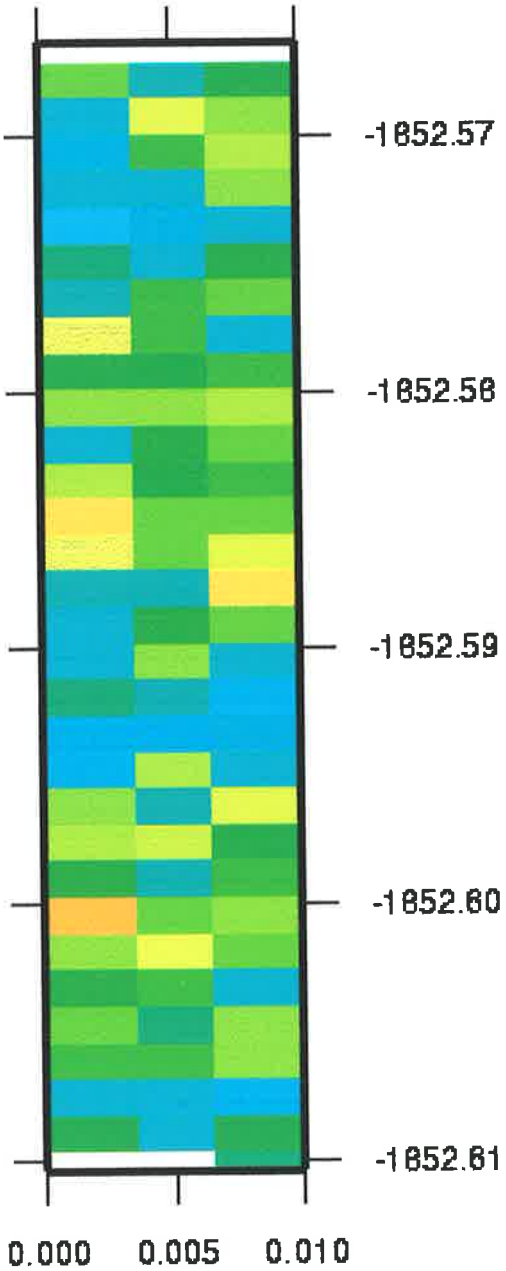
-1652.57
-1652.58
-1652.59
-1652.60
-1652.61
0.000
0.005
0.010

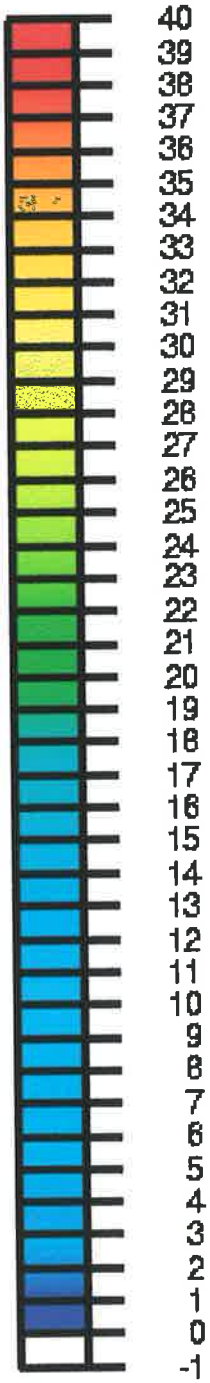
40
39
38
37
36
35
34
33
32
31
30
29
28
27
26
25
24
23
22
21
20
19
18
17
16
15
14
13
12
11
10
9
8
7
6
5
4
3
2
1
0
-1

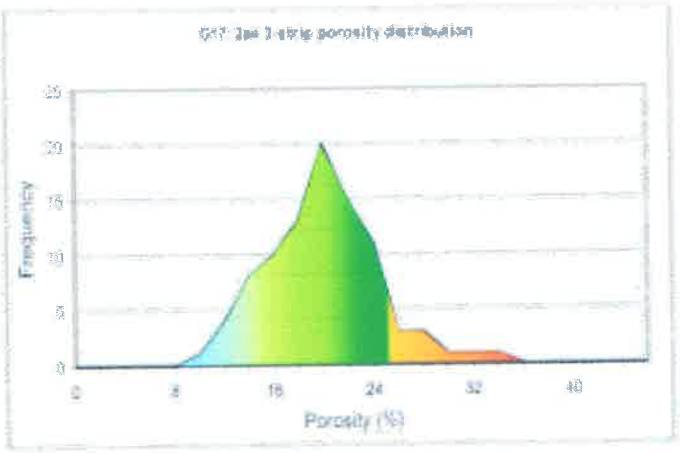
Frequency
Porosity (%)

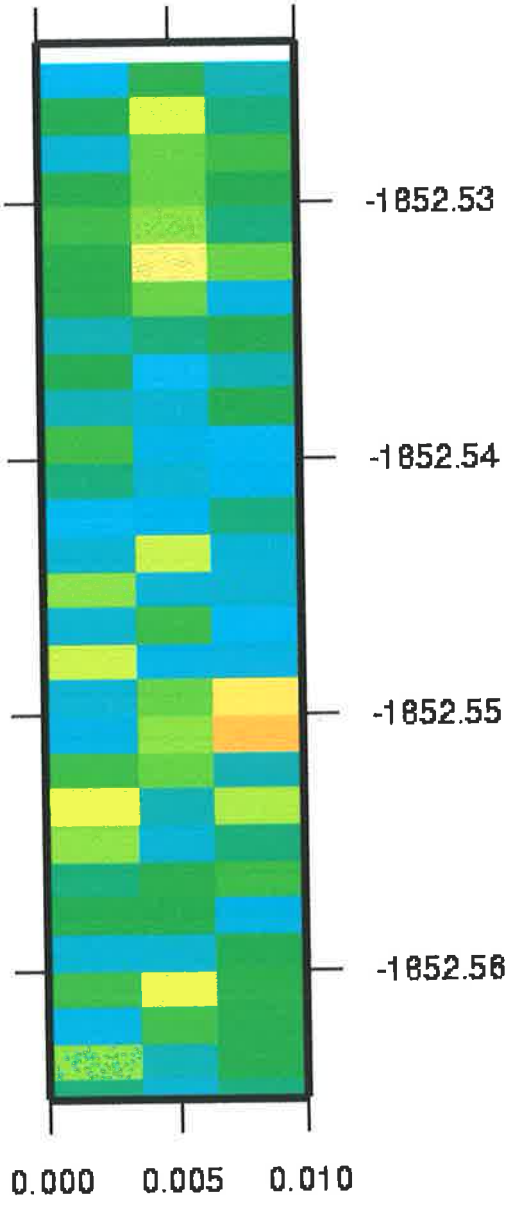
-1852.53
-1852.54
-1852.55
-1852.56
0.000
0.005
0.010

2a II

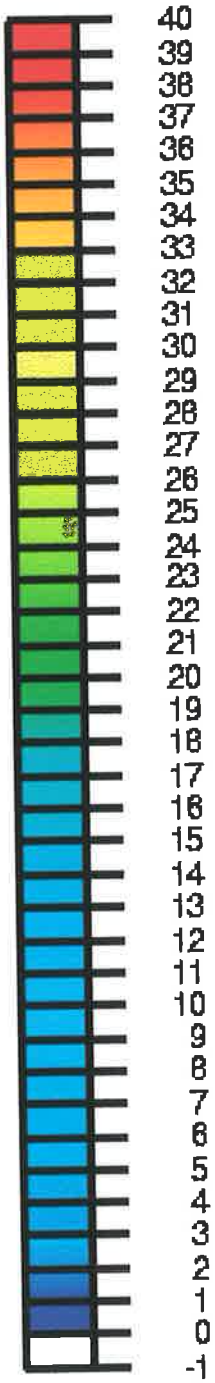
40
39
38
37
36
35
34
33
32
31
30
29
28
27
26
25
24
23
22
21
20
19
18
17
16
15
14
13
12
11
10
9
8
7
6
5
4
3
2
1
0
-1

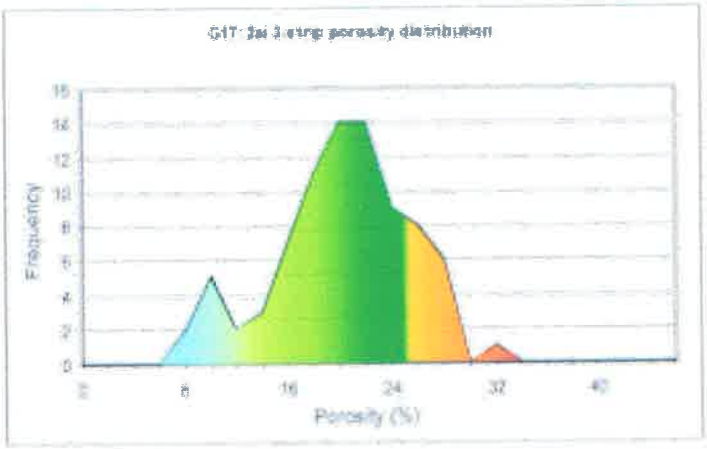
Frequency
Porosity (%)

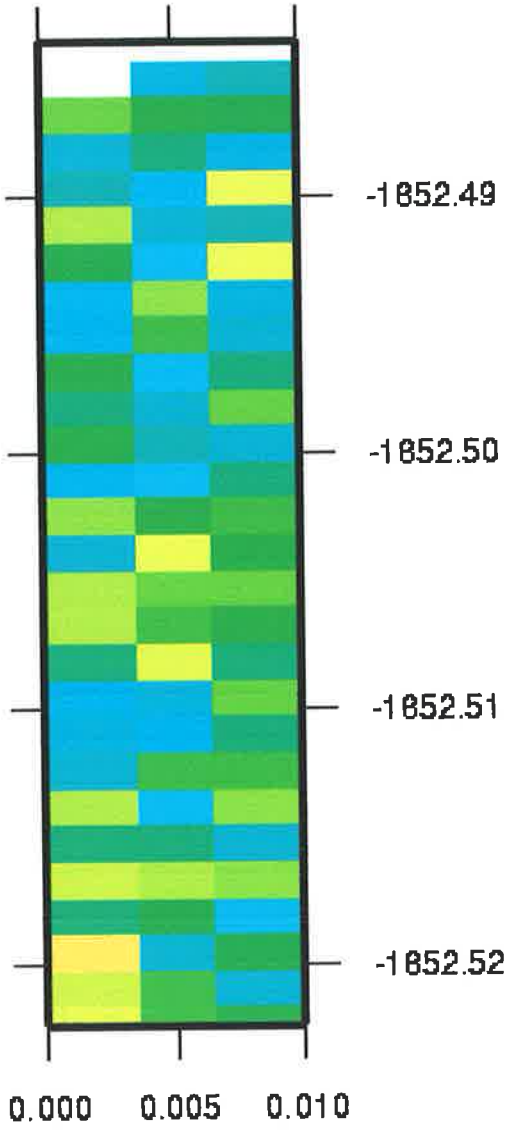
-1652.49
-1652.50
-1652.51
-1652.52
0.000
0.005
0.010

2a l

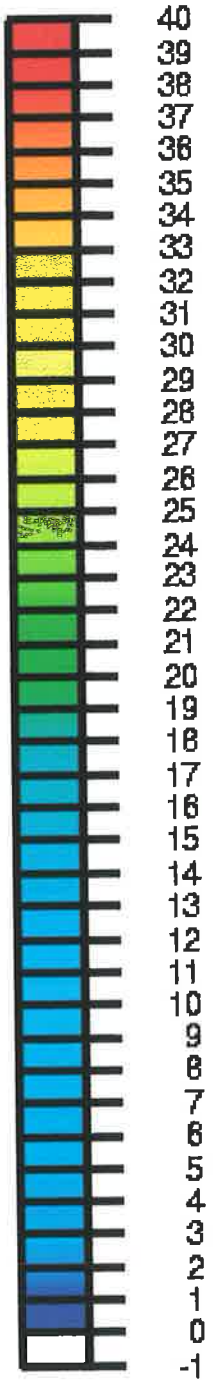
40
39
38
37
36
35
34
33
32
31
30
29
28
27
26
25
24
23
22
21
20
19
18
17
16
15
14
13
12
11
10
9
8
7
6
5
4
3
2
1
0
-1

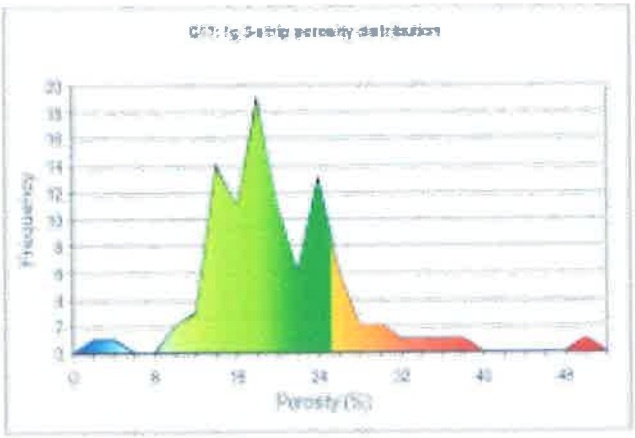
Frequency
Porosity (%)

1g

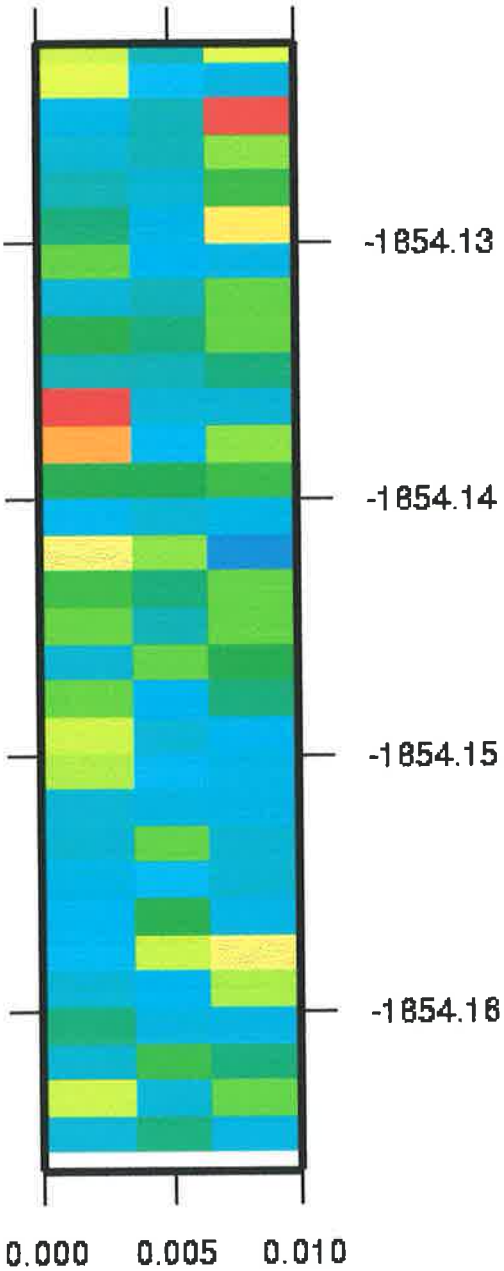
-1854.13
-1854.14
-1854.15
-1854.16
0.000
0.005
0.010

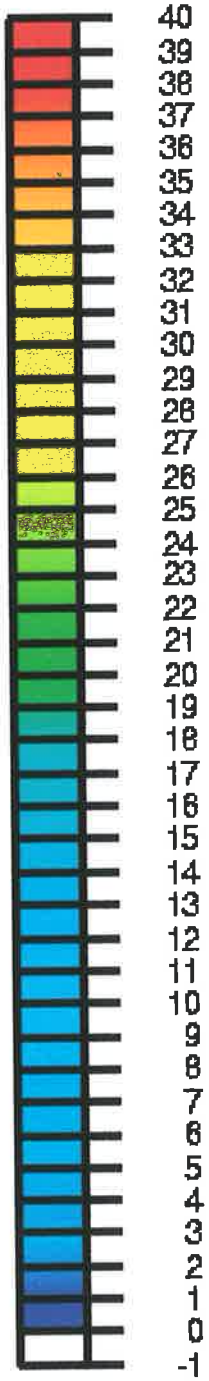
40
39
38
37
36
35
34
33
32
31
30
29
28
27
26
25
24
23
22
21
20
19
18
17
16
15
14
13
12
11
10
9
8
7
6
5
4
3
2
1
0
-1

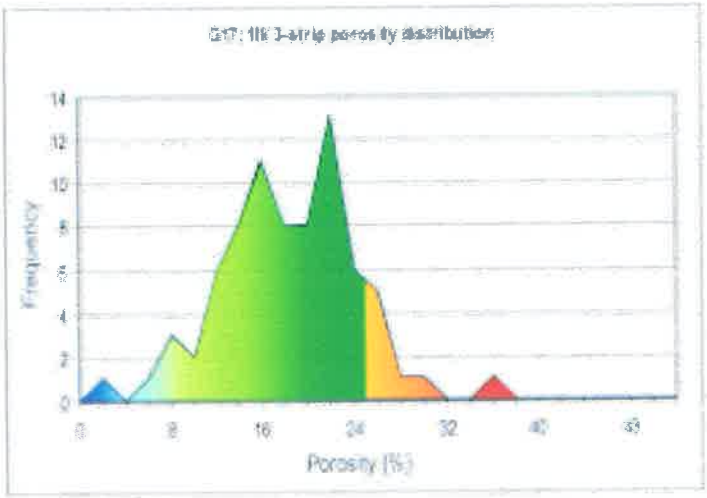
Frequency
Porosity (%)

1f II

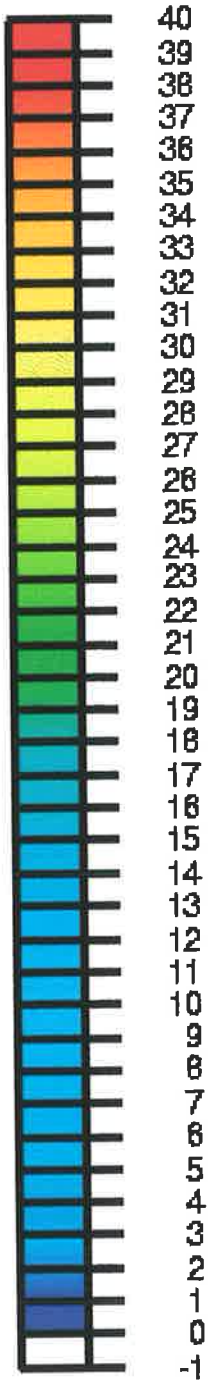
40
39
38
37
36
35
34
33
32
31
30
29
28
27
26
25
24
23
22
21
20
19
18
17
16
15
14
13
12
11
10
9
8
7
6
5
4
3
2
1
0
-1

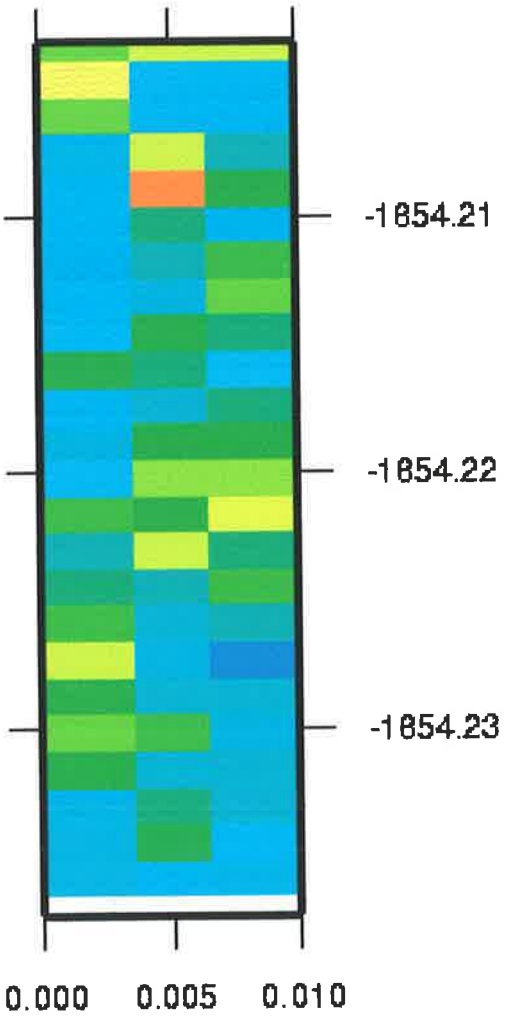
-1654.21
-1654.22
-1654.23
0.000
0.005
0.010

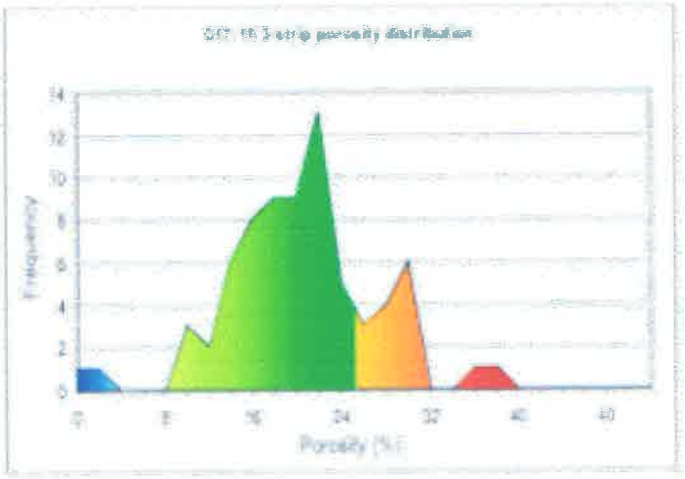
Frequency
Porosity (%)

1f l

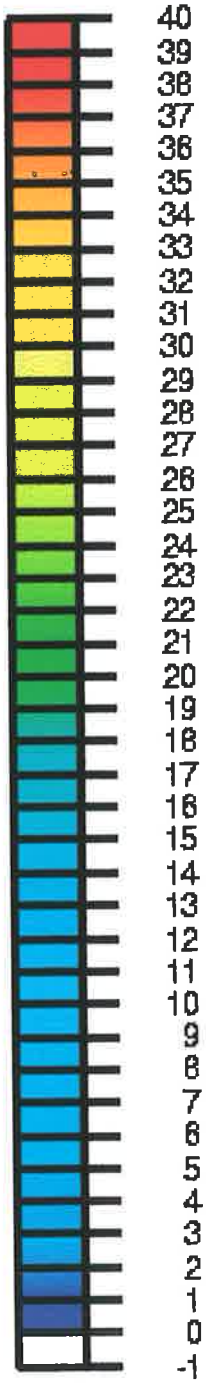
40
39
38
37
36
35
34
33
32
31
30
29
28
27
26
25
24
23
22
21
20
19
18
17
16
15
14
13
12
11
10
9
8
7
6
5
4
3
2
1
0
-1

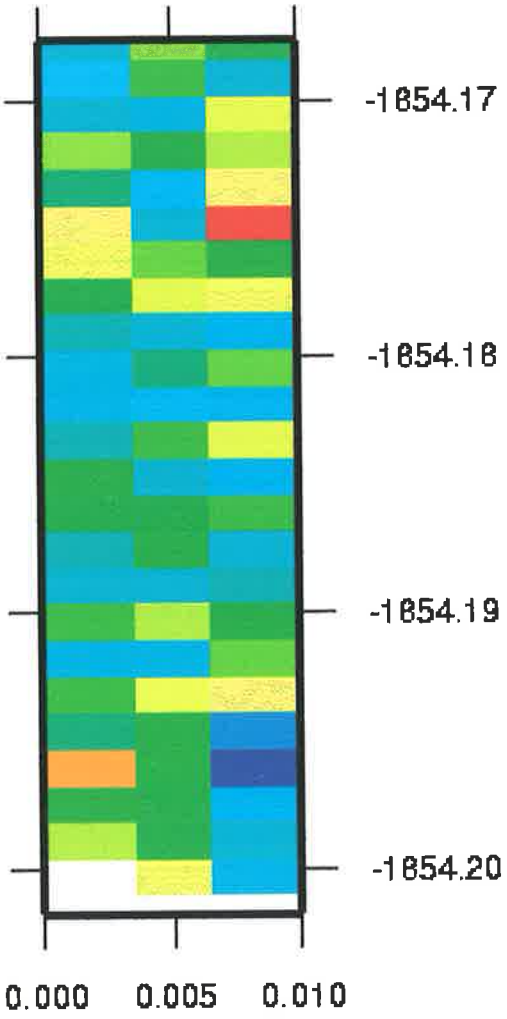
-1654.17
-1654.18
-1654.19
-1654.20
0.000
0.005
0.010

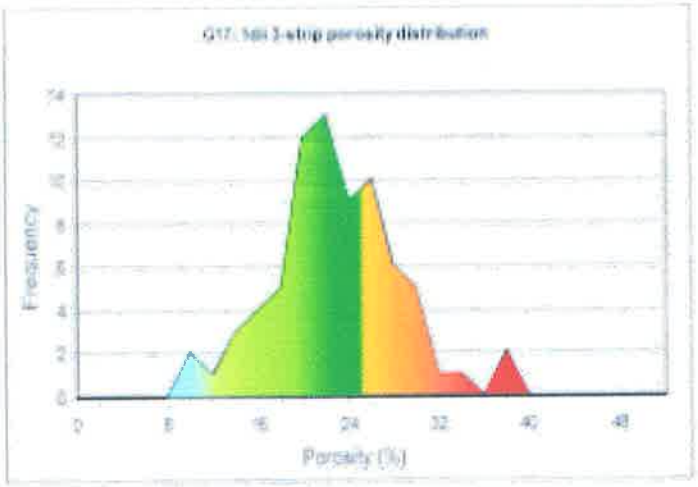
Frequency
Porosity (%)

1dll

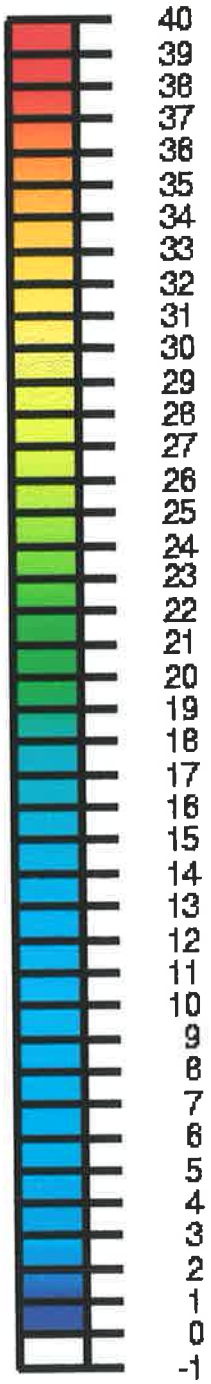
40
39
38
37
36
35
34
33
32
31
30
29
28
27
26
25
24
23
22
21
20
19
18
17
16
15
14
13
12
11
10
9
8
7
6
5
4
3
2
1
0
-1

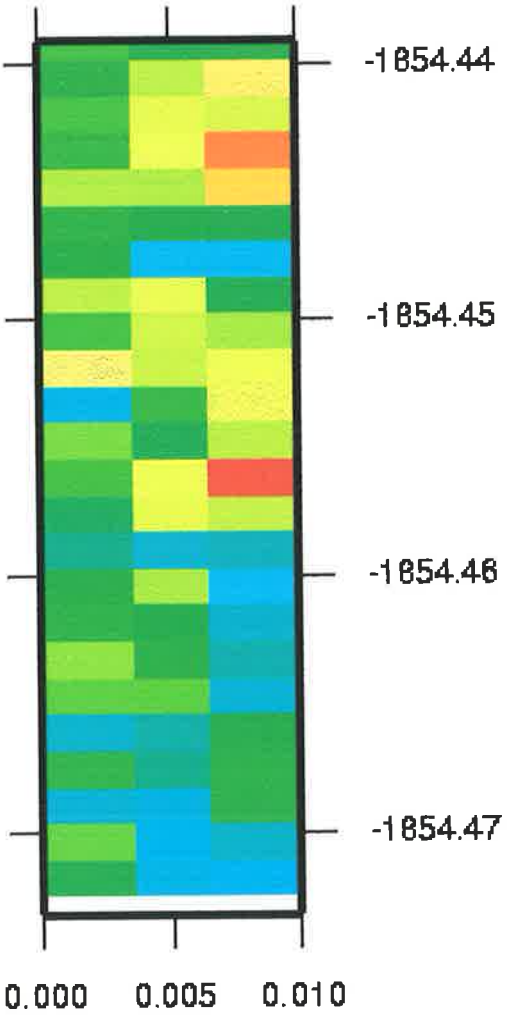
-1654.44
-1654.45
-1654.46
-1654.47
0.000
0.005
0.010

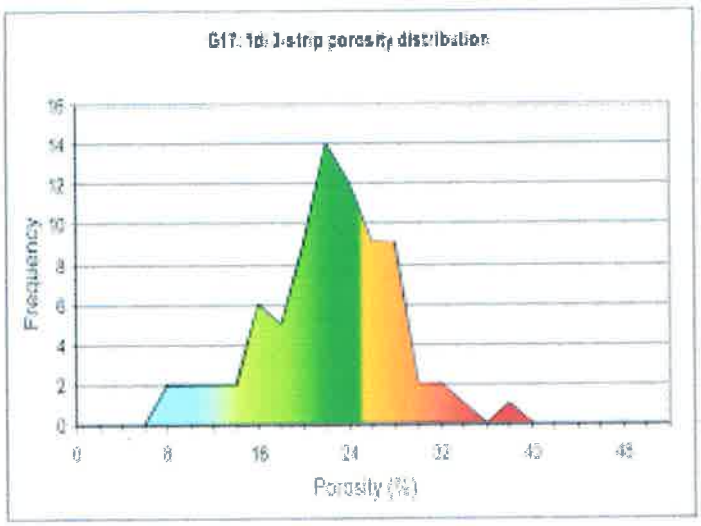
Frequency
Porosity (%)

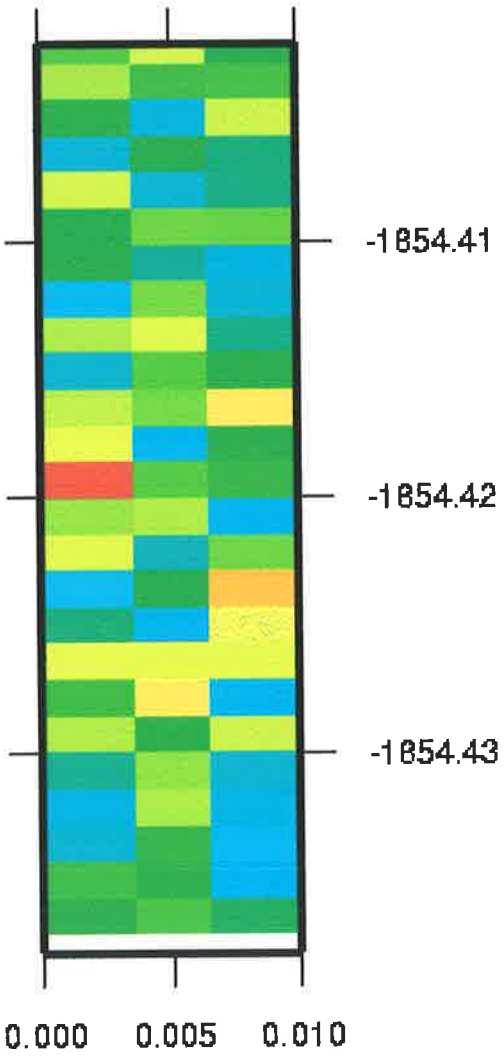
-1654.41
-1654.42
-1654.43
0.000
0.005
0.010

1dl

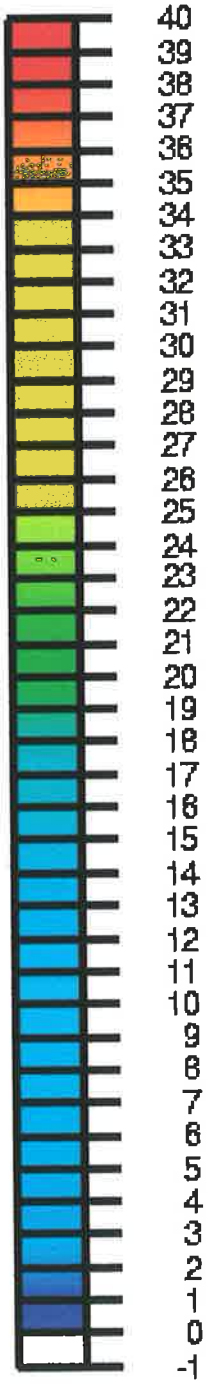
40
39
38
37
36
35
34
33
32
31
30
29
28
27
26
25
24
23
22
21
20
19
18
17
16
15
14
13
12
11
10
9
8
7
6
5
4
3
2
1
0
-1

1c

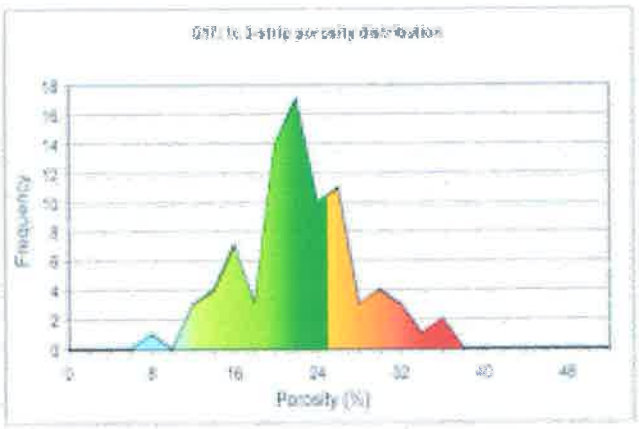
Frequency
Porosity (%)

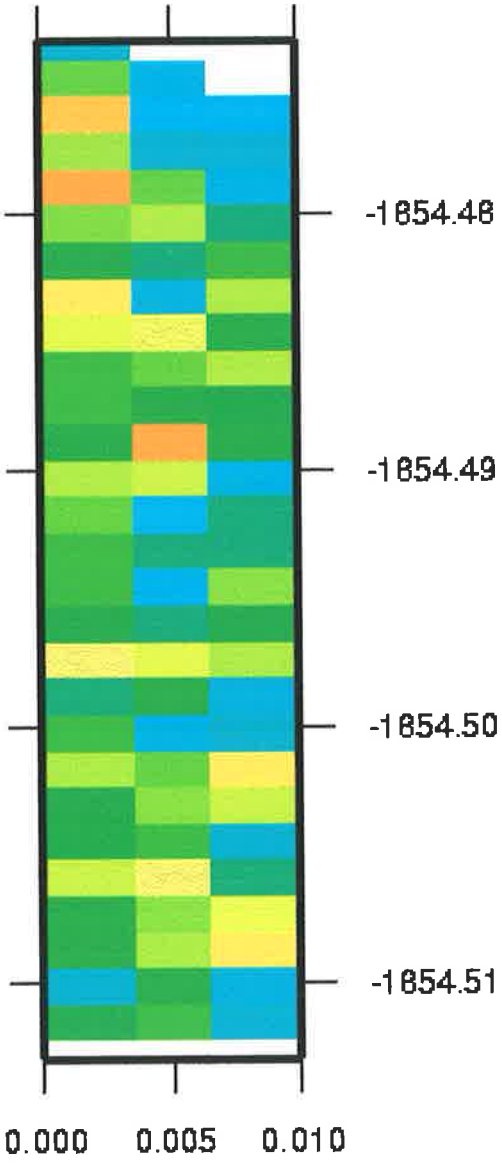
-1654.48
-1654.49
-1654.50
-1654.51
0.000
0.005
0.010

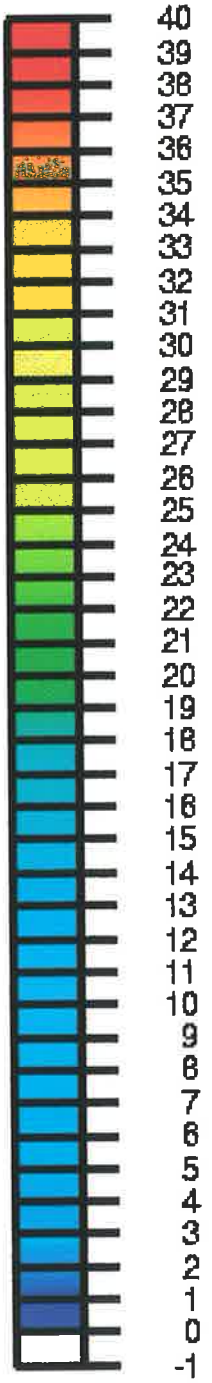
40
39
38
37
36
35
34
33
32
31
30
29
28
27
26
25
24
23
22
21
20
19
18
17
16
15
14
13
12
11
10
9
8
7
6
5
4
3
2
1
0
-1

1bl

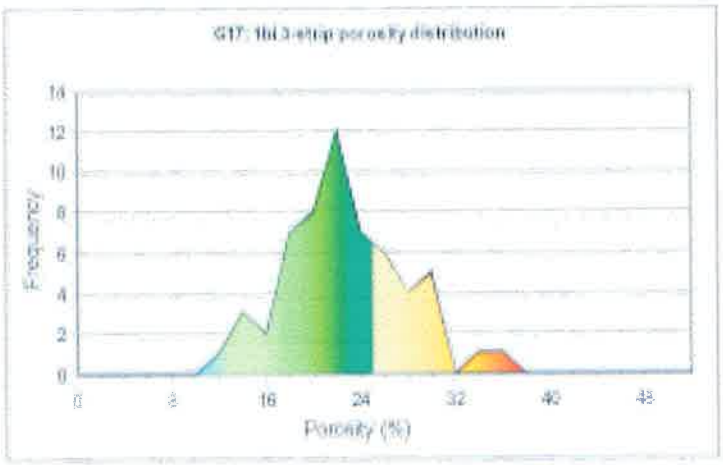
Frequency
Porosity (%)

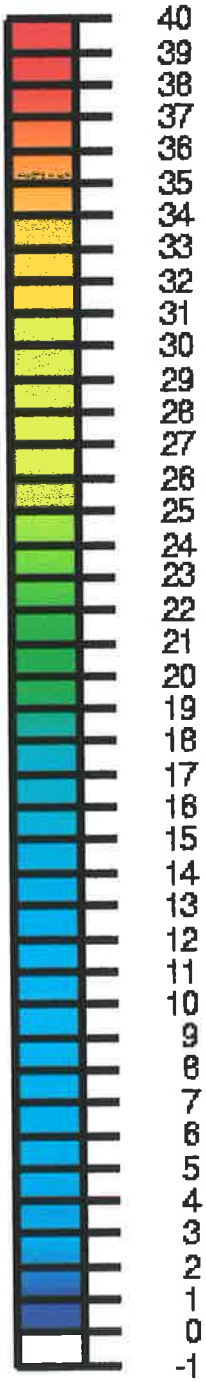
40
39
38
37
36
35
34
33
32
31
30
29
28
27
26
25
24
23
22
21
20
19
18
17
16
15
14
13
12
11
10
9
8
7
6
5
4
3
2
1
0
-1

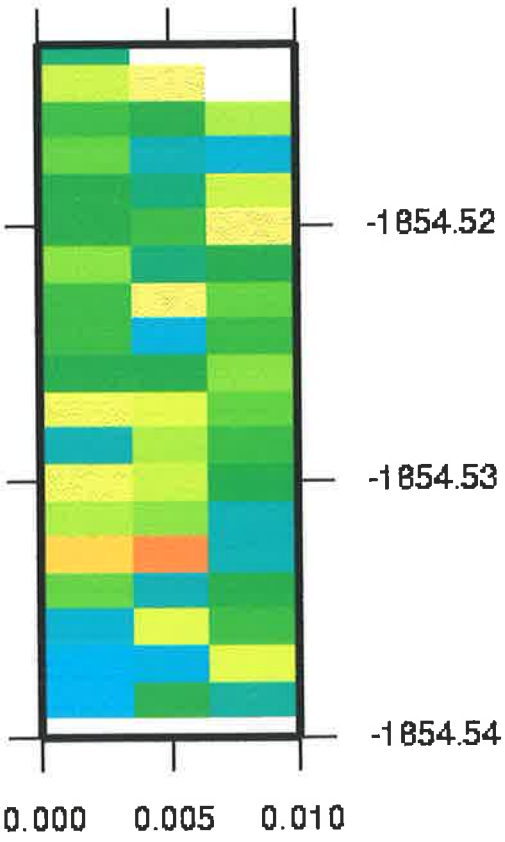
-1854.52
-1854.53
-1854.54
0.000
0.005
0.010

1bii

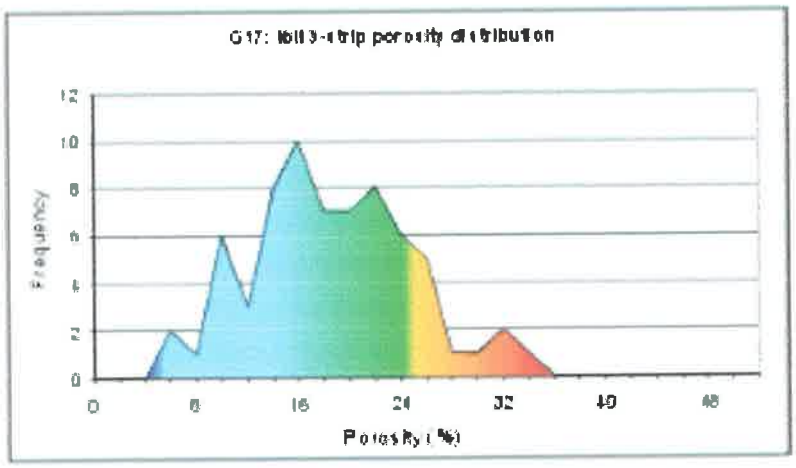
G17: bill3-4 trip porosity distribution
Frequency
Porosity (%)

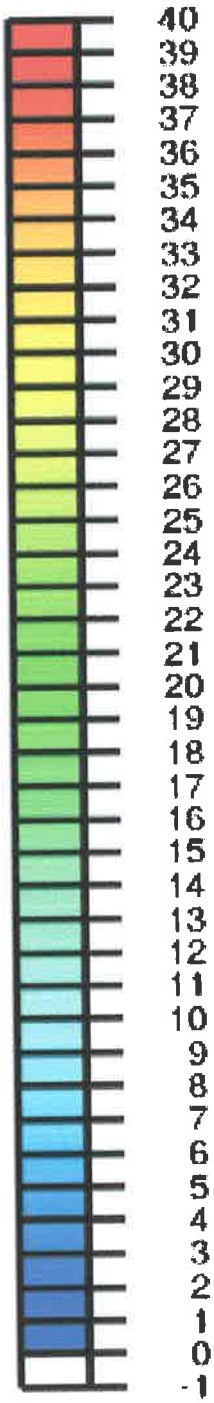
40
39
38
37
36
35
34
33
32
31
30
29
28
27
26
25
24
23
22
21
20
19
18
17
16
15
14
13
12
11
10
9
8
7
6
5
4
3
2
1
0
-1

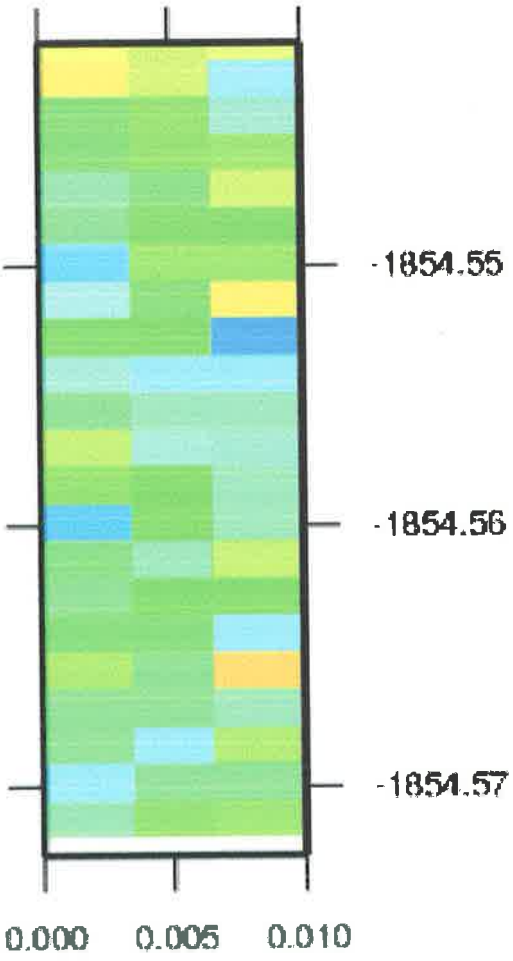
-1854.55
-1854.56
-1854.57
0.000
0.005
0.010

1ai upper

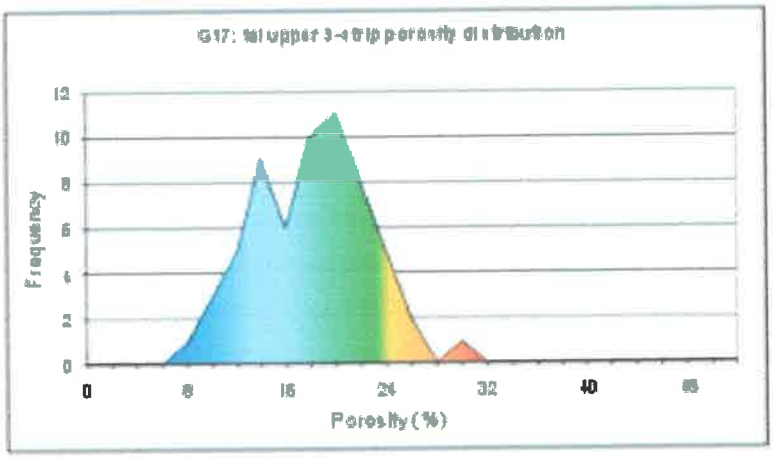
Frequency
Porosity (%)

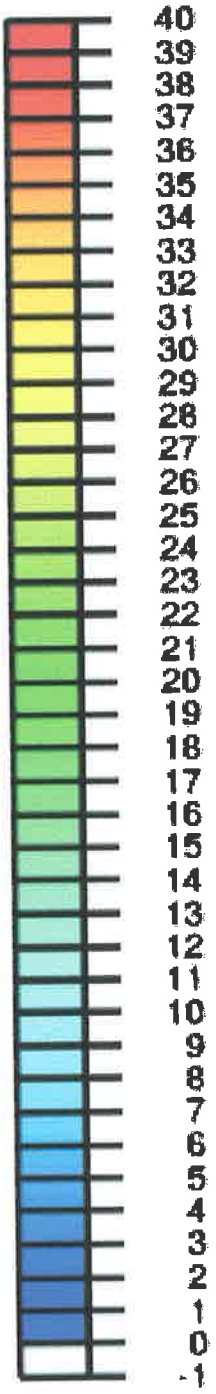
40
39
38
37
36
35
34
33
32
31
30
29
28
27
26
25
24
23
22
21
20
19
18
17
16
15
14
13
12
11
10
9
8
7
6
5
4
3
2
1
0
-1

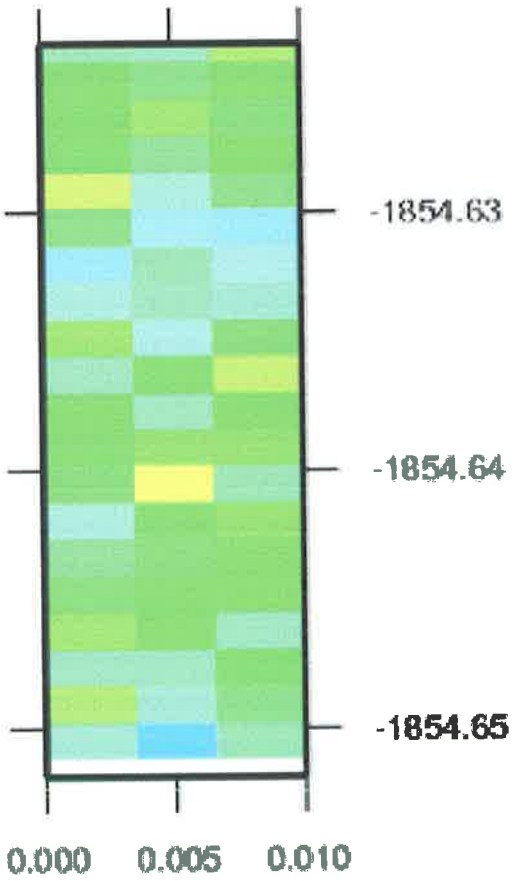
-1854.63
-1854.64
-1854.65
0.000
0.005
0.010

1a II upper

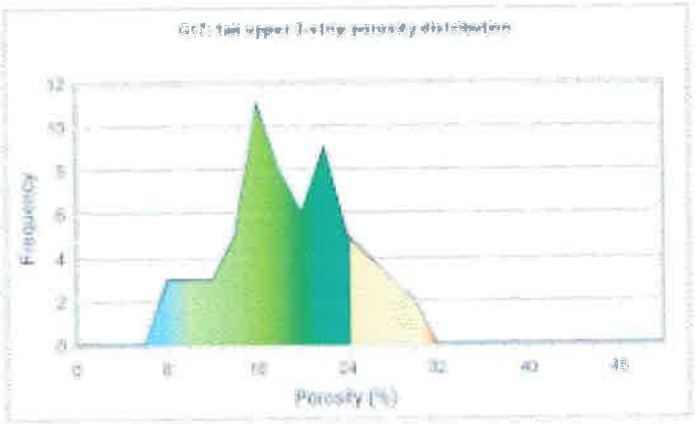
Frequency
Porosity (%)

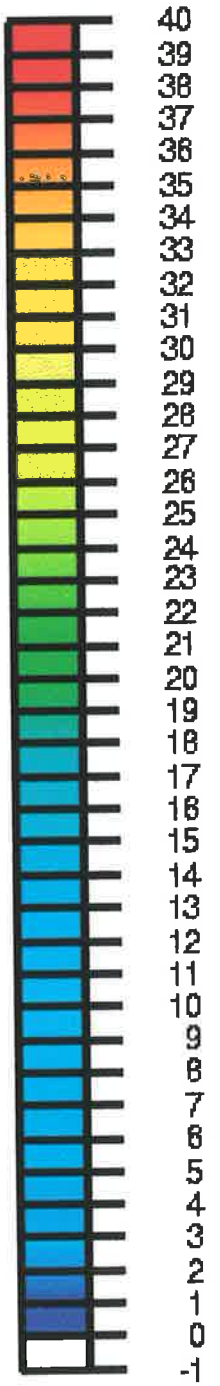
40
39
38
37
36
35
34
33
32
31
30
29
28
27
26
25
24
23
22
21
20
19
18
17
16
15
14
13
12
11
10
9
8
7
6
5
4
3
2
1
0
-1

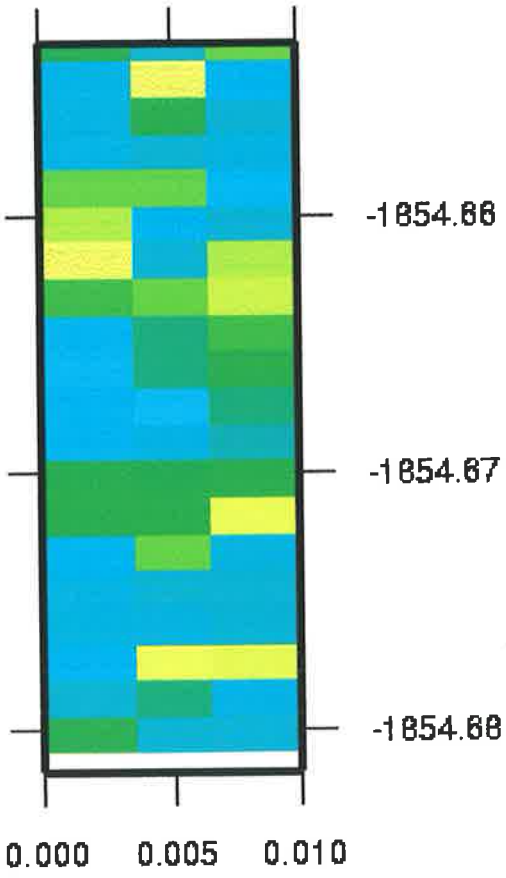
-1854.66
-1854.67
-1854.68
0.000
0.005
0.010

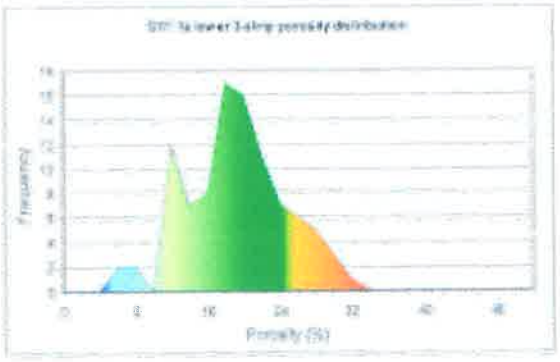

1a lower

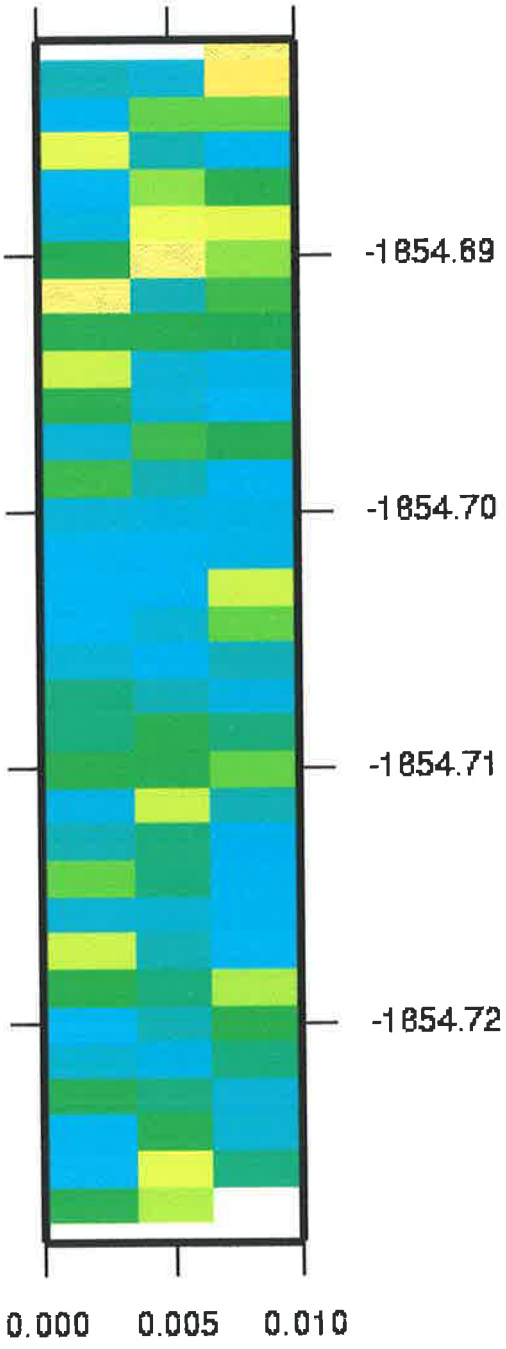
-1654.69
-1654.70
-1654.71
-1654.72
0.000
0.005
0.010

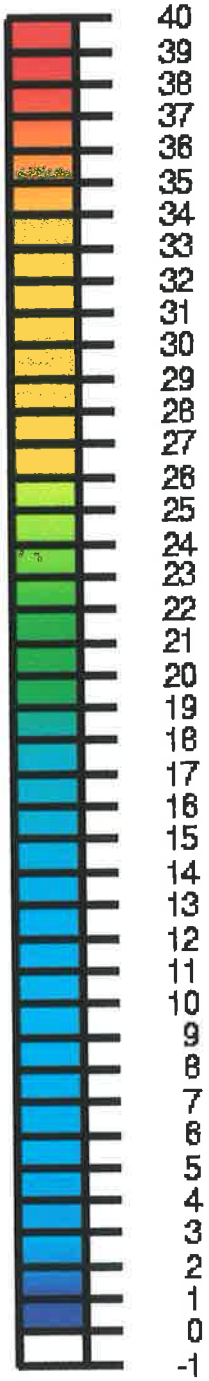
40
39
38
37
36
35
34
33
32
31
30
29
28
27
26
25
24
23
22
21
20
19
18
17
16
15
14
13
12
11
10
9
8
7
6
5
4
3
2
1
0
-1

APPENDIX 11

G17 HUTTON SANDSTONE THIN SECTIONS


G17 1a ii
upper
Shallowing
2.5 cm

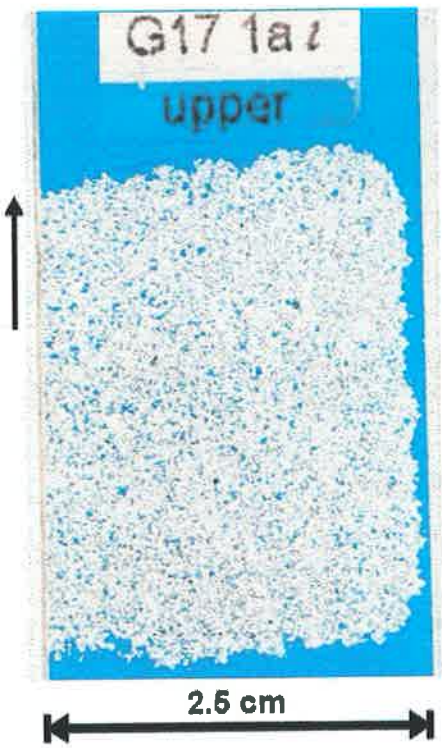
G17 1a i
upper
2.5 cm


G17 1a
lower
2.5 cm

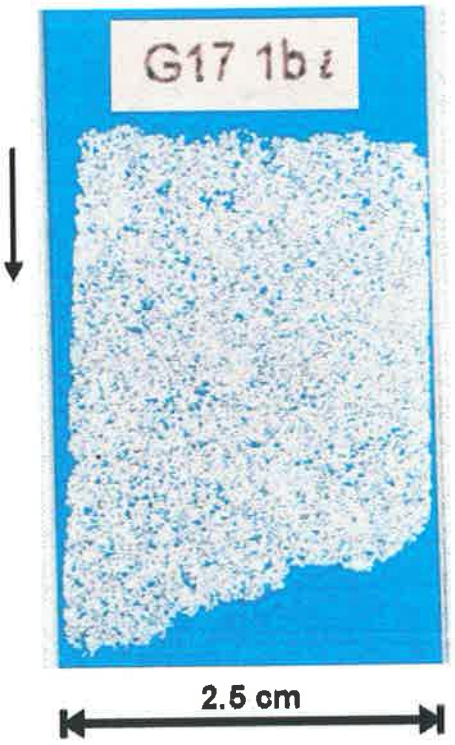
G17 1b i
2.5 cm

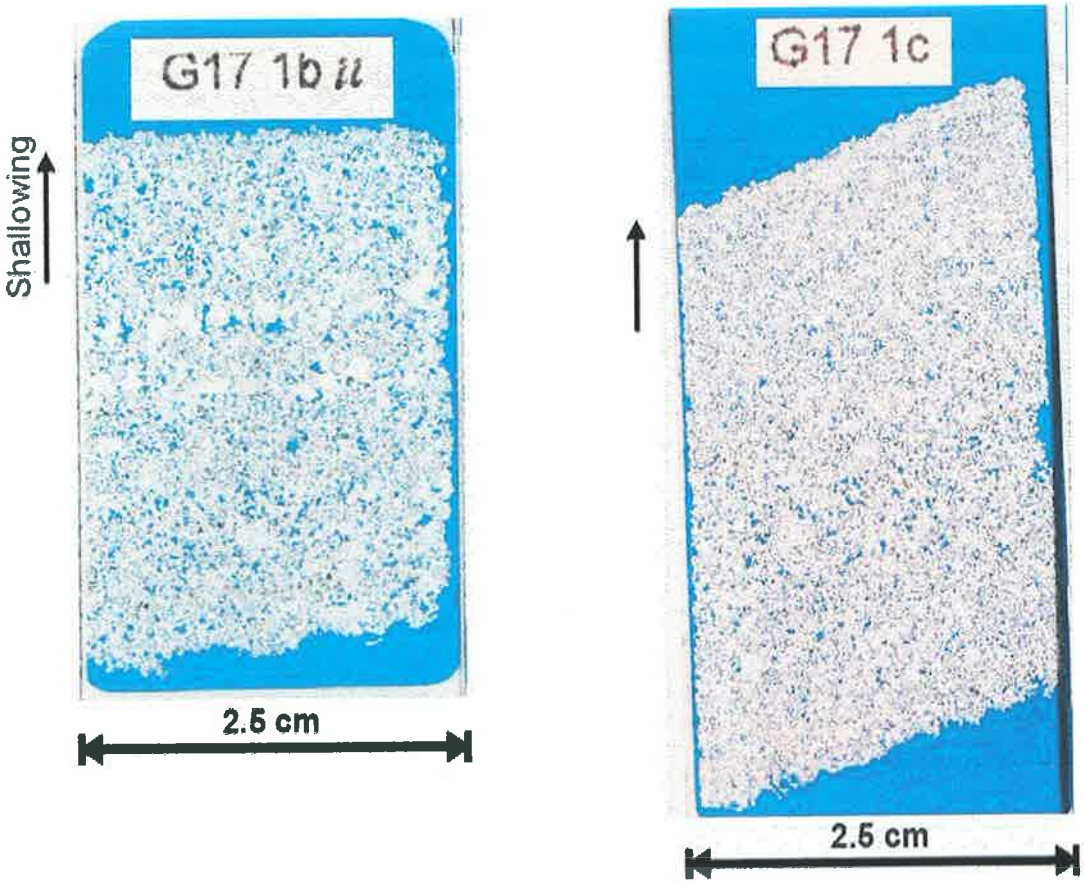
G17 1b ii
Shallowing
2.5 cm
G17 1c
2.5 cm
G17 1d i
2.5 cm
G17 1d ii
2.5 cm

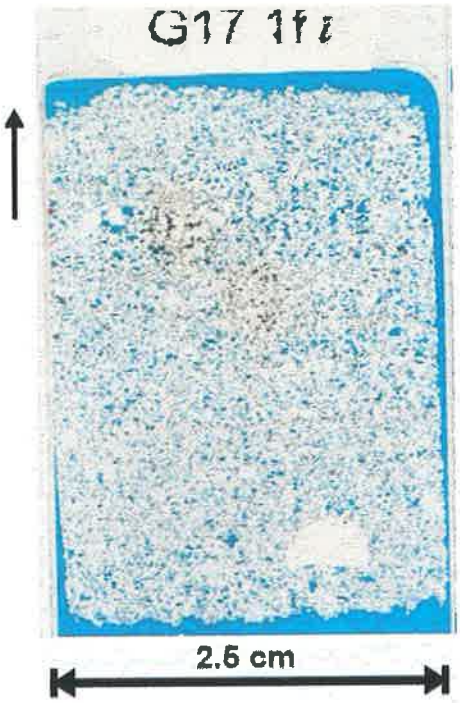
G17 1f i
2.5 cm

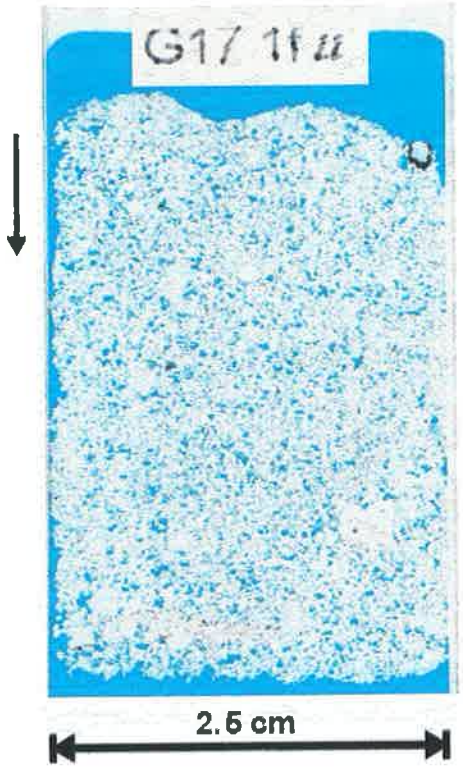
G17 1f ii
2.5 cm

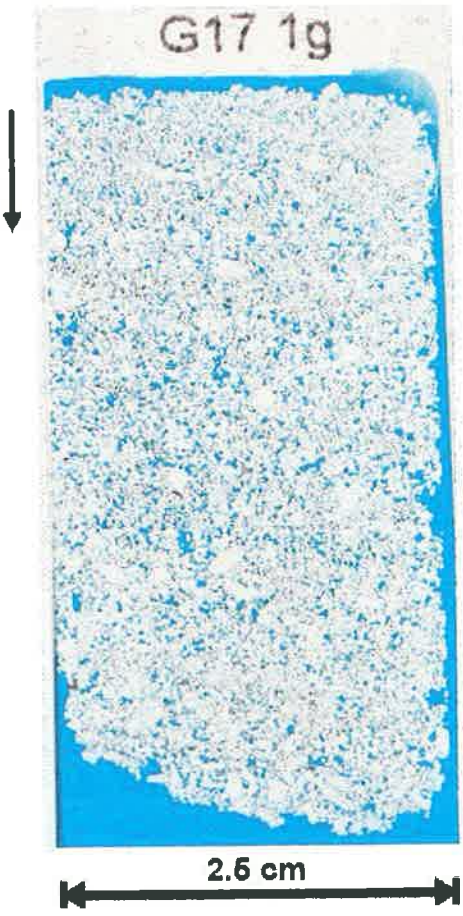
G17 1g
2.5 cm

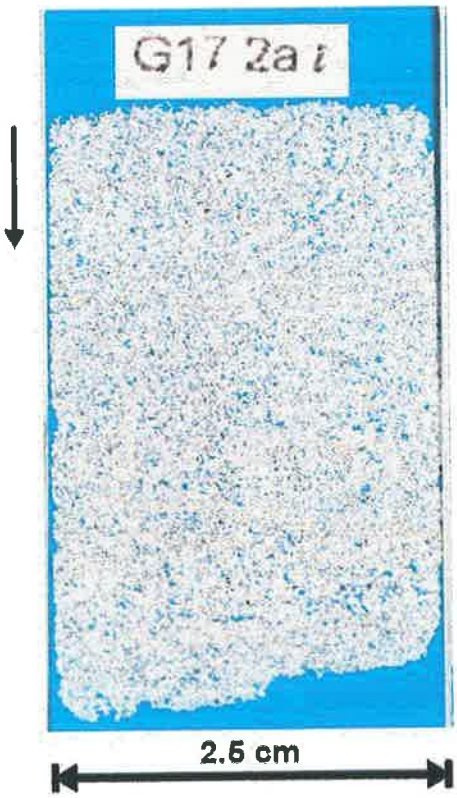
G17 2a i
2.5 cm

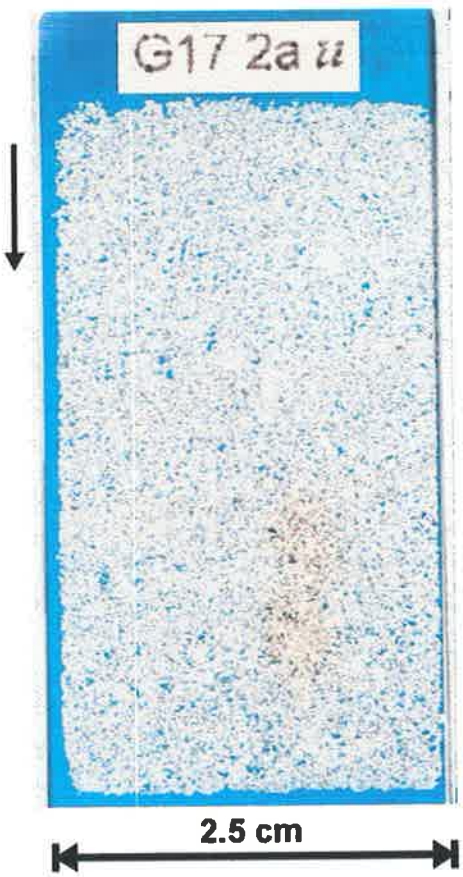
G17 2a ii
2.5 cm

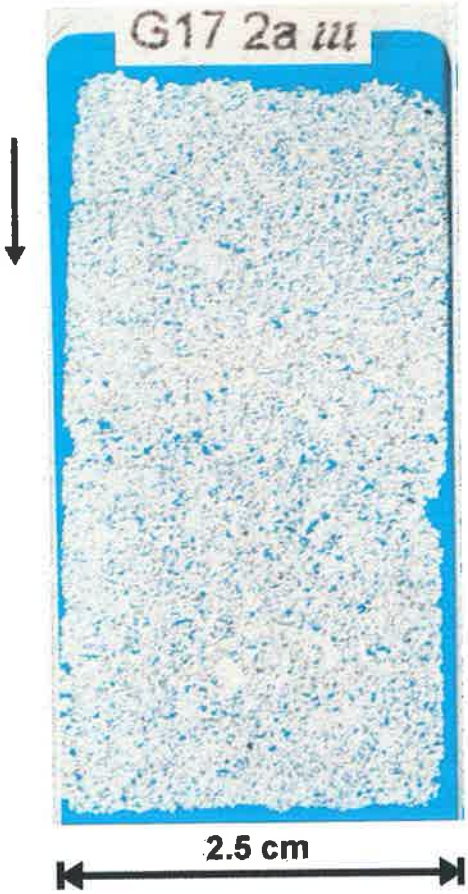
G17 2a iii
2.5 cm

APPENDIX 12

FULL COVERAGE POROSITY DATA

PSEUDO-COVERAGE DATA

(Thin sections 1aii upper & 2aii)

Slide Tail upper																								
	1000	1000	1000	1000	1000	1000	1000	1000	1000	1000	1000	1000	1000	1000	1000	1000	1000	1000	1000	1000	1000	1000		Depth (m)
1460	22	21	21	20	21	23	13	18	30	27	29	15	17	18	16	23	24	23	25	32	19	24		1854.65
1460	21	17	17	27	23	17	24	23	30	26	23	19	23	20	21	18	3	24	22	26	33	17		1854.652
1460	23	23	25	21	22	17	35	27	14	24	24	22	20	26	28	14	14	15	25	26	31	24		1854.653
1460	24	23	20	23	24	22	24	23	10	26	28	25	28	21	23	26	25	9	28	25	20	19		1854.655
1460	23	11	15	18	23	24	31	44	20	12	21	25	22	18	18	15	7	11	22	30	27	16		1854.656
1460	22	20	16	22	22	36	41	29	27	31	16	22	16	18	19	17	30	15	26	29	23	11		1854.658
1460	16	15	20	25	18	21	25	20	11	27	20	31	26	34	25	21	32	21	30	29	26	14		1854.659
1460	19	16	29	26	23	16	24	26	11	26	24	23	23	28	23	26	19	22	27	25	18	22		1854.661
1460	15	10	18	22	15	18	17	17	23	22	20	10	17	20	22	21	24	25	31	26	20	19		1854.662
1460	19	13	16	16	15	27	9	12	24	7	16	19	16	31	23	19	4	15	17	13	23	22		1854.664
1460	16	16	21	22	22	24	9	18	23	11	7	20	18	19	14	29	24	27	25	21	25	21		1854.665
1460	22	25	8	14	10	31	29	28	22	29	25	11	10	28	16	18	13	14	16	24	20	23		1854.666
1460	22	23	19	21	26	23	31	24	21	16	27	24	14	20	17	23	19	15	22	30	26	24		1854.668
1460	16	21	5	14	35	23	17	29	26	27	27	25	27	29	21	24	35	20	24	29	23	19		1854.669
1460	5	6	8	23	28	25	18	15	25	26	18	21	27	21	16	26	21	21	18	23	23	11		1854.671
1460	16	8	14	23	20	21	23	13	22	36	26	19	23	20	22	22	25	18	20	21	18	19		1854.672
1460	18	37	16	24	16	22	14	27	29	18	30	29	20	17	21	18	26	19	17	16	20	20		1854.674
1460	17	16	17	21	21	24	14	30	24	23	28	17	23	27	18	17	34	28	34	19	28	31		1854.675
1460	14	13	15	20	20	16	27	23	29	22	28	30	22	39	19	20	23	25	18	21	27	25		1854.677
1460	20	19	25	21	18	21	25	20	30	14	22	16	33	26	18	12	20	18	20	21	23			1854.678

		G17 2aii upper																						
		1000	1000	1000	1000	1000	1000	1000	1000	1000	1000	1000	1000	1000	1000	1000	1000	1000	1000	1000	1000	1000	1000	Depth
1460		25	30	28	17	10	16	25	24	19	23	28	19	24	20	16	21	22	16	18	18	20	20	1852.53
1460		25	32	24	26	26	29	24	13	7	22	27	23	13	21	23	26	14	11	27	17	28	12	1852.53
1460		25	22	19	18	14	16	26	19	22	18	26	20	14	19	23	15	20	20	25	20	17	18	1852.53
1460		14	18	17	21	20	23	22	21	15	22	17	26	21	18	21	16	19	18	20	18	21	20	1852.53
1460		25	17	19	22	12	18	20	20	16	26	16	16	18	15	18	20	13	16	31	17	45	24	1852.53
1460		24	26	16	15	24	19	23	13	22	18	24	17	26	18	25	14	20	25	25	17	15	23	1852.53
1460		28	17	18	22	18	24	25	28	21	25	20	20	20	13	17	13	9	13	13	13	14	12	1852.54
1460		23	25	22	17	14	15	10	17	17	21	22	19	18	9	22	19	13	13	10	16	14	21	1852.54
1460		20	14	10	9	17	14	14	15	14	23	21	12	19	13	20	22	16	24	10	21	28	18	1852.54
1460		21	20	17	22	18	25	29	18	20	21	21	15	20	20	17	19	18	17	30	25	15	17	1852.54
1460		22	18	23	19	14	15	24	26	24	12	18	24	17	19	25	17	17	16	17	13	24	22	1852.54
1460		19	27	23	25	23	25	15	15	24	5	14	22	21	26	16	19	12	14	14	17	16	12	1852.54
1460		24	26	22	15	20	15	14	13	15	9	6	20	18	13	19	15	14	11	15	25	16	14	1852.54
1460		22	17	12	9	14	13	12	17	14	24	21	12	8	19	19	22	45	8	14	28	35	23	1852.55
1460		25	17	10	14	23	18	25	25	14	18	23	19	15	37	19	24	24	22	25	21	15	28	1852.55
1460		31	21	24	31	26	18	18	24	22	21	19	27	18	19	17	18	20	21	31	21	22	27	1852.55
1460		29	21	18	26	25	22	29	20	23	25	25	26	17	19	21	23	16	15	16	7	20	22	1852.55
1460		19	20	17	22	19	9	20	22	11	21	19	25	25	21	23	26	18	16	17	20	24	12	1852.55
1460		18	26	15	18	18	9	18	32	21	21	18	19	24	23	22	35	22	22	19	18	30	20	1852.55
1460		21	30	26	20	23	20	23	23	23	27	20	27	25	19	21	18	15	26	19	21	13	19	1852.55
1460		24	27	27	26	21	25	19	26	25	22	23	19	20	23	29	17	17	23	23	12	19	21	1852.56
1460		18	22	19	20	19	24	19	29	26	24	25	20	24	20	23	18	27	25	18	15	17	21	1852.56

	1aii upper		**Pseudo 2.5x magnification data**										Depth
	20.25	21.25	21	19.5	28.25	21.5	19.5	19.5	18.5	26.25	23.25		1854.65
	23.25	22.25	21.25	27.25	18.5	24.75	23.75	22.75	15.75	26	23.5		1854.653
	19	17.75	26.25	36.25	22.5	21	18.5	17.25	15.75	26.75	19.25		1854.656
	16.5	25	19.5	23.75	18.75	24.5	27.75	23.75	23.5	27.75	20		1854.659
	14.25	18	18.75	13.75	19	16.25	21	21.25	17	21.75	21		1854.662
	20.25	16.25	21.75	21	21.25	15.75	18.75	19.25	19.5	21.5	22.25		1854.665
	20.5	14.75	26.75	25.25	22.5	25.75	22.5	21.25	22.25	26.25	23		1854.668
	8.75	17	23.5	17.25	27.25	21	22.75	21.5	21.25	20.5	17.75		1854.671
	22	19.5	20.75	21.25	23.5	26	21.75	18.5	26.75	21.5	24.75		1854.674
	16.5	20.25	18.75	23.75	23.75	24	30	17.25	21.5	20	25		1854.677

APPENDIX 13

RANDOM NUMBER GENERATOR

```
function out=randave(in,num)
%function out=randave(in,num)
%
%Function to select a randome number of samples from a dataset
%and then calculate the average of those samples
%
%Parameters
%in:  input matrix
%num: number of samples to select

%calculate how many data points in matrix
[cols,rows]=size(in);
ind=cols*rows;

%eliminate null value
ind=ind-1;

%select random samples
count=0;
while(count< 1)
    rnd=round(rand*ind);
    if(rnd~=0)
        index=rnd;
        count=count+1;
    end
end

while(count< num)
    rnd=round(rand*ind);
    if(rnd~=0)
        test=find(index==rnd);
        if(isempty(test))
            index=[index rnd];
            count=count+1;
        end
    end
end

%calculate mean of selected samples
out=mean(in(index));
```

```
function out=sampanal(in,num,iter)
%function out=sampanal(in,num,iter)
%
%Function to analyse the effect of sample size on average porosity
%
%Parameters
%in:     matrix of samples
%num:    vector of sample sizes to be used
%iter:   number of times the average should be calculated for each sample size

LastSample=length(num);

for(WhichSample=1:LastSample)
   for(Iteration=1:iter)
      out(WhichSample,Iteration)=randave(in,num(WhichSample));
   end
end
```

APPENDIX 14

10x & 50x MAGNIFICATION POROSITY DATA

SAMPLE 1aii upper		50x-magnification data									
Field of view:	x=	150 microns									
	y=	100 microns									
	100	100	100	100	100	100	100	100	100	100	
150	76	26	7	0	11	1	15	13	16	4	
150	25	2	6	21	0	0	5	33	27	10	
150	25	1	10	0	3	34	15	6	30	12	
150	12	26	61	2	15	48	9	1	6	20	
150	2	7	38	26	3	0	0	0	1	1	
150	27	14	20	1	20	16	1	0	7	47	
150	8	9	3	0	0	14	37	8	35	4	
150	8	0	4	25	18	6	5	15	54	28	
150	22	11	3	2	3	5	33	0	19	3	
150	3	57	19	38	76	29	15	4	6	3	
150	22	64	1	0	2	80	29	0	0	16	
150	20	0	0	10	8	0	5	27	1	26	
150	28	1	0	0	4	12	5	0	6	2	
150	13	33	10	1	45	28	18	11	37	72	
150	14	25	5	2	22	6	5	13	0	12	
150	44	24	2	0	34	54	29	62	23	17	
150	7	27	42	24	39	5	24	93	98	41	
150	39	7	23	70	28	33	0	23	56	21	
150	2	1	0	24	1	28	53	0	0	0	
150	13	0	0	3	3	7	54	61	11	6	
150	35	14	8	55	26	4	0	3	12	0	
150	45	19	6	12	3	1	0	0	5	39	
150	0	0	8	1	0	0	45	60	44	53	
150	1	4	51	86	32	2	1	69	40	0	
150	0	0	11	44	25	2	23	30	10	0	

	SAMPLE 1aii		**10x-magnification data**				fov (length)	725microns	
							fov (width)	480microns	
		480	480	480	480	480	480	480	480
725		11	15	25	19	14	31	15	34
725		29	18	20	21	14	34	23	28
725		28	18	17	31	25	21	34	26
725		12	19	18	14	41	10	20	18
725		24	12	22	14	15	21	11	4
725		16	19	29	19	36	25	16	4
725		26	25	26	17	29	24	21	14
725		16	27	23	3	22	12	9	24
725		15	12	21	12	19	6	7	4
725		22	26	27	15	25	45	24	27
725		11	25	26	16	20	23	23	33
725		22	41	30	15	27	21	17	9
725		14	26	6	15	19	28	2	5
725		21	14	27	34	15	17	7	5
725		30	13	23	27	14	28	40	18
725		20	15	23	26	15	15	4	11
725		2	6	9	26	20	15	19	21
725		22	22	15	15	18	5	19	30
725		3	25	19	18	12	6	5	17
725		7	24	17	12	7	5	4	9
725		18	11	19	9	7	14	17	26
725		5	10	12	9	12	40	24	20
725		5	17	25	20	42	26	10	15
725		12	25	20	20	15	25	11	25
725		19	23	14	25	12	8	5	26
725		18	17	21	24	16	27	18	16
725		20	33	22	37	23	22	27	11
725		20	9	16	21	24	16	22	28
725		50	26	17	20	34	32	5	16
725		18	22	16	15	31	34	14	18
725		13	11	16	14	23	25	19	20
725		11	16	33	18	13	12	12	30
725		46	39	36	20	39	24	12	16
725		21	7	25	28	33	18	21	25
725		22	21	23	18	16	11	9	20
725		35	23	26	29	35	15	14	18

APPENDIX 15

PORE CAST 3D STEREO IMAGES FROM SEM

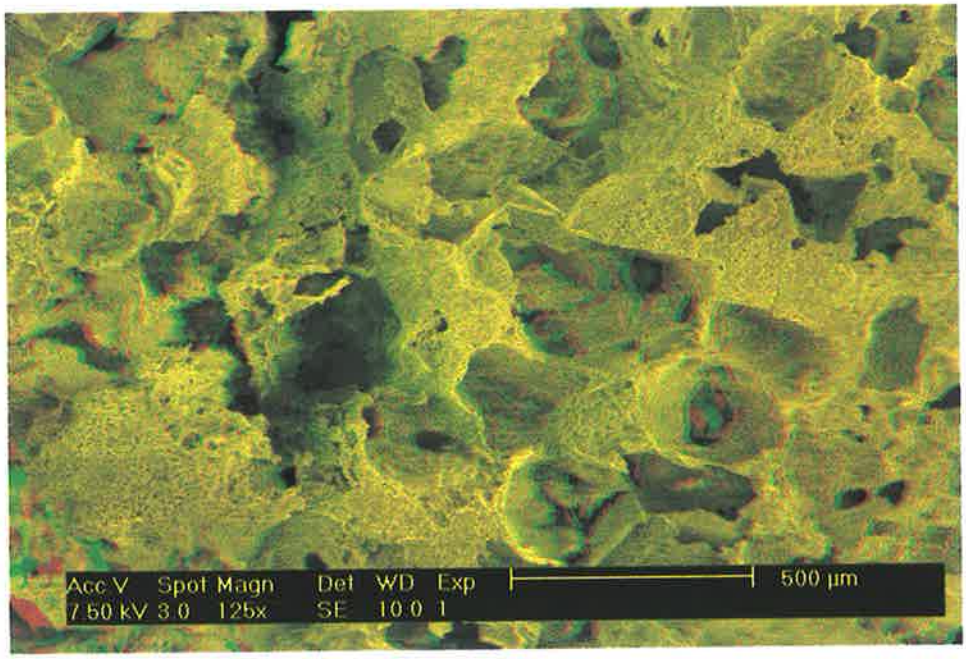

(2ae2_stereo)

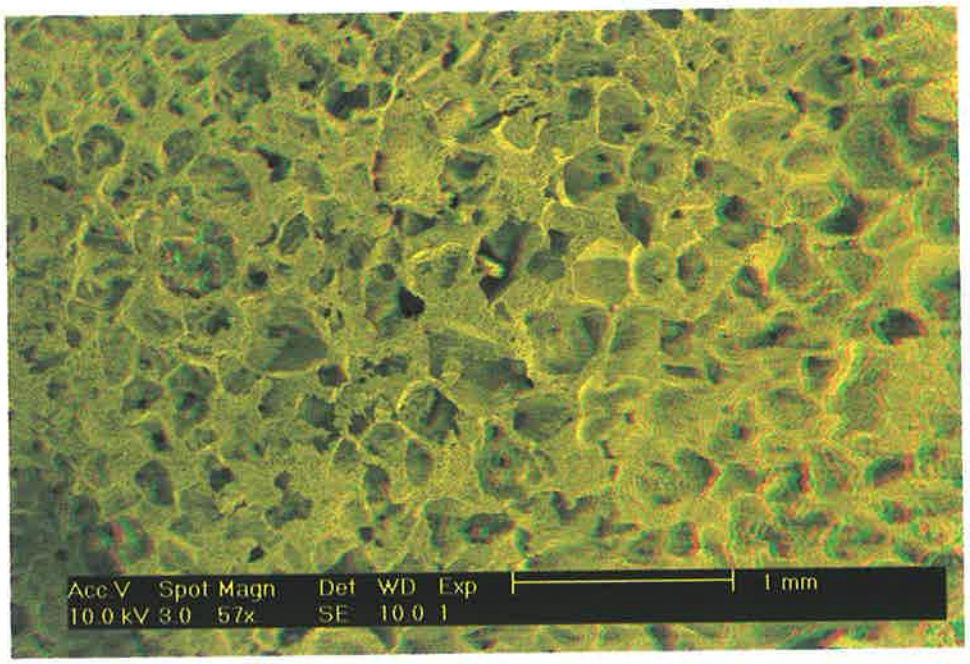

(2af2_stereo)

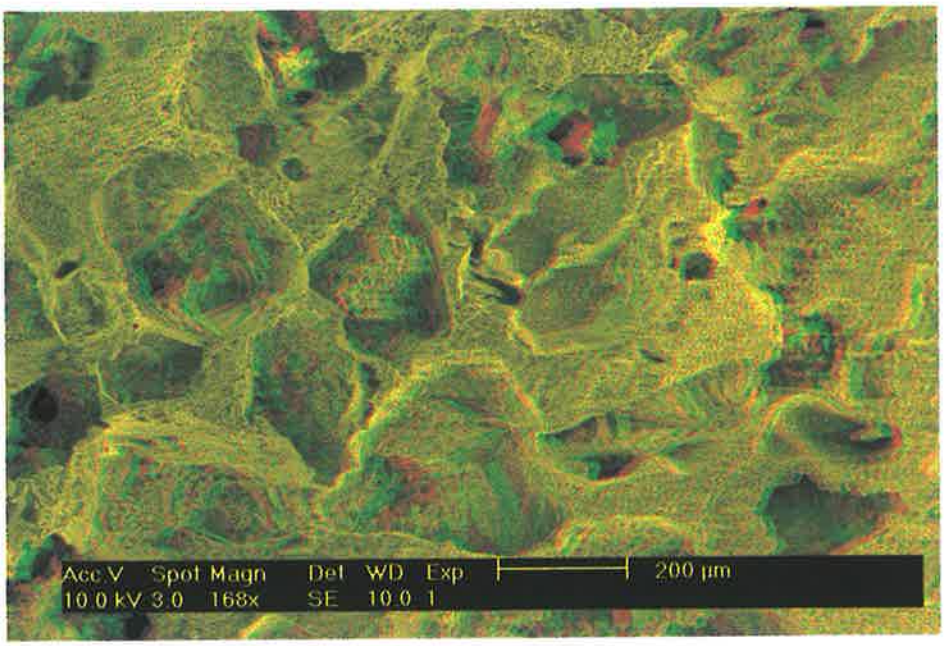

(2aa2_stereo)

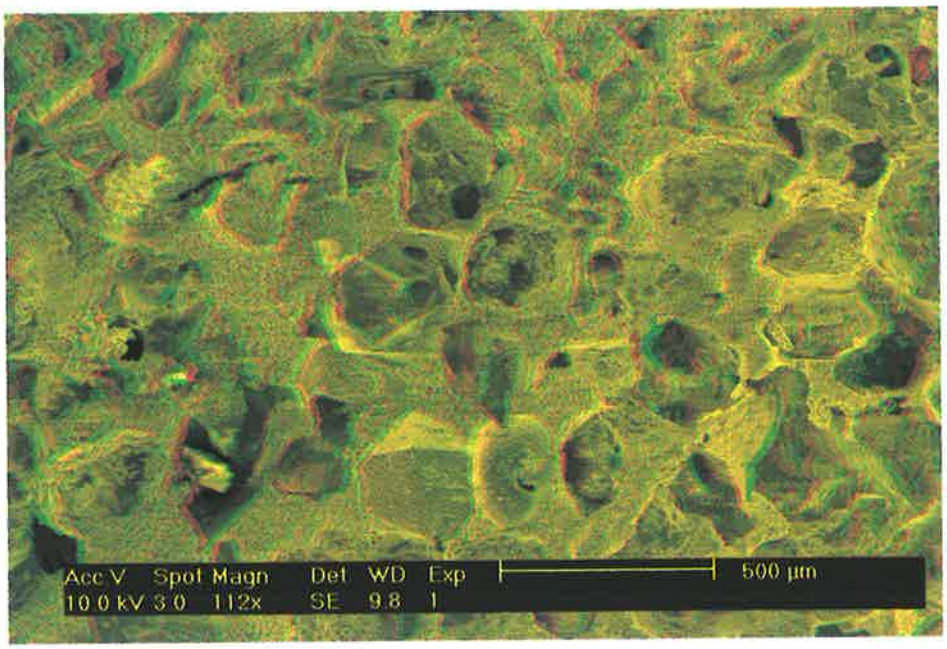

(2ac2_stereo)

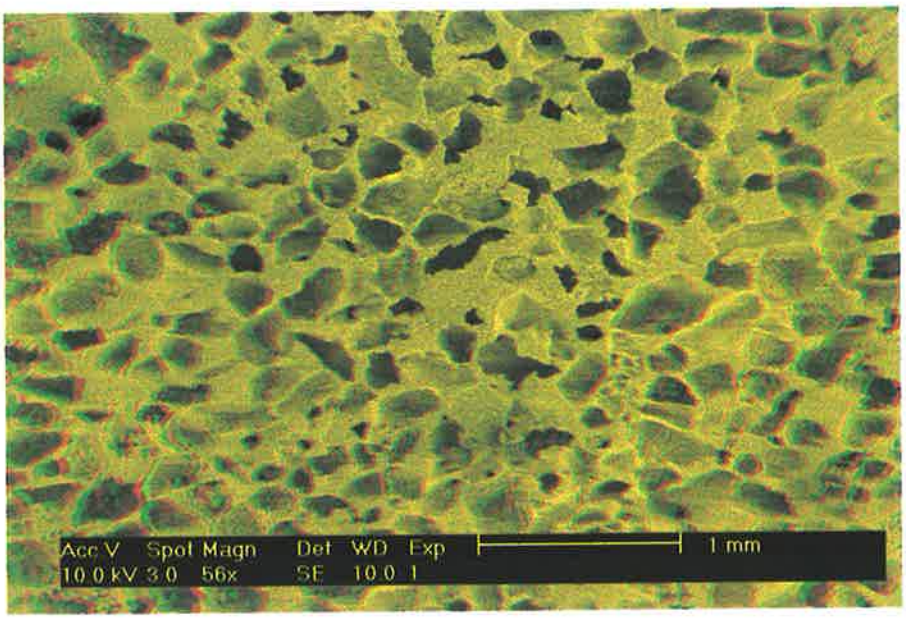

(1dh2_stereo)

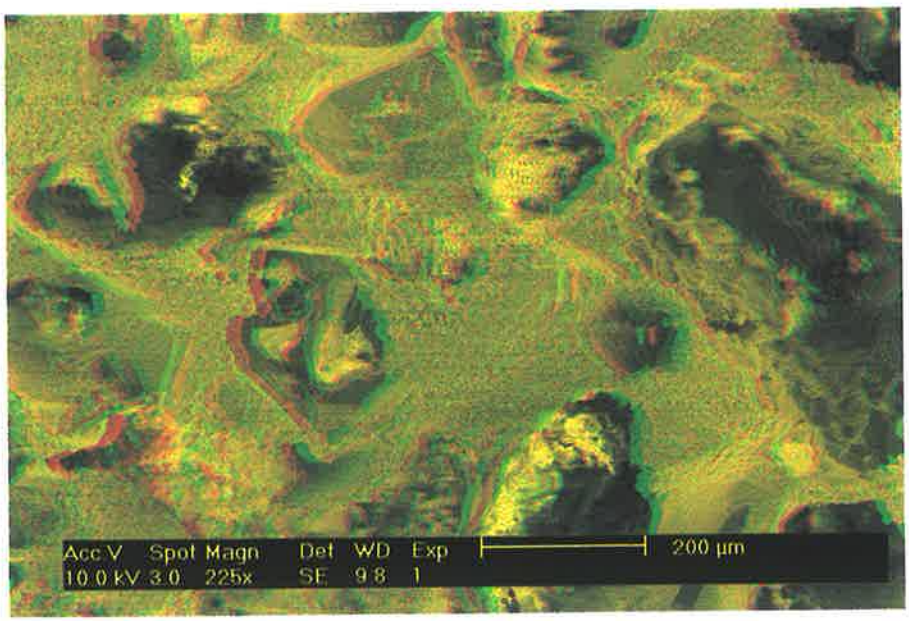

(1fc2_stereo)

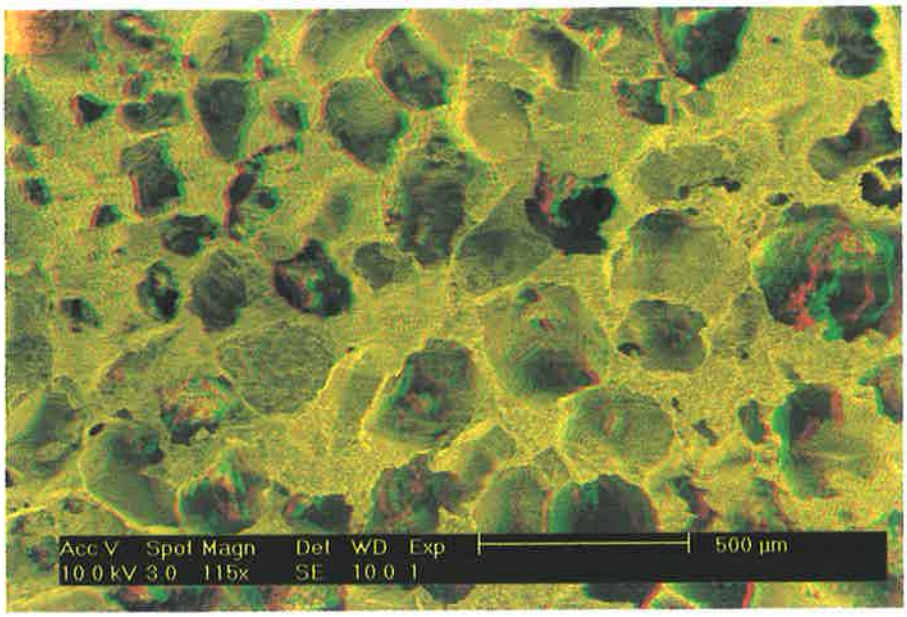

(1df2_stereo)

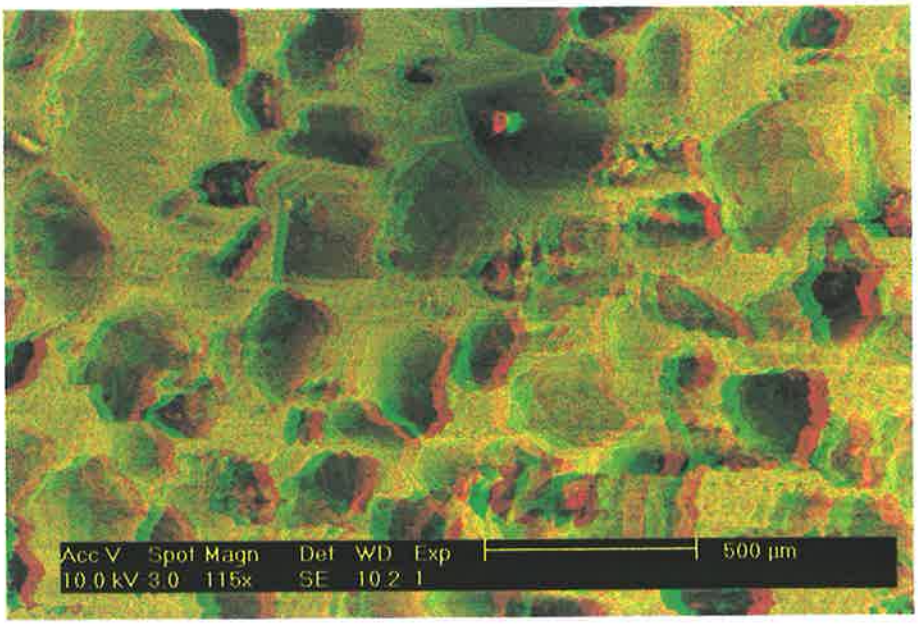

(1dg2_stereo)

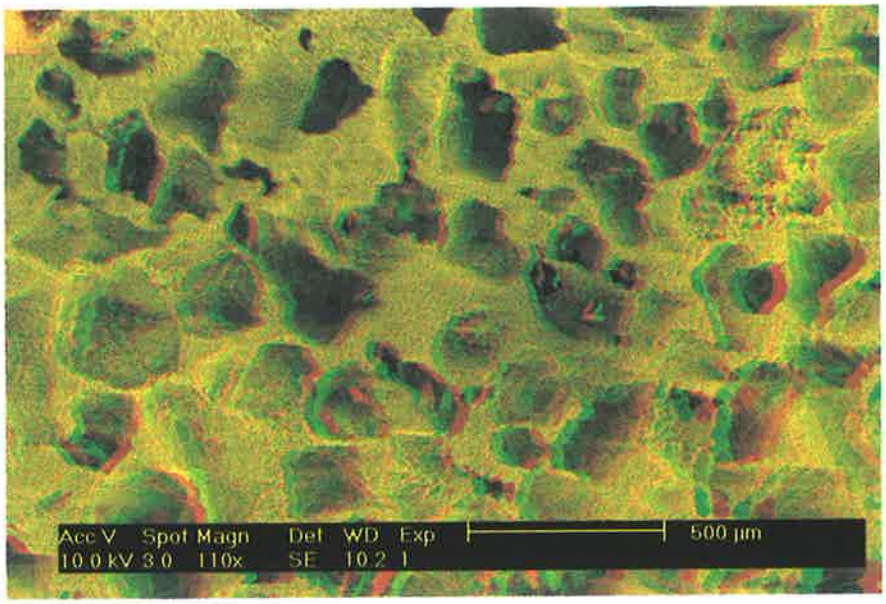

(1dc2_stereo)

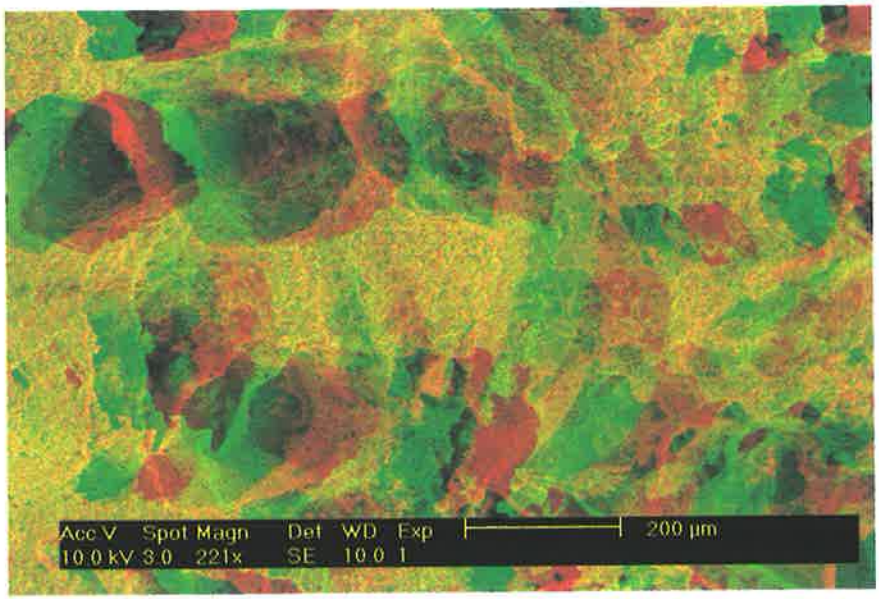

(1dd2_stereo)

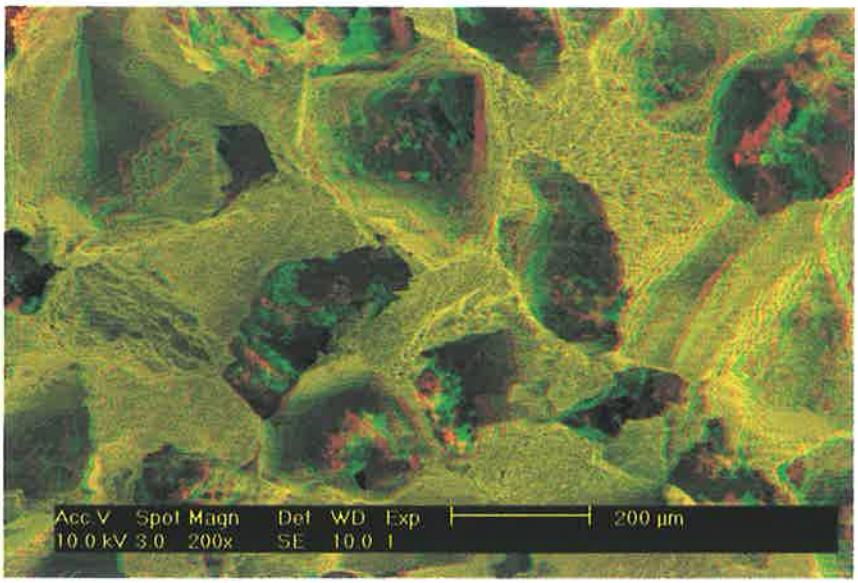

(1ae2_stereo)

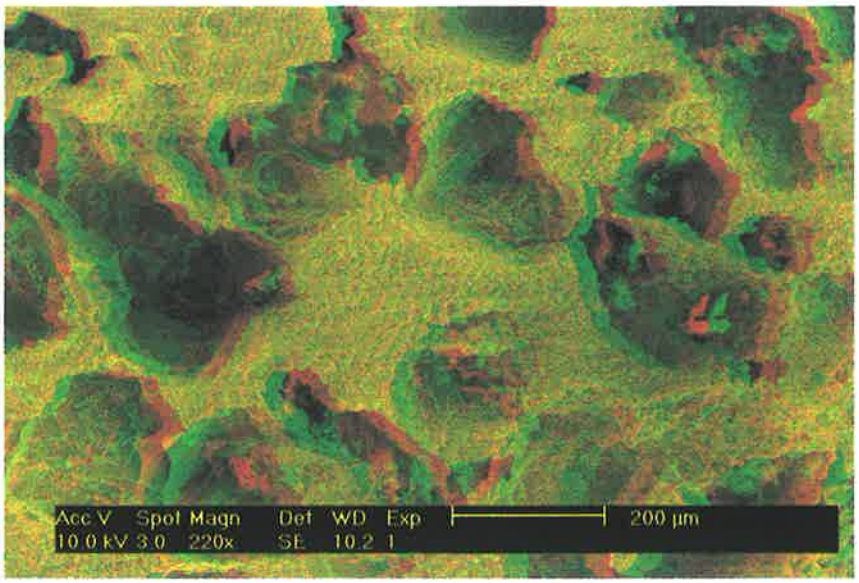

(1db2_stereo)

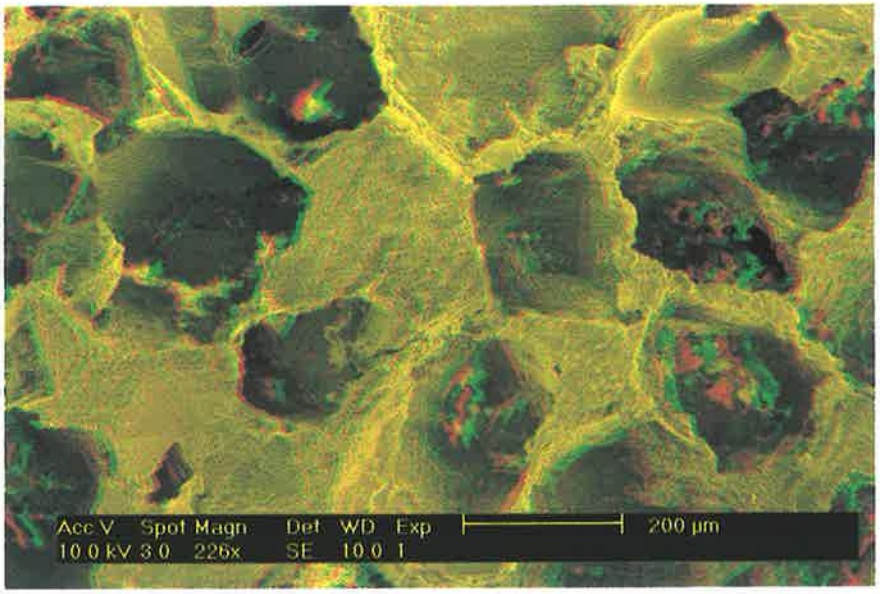

(1ac02_stereo)

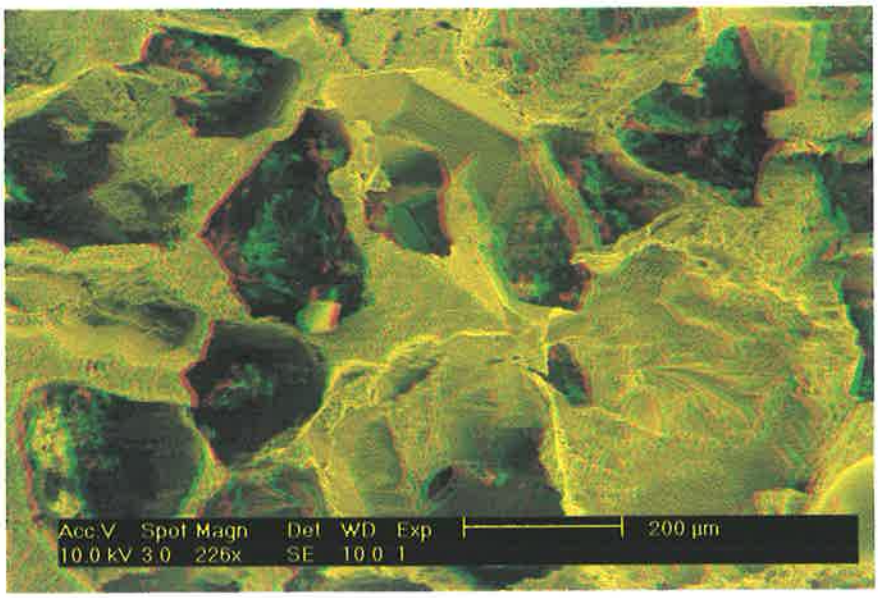

(1ad2_stereo)

APPENDIX 16
MICP WORKSHEETS

National Centre for Petroleum Geology & Geophysics

Mercury Injection Capillary Pressure Test Results

Sample	**NEJ G17 1ai lower**
Date	27\11\2000
Sample Weight	4.7820
Pen. Weight:	61.7370
Assembly Weight:	250.9300
Hg Surface Tension:	485.0000
Pen. Volume:	15.9220
Stem Volume:	1.1310
Hg Density:	13.5335
Hg volume	-
Sample volume	-
Bulk density	2.0830
Skeletal volume	-
Skeletal density	**2.6806**
Porosity	**22.2941**
% Intrusion	45.0000

x				y	
Pressure (psia)	Incremental pore volume	Cumulative pore volume	Pore Throat Size	% Hg Inj	Pore volume
2	0	0	90.4318	0.000	0.000
2.1	0.0009564	0.0009564	88.2995	0.186	0.186
2.6	0.004782	0.0057384	77.9156	1.116	0.930
3.12	0.007173	0.0129114	63.859	2.512	1.395
3.6	0.0153024	0.0282138	54.162	5.488	2.977
4.2	0.0425598	0.0707736	46.6697	13.767	8.279
5.09	0.0784248	0.1491984	39.3113	29.023	15.256
7.09	0.0951618	0.2443602	30.5357	47.535	18.512
8.58	0.0315612	0.2759214	23.3003	53.674	6.140
10.05	0.0186498	0.2945712	19.5355	57.302	3.628
12.07	0.0181716	0.3127428	16.4896	60.837	3.535
14.06	0.0129114	0.3256542	13.9282	63.349	2.512
16.05	0.009564	0.3352182	12.0684	65.209	1.860
20.01	0.0138678	0.349086	10.1549	67.907	2.698
24	0.0090858	0.3581718	8.2877	69.674	1.767
27.98	0.0066948	0.3648666	7.0008	70.977	1.302
33.96	0.007173	0.3720396	5.8952	72.372	1.395
40.22	0.0057384	0.377778	4.911	73.488	1.116
50.71	0.0081294	0.3859074	4.0318	75.070	1.581
60.53	0.0057384	0.3916458	3.2773	76.186	1.116
69.94	0.0043038	0.3959496	2.7868	77.023	0.837
85.28	0.0052602	0.4012098	2.3533	78.047	1.023
100.81	0.0052602	0.40647	1.9575	79.070	1.023
121.46	0.0038256	0.4102956	1.6416	79.814	0.744
140.05	0.0038256	0.4141212	1.3903	80.558	0.744
169.42	0.0033474	0.4174686	1.1795	81.209	0.651
200.74	0.0033474	0.420816	0.9843	81.860	0.651

241.04	0.0033474	0.4241634	0.8257	82.512	0.651
292.49	0.0028692	0.4270326	0.6844	83.070	0.558
345	0.0028692	0.4299018	0.5713	83.628	0.558
416.58	0.002391	0.4322928	0.4792	84.093	0.465
495.05	0.0009564	0.4332492	0.3998	84.279	0.186
601.59	0.0009564	0.4342056	0.333	84.465	0.186
721.18	0.0028692	0.4370748	0.2757	85.023	0.558
875.76	0.0038256	0.4409004	0.2287	85.767	0.744
1036.48	0.002391	0.4432914	0.1905	86.233	0.465
1261.77	0.0014346	0.444726	0.1589	86.512	0.279
1458.52	0.0014346	0.4461606	0.1337	86.791	0.279
1775	0.0028692	0.4490298	0.1129	87.349	0.558
2090.42	0.0019128	0.4509426	0.0942	87.721	0.372
2529.72	0.0014346	0.4523772	0.079	88.000	0.279
2941.88	0.0014346	0.4538118	0.0665	88.279	0.279
3558.31	0.0014346	0.4552464	0.0562	88.558	0.279
4284.3	0.0019128	0.4571592	0.0465	88.930	0.372
5008.03	0.0014346	0.4585938	0.0392	89.209	0.279
5992.98	0.0004782	0.459072	0.0331	89.302	0.093
6971.89	0.0014346	0.4605066	0.0281	89.581	0.279
8489.96	0.0004782	0.4609848	0.0236	89.674	0.093
9955.85	0.0009564	0.4619412	0.0197	89.860	0.186
11985.38	0.0028692	0.4648104	0.0166	90.419	0.558
14437.28	0.0028692	0.4676796	0.0138	90.977	0.558
17342.08	0.0028692	0.4705488	0.0115	91.535	0.558
20728.18	0.0028692	0.473418	0.0096	92.093	0.558
24902.25	0.0028692	0.4762872	0.008	92.651	0.558
29953.71	0.0057384	0.4820256	0.0067	93.767	1.116
34962.94	0.0062166	0.4882422	0.0056	94.977	1.209
40031.8	0.004782	0.4930242	0.0048	95.907	0.930
45046.01	0.0052602	0.4982844	0.0043	96.930	1.023
49899.77	0.007173	0.5054574	0.0038	98.326	1.395
54730.48	0.0028692	0.5083266	0.0035	98.884	0.558
59795.79	0.0057384	0.514065	0.0032	100.000	1.116

National Centre for Petroleum Geology & Geophysics

Mercury Injection Capillary Pressure Test Results

Sample	**NEJ G17 1fi**
Date	27\11\2000
Sample Weight	3.2190
Pen. Weight:	61.6630
Assembly Weight:	133.3880
Hg Surface Tension:	485.0000
Pen. Volume:	6.5979
Stem Volume:	1.1310
Hg Density:	13.5335
Hg volume	-
Sample volume	-
Bulk density	2.0958
Skeletal volume	-
Skeletal density	**2.5941**
Porosity	**19.2107**
% Intrusion	26.0000

x				y	
Pressure (psia)	Incremental pore volume	Cumulative pore volume	Pore Throat Size	% Hg Inj	Pore volume
2	0	0	90.4318	0.000	0.000
2.11	0.0006438	0.0006438	88.0694	0.219	0.219
2.62	0.0028971	0.0035409	77.3996	1.204	0.985
3.11	0.0051504	0.0086913	63.5875	2.954	1.751
3.6	0.0093351	0.0180264	54.1871	6.127	3.173
4.2	0.0196359	0.0376623	46.6813	12.801	6.674
5.08	0.0550449	0.0927072	39.3303	31.510	18.709
7.07	0.0666333	0.1593405	30.5922	54.158	22.648
8.57	0.0218892	0.1812297	23.3515	61.597	7.440
10.06	0.0131979	0.1944276	19.5476	66.083	4.486
12.05	0.0112665	0.2056941	16.4972	69.912	3.829
14.03	0.0083694	0.2140635	13.9483	72.757	2.845
16.02	0.006438	0.2205015	12.0889	74.945	2.188
20.03	0.0099789	0.2304804	10.159	78.337	3.392
24.01	0.0067599	0.2372403	8.2819	80.635	2.298
27.97	0.0048285	0.2420688	7	82.276	1.641
33.97	0.0057942	0.247863	5.8953	84.245	1.969
40.34	0	0.247863	4.9041	84.245	0.000
50.35	0.0035409	0.2514039	4.0379	85.449	1.204
59.92	0.0051504	0.2565543	3.3053	87.199	1.751
71.05	0.0028971	0.2594514	2.7819	88.184	0.985
85.61	0.0025752	0.2620266	2.329	89.059	0.875
101.05	0.0038628	0.2658894	1.9512	90.372	1.313
120.2	0.0048285	0.2707179	1.6472	92.013	1.641
139.76	0.003219	0.2739369	1.3994	93.107	1.094
169.36	0	0.2739369	1.181	93.107	0.000
201.16	0.0012876	0.2752245	0.9835	93.545	0.438

240.73	0.0016095	0.276834	0.8252	94.092	0.547
298.72	0.0016095	0.2784435	0.6784	94.639	0.547
341.38	0.0016095	0.280053	0.5676	95.186	0.547
417.87	0.0022533	0.2823063	0.4813	95.952	0.766
490.88	0.0006438	0.2829501	0.4006	96.171	0.219
640.49	0.0019314	0.2848815	0.3254	96.827	0.656
702.67	0.0006438	0.2855253	0.2699	97.046	0.219
921.32	0.0019314	0.2874567	0.2269	97.702	0.656
1003.77	0.0009657	0.2884224	0.1882	98.031	0.328
1269.4	0.0003219	0.2887443	0.1613	98.140	0.109
1436.7	0.0012876	0.2900319	0.1342	98.578	0.438
1755.26	0.0016095	0.2916414	0.1145	99.125	0.547
2086.64	0.0009657	0.2926071	0.0949	99.453	0.328
2480.45	0	0.2926071	0.0798	99.453	0.000
2966.21	0	0.2926071	0.0669	99.453	0.000
3554.65	0.0012876	0.2938947	0.0559	99.891	0.438
4317.33	0.0003219	0.2942166	0.0464	100.000	0.109

National Centre for Petroleum Geology & Geophysics

Mercury Injection Capillary Pressure Test Results

Sample	**NEJ G17 2ai**
Date	27\11\2000
Sample Weight	3.9950
Pen. Weight:	61.7500
Assembly Weight:	254.5380
Hg Surface Tension:	485.0000
Pen. Volume:	15.9220
Stem Volume:	1.1310
Hg Density:	13.5335
Hg volume	-
Sample volume	-
Bulk density	2.0259
Skeletal volume	-
Skeletal density	**2.6557**
Porosity	**23.7136**
% Intrusion	41.0000

x				y	
Pressure (psia)	Incremental pore volume	Cumulative pore volume	Pore Throat Size	% Hg Inj	Pore volume
2	0	0	90.4318	0.000	0.000
2.1	0.001598	0.001598	88.3028	0.342	0.342
2.61	0.005593	0.007191	77.6909	1.541	1.199
3.1	0.0107865	0.0179775	63.7828	3.853	2.312
3.61	0.033558	0.0515355	54.25	11.045	7.192
4.2	0.0667165	0.118252	46.61	25.342	14.298
5.1	0.071111	0.189363	39.2866	40.582	15.240
7.06	0.057528	0.246891	30.562	52.911	12.329
8.58	0.019975	0.266866	23.3556	57.192	4.281
10.06	0.0131835	0.2800495	19.5288	60.017	2.825
12.06	0.012784	0.2928335	16.4881	62.757	2.740
14.05	0.009588	0.3024215	13.9383	64.812	2.055
16.02	0.0075905	0.310012	12.0837	66.438	1.627
20.01	0.010387	0.320399	10.1644	68.664	2.226
24	0.007191	0.32759	8.2866	70.205	1.541
27.99	0.0051935	0.3327835	6.9992	71.318	1.113
33.98	0.0059925	0.338776	5.8926	72.603	1.284
40.37	0.0019975	0.3407735	4.9017	73.031	0.428
50.16	0.0043945	0.345168	4.0431	73.973	0.942
60.27	0.005593	0.350761	3.3035	75.171	1.199
70.32	0.004794	0.355555	2.7865	76.199	1.027
85.39	0.0067915	0.3623465	2.3451	77.654	1.455
100.33	0.0051935	0.36754	1.9604	78.767	1.113
121.14	0.0051935	0.3727335	1.6479	79.880	1.113
140.44	0.0043945	0.377128	1.3904	80.822	0.942
170.43	0.0051935	0.3823215	1.1745	81.935	1.113
199.07	0.003196	0.3855175	0.9849	82.620	0.685

239.7	0.0027965	0.388314	0.8315	83.219	0.599
295.88	0.0035955	0.3919095	0.6829	83.990	0.771
344.38	0.0019975	0.393907	0.5682	84.418	0.428
409.59	0.003196	0.397103	0.4834	85.103	0.685
496.66	0.002397	0.3995	0.4029	85.616	0.514
612.13	0.0027965	0.4022965	0.3298	86.216	0.599
713.39	0.0019975	0.404294	0.2745	86.644	0.428
934.83	0.003196	0.40749	0.2235	87.329	0.685
999.53	0.0011985	0.4086885	0.1872	87.586	0.257
1269.98	0.0003995	0.409088	0.1617	87.671	0.086
1464.59	0	0.409088	0.133	87.671	0.000
1784.25	0.0003995	0.4094875	0.1124	87.757	0.086
2070.18	0	0.4094875	0.0944	87.757	0.000
2536.21	0.000799	0.4102865	0.0793	87.928	0.171
2984.77	0.000799	0.4110855	0.066	88.099	0.171
3537.41	0	0.4110855	0.0559	88.099	0.000
4302.6	0.000799	0.4118845	0.0466	88.271	0.171
4997.25	0.000799	0.4126835	0.0391	88.442	0.171
5974.39	0	0.4126835	0.0332	88.442	0.000
6974.95	0.001598	0.4142815	0.0281	88.784	0.342
8506.86	0.001598	0.4158795	0.0236	89.127	0.342
9995.47	0.0003995	0.416279	0.0197	89.212	0.086
11952.59	0.0019975	0.4182765	0.0166	89.640	0.428
14441.75	0.0035955	0.421872	0.0138	90.411	0.771
17323.13	0.002397	0.424269	0.0115	90.925	0.514
20792.64	0.0043945	0.4286635	0.0096	91.866	0.942
24879.75	0.0011985	0.429862	0.008	92.123	0.257
29944.71	0.003995	0.433857	0.0067	92.979	0.856
34919.16	0.004794	0.438651	0.0056	94.007	1.027
40093.78	0.00799	0.446641	0.0048	95.719	1.712
44933.36	0.003995	0.450636	0.0043	96.575	0.856
50071.07	0.00799	0.458626	0.0038	98.288	1.712
54975.95	0.0059925	0.4646185	0.0035	99.572	1.284
59928.05	0.0019975	0.466616	0.0032	100.000	0.428

National Centre for Petroleum Geology & Geophysics

Mercury Injection Capillary Pressure Test Results

Sample	**NEJ G17 1dii**
Date	27\11\2000
Sample Weight	3.4940
Pen. Weight:	61.5400
Assembly Weight:	257.0060
Hg Surface Tension:	485.0000
Pen. Volume:	15.9220
Stem Volume:	1.1310
Hg Density:	13.5335
Hg volume	-
Sample volume	-
Bulk density	2.0115
Skeletal volume	-
Skeletal density	**2.5882**
Porosity	**22.2845**
% Intrusion	34.0000

x				y	
Pressure (psia)	Incremental pore volume	Cumulative pore volume	Pore Throat Size	% Hg Inj	Pore volume
2	0	0	90.4318	0.000	0.000
2.11	0.001747	0.001747	88.175	0.451	0.451
2.62	0.0062892	0.0080362	77.5288	2.076	1.625
3.1	0.0080362	0.0160724	63.7516	4.152	2.076
3.6	0.0150242	0.0310966	54.2745	8.032	3.881
4.18	0.026205	0.0573016	46.7313	14.801	6.769
5.08	0.0468196	0.1041212	39.4249	26.895	12.094
7.07	0.075121	0.1792422	30.585	46.300	19.404
8.58	0.0290002	0.2082424	23.3355	53.791	7.491
10.07	0.0178194	0.2260618	19.5165	58.394	4.603
12.05	0.0150242	0.241086	16.4851	62.274	3.881
14.04	0.0108314	0.2519174	13.9451	65.072	2.798
16.02	0.0080362	0.2599536	12.0844	67.148	2.076
20.01	0.0115302	0.2714838	10.1632	70.126	2.978
24	0.0073374	0.2788212	8.2872	72.022	1.895
27.98	0.0055904	0.2844116	7.0011	73.466	1.444
33.96	0.0062892	0.2907008	5.8953	75.090	1.625
40.15	0	0.2907008	4.9152	75.090	0.000
50.33	0.0055904	0.2962912	4.0491	76.534	1.444
60.6	0.0048916	0.3011828	3.289	77.798	1.264
70.47	0.0031446	0.3043274	2.7757	78.610	0.812
84.74	0.0031446	0.307472	2.3505	79.422	0.812
100.4	0.0041928	0.3116648	1.9678	80.505	1.083
121.66	0.0024458	0.3141106	1.644	81.137	0.632
139.76	0.0024458	0.3165564	1.3904	81.769	0.632
171.78	0.003494	0.3200504	1.1735	82.671	0.903

199.39	0.0020964	0.3221468	0.98	83.213	0.542
239.88	0.0027952	0.324942	0.8305	83.935	0.722
296.9	0.0013976	0.3263396	0.6816	84.296	0.361
345.34	0.0020964	0.328436	0.5664	84.838	0.542
421.49	0.001747	0.330183	0.4764	85.289	0.451
491.44	0.0013976	0.3315806	0.3986	85.650	0.361
623.98	0.001747	0.3333276	0.3289	86.101	0.451
708.74	0.001747	0.3350746	0.2725	86.552	0.451
910.21	0.0020964	0.337171	0.2269	87.094	0.542
999.09	0.0020964	0.3392674	0.1899	87.635	0.542
1277.13	0.0020964	0.3413638	0.1613	88.177	0.542
1452	0.0010482	0.342412	0.1331	88.448	0.271
1785.12	0.001747	0.344159	0.1129	88.899	0.451
2075.12	0.0003494	0.3445084	0.0942	88.989	0.090
2520.04	0.0013976	0.345906	0.0795	89.350	0.361
2959.38	0.0010482	0.3469542	0.0664	89.621	0.271
3570.5	0.0003494	0.3473036	0.0559	89.711	0.090
4306.2	0.001747	0.3490506	0.0463	90.162	0.451
5013.37	0.0013976	0.3504482	0.039	90.523	0.361
5983.06	0	0.3504482	0.0332	90.523	0.000
6969.78	0	0.3504482	0.0281	90.523	0.000
8519.08	0.001747	0.3521952	0.0236	90.975	0.451
10004.85	0	0.3521952	0.0197	90.975	0.000
11991.08	0.001747	0.3539422	0.0166	91.426	0.451
14456.83	0.001747	0.3556892	0.0138	91.877	0.451
17384.7	0.0024458	0.358135	0.0115	92.509	0.632
20733.89	0.0010482	0.3591832	0.0096	92.780	0.271
24902.63	0.0027952	0.3619784	0.008	93.502	0.722
29933.17	0.0031446	0.365123	0.0067	94.314	0.812
34877.81	0.0027952	0.3679182	0.0056	95.036	0.722
40114.91	0.005241	0.3731592	0.0048	96.390	1.354
45011.65	0.0013976	0.3745568	0.0043	96.751	0.361
49956.3	0.0027952	0.377352	0.0038	97.473	0.722
54898.1	0.0038434	0.3811954	0.0035	98.466	0.993
59911.59	0.0059398	0.3871352	0.0032	100.000	1.534

National Centre for Petroleum Geology & Geophysics

Mercury Injection Capillary Pressure Test Results

Sample	**NEJ G17 1ai upper**
Date	27\11\2000
Sample Weight	4.8630
Pen. Weight:	61.5660
Assembly Weight:	249.9170
Hg Surface Tension:	485.0000
Pen. Volume:	15.9220
Stem Volume:	1.1310
Hg Density:	13.5335
Hg volume	-
Sample volume	-
Bulk density	2.0572
Skeletal volume	-
Skeletal density	**2.6160**
Porosity	**21.3614**
% Intrusion	45.0000

x				y	
Pressure (psia)	Incremental pore volume	Cumulative pore volume	Pore Throat Size	% Hg Inj	Pore volume
2	0	0	90.4318	0.000	0.000
2.12	0.0014589	0.0014589	87.8531	0.289	0.289
2.6	0.0077808	0.0092397	77.4291	1.830	1.541
3.1	0.0141027	0.0233424	63.9982	4.624	2.794
3.6	0.0233424	0.0466848	54.3023	9.249	4.624
4.21	0.0505752	0.09726	46.5669	19.268	10.019
5.09	0.1152531	0.2125131	39.2474	42.100	22.832
7.08	0.1157394	0.3282525	30.5427	65.029	22.929
8.56	0.0252876	0.3535401	23.3333	70.039	5.010
10.06	0.014589	0.3681291	19.5539	72.929	2.890
12.05	0.0131301	0.3812592	16.4887	75.530	2.601
14.03	0.0092397	0.3904989	13.9479	77.360	1.830
16.04	0.0072945	0.3977934	12.0833	78.805	1.445
20.03	0.0092397	0.4070331	10.1522	80.636	1.830
24.01	0.0063219	0.413355	8.282	81.888	1.252
27.99	0.004863	0.418218	6.9978	82.852	0.963
33.96	0.0058356	0.4240536	5.8937	84.008	1.156
40.48	0	0.4240536	4.8966	84.008	0.000
50.49	0.004863	0.4289166	4.0249	84.971	0.963
60.01	0.0111849	0.4401015	3.298	87.187	2.216
70.45	0.0043767	0.4444782	2.7905	88.054	0.867
85.74	0.004863	0.4493412	2.3384	89.017	0.963
100.46	0.0004863	0.4498275	1.9549	89.114	0.096
120.35	0.0043767	0.4542042	1.6516	89.981	0.867
141.07	0.0038904	0.4580946	1.3924	90.751	0.771
172.04	0.0009726	0.4590672	1.1667	90.944	0.193
199.51	0	0.4590672	0.9789	90.944	0.000

239.93	0	0.4590672	0.8302	90.944	0.000
295.92	0.0034041	0.4624713	0.6825	91.618	0.674
347.21	0.0043767	0.466848	0.5661	92.486	0.867
415.08	0.0034041	0.4702521	0.4783	93.160	0.674
497.73	0.0014589	0.471711	0.3996	93.449	0.289
627.58	0.0009726	0.4726836	0.3258	93.642	0.193
708.13	0.0029178	0.4756014	0.2718	94.220	0.578
882.69	0.0072945	0.4828959	0.2302	95.665	1.445
1064.38	0.0034041	0.4863	0.1874	96.339	0.674
1272.5	0.0014589	0.4877589	0.156	96.628	0.289
1453.78	0.0004863	0.4882452	0.1333	96.724	0.096
1777.48	0.0014589	0.4897041	0.1131	97.013	0.289
2099.55	0.0009726	0.4906767	0.0939	97.206	0.193
2515.76	0.0004863	0.491163	0.079	97.303	0.096
2955.56	0.0004863	0.4916493	0.0665	97.399	0.096
3550.8	0.0009726	0.4926219	0.0561	97.592	0.193
4301.07	0.0004863	0.4931082	0.0465	97.688	0.096
4984.99	0.0004863	0.4935945	0.0392	97.784	0.096
5978.1	0.0009726	0.4945671	0.0333	97.977	0.193
6975.12	0	0.4945671	0.0281	97.977	0.000
8514.84	0.0004863	0.4950534	0.0236	98.073	0.096
9979.32	0	0.4950534	0.0197	98.073	0.000
11957.03	0	0.4950534	0.0166	98.073	0.000
14466.09	0	0.4950534	0.0138	98.073	0.000
17430.89	0	0.4950534	0.0114	98.073	0.000
20700.58	0	0.4950534	0.0096	98.073	0.000
24912.29	0	0.4950534	0.008	98.073	0.000
29873.6	0.0029178	0.4979712	0.0067	98.651	0.578
34898.47	0	0.4979712	0.0056	98.651	0.000
39934.36	0	0.4979712	0.0049	98.651	0.000
45044.75	0.0009726	0.4989438	0.0043	98.844	0.193
50007.52	0	0.4989438	0.0038	98.844	0.000
55045.86	0.0019452	0.500889	0.0035	99.229	0.385
59985.18	0.0038904	0.5047794	0.0032	100.000	0.771